Study of micro-plasma jets as sources of reactive species for biomedical applications

Kyriakos Sklias

université PARIS-SACLAY

Study of micro-plasma jets as sources of reactive species for biomedical applications

Etude de microjets de plasma comme sources d'espèces réactives pour des applications biomédicales

Thèse de doctorat de l'université Paris-Saclay

École doctorale n°572 : ondes et matière (EDOM)
Spécialité de doctorat : Physique
Graduate School : Physique Référent : Faculté des Sciences d'Orsay

Thèse préparée dans l'unité de recherche LPGP Laboratoire de physique des gaz et des plasmas (Université Paris-Saclay, CNRS), sous la direction de **Stéphane PASQUIERS**, Directeur de recherche, et la co-encadrement de **João SANTOS SOUSA**, Chargé de recherche

Thèse soutenue à Paris-Saclay, le 30 Mars 2022 par

Kyriakos SKLIAS

Composition du Jury

Emmanuel ODIC Professeur, Centrale Supélec, Université Paris-Saclay	Président
Annemie BOGAERTS Professeur, Department of Chemistry, University of Antwerp	Rapporteur & Examinatrice
Cristina CANAL Professeur agrégé, Department of Materials Science and Engineering, Technical University of Catalonia	Rapporteur & Examinatrice
Stephan REUTER Professeur agrégé, Département de génie physique, Polytechnique Montréal	Examinateur
Stéphane PASQUIERS Directeur de recherche, LPGP, CNRS & Université Paris-Saclay	Directeur de thèse

THESE DE DOCTORAT

NNT : 2022UPASP036

université PARIS-SACLAY | ÉCOLE DOCTORALE Ondes et matière (EDOM)

Title : STUDY OF MICRO-PLASMA JETS AS SOURCES OF REACTIVE SPECIES FOR BIOMEDICAL APPLICATIONS

Keywords : Cold plasma jet, microplasma, atmospheric pressure discharge, high frequency high voltage pulsed discharge, plasma medicine, plasma oncology

In this work, three different cold atmospheric-pressure plasma reactors were studied as sources of reactive oxygen and nitrogen species for biomedical applications. The reactors used were a single-plasma jet, a multi-plasma jet and a micro-cathode sustained discharge. This work is divided in three parts. The first part contains the study of the gaseous phase of the plasmas and its main purpose is to provide information on the physical and chemical properties of the produced plasmas. We found that the electric field in the front of the ionization wave increases when the plasma approaches the treated liquid. As a result, the gas temperature as well as the electron density of the plasma are also greater closer to the liquid. The second part of this work is a study of the chemical composition of plasma-treated PBS (pPBS). Thus, the production of H_2O_2, NO_2^-, NO_3^-, •OH, $O_2(a^1\Delta g)$, O_3, HCl^- and $ONOO^-$ was investigated in the pPBS. Alongside, the pH and conductivity of the pPBS were also measured. On top of that, the ability to conserve the long-lived reactive species (H_2O_2, NO_2^- and NO_3^-) over a long period was investigated as a function of the time and temperature of storage of the pPBS. It is shown in this work that if the pPBS is stored at pertinent conditions, the concentration of these long-lived reactive species, and, thus, the anti-cancer capacity of the pPBS remains stable for more than 75 days. Knowing that these long-lived reactive oxygen and nitrogen species are the main drivers of the anti-cancer capacity of plasma treatment in oncology, the third part of this work, performed in close collaboration with biologists, was the plasma application on biological targets and the assessment of these reactive species' contribution to its cytotoxicity. Thus, the anti-tumor capacity of direct and indirect plasma treatments, using two models of head & neck cancer cells and three normal cell lines, was assessed in terms of metabolic cell activity, cell viability, lipid peroxidation, intracellular ROS production and caspase 3/7 induction. We found that the selectivity of plasma treatment towards killing cancer cells instead of normal cells is highly dependent on the short-, intermediate- and long-lived reactive species that are present in the pPBS. More specifically, when the cells are treated directly with the plasma, we observed a strong effect on the normal cells, while the cancer cells were moderately affected. On the other hand, when indirect plasma treatment was used, the effect on the normal cells was minor, while the effect on the cancer cells was significant (slightly less efficient than direct plasma treatment). Our hypothesis is that short- and intermediate-lived reactive species that are present only during the direct plasma treatment damage the cellular membrane of the normal cells allowing the long-lived reactive species to penetrate into the cells. To support this hypothesis and to better understand the interaction of the cellular membrane with these reactive species, the effect of the plasma treatment on bovine serum albumin proteins and different types of phospholipids was investigated. Followingly, we investigated the potential capabilities of the combined application of indirect plasma treatment and microsecond pulsed electric fields (μsPEFs) to outperform *in vitro* cell electropermeabilisation, the basis of electrochemotherapy (ECT). We showed that the combined treatment opens the possibility to reduce the amplitude of the electric pulses used in ECT, allowing an ECT treatment with reduced side-effects. Finally, the *in vivo* application of the pPBS on inbred female immunocompetent C57Bl/6J mice was also studied. It is shown that the combination of indirect plasma treatment and μsPEFs delays the tumour growth of the mice.

Titre : ETUDE DE MICROJETS DE PLASMA COMME SOURCES D'ESPÈCES RÉACTIVES POUR DES APPLICATIONS BIOMÉDICALES

Mots clés : Jet de plasma froid, Micro-plasma, Décharge à pression atmosphérique, Décharge impulsionnelle à haute tension et à haute fréquence, Plasma Médecine, Plasma Oncologie

Dans ce travail, trois différents réacteurs à plasma froid à pression atmosphérique ont été étudiés comme sources d'espèces réactives d'oxygène et d'azote pour des applications biomédicales. Les réacteurs utilisés étaient un jet de plasma, un multi-jet de plasma et une micro-cathode sustained discharge. Ce travail est divisé en trois parties. La première partie concerne l'étude de la phase gazeuse des plasmas et son objectif principal est de fournir des informations sur les propriétés physiques et chimiques des plasmas produits. Nous avons constaté que le champ électrique sur le front de l'onde d'ionisation augmente lorsque le plasma s'approche du liquide traité. En conséquence, la température du gaz ainsi que la densité électronique du plasma sont également plus importantes plus près du liquide. La deuxième partie de ce travail est une étude de la composition chimique du PBS traité au plasma (pPBS). Ainsi, la production de H_2O_2, NO_2^-, NO_3^-, •OH, $O_2(a1\Delta g)$, O_3, HCl^- et $ONOO^-$ a été étudiée dans le pPBS. Parallèlement, le pH et la conductivité du pPBS ont également été mesurés. De plus, la capacité à conserver les espèces réactives à longue durée de vie (H_2O_2, NO_2^- et NO_3^-) sur une longue période a été étudiée en fonction du temps et de la température de stockage du pPBS. Il est montré dans ce travail que si le pPBS est stocké dans des conditions pertinentes, la concentration de ces espèces réactives à longue durée de vie, et donc la capacité anticancéreuse du pPBS, reste stable pendant plus de 75 jours. Sachant que ces espèces réactives de l'oxygène et de l'azote sont les principaux moteurs de la capacité anticancéreuse du traitement par plasma en oncologie, la troisième partie de ce travail, réalisée en étroite collaboration avec des biologistes, concerne l'application du plasma sur des cibles biologiques et l'évaluation de la contribution de ces espèces réactives à sa cytotoxicité. Ainsi, en utilisant deux modèles de cellules cancéreuses de la tête et du cou et trois lignées cellulaires normales, la capacité anti-tumorale des traitements directs et indirects au plasma a été évaluée selon l'activité métabolique cellulaire, la viabilité cellulaire, la peroxydation lipidique, la production de ROS intracellulaires et l'induction de la caspase 3/7. Nous avons constaté que la sélectivité du traitement au plasma pour tuer les cellules cancéreuses au lieu des cellules normales dépend fortement des espèces réactives à courte, moyenne et longue durée de vie présentes dans le pPBS. Plus précisément, lorsque les cellules sont traitées directement avec le plasma, nous avons observé un fort effet sur les cellules normales, tandis que les cellules cancéreuses étaient modérément affectées. En revanche, lorsque le traitement indirect au plasma était utilisé, l'effet sur les cellules normales était mineur, tandis que l'effet sur les cellules cancéreuses était significatif (légèrement moins efficace que le traitement direct au plasma). Notre hypothèse est que les espèces réactives à courte et moyenne durée de vie présentes uniquement lors du traitement direct au plasma endommagent la membrane cellulaire des cellules normales, permettant aux espèces réactives à longue durée de vie de pénétrer dans les cellules. Par la suite, nous avons étudié les capacités potentielles de l'application combinée du traitement indirect au plasma et des champs électriques pulsés microsecondes (μsPEF), pour surpasser l'électroperméabilisation cellulaire in vitro, la base de l'électrochimiothérapie (ECT). Nous avons montré que le traitement combiné ouvre la possibilité de réduire l'amplitude des impulsions électriques utilisées en ECT, permettant un traitement ECT avec des effets secondaires réduits. Enfin, l'application in vivo du pPBS sur des souris femelles consanguines immunocompétentes C57Bl/6J a également été étudiée. Il est démontré que la combinaison du traitement indirect au plasma et des μsPEF retarde la croissance tumorale des souris.

“The mind is not a vessel to be filled but a fire to be kindled.”
Plutarch

Acknowledgements

The present work was carried out in Laboratoire de physique des gaz et des plasmas (LPGP) and more specifically in the DIREBIO group. First of all, I would like to tremendously thank my thesis co-supervisor João SANTOS SOUSA who allowed me to carry out this thesis in the best conditions and who was able to pass me over his knowledge, his academic and professional skills as well as his precious advices while in parallel he supported all the ideas I had and encouraged me to attend several workshops and conferences. I would also like to thank him warmly for scarifying a lot of time to help me ameliorate my professional and personal skills like my organizing and linguistic capabilities (thank you for your patience with my French!). Nonetheless, I would like to thank my supervisor Stéphane PASQUIERS for our numerous exchanges and his continuous help during my thesis. A big thank you also to Pierre-Marie GIRARD for his continuous help and his availability. An important part of this thesis was due to our collaboration. You have all been very supporting and caring to me, helped me improve scientifically, academically and personally. Thank you!

I would like to thank the reviewers of my manuscript and members of the Jury, Annemie BOGAERTS and Cristina CANAL for devoting their precious time in creating very detailed reports that helped me a lot to ameliorate the present manuscript. I would like also to thank Stephan REUTER and Emmanuel ODIC for being members of my Jury. Finally, I would like to thank you all for being so interested in my work and having such an interesting and prosperous discussion the day of my presentation.

During these three and a half years, I had the opportunity to meet and collaborate with several people from different scientific backgrounds. I would like to thank the members of the GREMI laboratory with which I had a very nice collaboration and especially, Augusto STANCAMPIANO, Eric ROBERT, Jean-Michel POUVESLE and CLAIRE DOUAT. Alongside, I would also like to thank the people from Gustave Roussy Institute that completed this very nice and productive collaboration and especially, Thai-Hoa CHUNG, Luis MIR and Alain DEROUSSENT. You were all very supportive and helped me also to ameliorate both my academic and personal skills.

Moreover, I would like to thank enormously all the members of the DIREBIO team for helping me throughout my Ph.D. thesis. Especially, I would like to thank Gérard BAUVILLE for helping me in a daily basis in the preparation of the experimental configurations that I used. I would also like to thank Michel FLEURY for his continuous help on the preparation and use of different high voltage power supplies. I would also like to thank Marc BISSON for all the help with IT both during

my thesis and for the preparation of my presentation. Finally, I would like to thank Duarte Gonçalves and Thibault DARNY for all the fruitful discussions we had during our common term in LPGP.

I would also like to thank Nicolas DESSAINTS and Thierry DEVILLERS for their immediate help on logistics and all administrative services during my thesis.

The transition from being an undergraduate electrical and computer engineering student to being a Ph.D. candidate in plasma physics was a big step for me that I wouldn't have done without help. Thus, I would like to warmly thank my professor and master thesis supervisor in Greece, Panagiotis SVARNAS. He was by my side for two years and taught me numerous things regarding plasma physics, especially in an experimental level. I would also like to thank him for helping me, with his advices, to acquire my Ph.D. grant. Alongside, I would like to thank Dimitrios ATHANASOPOULOS for his patience and his invaluable advices during the two years that we worked together in Greece.

I would also like to thank Kristaq GAZELI for his continuous help all these past years. He helped me actively with his advices to acquire my Ph.D. grant and made my integration to both LPGP and France a lot easier. On top of that, I would like to thank him for being by my side as a colleague and especially as a friend throughout my Ph.D thesis.

Moreover, I would like to express my gratitude to my Greek "family" here in Paris without whom this journey might not have been possible. First, I would like to thank Sofia and Kapsalis for their support and our endless discussions. I would also like to thank Dasoulas, Papanagiotou, Nikoletzos, Panagopoulos and Mpournias which have been a great companion especially during COVID times. Having finished with the 3rd floor of the Fondation I would like to thank Sissy, Manolis and Michalis that completed this wonderful group of people with which I shared a big part of my daily life. In addition, I would like to thank the "voreious" that arrived a little bit later in my life here in Paris but managed to have a very positive impact on my daily life during the last year of my Ph.D. thesis. Mina, Stelio, Stavro, Mary, Anna and Maria thank you very much for your support, funny moments, endless discussions and nights (with drinks of course).

I would like to specially thank Maria (Mitro), with whom I have experienced many stages of my journey before and during my PhD. Maria supported me in every step I made, before, during and after my Ph.D. both psychologically and with her knowledge. Without her I wouldn't be the person I am today.

I would also like to thank my friends from Greece, Alex, Sotiria, Spyros,

Chiotis, Panagou, Katerina, Pagonis, Kostas, Mallios, Sotiriou and Drosopoulos for discussing even from far away, for mentally supporting me and for warmly welcoming me (with drinks one more time) each time I returned to Greece.

Moving towards the end, I would like to thank my partner, Lena with whom I was fortunate enough to share the most difficult but at the same time the most beautiful years of my life. She was my crutch throughout all my difficulties both from distance and up close. Without her support and patience all the things that I have accomplished might not have been possible.

Finally, my greatest gratitude goes to my parents and my grandparents, who have let me grow to a person without fear, strong and independent. Mama and Mpampa thanks for letting me decide what I want to do even if it was far away from you and for supporting me psychologically in a daily basis. Now, if I would dedicate this PhD to someone that would be my sister, who has always been by my side, patiently, without ever complaining about anything. I am sure she will have an excellent future both as a person and as a young scientist.

Résumé en français

Les plasmas froids à pression atmosphérique ont été largement étudiés au cours de la dernière décennie pour leurs propriétés anticancéreuses. Il est maintenant bien établi que le plasma produit par de nombreux réacteurs différents peut être une stratégie anti-cancer efficace. La capacité anticancéreuse des plasmas est principalement due aux espèces réactives de l'oxygène et de l'azote, produites en phase gazeuse et transférées au liquide par le flux gazeux ou directement produites dans le liquide traité par plasma, constituant des sous-produits des espèces en phase liquide et en phase gazeuse. Les propriétés physiques du plasma, comme le champ électromagnétique, le rayonnement ultraviolet et la chaleur peuvent augmenter l'efficacité du plasma contre les tumeurs même si leur contribution à sa capacité anticancéreuse est moins importante que les propriétés chimiques du plasma. Néanmoins, ces propriétés physiques sont directement responsables de la composition chimique du plasma et du liquide traité au plasma. Ainsi, on peut facilement en déduire que pour que le plasma soit utilisé comme stratégie anticancéreuse efficace, il doit d'abord être largement étudié en trois étapes différentes. Tout d'abord, ses propriétés en phase gazeuse doivent être déterminées. Cela comprend l'étude de la température du gaz, des propriétés électriques du plasma et de sa composition chimique. La température du gaz et ses propriétés électriques doivent être étudiées principalement pour s'assurer que lorsque le plasma va traiter un cancer in vivo, il sera sûr et ne causera pas de brûlures ni des chocs électriques au patient et secondairement parce que la chaleur et le les propriétés électriques du plasma pourraient aussi contribuer au traitement du cancer. La composition chimique de la phase gazeuse du plasma doit être étudiée pour deux raisons principales. Elle est directement liée à la chimie en phase liquide résultante du traitement du liquide au plasma, et même si la plupart des cibles biologiques se trouvent dans un liquide ou recouvertes d'une couche liquide, il pourrait y avoir des exceptions où la cible est solide et, donc, le plasma est directement en contact avec la tumeur. Deuxièmement, l'efficacité du plasma contre une tumeur est principalement due aux espèces réactives à courte, intermédiaire et longue durée de vie qui sont produites et/ou transférées dans un liquide et qui sont toxiques pour les cellules cancéreuses. Ainsi, une étude approfondie de la composition chimique du liquide traité par plasma est indispensable. Au-delà de la composition en espèces réactives, d'autres propriétés chimiques du liquide doivent également être étudiées telles que son pH et sa conductivité car elles pourraient également jouer un rôle dans son action cytotoxique. Enfin, l'effet du plasma et du liquide traité au plasma sur les cellules, in vitro, et sur la tumeur, in vivo, doit être étudié. Avec cette dernière étape, nous devrions être en mesure de déterminer quelles espèces réactives sont toxiques contre les cellules cancéreuses et à quelles

concentrations, si ces espèces réactives présentent une quelconque sélectivité pour tuer les cellules cancéreuses au lieu des normales et enfin si le plasma pourrait être une solution légitime contre les tumeurs qui se trouvent dans les organismes vivants.

Le but de notre travail était de caractériser adéquatement notre plasma, produit par trois configurations de réacteurs différentes, comme un outil anticancéreux efficace. Ainsi, notre étude contient les trois étapes susmentionnées de l'application plasma.

Afin d'étudier ces points clés et de parvenir à un traitement plasmatique efficace du cancer, cette thèse est divisée en 5 chapitres.

Sur la base du contexte mentionné ci-dessus, dans le chapitre 1, une étude bibliographique est proposée. Il couvre des aspects des grands principes de la physique des plasmas et sert de brève introduction aux notions nécessaires à la description des travaux effectués dans cette thèse.

Dans le chapitre 2, tous les différents montages expérimentaux et équipements utilisés au cours de cette thèse de doctorat sont décrits. De plus, toutes les procédures expérimentales et théoriques qui nous ont aidés à recueillir les données et à les analyser sont présentées en détail.

Le chapitre 3 contient l'étude de la phase gazeuse des plasmas. Le champ électrique localisé à l'avant de l'onde d'ionisation a été estimé par spectroscopie d'émission optique en se basant sur la division et le décalage de Stark dépendant de la polarisation. Ensuite, pour déterminer la densité électronique, l'élargissement de Stark a été utilisé. Enfin, la température du plasma a été estimée en utilisant les distributions rotationnelles de molécules sondes sélectionnées (OH et N2). Nous avons constaté que le champ électrique à l'avant de l'onde d'ionisation augmente lorsque le plasma s'approche du liquide traité. En conséquence, la température du gaz ainsi que la densité électronique du plasma augmentent également dans les positions les plus proches du liquide.

Dans le chapitre 4, nous avons fait une investigation de la composition chimique du PBS traité par plasma (pPBS). Ainsi, la production de H_2O_2, NO_2^-, NO_3^-, •OH, $O_2(a1\Delta g)$, O_3, HCl^- et $ONOO^-$ a été étudiée dans le pPBS en réalisant de la colorimétrie couplée à la spectroscopie d'absorption et de fluorescence. De plus, la capacité à conserver les espèces réactives du pPBS à longue durée de vie (H_2O_2, NO_2^- et NO_3^-) sur une longue période a été étudiée en fonction du temps et de la température de stockage. On montre que si le pPBS est stocké dans des conditions pertinentes, la concentration de ces espèces réactives reste stable

pendant plus de 75 jours.

Sachant que ces espèces réactives de l'oxygène et de l'azote à longue durée de vie sont les principaux moteurs de la capacité anticancéreuse du traitement par plasma, le chapitre 5 est consacré à l'application du plasma sur des cibles biologiques et à l'évaluation de la contribution de ces espèces réactives à sa cytotoxicité du plasma. Ces études ont été réalisées en étroite collaboration avec des biologistes. Ainsi, en utilisant deux modèles de cellules cancéreuses (CAL27 et FaDu) et trois lignées cellulaires normales (fibroblastes humains primaires, kératinocytes gingivaux primaires et cellules épithéliales), la capacité anti-tumorale des traitements directs et indirects par plasma a été évaluée selon l'activité métabolique cellulaire, la viabilité cellulaire, la peroxydation lipidique, la production de ROS intracellulaires et l'induction de la caspase 3/7. Nous avons constaté que la sélectivité du traitement par plasma pour tuer les cellules cancéreuses plutôt que les cellules normales dépend fortement des espèces réactives qui sont présentes dans le pPBS. Plus précisément, lorsque les cellules sont traitées directement avec le plasma, nous avons observé un fort effet sur les cellules normales, tandis que les cellules cancéreuses étaient modérément affectées. En revanche, lorsque le traitement indirect au plasma était utilisé, l'effet sur les cellules normales était mineur, tandis que l'effet sur les cellules cancéreuses était significatif (légèrement moins efficace que le traitement direct au plasma). Notre hypothèse est que les espèces réactives à courte et moyenne durée de vie, présentes uniquement lors du traitement direct au plasma, endommagent la membrane cellulaire des cellules normales, permettant aux espèces réactives à longue durée de vie de pénétrer dans les cellules. Pour étayer cette hypothèse et mieux comprendre l'interaction de la membrane cellulaire avec ces espèces réactives, l'effet du traitement au plasma sur les protéines et sur différents types de phospholipides a été étudié. Comme pour les cellules normales, les protéines ont également été endommagées lors du traitement direct au plasma, tandis que l'effet du traitement indirect était mineur. Ensuite, nous avons étudié l'application combinée du traitement indirect au plasma et des champs électriques pulsés microsecondes (μsPEFs) pour surpasser l'électroperméabilisation des cellules in vitro, la base de l'électrochimiothérapie (ECT). Nous avons montré que le traitement combiné ouvre la possibilité de réduire l'amplitude des impulsions électriques utilisées dans l'ECT, permettant un traitement ECT avec des effets secondaires réduits. Enfin, l'application in-vivo du pPBS sur des souris femelles consanguines immunocompétentes C57Bl/6J a également été étudiée. Il est démontré que la combinaison du traitement indirect au plasma et des μsPEFs retarde la croissance tumorale des souris par rapport aux traitements μsPEF ou ECT seuls.

General Introduction

Cold atmospheric-pressure plasmas (CAPPs) have been extensively studied over the last decade for their anti-cancer properties. It is now well established that the plasma produced by many different reactors can be an effective anti-cancer strategy. The anti-cancer capacity of plasmas is mainly due to reactive oxygen and nitrogen species, produced in the gaseous phase and transferred to the liquid by the gas flow or directly produced in the plasma treated liquid constituting secondary products of the liquid phase and gaseous phase species. The physical properties of the plasma, like the electro-magnetic field, the ultraviolet radiation and the heat can increase the efficiency of the plasma against tumours even if their contribution to its anti-cancer capacity is less significant than the chemical properties of the plasma. Nevertheless, these physical properties are directly responsible for the chemical composition of both the plasma and the plasma-treated liquid. Thus, one can easily infer that for plasma to be used as an efficient anti-cancer strategy, it must have been extensively studied in three different steps. Firstly, its gaseous phase properties should be determined. That would include the gas temperature, the electrical properties of the plasma and its chemical composition. Its hydrodynamic behaviour is crucial because it will help us understand how the plasma is interacting with the target regardless if this is a liquid solution or a tissue. The gas temperature and its electrical properties should be studied primarily to ensure that when the plasma is going to treat a cancer *in vivo*, it will be safe and will not cause any burns or electrical shock to the patient and secondarily because both the heat and the electrical properties of the plasma could contribute to the cancer treatment. The chemical composition of the gaseous phase of the plasma should be studied for two main reasons. It is directly linked with the resulting liquid phase chemistry of the plasma-treated liquid and even if most of the targets are located in a liquid or covered by a liquid layer there could be exceptions where the target is solid and thus, the plasma is directly in touch with the tumour. Secondly, the efficiency of the plasma against a tumour is mainly due to short-, intermediate- and long-lived reactive species that are produced and/or transferred to a liquid and are toxic to the cancer cells. Thus, an in-depth study of the chemical composition of the plasma-treated liquid is essential. Except for the different reactive species, other chemical properties of the liquid should also be studied such as its pH and conductivity as they could also play a significant role to its cytotoxic action. Finally, the effect of the plasma and the plasma-treated liquid on the cells, *in vitro*, and on the tumour, *in vivo*, should be investigated. With this final step, we should be able to determine which reactive species are toxic against the cancer cells and at which concentrations, if these reactive species exhibit any selectivity towards killing the cancer cells instead of the normal ones and finally if the plasma could be proven a legitimate solution

against tumours that are found in living organisms.

The purpose of our work was to adequately characterize our plasma, produced by three different reactor configurations, as an efficient anti-cancer tool. Thus, our study contains all the three aforementioned steps of the plasma application.

In order to investigate these key points and achieve an efficient plasma-cancer treatment, this Thesis is divided in 5 chapters.

Based on the above-mentioned context, in Chapter 1, a bibliographic study is provided. It covers aspects of the main principles of Plasma Physics and serves as a brief introduction to the notions that are necessary for the description of the work carried out in this Thesis.

In Chapter 2, all the different experimental setups and equipment used during this Ph.D. Thesis are mentioned. On top of that, all the experimental and theoretical procedures that helped us to gather the data and analyse them are presented in detail.

Chapter 3 contains the study of the gaseous phase of the plasmas and its main purpose is to provide information on the physical and chemical properties of the produced plasmas. Firstly, the localized electric field in the front of the ionization wave was measured by optical emission spectroscopy, based on the polarization-dependent Stark splitting and shifting of different He lines and their forbidden components. Secondly, to determine the electron density, Stark broadening of different hydrogen lines was used. Finally, the gas temperature of the plasma was estimated using the rotational distributions of appropriately selected probe molecules (OH and N2 at 309 and 316 nm, respectively). We found that the electric field in the front of the ionization wave increases when the plasma approaches the treated liquid. As a result, the gas temperature as well as the electron density of the plasma are also larger/greater closer to the liquid.

In Chapter 4, a in depth study of the chemical composition of plasma-treated PBS (pPBS). Thus, the production of H2O2, NO2–, NO3–, •OH, O2(a1Δg), O3, HCl– and ONOO– was investigated in the pPBS by performing liquid phase colorimetry coupled with absorption and fluorescence spectroscopy. Alongside, the pH and conductivity of the pPBS were also measured. On top of that, the ability to conserve the long-lived reactive species (H2O2, NO2– and NO3–) over a long period was investigated as a function of the storage time and temperature of the pPBS. It is shown in this work that if the pPBS is stored at pertinent conditions, the concentration of these long-lived reactive species, and, thus, the anti-cancer

capacity of the pPBS is stable for more than 75 days.

Knowing that these long-lived reactive oxygen and nitrogen species are the main drivers of the anti-cancer capacity of plasma treatment in oncology, Chapter 5, performed in close collaboration with biologists, was the plasma application on biological targets and the assessment of these reactive species' contribution to its cytotoxicity. Thus, the anti-tumor capacity of direct and indirect plasma treatments, using two models of head & neck cancer cells (CAL27 and FaDu) and three normal cell lines (primary human fibroblasts, primary gingival keratinocytes, and epithelial cells), was assessed in terms of metabolic cell activity, cell viability, lipid peroxidation, intracellular ROS production and caspase 3/7 induction. We found that the selectivity of plasma treatment towards killing cancer cells instead of normal cells is highly dependent on the short-, intermediate- and long-lived reactive species that are present in the pPBS. More specifically, when the cells are treated directly with the plasma, we observed a strong effect on the normal cells, while the cancer cells where moderately affected. On the other hand, when indirect plasma treatment was used the effect on the normal cells was minor, while the effect on the cancer cells was significant (slightly less efficient than direct plasma treatment). Our hypothesis is that short- and intermediate-lived reactive species that are present only during the direct plasma treatment damage the cellular membrane of the normal cells allowing the long-lived reactive species to penetrate the cells. To support this hypothesis and to better understand the interaction of the cellular membrane with these reactive species, the effect of the plasma treatment on bovine serum albumin proteins and different types of phospholipids (DLPC, DHAPC and DOPC) was investigated. As for the normal cells, the proteins where also significantly damaged when direct plasma treatment was applied, while the effect of indirect plasma treatment was minor. Followingly, we investigated the potential capabilities of the combined application of indirect plasma treatment and microsecond pulsed electric fields (μsPEFs) to outperform in vitro cell electropermeabilisation, the basis of electrochemotherapy (ECT). We showed that the combined treatment opens the possibility to reduce the amplitude of the electric pulses used in ECT, allowing an ECT treatment with reduced side-effects. Finally, the in vivo application of the pPBS on inbred female immunocompetent C57Bl/6J mice was also studied. It is shown that the combination of indirect plasma treatment and μsPEFs delays the tumour growth of the mice compared to microsecond PEFs or ECT treatments alone.

General Table of Contents

Chapter 1

Chapter 2

Chapter 3

Chapter 4

Chapter 5

Chapter 1

Low-temperature plasmas in plasma medicine

This section covers aspects of the main principles of Plasma Physics and serves as a brief introduction to the notions that are necessary for the description of the work carried out in this Thesis. It is not an exhaustive review of the physical processes of plasmas. Readers can find more basic principles explained in detail in the textbooks that are frequently cited in this chapter.

This chapter is divided into three main parts. The first part (relevant results presented in Chapter 5) contains the application of plasma and plasma-treated solutions on different biological targets. The second part contains the study of the gaseous phase of the plasma and its main purpose is to provide information on the physical and chemical properties of the plasma used (relevant results presented in Chapter 3) while the last part (relevant results presented in Chapter 4) is an analytical investigation of the chemical composition of plasma-treated solutions Thus, the purpose of this introduction is to provide the reader with some essential information regarding the three aforementioned parts of this work while in several cases, references are provided for more details.

Table of Contents

1.1 Plasmas: a powerful tool in cancer treatment

To date, the three main anti-cancer therapies remain surgery, chemotherapy, and radiotherapy[1]. However, each of these therapies has its own advantages and drawbacks. For example, even if surgery is the most efficient to eradicate the tumor, it can be traumatic for the patient because of residual scars and/or ablation of an organ (e.g., breast during mastectomy). In contrast to surgery, chemotherapy and radiation therapy are only capable of killing a fraction of the tumor cells at each treatment. Therefore, the more common use of radiation therapy is in combination with surgery and/or chemotherapy. Despite major improvements in the use of combined modality therapy, therapy resistance has been observed for every therapeutic regimen available today, including poly-chemotherapy, radiation therapy, immunotherapy, and molecular targeted therapy[2]. Deep RNA sequencing of the primary tumors has revealed the presence of resistant clones within the tumor before the beginning of therapy, suggesting that intra-tumor heterogeneity is an emerging mechanism of therapy resistance, not acquired under therapy selection, but inherent to tumor progression[2,3]. Consequently, there is still a need to develop new anti-cancer strategies to overcome those problems, and one of the most innovative aspects of Cold Atmospheric Pressure Plasmas (CAPPs) use over the last 20 years undoubtedly lies in cancer treatment. Indeed, since the first proof-of-concept that CAPPs can damage mammalian cells *in vitro*[4], the effectiveness of CAPPs as an anti-cancer tool, both *in vitro* and *in vivo*, has been reported in several human cancers[5]. This includes brain cancer, skin cancer, breast cancer, colorectal cancer, lung cancer, cervical cancer, leukemia, hepatoma, head and neck cancer, as well as osteosarcoma[5–8]. Moreover, CAPPs treatment can be combined with chemotherapy[9–12], nanoparticles[13–16], hyperthermia[17], radiotherapy[17,18], photodynamic therapy[19], and magnetic field[20]. Several clinical studies reported the use of CAPPs for treatment of (pre-) cancerous tissues[21] and two clinical trials using CAPPs are currently undergoing treatment of cervical intraepithelial neoplasia (ClinicalTrials.gov Identifier: NCT03218436) and Canady Helios cold plasma scalpel treatment at the surgical margin and macroscopic tumor sites (ClinicalTrials.gov Identifier: NCT04267575). CAPPs is an ionized gas at near-room temperature, composed of a high number of reactive species, ions, electrons, metastable species, and of the electromagnetic field and ultraviolet, visible or infrared radiation. Several CAPPs devices for medical applications have been described in the literature. The most used devices are Atmospheric Pressure Plasma Jets (APPJs). Since He or Ar plasma jets propagate into ambient air, molecular oxygen and nitrogen, and also water molecules, present in the air, diffuse inside the noble gas channel and interact with the excited states of the noble gas, producing various Reactive Oxygen (ROS) and Nitrogen (RNS) Species[22,23]. Among the various components produced in a plasma, ROS and RNS

remain the most studied since these species have been shown to play a major role in the anti-cancer property of CAPPs[24–26]. *In vitro*, plasma treatment is usually performed in the presence of a liquid phase covering the biological target. Several types of short-lived (e.g., radical hydroxyl •OH, anion superoxide $O_2^{\bullet-}$, and singlet delta oxygen $O_2(a^1\Delta_g)$) and long-lived (hydrogen peroxide H_2O_2, nitrite NO_2^-, and nitrate NO_3^-) ROS/RNS have been detected in the gas and liquid phases[22,27–30]. Most of the reactive species found in the liquid phase are either primarily generated in the gas phase and at the gas-liquid interface or are the end-products of the transformation of primary ROS/RNS in liquid[22,23,30,31]. While H_2O_2 is a central player in the anti-cancer capacity of CAPPs treatment[32–42], H_2O_2 and NO_2^- act synergistically to induce cell death after plasma treatment[39,40,43,44]. The use of cold plasma in oncology is limited by the accessibility of the tumor. As such, we must consider two types of plasma application modalities that are currently used to treat cancer cells: the direct and indirect treatments[45]. Direct treatment involves direct exposure of the biological target to plasma in the presence of a liquid solution (e.g., cancer cells *in vitro*) or not (e.g., superficial tumors *in vivo*), while indirect treatment involves the treatment of a solution (e.g., a saline solution like PBS (Phosphate-buffered saline), and cell culture medium), and subsequent application of these plasma-activated solutions onto the biological target, *in vitro* or *in vivo*[46]. *In vivo*, the treatment of superficial tumors such as skin tumors and head and neck tumors can be achieved by direct treatment. However, the big challenge for the plasma community is the treatment of non-superficial cancers. One approach is as an intra-operative adjuvant treatment. Another method of delivering "plasma species" to deep tissues could be via plasma-treated solutions (PTS). The type of plasma application has several implications with regards to the nature of the physicochemical parameters that interact with the biological target. In the case of direct treatment, physical factors (ultraviolet, heat, and electromagnetic field) and chemical factors (long- and short-lived ROS/RNS) are present during the treatment, while only chemical factors, and among them essentially long-lived species such as H_2O_2 and NO_2^-, should be considered in indirect treatment. While several groups have shown that, *in vitro*, both treatments were equivalent in inducing cancer cell death, in altering cell surface adhesion molecules, or in inactivating enzymatic functions[40,47–49], others have reported that direct treatment is more effective than indirect treatment at killing tumor cells[50–53]. Moreover, there is still a debate regarding the selectivity of cold plasma at inducing cell death preferentially in tumor cells over healthy cells[39,40,54–61]. These discrepancies between reports can be attributed to the fact that the anti-cancer capacity of PTS depends on several factors such as the size of the wells in which cells are seeded, the volume of the treated solution, the solution composition (e.g., PBS versus culture medium), the gap between the plasma source and the solution, the gas flow rate, the gas admixture, and the plasma device itself [42,61–63]. On top of that, as reported by *Biscop et al.*, the type of the

cells, the type of the cancer studied as well as the culture medium in which they are cultured and/or treated could also play a major role on the selective action of plasma treatment[61].

Especially when it comes to indirect plasma treatment, i.e., the application of PTS on the tumor or the organism, there are several prerequisites. To be considered as effective anti-cancer agents, it is essential that these PTS maintain their anti-cancer properties over time. One key parameter for the conservation of PTS, as well as of any other agent, is the storage temperature. Shen *et al.* investigated the evolution of Plasma-treated Water (PTW) when stored at 4 different temperatures (+25, +4, −20, and −80 °C) over 30 days in terms of H_2O_2, NO_2^- and NO_3^- concentrations as well as its bactericidal activity[64]. They found that the bactericidal ability of PTW increased with decreasing storage temperature. Besides, they also found that the concentrations of H_2O_2, NO_2^- and NO_3^- decreased over time for all storage temperatures except for –80 °C. Contrariwise, Judée *et al.*, who used Plasma-activated Medium (PAM) to treat colon adenocarcinoma multicellular tumor spheroid (MCTS), found that, when the PAM was stored at +4 °C or –80 °C, it retained its genotoxic activity, which was not the case for the PAM stored at +37 °C or –20 °C[65]. Thus, they suggested that H_2O_2 concentration in PAM remained stable during at least 7 days of storage at +4 °C and −80 °C, while storage at +37 °C and −20 °C certainly decomposed H_2O_2. Yan *et al.* showed that while the H_2O_2 was stable in plasma-treated PBS stored at +8 °C and –25 °C for up to 3 days, its concentration was reduced as a function of storage time (and for the same storage conditions) when the PTS was cell culture medium[66]. These discrepancies between reports can be attributed to both the different types of plasmas used for the treatment of the solutions and to the different treated solutions. Indeed, different working conditions such as gas flow rate, gas composition, treatment distance, room conditions (e.g. humidity and temperature), and high voltage amplitude result in the production/transfer of different reactive species in/into the solution, the composition of which also plays a major role in its final complex chemistry[40,67,68]. Besides the fluctuation of the Reactive Oxygen and Nitrogen Species (RONS) concentration, the chemical reactivity of PTS is also highly dependent on the final pH of the solution after plasma treatment. In fact, the pH of the plasma-treated solutions could be one of the crucial parameters that may explain the choice of the different storage temperatures proposed by the aforementioned authors. Indeed, not only the acidic pH of plasma-treated solutions may contribute alongside RONS to their cytotoxic capacity, but it is also an important parameter for the stability of RONS[39,69].

1.2 Non-thermal plasmas

The characteristics of CAPPs are principally based on the notion of non-equilibrium. Non-thermal plasmas (NTPs) are generally electrical discharges that are not in thermodynamic equilibrium. In non-equilibrium plasmas, the temperatures of electrons, ions, neutral atoms and/or molecules differ significantly, i.e., Te>Tv>Ti≈Tg (for cold plasmas)[70,71], where Te = electron temperature, Tv = vibrational temperature, Ti = ionic temperature and Tg = gas temperature. This non-equilibrium character is possible due to the much faster and more efficient energy transfer to the electrons, from the electric field, than the subsequent collisional energy transfer between electrons and heavy particles[72]. In cold plasmas, the electronic temperature is approximately 1 eV≈11.600 K[70], while the gas temperature can be close to the ambient temperature[70,73] (~ 0.026 eV). It is mainly for this reason that some cold plasmas can operate at ambient temperature. In the field of non-thermal plasmas, the term cold plasma has been used in numerous works[74–81] to describe discharges that operate at room temperature and atmospheric pressure. The remarkable characteristics of cold plasmas (non-thermodynamic equilibrium, low gas temperature, production of reactive chemical species) offer enormous potential for their use in a wide range of applications and specifically in biomedicine. Apart from the temperature, plasmas generated in the laboratory can be classified according to their operating pressure. Thus, discharges can be produced either a) at low pressure or b) at high pressure. Low-pressure glow discharges (10^{-3}-10^{-1} torr) are of great interest in basic research, as well as in industrial and materials technology and microelectronics. But these plasmas must be contained in sealed chambers (vacuum reactors), which makes them expensive and time-consuming. In addition, their particles density is relatively low. Therefore, during the last decades, several research groups focus on the development of new plasma sources, which operate at atmospheric pressure. The economical and operational advantages of working at atmospheric pressure have led to the development of a variety of atmospheric plasma sources for several applications, both scientific and industrial. Concerning the plasmas produced and tested within the framework of this thesis, they are generated at atmospheric pressure with small-sized reactors (their dimensions vary from a few micrometres to a few millimetres). Therefore, these micro-plasmas, are at least an order of magnitude smaller than conventional low-pressure discharges used for processing materials in microelectronics.

1.3 Cold atmospheric-pressure plasma reactors

There are mainly three different types of sources used for the production of CAPPs: Dielectric Barrier Discharges (DBDs), APPJs[82,83] and Micro Hollow Cathode Discharges (MHCDs). On the one hand, APPJs have been widely used, especially during the last decade, because they can generate a stable and controllable plasma that propagates outside the confinement area of the electrodes. This advantage of the APPJs is crucial for the majority of biomedical applications for which these devices are designed[75,82]. On the other hand, MHCDs can produce high fluxes of reactive oxygen and nitrogen species that play a crucial role in certain biomedical applications such as cancer treatment.

1.3.1 Dielectric barrier discharges (DBDs)

Dielectric barrier discharges have been extensively studied over the last decades[84–87]. They use a dielectric material, such as quartz, alumina, or glass, which covers at least one of the two electrodes or is placed in the gap between the two electrodes. The electrodes are driven by high AC or pulsed DC voltages, and mainly at frequencies in the kHz range. Plasmas generated by DBDs have been used for ozone generation, for material surface modification, as flow control actuators, for pollutants treatment[88], etc. DBDs' most recent domain of application has been in biomedicine after their successful early use in the mid-1990s to inactivate bacteria. Today, they are used in various biomedical applications including wound healing and the destruction of cancer cells and tumours. Typical DBD reactor configurations can be found in Figure 1.1[89].

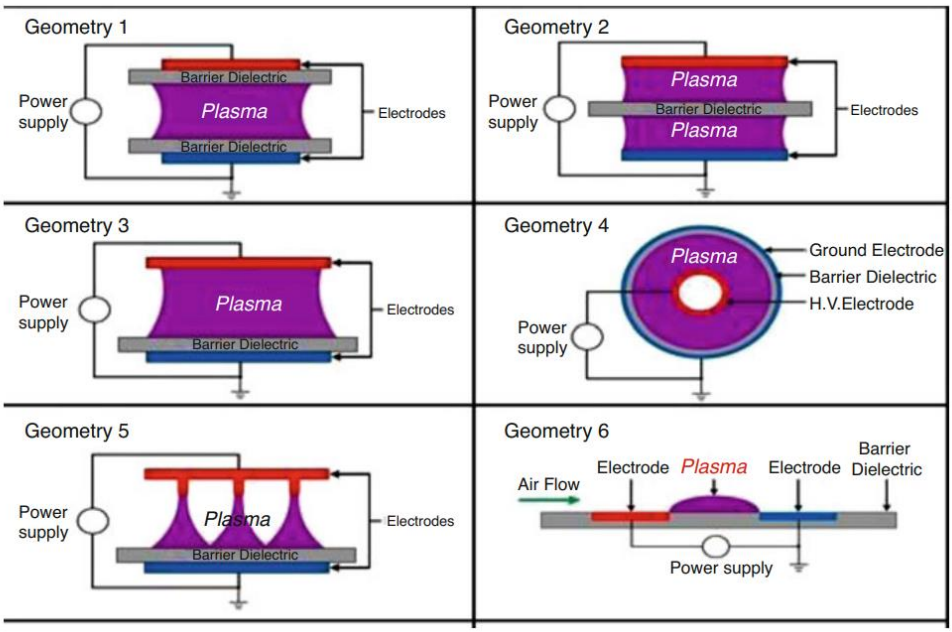

Figure 1.1 Various DBD configurations (figure non-modified taken from [89]).

1.3.2 Atmospheric pressure plasma jets (APPJs)

APPJs are devices that produce low-temperature plasmas in the surrounding air[82,89]. There are two key characteristics of these devices that allow their safe use in biomedical applications. First, given that the gas temperature is maintained relatively low (close to room temperature), they can come in touch with soft matter, including biological tissues, without causing thermal damage. Secondly, because the plasma propagates away from the high-voltage region and into a region where there is no externally applied high voltage, the plasma is electrically safe and does not cause electrical shock/damage to the treated sample that can be exposed, cells or tissues[89]. Various types of APPJs with different configurations have been reported. Most of the plasma jets work with air[90] or noble gases such as He[91], Ar[92], Ne[93], H_2O[94] and Kr[95], mixed with a small percentage of reactive molecular gases, such as O_2[39] or N_2[96]. Atmospheric pressure plasma jets operating with noble gases can be classified into four basic categories: dielectric-free electrode (DFE) jets, DBD jets, DBD-like jets, and single electrode (SE) jets, as shown in figure 1.2. An analytical study of all possible plasma jet arrangements was given by Lu, Laroussi, and Puech and will not be repeated here[97]. From the configurations presented in Figure 1.2, we can classify the reactors used in this study (named Reactors 1 and 2 in Chapter 2) as DBD-like plasma jets.

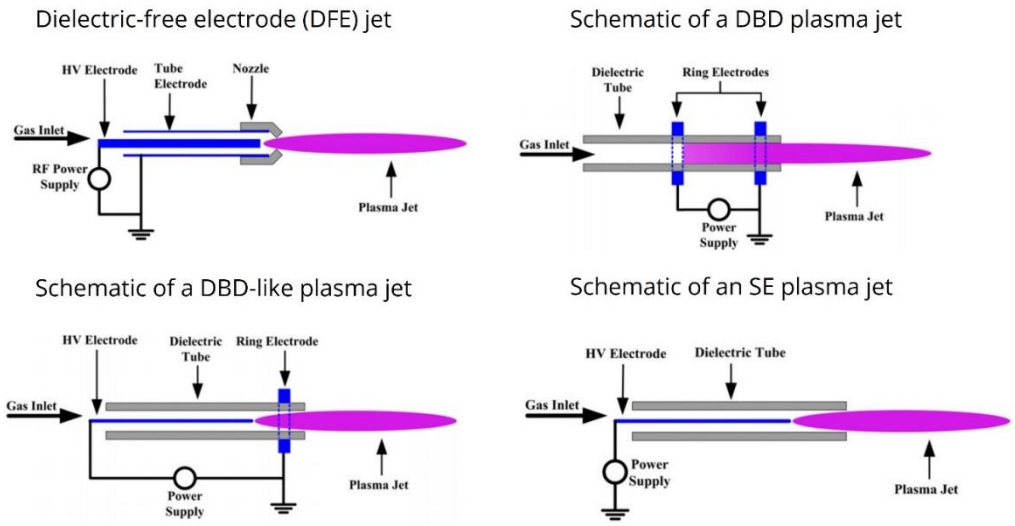

Figure 1.2 Different configurations of atmospheric-pressure plasma jets (figure non-modified taken from [97]).

Besides the different geometries used, the local power or energy dissipation must also be considered for the different reactors used for the

production of plasmas. This parameter determines the plasma properties such as the temperatures and densities of reactive species. Plasma jets can be generated at nearly all frequencies as well as dc voltage, and several detailed overviews are available in the literature[75,98]. Briefly, most of these devices are operated with DC[99,100], pulsed[39], or sinusoidal[101] high voltages of frequencies up to several hundred kHz. For higher frequencies, the radiofrequency (RF) and microwave (MW)[102] regime is applied. RF jets usually operate in the frequency range of 1–100 MHz, where ions are not able to follow the electric field as easily as the lighter electrons[103]. Microwave (MW) plasmas are generated and sustained by electromagnetic radiation within the microwave frequency range (300 MHz–300 GHz). Typically, MW power with a frequency of 2.45 GHz or 915 MHz supplied by a magnetron is used.[98]

1.3.3 Micro hollow cathode discharges (MHCDs)

"Hollow cathode discharges are gas discharges between a cathode which contains a hollow structure, and an arbitrarily shaped anode" wrote Schoenbach *et al.*, who first suggested the term micro-hollow cathode discharges[104]. A typical schematic of a MHCD and a MCSD is given in Figure 1.3. The MCSD is the discharge between the cathode C and the anode A1. A modest DC voltage applied across the electrodes is sufficient to generate and maintain a stable glow discharge, the micro-hollow cathode discharge (MHCD), at pressures up to atmospheric, without undergoing the glow-to-arc transition, and for power densities as high as some hundred kW/cm^3. The MHCD can also be operated in pulsed mode, which allows the production of high current peaks (hundreds of mA) at repetition rate frequencies in the range of! 1–100 kHz, depending on the average charging current of the MHCD capacitance.

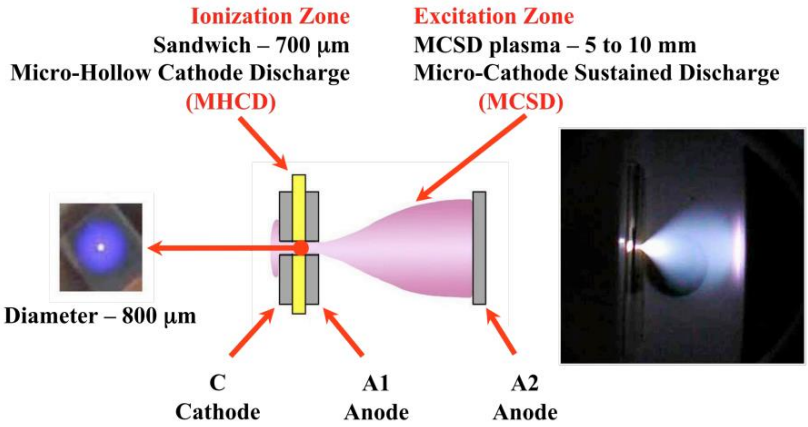

Figure 1.3 Schematic of the plasma created in a MCSD showing on the left a picture of the discharge spreading on the back surface of the MHCD cathode and on the right a picture of the MCSD in pure oxygen at a pressure of 67 mbar. The drawing in not to scale[105].

The MHCD with some additions constitutes the reactor used in this study, called micro-cathode sustained discharge (MCSD), shown in Figure 1.4. More precisely, when a third, planar electrode is placed at a certain distance from the MHCD (8 mm in our case), a stable discharge of larger volume is generated between this third electrode, which plays the role of the anode, while the MHCD is the cathode[106,107].

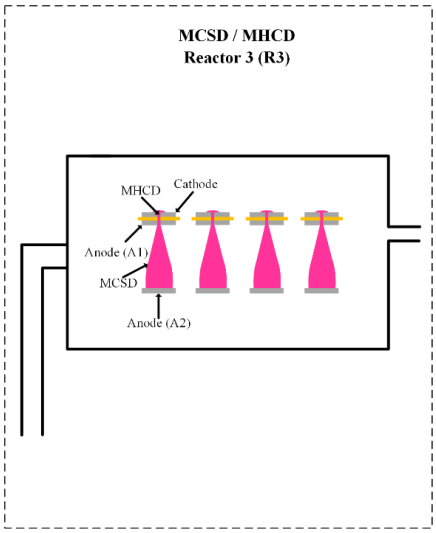

Figure 1.4 Schematic illustration of the MCSD used in this Ph.D. Thesis.

This reactor (MCSD) can also generate stable DC glow discharges, while avoiding a glow-to-arc transition at atmospheric pressure. One of their great advantages is their capability to produce high fluxes of reactive oxygen species like singlet delta oxygen and ozone[105]. On top of that by controlling their working parameters the production of certain reactive species can be favored, while the production of others can be minimized.

1.3.4 Plasma cancer treatment modalities

In plasma cancer therapy, two different plasma treatment modalities are mainly used, direct and indirect plasma treatments (Figure 1.5). Firstly, direct plasma treatment consists of two different phases: Phase I (Immediate effects), during which, cells covered by a liquid solution are directly exposed to the plasma, and Phase II (Early effects), during which the plasma is turned off and the cells are incubated in the plasma-treated solution for a certain time period. During Phase I, of the direct plasma treatment, there are both physical (electric field, ultraviolet radiation, heat, etc.) and chemical factors (short-, median-, and long-lived reactive species) that could play a key role to induce cell death. During Phase II, given that the plasma is turned off, there are only chemical factors that could play a role. From these chemical factors we can observe the contribution of short-, median-

and long-lived reactive species because the incubation time starts exactly when the plasma is turned off. Secondly, indirect plasma treatment consists only of the Phase II. More precisely, a solution is treated by the plasma in the absence of cells and then is transferred onto the cells. The transfer of the solution onto the cells can take place immediately after the plasma is turned off, or after several minutes or even after several days/weeks. During the indirect plasma treatment there are only chemical factors that could lead to cell death. Which of those chemical factors contribute each time highly depends on the time between the turn off of the plasma and the addition of the solution onto the cells. If this time is negligible (some seconds), we can witness the effect of short-, median- and long-lived reactive species. The main reason why the effect of short-lived reactive species is considered here is that they can also be the products of secondary reactions. For example, ozone, that is produced during plasma treatment, can undergo decomposition via a chain reaction mechanism resulting in the production of free hydroxyl radicals (•OH)[108]. This reaction cannot take place in the case of indirect plasma treatment as the plasma-treated PBS is added to the cells after a period of time that exceeds the lifetime of O3 (~ 200s in water).If this time is several minutes, we can have an effect only of median- and long-lived reactive species, while if the solution is added onto the cells several hours or days after plasma treatment, there are only long-lived reactive species that could harm the cells.

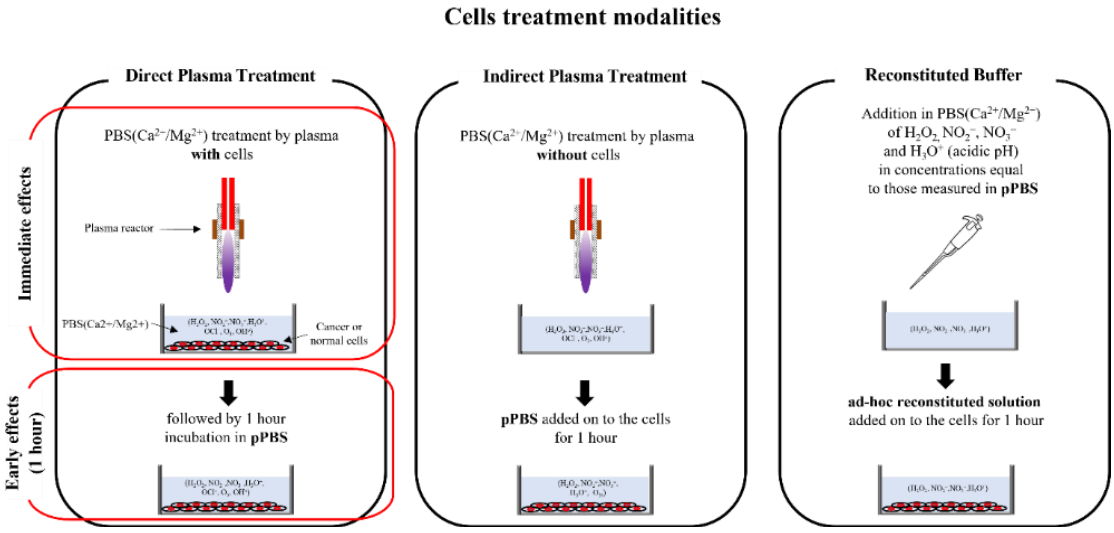

Figure 1.5 Schematic illustration of the different modalities used in plasma cancer treatment.

Plasma-treated solutions, as it will be analysed later in this chapter (section 1.4), consist of a complex chemistry with a lot of different reactive oxygen and nitrogen species. Thus, even if the effect on the cells of this cocktail of reactive species can be monitored both through the Early effects (Phase II) of the direct plasma treatment and through the indirect plasma treatment, the investigation of the effect of each of the reactive species or of simple combinations of them is a rather difficult task. Thus, recently, a third treatment modality has been widely

used in the context of plasma cancer treatment studies (Figure 1.5)[39]. This third treatment modality is called reconstituted buffer[39] (or mimicking solution). Even if plasma is not actually involved in any part of this modality, we call it the third plasma treatment modality as it simulates, in a certain level, a plasma-treated solution. It consists of an untreated solution into which ad-hoc concentrations of reactive species, at the exact concentrations measured in the plasma-treated solution, are added. In this work, the added reactive species were hydrogen peroxide (H_2O_2), nitrites (NO_2^-) and nitrates (NO_3^-), as these reactive species have been previously reported to be the main drivers of the anti-cancer capacity of plasma-treated solutions[40]. Also, to better simulate the chemical composition of the plasma-treated solution, in this Thesis, the pH of the reconstituted buffer was also slightly reduced (to be the same as in the plasma-treated solution).

1.3.5 Plasma gaseous phase and diagnostics

Various terms have been used over the last decades to describe plasmas that are produced from atmospheric pressure plasma jets and propagate for several centimetres into the ambient air, like “jets”, “plumes” and “bullets”, just to name a few[109]. In spite of the term that we use to name them, it is well-known that, despite their luminous continuum look, they consist of discrete ionizing waves travelling with supersonic velocities in a channel formed by the feeding gas during its interaction with the ambient air[97,110,111]. These discrete ionization waves are characterized by an enhanced electric field that can be found especially in the wave fronts. The value of the enhanced electric field in the front region is highly dependent on the density of the volumetric electric charge formed by the wave itself and can exceed greatly the local applied (external) electric field[110]. In the bibliography, one can find that, in many cases, this localized electric field in the front of the ionization wave (or guided streamer) increases as the plasma exits the dielectric tube and propagates into the ambient air[112]. This fact is very important when it comes to the application of plasmas in biomedicine because this electric field could be one of the key factors leading to the disruption of the cellular membrane and, thus, to cancer cell death when treated by an atmospheric-pressure plasma jet. As we know from the literature, these ionization waves propagate with a speed of ~10^5 - 10^8 cm s^{-1} in rare gases[97]. Because of that, diagnostic methods with high temporal and spatial resolution are needed to characterize the gaseous phase of cold-atmospheric pressure plasmas jets.

To study the behavior of the aforementioned ionization waves, different diagnostics are used, such as iCCD imaging, optical emission spectroscopy (OES), laser-induced fluorescence (LIF), absorption spectroscopy, and Thomson scattering, among others. In this introduction, only the first two diagnostics are discussed as they are the ones that were used in this thesis work. The reader can

obtain information on the others from interesting published reviews and articles[35,114,39].

The optical emission spectrum of a chemical species is the spectrum of frequencies of electromagnetic radiation emitted when a transition from a high-energy state to a lower-energy state of an excited atom or molecule takes place[115]. The energetic difference between the two states is expressed as the energy of the emitted photons. The collection of the many different possible electron transitions for each atom/molecule, with each one having a specific energy difference, which leads to different radiated wavelengths, produce an emission spectrum. Each species' emission spectrum is unique and because of that, spectroscopy can be used to identify chemical species. By using OES, time- and space-resolved measurements of the excited species in the plasma can be obtained.[110]

Despite some limitations of optical emission spectroscopy, which concern mainly the investigation of ground-state species (for which other methods must be used, such as LIF or absorption spectroscopy), there are numerous information that can be exported from an optical emission spectrum. Some of them are the localized electric field of the ionization wave, the electronic density and temperature, and the rotational temperature of certain molecules that can be used to estimate the gas temperature.

To determine the electron density and the electron temperature, Stark broadening of a certain spectral line can be used. The measured profile of an atomic emission line can be affected by different broadening mechanisms: natural broadening, Doppler (thermal) broadening, Stark broadening, instrumental broadening, resonant broadening, etc. Different hydrogen spectral lines can be used for the determination of the Stark broadening, namely the H_α, the H_β, the H_γ and the H_δ lines (at 656.28 nm, 486.13 nm, 434.05 nm, and 410.17 nm, respectively)[116]. In this work, we principally studied the H_α and H_β lines.

As described by Obradovic *et al.*, the electric field in the front of the ionization wave can be determined with optical emission spectroscopy, based on the application of the polarization-dependent Stark splitting and shifting of different He lines and their forbidden components[117].

Finally, the gas temperature of the plasma can be estimated using the rotational distributions of appropriately selected probe molecules[118,119]. In principle, the rotational structure of an excited molecule contains information about the rotational temperature (Trot). For an excited state, this can be obtained from a graph of Boltzman of the P, Q, and R branches of the rotational band[120]. If

the rotational population comes only from heavy particle collisions, Trot represents the gas temperature (Tg). Thus, the temperature of the gas, which is defined as the kinetic (translational) temperature of heavy particles in out-of-equilibrium plasmas generated at atmospheric pressure, can be estimated from the rotational temperature.

More information on these methods and how they are used in this Thesis are provided in Chapter 2.

1.4 Plasma-solution interactions

As mentioned before, non-equilibrium plasmas result in rich plasma chemistry, which becomes much more complex when the treating target is a liquid solution. Plasma–solution interactions have become an increasingly important topic in the field of plasma science and technology during the last two decades[31]. Cavendish's famous work 'experiments on air' from 1785 might be the first report involving plasma–solution interaction and dealing with the production of nitric acid by an electric spark in air[31,121].

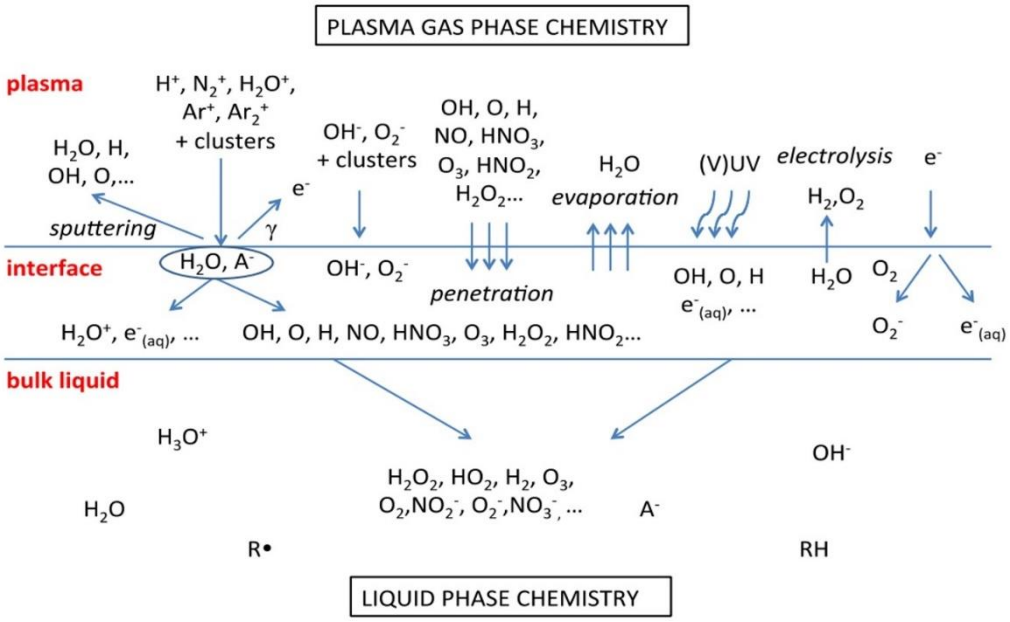

Figure 1.6 Schematic diagram of some of the most important species and mechanisms for an argon/humid air plasma in contact with water (figure non-modified taken from [31]).

When it comes to plasma cancer treatment, which is the main objective of this work, both in the cases of direct or indirect plasma treatments, the plasma is primarily in contact with a solution or a solution interface that covers the cells or

the tissue. Thus, the study of the gas-solution interface chemistry and of the liquid phase chemistry is of high importance for the evaluation of the plasma treatment efficacy. In plasma medicine and especially in plasma cancer therapy, there are several reactive oxygen and nitrogen species (RONS), both short- and long-lived, that could play a key role in inducing cell death[39,122]. In this section of Chapter 1, a brief introduction on the mechanisms leading to the formation of these RONS is presented. More precisely, in Figure 1.6, we can see an overview of most of the reactive species that are transferred to and/or produced in a solution when treated by plasma. From this cocktail of reactive species, we studied, in this thesis work, certain reactive oxygen and nitrogen species: H_2O_2 (hydrogen peroxide), NO_2^- (nitrite), NO_3^- (nitrate), •OH (hydroxyl), $O_2(a^1\Delta_g)$ (singlet delta oxygen), O_3 (ozone), ClO^- (hypochlorite) and ONOO− (peroxynitrite).

1.4.1 Long-lived reactive oxygen and nitrogen species (H_2O_2, NO_2^-, and NO_3^-)

H_2O_2 and NO_2^- have been reported to be the key factors of the cytotoxic efficiency of plasma-treated solutions[12,39,40]. This fact constituted our motivation to study in detail in this thesis work these long-lived reactive species. Our work is experimental and depicts the absolute concentrations of these RONS for a wide range of different plasma operation parameters as well as their pertinent storage conditions to stabilize their concentrations over time. Nevertheless, hereby we will provide an introduction on the mechanisms that are responsible for the presence of these species in the plasma-treated solution. This introduction is based on the work of Van Boxem *et al.*[42], and we think that it will contribute to the understanding of these species' production.

Van Boxem *et al.* performed computer simulations with a 0D chemical kinetics model for an argon cold atmospheric pressure plasma jet in contact with water[42]. Through this model, they solved balance equations for the different reactive species, based on production and loss. Figure 1.7 provides a general overview of the calculated liquid-phase concentrations of NO_2^- and H_2O_2 as obtained from their model. Of course, there are also numerous other excellent works from which we and the reader could obtain also information on the origin of these reactive species in plasma-treated solutions, like for instance the work of Khlyustova *et al.*[123].

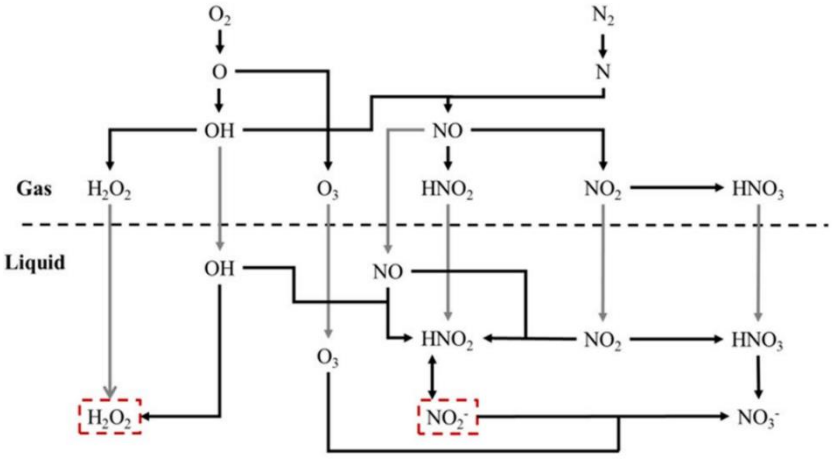

Figure 1.7 Main pathways in both the gas and liquid chemistry leading to the generation of NO_2^- and H_2O_2. The relative contributions of the different processes (i.e., chemical reactions (black lines) or diffusion processes (gray lines)) depend on the specific treatment conditions. The gas-solution interface is illustrated by the dashed horizontal line[42].

H_2O_2 molecules, which can be finally found in the plasma-treated solution, are the products of the reaction of oxygen atoms with water molecules. The O atoms are principally generated in the plasma by electron-impact dissociation (Eq. 4) or by collisions of O_2 with excited N_2 molecules (Eq. 5).

$$O_{2,gas}(\,^3P) + e^- \rightarrow O_{gas}(\,^1D) + O_{gas}(\,^1D) + e^- \qquad \text{(Eq. 4)}$$

$$O_{2,gas} + N^*_{2,gas} \rightarrow O_{gas} + O_{gas} + N_{2,gas} \qquad \text{(Eq. 5)}$$

The O atoms react then with H_2O molecules (present in the ambient air and as impurities within the feed gas), generating •OH radicals (Eq. 6). The O atoms could also react with H_2O molecules in the vapor layer above the liquid (i.e., H_2O molecules originating from liquid evaporation). In some cases, this is the major source of •OH radicals.

$$O_{gas}(\,^2P) + H_2O_{gas} \rightarrow \bullet OH_{gas} + \bullet OH_{gas} \qquad \text{(Eq. 6)}$$

Subsequently, two processes that result in the generation of H_2O_2 in the liquid phase may occur, of which the relative contribution depends on the distance between the nozzle of the reactor and the solution surface. For a larger treatment distance, the hydroxyl radicals will have the time to recombine in the gaseous plasma, generating H_2O_2 in the gas phase, which is then transported into the solution (Eq. 7). For a shorter treatment distance, the gaseous •OH radicals will be transported into the solution themselves, where most of them will recombine to

aqueous H_2O_2 (Eq. 8).

$$\bullet OH_{gas} + \bullet OH_{gas} + M \rightarrow H_2O_{2,gas} + M \rightarrow H_2O_{2,liquid} \quad \text{(Eq. 7)}$$

$$\bullet OH_{gas} \rightarrow \bullet OH_{liquid} + \bullet OH_{liquid} \rightarrow H_2O_{2,liquid} \quad \text{(Eq. 8)}$$

Thus, if the time required for the plasma or the plasma effluent to reach the solution is short (i.e., short gap and high gas flow rate), •OH radicals that are transported into the gas-solution interface (where they recombine) are the main source for aqueous H_2O_2. For longer distances between the tube orifice and the surface of the solution and/or lower flow rates, aqueous H_2O_2 mainly originates from gaseous H_2O_2, which is generated by •OH radical recombination in the gas phase. The different treatment conditions not only affect the contribution of different pathways resulting in the generation of H_2O_2, but they also have a great impact on the absolute concentration of H_2O_2 generated in the solution (as we will also witness in Chapter 4). Indeed, at high gas flow rates and short treatment distances, a large fraction of gaseous •OH radicals seem to survive transportation into the solution. Thus, the aqueous •OH concentration will be higher, which facilitates the recombination of •OH radicals into H_2O_2 in the solution, as this reaction rate is linearly dependent on the •OH concentration squared. On the other hand, at lower flow rates and longer treatment distances, many of the gaseous •OH radicals will have already recombined before reaching the solution. This recombination will, however, occur mostly with N-species (such as NO or NO_2), because their density in the gas is much higher than that of O-species (~80% of ambient air consists of N_2). This has a double effect on the concentration of H_2O_2 in the solution: (i) the gaseous density of H_2O_2 will not increase upon increasing the treatment distance, so its contribution to the aqueous H_2O_2 is similar in all cases (at the same gas flow rate), but (ii) because the aqueous •OH concentration is significantly lower at larger treatment distances, the recombination rate into H_2O_2 in the solution will be much lower. Consequently, the aqueous H_2O_2 concentration will decrease upon increasing the treatment distance. For NO_2^-, a similar analysis can be done. HNO_2 is mainly generated in the solution by three processes (Eq 9-11):

$$\bullet OH_{gas} + NO_{gas} \rightarrow HNO_{2,gas} \rightarrow HNO_{2,liquid} \quad \text{(Eq. 9)}$$

$$OH_{liquid} + NO_{liquid} \rightarrow HNO_{2,liquid} \quad \text{(Eq. 10)}$$

$$NO_{liquid} + NO_{2,liquid} + H_2O_{liquid} \rightarrow HNO_{2,liquid} + HNO_{2,liquid} \quad \text{(Eq. 11)}$$

At lower gas flow rates, ambient air species can easily diffuse into the

plasma, and, thus, the HNO_2 concentration highly increases in the gas phase, which explains why it is the most important source of aqueous HNO_2 in this case. Upon increasing the gas flow rate, it becomes more difficult for ambient air species to diffuse into the plasma. Moreover, the species that are initially generated in the gas phase (i.e., •OH and NO) have less time to recombine before reaching the gaseous-liquid interphase. Thus, the relative contribution of Eq. 9 decreases. By increasing the treatment distance, the species have more time to recombine in the gaseous phase, and, thus, the contribution of Eq. 9 will increase compared to Eq. 10. To explain the absolute concentrations of NO_2^- for the different conditions investigated, we must keep in mind that to generate HNO_2 (and thus NO_2^- generating species), both O_2 and N_2 are required. As mentioned before, by increasing the gas flow rate, the ability of these species to diffuse into the plasma decreases. Therefore, the HNO_2 concentration measured in the solution is much more dependent on the gas flow rate than H_2O_2 (as we present in Chapter 4 with our own experimental conditions). Moreover, the main loss process of NO_2^- is the reaction with O_3:

$$NO_{2,liquid}^- + O_{3,liquid} \rightarrow NO_{3,liquid}^- + O_{2,liquid} \quad \text{(Eq. 12)}$$

By increasing the treatment distance, the amount of O_2 that can diffuse into the plasma increases, leading, thus, to the increase of the concentration of O_3 generated in the plasma. This gaseous O_3 is subsequently transported into the solution, where it reacts with NO_2^-. This can explain the decrease in NO_2^- concentration when the treatment distance is increased. Except from that, another dominant loss process of NO_2^- is the reaction with H_2O_2 (Eq. 13).

$$H_2O_2 + NO_2^- + H^+ \rightarrow NO_3^- + H^+ + H_2O \quad \text{(Eq. 13)}$$

If these reactive species (NO_2^- and H_2O_2) are found in sufficient concentrations in an acidic environment of a pH ≤ 3.5, H_2O_2 can efficiently oxidize NO_2^- and transform it into NO_3^-. This reaction is also witnessed in our own experimental results (Chapter 4), and it could play a crucial role on the long-term chemical stability of these RONS. The reason for that is that in this case, short- or intermediate-lived reactive species that normally participate in the loss processes of these molecules, are not any more present in the liquid.

In summary, both H_2O_2 and HNO_2 can be generated either (i) from the diffusion of these species into the solution from the gas phase, or (ii) from aqueous reactions of short-lived species, and the relative contribution of both pathways strongly depends on the treatment conditions (gas flow rate and distance between the tube orifice and the surface of the solution).

1.4.2 Intermediate-lived reactive oxygen and nitrogen species (O_3)

Besides the long-lived reactive species mentioned above, also O_3, which has an intermediate lifetime of several minutes to hours in the liquid phase, has been reported to contribute to the anti-cancer capacity of plasma-treated solutions[39,108,124,125]. Ozone is primarily produced in the gaseous phase and transferred into the solution by the flow of the gas (Eq. 14). Nevertheless, it is also possible to generate ozone directly in the solution.

$$\bullet O_{gas} + O_{2,gas} \rightarrow O_{3gas} \rightarrow O_{3,liquid} \quad \text{(Eq. 14)}$$

Even if ozone possesses the highest oxidation redox potential (ORP) among typical oxidants (E^0 = 2.07 V), including chlorine, chlorine dioxide, hydrogen peroxide, and permanganate, its actual role on the anti-cancer efficiency of plasma-treated solutions is still under debate. The main reason for that is its low solubility in the solution. For example, Lukes *et al.* suggested that ozone is not contributing to plasma-treated solution chemical liquid phase interactions due to ozone's destruction by gaseous reactions with HNO_2 and NO or reactions in the liquid phase with nitrites after the treatment. Machala *et al.*[126] detected O_3 in the solution, even though the detected concentration was very small compared to what they found in the gaseous phase.

1.4.3 Short-lived reactive oxygen and nitrogen species ($O_2(^1\Delta g)$, $ONOO^-$/ONOOH, •OH)

It has been previously reported by He *et al.* that, because of a fleeting lifetime, it is usually difficult for •OH to originate from the gaseous phase of the plasma. Most of the •OH that can be found in plasma-treated solutions results mainly from secondary reactions (Eqs. 15-17).

$$H_2O_{2,liquid} \rightarrow \bullet OH_{liquid} + \bullet OH_{liquid} \quad \text{(Eq 15)}$$

$$O_{3,liquid} + H_2O_{2,liquid} \rightarrow HO_{2,liquid} + OH_{2,liquid} + O_2 \quad \text{(Eq 16)}$$

$$O_3 + HO_2 \rightarrow 2O_2 + \bullet OH \quad \text{(Eq 17)}$$

Peroxynitrite ($ONOO^-$/ONOOH) is formed in plasma-treated solutions due to a

post-discharge reaction between H_2O_2 and nitrite ions (Eq 18). This reaction is highly favored in acidic environments with a pH lower than 4.

$$NO_{2,liquid}^{-} + H_2O_{2,liquid} + H^+ \rightarrow O = NOOH_{liquid} + H_2O \qquad \text{(Eq 18)}$$

In the presence of superoxide anion radicals, $O_2^{\bullet -}$, singlet delta oxygen $O_2(a^1\Delta_g)$ can be produced. The singlet delta oxygen can be originated only by superoxide anion radicals (Eq. 19) or by their reaction with hydroxyl radicals (Eq. 20) and/or hydrogen peroxide (Eq. 21)[30]. If H_2O_2 and hypochlorite (ClO^-) are simultaneously present in the solution, $O_2(a^1\Delta_g)$ can be generated directly in the solution (Eq. 22)[127].

$$O_{2,gas}^{\bullet -} \rightarrow O_{2,gas}(a^1\Delta_g) + e^- \qquad \text{(Eq 19)}$$

$$O_{2gas}^{\bullet -} + \bullet OH_{gas} \rightarrow O_{2.gas}(a^1\Delta_g) + \bullet OH_{gas}^{-} \qquad \text{(Eq 20)}$$

$$O_{2,gas}^{\bullet -} + H_2O_{2,gas} \rightarrow O_{2,gas}(a^1\Delta_g) + OH_{gas}^{-} + \bullet OH_{gas} \qquad \text{(Eq 21)}$$

$$ClO_{liquid}^{-} + H_2O_{2,liquid} \rightarrow Cl_{liquid}^{-} + H_2O_{liquid} + O_{2,liquid} \qquad \text{(Eq 22)}$$

1.5 Aim and Experimental Strategy of the Thesis

Firstly, we saw in section 1.1 the key role that all these RONS could play in various plasma applications and especially in plasma medicine and plasma cancer treatment. In section 1.3, the main physical characteristics of cold atmospheric-pressure plasmas are discussed as well as the different types of reactors and working conditions that are used for their production. Finally, in Section 1.4, we analyzed the different reactive oxygen and nitrogen species (RONS) that are produced in the gaseous phase of plasmas and transferred to the target, solutions in our case, or are directly formed in the liquid phase.

Despite the numerous excellent works that have been reported, especially during the last decade, in the field of plasma medicine and especially plasma cancer treatment, there are still numerous questions that need to be answered for plasma to be considered as a safe and efficient anti-cancer solution.

Some of them, that also constituted our motivation for this work, are:

- Can the electric field in the front of the ionization wave be held responsible for the cells permeabilization during direct plasma treatment?

- What are the mechanisms leading to cancer cell death when in contact with these RONS?

- Is the plasma treatment selective towards killing cancer cells instead of normal ones?

- Can a plasma-treated solution conserve its anti-cancer characteristics through time to be considered an efficient anti-cancer drug?

Thus, the purpose of this work was the identification and quantification (where possible), in the liquid phase, of the vast majority of the reactive oxygen and nitrogen species that have been reported to play an important role in plasma medicine. On top of that, the actual contribution of these reactive species to the treatment of different biological targets was examined. In parallel the characteristics of the gaseous plasma phase like the localized electric field, the gas temperature and the electron density were studied. As mentioned previously, for each different biomedical application, an especially designed plasma reactor that addresses the needs of the application should be used. In our study, we used three entirely different reactors. Each one of these plasma reactors services a specific purpose, which is analysed in the following chapter.

Chapter 2

Materials and Methods

For the successful elaboration of our experimental work, several experimental systems were used. We used three different cold atmospheric pressure plasma reactors that were coupled each time with the necessary experimental setups to meet the needs of each experiment. This Chapter is divided in two parts. In the first part, the reactors used for the plasma production in this Thesis' work are presented. In the second part, all the different experimental setups and the diagnostics implemented in this Thesis' study are presented. On top of that, the analytical procedure of the preparation and the implementation of each experiment is described.

Table of contents

2.1 Cold atmospheric pressure plasma reactors

As mentioned before, in this Ph.D. Thesis we used three different plasma reactors as each one of them satisfies different needs in plasma medicine.

The three aforementioned reactors that were used in this study are presented schematically in Figure 2.1.

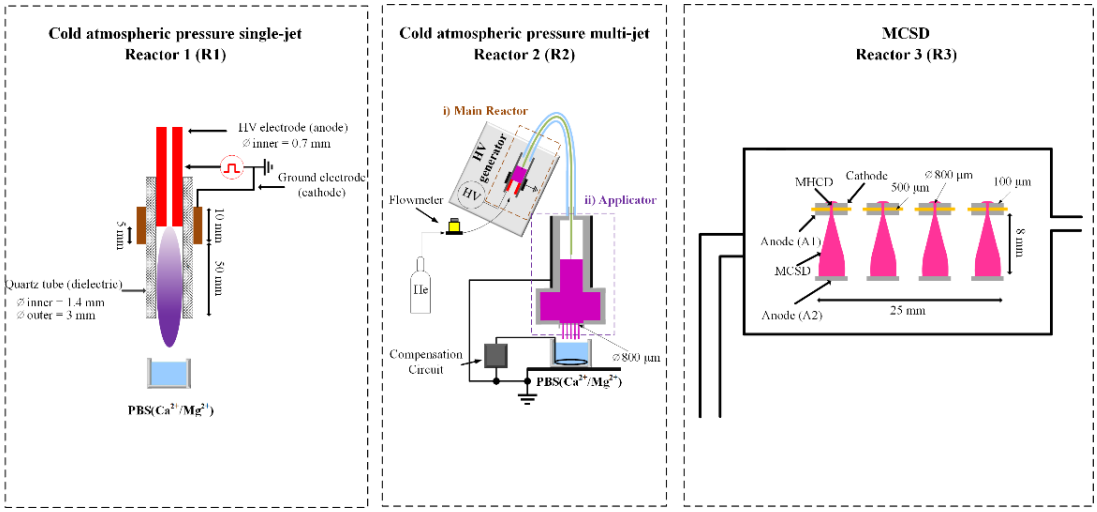

Figure 2.1 The three different plasma reactors used in this Thesis work.

The first reactor, R1, is a typical atmospheric pressure plasma jet or micro-plasma jet, that was designed and implemented in the Laboratoire de Physique des Gaz et des Plasmas (LPGP, CNRS & Univ. Paris-Saclay). It consists of a stainless-steel needle (0.7 mm inner and 1.4 mm outer diameters), inserted inside a dielectric tube made of quartz, and biased electrically by applying high voltage square positive pulses (amplitude of 6 kV, pulse width of 4.8 µs, rise and fall times of around 25 ns) at a repetition rate of 10 kHz using a commercial power supply (DEI PVX-4110). The distance between the needle's tip and the reactor's nozzle is fixed (55 mm). The ground electrode (10 mm width), made of copper, is wrapped around the dielectric tube, centred at the tip of the needle[39,40]. Pure helium (Alphagaz 1 He, He ≥ 99,999 %, Air Liquide, Corbeil-Essonnes, France) or helium with an admixture of 0.2% of molecular oxygen (Alphagaz 1 O_2, O_2 ≥ 99,995 %, Air Liquide) are injected through the needle at different flow rates, varying from 0.1 to 2 standard litres per minute (slm), regulated by flowmeters (GF40-SA46 (for He) and SLA5800 (for O_2), Brooks instrument, Serv'Instrumentation, Irigny, France). Thus, a dielectric barrier discharge (DBD) is formed, and a plasma jet propagates outside the quartz tube through the He channel into the surrounding ambient air. The distance between the tube orifice and the surface of the treated solution has been varied between 2 and 20 mm.

For all our experiments, the micro-plasma jet reactor was placed vertically with the gas flowing downwards for interaction with the solution alone (for the experiments on the chemical composition of the plasma-treated solution), or with the solution that covered the different biological models (for the *in vitro* experiments with cells, lipids or proteins). The plasma propagated through the capillary tube and the He channel into the surrounding atmosphere, and either the plasma or its gaseous effluent interacted with the buffer solutions with a small admixture of the surrounding air. The plasma-treated solutions were, for the vast majority of the experiments presented in this Thesis, Phosphate-buffered saline solutions (PBS) containing Ca and Mg. After plasma treatment, we refer to them as pPBS. Adherent cells produce proteins that aid the attachment to the plate and to each other. Mg and Ca are divalent cations that are essential to protein activity. When we want our cells to adhere and grow, we need these cations. If we want to suspend them, we want to avoid/reduce the cations.

Reactor 1 produces high concentrations of reactive oxygen and nitrogen species (measured in the plasma-treated liquid in this Thesis) that play a key role in plasma cancer therapy such as hydrogen peroxide, nitrites, nitrates, hydroxyl radicals, singlet delta oxygen, among others. On top of that, the gas temperature remains relatively low (close to room temperature; see Chapter 3, section 3.3) and the current arriving at the target is also relatively low. All these facts make this reactor a safe and reliable solution for cancer treatment. Nevertheless, we need to mention that the small diameter of the tube, that, on one hand, is necessary to sustain the discharge with the present experimental conditions, imposes, on the other hand, limitations regarding the solution volume or the target size that can be treated by this device.

The second reactor, R2, used in this study consists of a cold atmospheric pressure multi-plasma jet, that was based on the configuration of the Plasma GUN[12,128]. Briefly, it consists of a high voltage electrode inserted inside a quartz dielectric tube and driven by high voltage pulses with an amplitude of 7 or 11 kV (FWHM of about 2.3 μs) at a repetition rate of 2 kHz provided by a custom-made power supply, designed and implemented in the Groupe de Recherches sur l'Energétique des Milieux Ionisés (GREMI, CNRS & Univ. d'Orléans). A second electrode is placed outside the dielectric tube and is connected to the ground. Thus, a coaxial dielectric barrier discharge (DBD) is formed. The working gas used was pure helium (Alphagaz 1 He, >99.9999%, Air Liquide) at a flow rate of 1 slm, regulated by a digital flowmeter (Vögtlin Instruments, ALTO Instruments, France). The main plasma reactor, where the plasma is produced, is located inside the power supply. At the reactor's orifice, a flexible dielectric tube is mounted, containing a floating-potential electrode (conductive wire of ca. 1 mm^2 section).

The dielectric tube connects the main reactor with a second plasma reactor. This second part of the plasma device, the applicator, is essentially a second coaxial DBD reactor that is made of a PTFE (polytetrafluoroethylene) body with the floating electrode placed in its centre and a grounded electrode on the outside. The outlet of the second plasma reactor has five micro-orifices (Øint = 800 µm), producing, thus, five distinct plasma jets covering a larger solution surface area during the plasma treatment. Four of the orifices are disposed at the corner of a 4.2 mm square, with the fifth orifice located at the crossing of the square diagonals. The solution treated by the plasma is placed in wells of a x24 well plate and is connected to the ground thanks to a ring-shaped wire electrode (stainless-steel wire Ø = 1 mm) located at the bottom of the wells. The distance between the applicator orifices and the surface of the solution was maintained at 4 mm thanks to a customized 3D-printed spacer. Between the electrode and the ground, it was placed a compensation circuit designed to impose a total target impedance equal to that of a human body standard model, as previously presented[128]. This grants additional control of the process parameters (which always include the target impedance) and eases the possible future translation of the results to a direct plasma application on animal models and human patients. This reactor produces also high concentrations of reactive oxygen and nitrogen species (measured in the plasma-treated liquid in this Thesis) and, on top of that, it can treat a relatively large area or a significant volume if the goal is the production of plasma-treated solutions. On the other hand, because the plasma-treated solution is grounded (through the compensation circuit) the current arriving at the target is significantly higher than in the previous reactor and, thus, discomfort could be caused if it is used to directly treat a living organism.

The third reactor, R3, consists of four micro-hollow cathode discharges (MHCD), electrically in parallel, but in series in what concerns the gas flow. Each MHCD is made of 100 µm thick molybdenum electrodes separated by a 500 µm thick alumina plate. An 800 µm diameter hole is drilled through each of these sandwiches. The distance between the individual MHCDs is 12.5 mm. It is powered from only one negative DC power supply [for the four micro-hollow cathode discharges (MHCD) cathodes] and from only one positive DC power supply for the four MCSD anodes A2 (Figure 2.1), through individual ballasting resistors. The MHCD anodes A1 are directly grounded. The distance between the individual MHCD, as well as the distance between the MHCD and the anodes A2, is 8 mm[129–131]. The working gas is He with a percentage of molecular oxygen that varied from 0 to 3%. The gas flow rate is also variable with values from 1 to 8 slm. The unique characteristic of this reactor is its capability to produce high fluxes of ozone and singlet delta oxygen[105]. As a matter of fact, by controlling the percentage of molecular oxygen in the gas, it is possible to minimize the

concentration of one and maximize the concentration of the other. For example, if a percentage of 0.5% of molecular oxygen is used, the reactor produces high concentrations of singlet delta oxygen and very low concentrations of ozone, while, on the other hand, if an oxygen percentage of 3% is used, it produces high concentrations of ozone and low concentrations of singlet delta oxygen[105]. Thus, these arrays of MCSD appear to be ideal tools to study in detail the reactivity of this reactive oxygen species with biological targets, such as DNA, lipids, or cells[132].

2.2 Experimental setups and equipment's

Here are presented all the different experimental setups, diagnostics, and protocols used in this Thesis' work. We follow here the structure of the Thesis' manuscript. Firstly, the diagnostics that were used to study the gaseous phase of the plasmas are described. Note that, in the frame of this Thesis' work, only the gaseous phase of the single jet (R1) was studied. Secondly, the means used for the electrical characterization of both reactors R1 and R2 are presented. Thirdly, the protocols used for the study of the liquid phase chemistry are described. We investigated solutions treated by all three plasma reactors, but as the protocols followed for their study were the same, they are presented only once. Finally, the preparation, treatment, and analysis of all the biological targets used in this study are described. Here, the protocols used for the treatment by each different plasma reactor are separated, as they differ.

2.2.1 Gaseous phase diagnostics

2.2.1.1 Electric field measurements using Stark polarization emission spectroscopy of helium atoms

To determine the electric field in the front of the ionization wave, Stark polarization emission spectroscopy was used. This setup is shown schematically in Figure 2.2. The electric field can be determined from the peak-to-peak wavelength difference between the allowed and the forbidden component of a certain helium line. To get this wavelength difference, a high-resolution spectrum of the desired helium line emitted by the plasma needs to be obtained. The light emission from the plasma is focused with a plano-convex lens (Thorlabs LA4236, f = 12.54 cm) onto the slit of a 0.75 m spectrometer (SpectraPro 2750, Princeton Instruments, equipped with a 68 x 68 mm grating, blazed at 500 nm). The entrance slit has a width of 50 μm, yielding an instrumental broadening of 0.052 nm (Gaussian profile). Before entering the spectrometer, the light passes through a linear polarizer (Thorlabs) to make sure only linearly polarized light remains, in

order to be able to measure the axial electric field. At the exit of the spectrometer, an ICCD camera (PI-MAX3:1024i, Princeton Instruments) is mounted to capture the spectral images. The camera is controlled on a computer by the software WinSpec (Princeton Instruments), and it is triggered with an external trigger (same as the trigger of the discharge). The integration time is the time during which exposures (time between the gate opening and closing) are accumulated on the chip within one frame. In general, the delay is set between 350 and 380 ns, the exposure time to 20 ns, the gain to the maximum value of 95 %. Depending on the intensity of the light, each recorded image contains 20 accumulations, each with 20000-50000 gates. Thus, a temporal resolution of 20 ns was obtained. The spatial resolution was 1 mm.

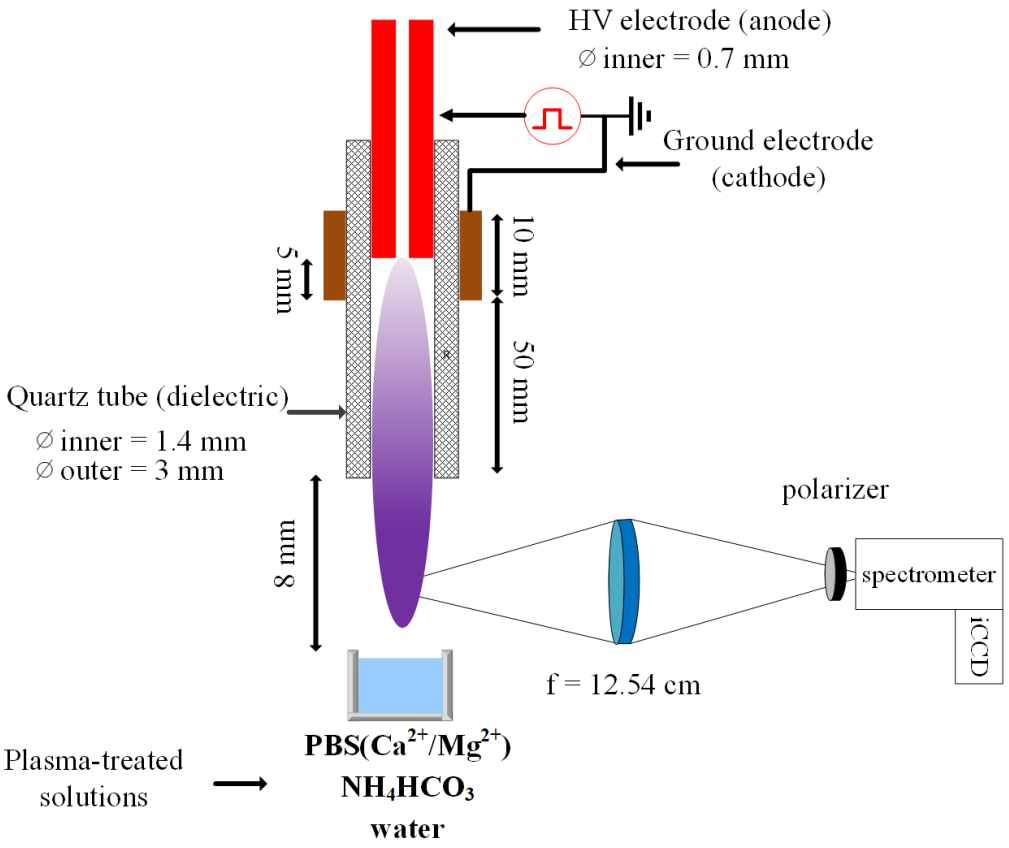

Figure 2.2 Experimental setup for the estimation of the electric field of the ionization wave by Stark polarization spectroscopy. The components of this experimental setup are not to scale.

In Figure 2.3, an indicative spectrum of the allowed and the forbidden lines of He at 447.15 nm is presented. The blue line depicts the spectrum registered by the spectrometer, while the green and red lines represent the pseudo-Voigt fittings for the allowed and the forbidden components separately (green line) and altogether (red line), respectively.

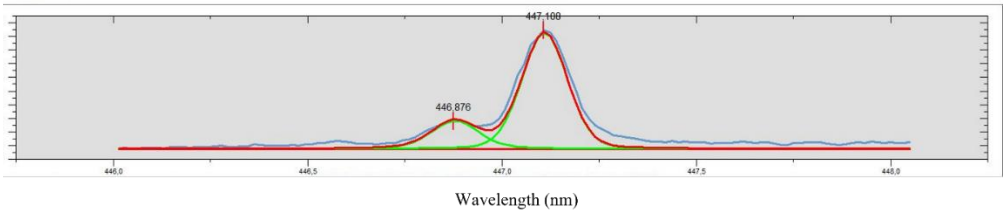

Figure 2.3 The allowed and forbidden components of the He line (2p $^3P^0$-4d ^3D at 447.15 nm) as registered in the spectrometer (blue line) and the pseudo-Voight fittings used to determine the distance of the two components peaks in nm (green lines).

As described by Obradovic *et al.*[117], the electric field in the front of the ionization wave can be determined by optical emission spectroscopy based on the application of the polarization-dependent Stark splitting and shifting of different He lines and their forbidden components[117]. According to these authors and Kuraica *et al.*[133] (who to our knowledge introduced the method), with the use of a polarizer mounted in the axis parallel to the external field, only one allowed and one forbidden π component can be detected. The $\Delta\lambda_{FA}$, which corresponds to the distance (in nanometres) between the peak of the allowed and the peak of the forbidden component, depends on the electric field E (kV/cm^{-1}). The lines that are mainly used for this detection are He lines that can be found at 447.15 nm (2p $^3P^0$-4d ^3D) and 492.19 nm (2p $^1P^0$-4d ^1D) and their forbidden components (2p $^3P^0$-4f ^3F) and (2p $^1P^0$-4f ^1F), respectively (other He lines can also be used but their intensity is usually significantly lower than the aforementioned ones). Kuraica *et al.* provided different polynomial equations (see Equations 1 and 2) for the He line at 447.15 nm and the 492.19 nm that, when solved (for a known $\Delta\lambda_{AF}$ in nm), result in the value of the axial local electric field of the ionization wave[133]. For the construction of these equations, the perturbation theory is used[133–135].

For the He I 492.19 nm:

$$\Delta\lambda_{AF} = -1.87 \times 10^{-5} \times E^3 + 8.8 \times 10^{-4} \times E^2 + 1.4 \times 10^{-3} \times E + 0.1316 \qquad \text{(Eq. 1)}$$

For the He I 447.15 nm:

$$\Delta\lambda_{AF} = -1.06 \times 10^{-5} \times E^3 + 5.95 \times 10^{-4} \times E^2 + 2.5 \times 10^{-3} \times E + 0.1479 \qquad \text{(Eq. 2)}$$

2.2.1.2 Electron density determined using the Stark broadening of the H_α and H_β lines

To determine the electron density (n_e) and the electron temperature, Stark broadening of a certain spectral line can be used. The measured profile of an atomic emission line can be affected by different broadening mechanisms: natural broadening, Doppler (thermal) broadening, Stark broadening,

instrumental broadening, etc. Different hydrogen spectral lines can be used for the determination of the Stark broadening, namely the Hα, the Hβ, the Hγ and the Hδ lines (at 656.28 nm, 486.13 nm, 434.05 nm, and 410.17 nm, respectively)[116]. In this Thesis' work, we principally studied the Hβ and Hα lines. In the GKS theory[136,137], with a quasi-static approximation using the classic Holtsmark field, the Stark broadening can be estimated using Equation 3. In this equation, $\Delta\lambda^{Stark}$ is measured in nm and the n_e in cm^{-3}. A certain value of the $a_{1/2}$ can be obtained for every specific set of electron temperatures and densities[138]. Generally, the spectral lines of hydrogen, H_β and H_γ, are characterized by a different dependence between the electron density and temperature. For H_β, this dependence is rather moderate (practically non-existent), while for H_γ, this dependence is more pronounced. As a result, by studying both spectral lines simultaneously, we can have at the end two different equations that both describe a relation between $\Delta\lambda^{Stark}$ and n_e. By numerically solving these equations we can obtain both the electron density and the electron temperature. Unfortunately, in our own experimental system, the H_γ cannot be obtained because it is overlapped with other spectral molecular lines. Thus, we only calculated the electron density by using the H_α and H_β lines.

$$n_e = \frac{\left[\Delta\lambda^{Stark}\times 10^9\right]^{3/2}}{\left[2.5a_{\frac{1}{2}}\right]} \qquad \text{(Eq. 3)}$$

The experimental setup used to obtain the H_α (Figure 2.4) and H_β lines at 656.28 nm and 486.13 nm, respectively, is the exact same used for the electric field measurements and it is depicted in Figure 2.2. The acquired spectral lines were fitted using a Voight (Gaussian-Lorentzian) profile with OriginPro 2020. These specific lines were deliberately chosen as each one of them has different advantages and disadvantages regarding their use for the estimation of the electron density and the electron temperature of the plasma. The intensity of the H_α is relatively high and, thus, it is easier to record it and implement the necessary fitting for the calculation of the line broadening. Nevertheless, H_α is a very problematic line because self-absorption can be important, but the principal problem is that H_α is a line without a good theoretical description for its Stark broadening. The intensity of H_β is also relatively high (smaller than that pf H_α though), and in this case there are good theoretical descriptions for its Stark broadening. Unfortunately, like for H_α, the dependency of and the electron density and temperature is again very low.

To calculate the Stark broadening of the spectral lines, we also considered the instrumental broadening (0.052 nm) and the Van der Waals broadening (0.03 nm) with Eq. 4, where M is the atomic mass. The doppler broadening was also calculated with Eq. 5, but its value is very low (~0.003 nm) and, thus, was not

considered in this study[139]. After having calculated the FWHM of each line that is caused by the Stark broadening alone (by subtracting the instrumental and Van der Waals broadening), the electron density and temperature were estimated using the tables provided by Gigosos *et al.*[140]

$$\omega_V = 8.18 * 10^{-19} \lambda^2 (aR^2)^{0.4} (\frac{T_{gas}}{\mu})^{0.3} * \frac{P}{k_B} * \frac{1}{T_{gas}} \qquad \text{(Eq. 4)}$$

$$\omega_D = 7.612 * 10^{-7} \lambda \sqrt{T_{gas}/M} \qquad \text{(Eq. 5)}$$

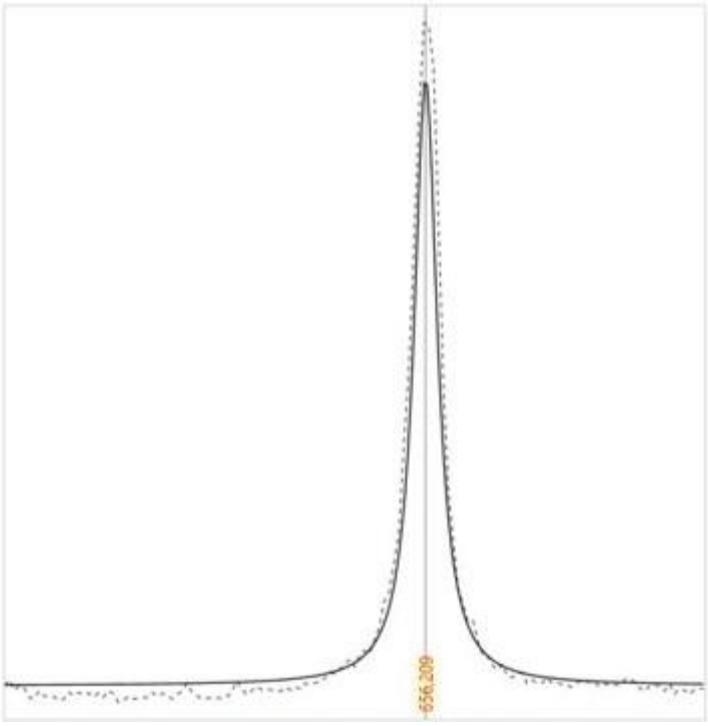

Figure 2.4 In this Figure, the H_α line is presented (located at 656.2 nm) as recorded in the spectrometer (dashed line) as well as the pseudo-Voight fitting used for the determination of its broadening (continuous line).

2.2.1.3 Estimation of the gas temperature

The experimental setup used to record the OH ($A^2\Sigma^+$-$X^2\Pi$) and N_2 (FNS / $B^2\Sigma^+_u$-$X^2\Sigma^+_u$) bands at 309 nm and 316 nm, respectively, is the exact same used for the electric field measurements and it is depicted in Figure 2.2, apart from a few small differences. Firstly, the polarizer was not used. Secondly, the gate opening was fixed at 200 ns (instead of 20 ns) as with smaller values it was not possible to obtain an exploitable signal for these two probe molecules. The acquired spectral lines were fitted using a homemade fitting application. In Figures 2.5 and 2.6, typical spectra of the rotational distributions of the probe molecules used in this study are presented.

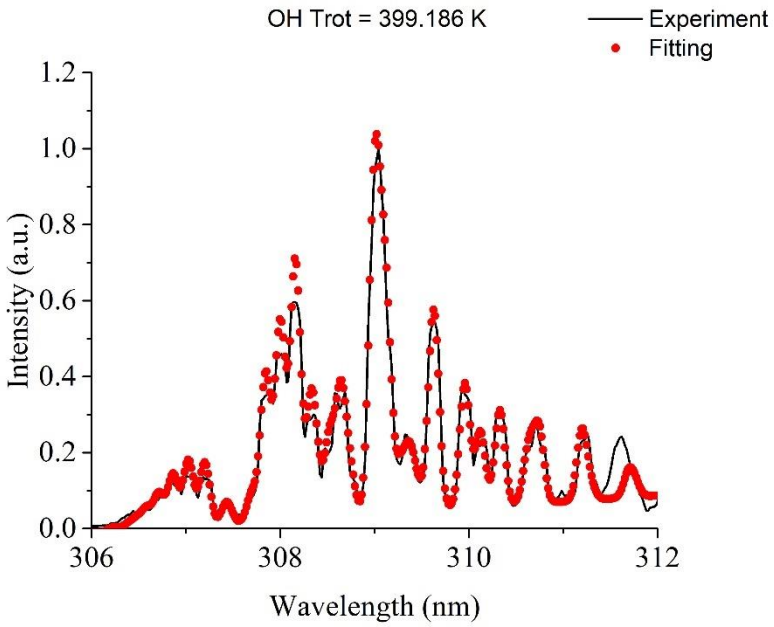

Figure 2.5 Typical spectrum of the rotational distribution of OH experimentally obtained (black line) and the applied fitting (red points) used for the determination of its rotational temperature (Trot). This spectrum was recorder at a position of 8 mm (Chapter 3, section 3.3).

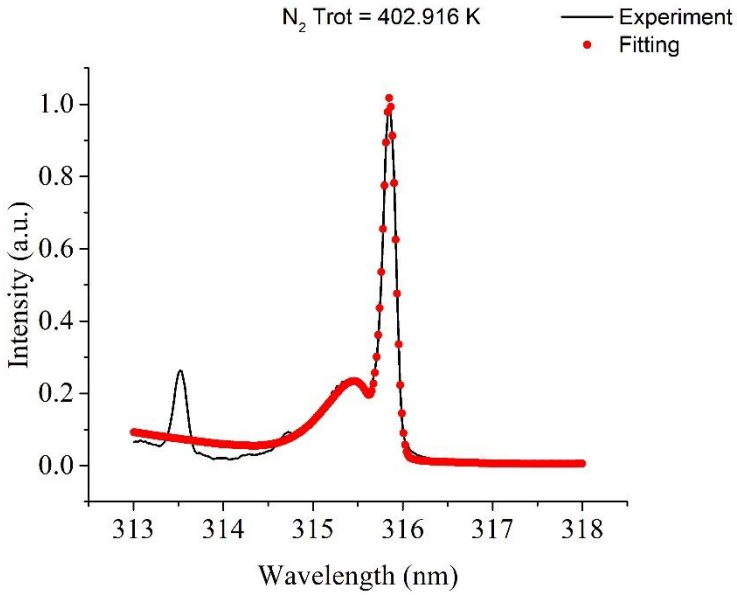

Figure 2.6 Typical spectrum of the rotational distribution of N_2 experimentally obtained (black line) and the applied fitting (red points) used for the determination of its rotational temperature (Trot). This spectrum was recorder at a position of 8 mm (Chapter 3, section 3.3).

2.2.2 Electrical and thermal characterization of the cold atmospheric pressure plasma jets (R1 and R2)

2.2.2.1 Electrical measurements of R1

The applied voltage was measured with a high-voltage passive probe (Lecroy, PPE 20 kV, France), while the DBD current was determined with a current probe (Rogowski coil). Both waveforms are read out on the oscilloscope (64Xi (Lecroy) 600 MHz, 10 GS/s).

The current that is measured when the plasma is on (total current, I_{tot}) consists of a capacitive component (I_{cap}) and a conductive component (I_{con}) as given by $I_{tot} = I_{cap} + I_{con}$. The capacitive current I_{cap}, also known as displacement current, is the current that arises from the circuit of the plasma reactor, which acts as a capacitor. The conductive current, I_{con}, is the current that flows through the plasma. In many cases, the conductive current is called plasma current but in our experimental conditions, this is not the case as the actual plasma current consists of the measured conductive current (in the main discharge – DBD) and the current in the plasma jet (outside the capillary). If all settings are kept constant, the capacitive current is the same when the plasma is on and off, when for instance the voltage is still applied but the flow is turned off. The DBD current, in which we are interested, is thus given by $I_{DBD} = I_{tot} - I_{cap}$. I_{tot} is measured as the total current when the plasma is on and I_{cap} as the total current when the plasma is off.

The energy that is dissipated in the DBD can then be calculated as

$$E = \int_0^T V * I_{con}\, dt \qquad \text{(Eq. 6)}$$

where the time integral is taken over one full voltage pulse. An example of signal of the applied voltage and current are shown below (Figure 2.7). The DBD energy per pulse is calculated with Eq. 6 and shown and discussed in Chapter 3. Typical waveforms of the high voltage and the current are presented in Figure 2.7. Here we have to underline once again that the current presented in Figure 2.7 is the conductive current measured in the DBD.

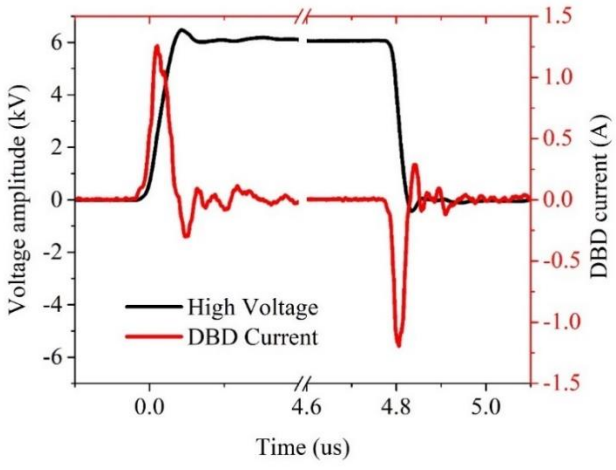

Figure 2.7 Electrical characteristics of the single-jet plasma source: high voltage measured on the power supply (black line) and current measured on the ground electrode of the DBD (red line). The gas flow rate was 1 slm (99.8% He / 0.2% O_2) and the treatment distance 8 mm.

2.2.2.2 Electrical measurements of R2

The applied voltage was measured with a high-voltage passive probe (Lecroy, PPE 20 kV, France), while the current passing through the solution and reaching the ring electrode was determined by measuring the voltage drop on the resistor in the compensation circuit with another high-voltage passive probe (Lecroy, PPE 6 kV, France). In Figure 2.8, the high voltage impulse and the total current of the multi-plasma jet are presented. The energy per pulse is calculated also here with equation 4 and shown and discussed in the Chapter 3. Nevertheless, in the case of the multi-plasma jet, the current is the total current of the system, measured in the compensation circuit (Figure 2.1) and, thus, the energy is the total energy of the system.

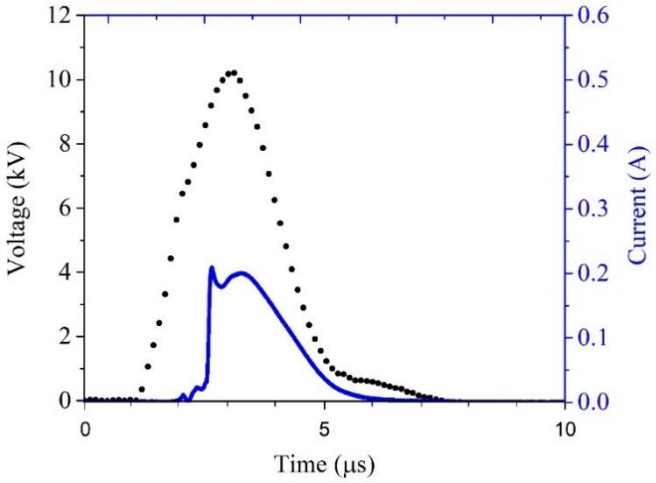

Figure 2.8 Electrical characteristics of the multi-jet plasma source: high voltage measured on the power supply (black dots) and current measured on the compensation circuit (blue line).

2.2.2.3 Thermal measurements

The temperature of the reactor's parts was measured with a FLIR infrared camera. The acquired images were analyzed with the application provided with the camera. In Figures 2.9 and 2.10, some typical infrared photos of the reactor are presented for the multi-plasma and the single-plasma jet, respectively.

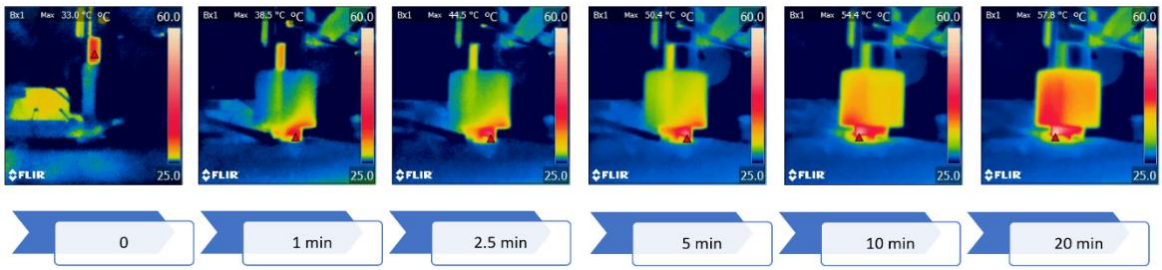

Figure 2.9 The temperature of the applicator of reactor 2 as a function of the treatment time. The treated target is PBS and the depicted temperature on the top of each photo corresponds to the hottest point of the reactor at the given treatment time (also marked with a red triangle in the photos). The infrared photos were obtained with an emissivity of 0.85.

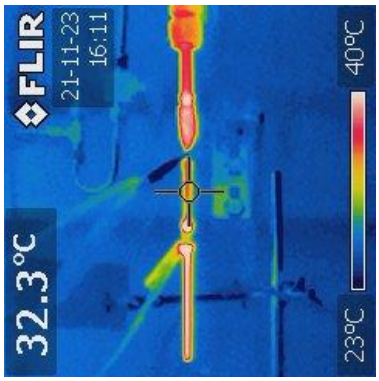

Figure 2.10 The temperature of reactor 1 after 20 minutes of treatment. The treated target is PBS. The infrared photos were obtained with an emissivity of 0.85.

2.2.3 Protocols used for the study of the liquid phase chemistry

In this part of Chapter 2, the protocols that were followed for the measurements of the reactive oxygen and nitrogen species in the liquid phase are discussed.

2.2.3.1 pH detection

The pH was measured in the pPBS using a SevenEasy™ pH meter S20 fitted with an InLab® 639 Micro electrode (Mettler Toledo, France). The pH meter was calibrated one time each week with the calibration samples provided by Mettler Toledo.

2.2.3.2 Quantification of hydrogen peroxide (H_2O_2), nitrite (NO_2^-), and nitrate (NO_3^-)

The concentration of hydrogen peroxide (H_2O_2) in pPBS was determined using

titanium oxysulfate ($TiOSO_4$), as previously described in published works[9]. Briefly, the concentration of H_2O_2 in the plasma-treated solutions was determined using $TiOSO_4$ to produce pertitanic acid, which is yellow. For the establishment of H_2O_2 standard curves (Figure 2.11) by $TiOSO_4$-based assay, serial dilutions of H_2O_2 were prepared in 100 µL of PBS(Ca^{2+}/Mg^{2+}), 4 µL of 200 mM NaN_3 were added and then 50 µl of 2 % $TiOSO_4$ diluted in 3 M H_2SO_4. NaN_3 is used to scavenge nitrites and other ROS that can interfere with $TiOSO_4$. The samples were incubated protected from light for 20 min at room temperature to allow the reaction to occur, and the absorbance was measured at 407 nm using a well plate reader (Infinite 627® M200 PRO Tecan, France).

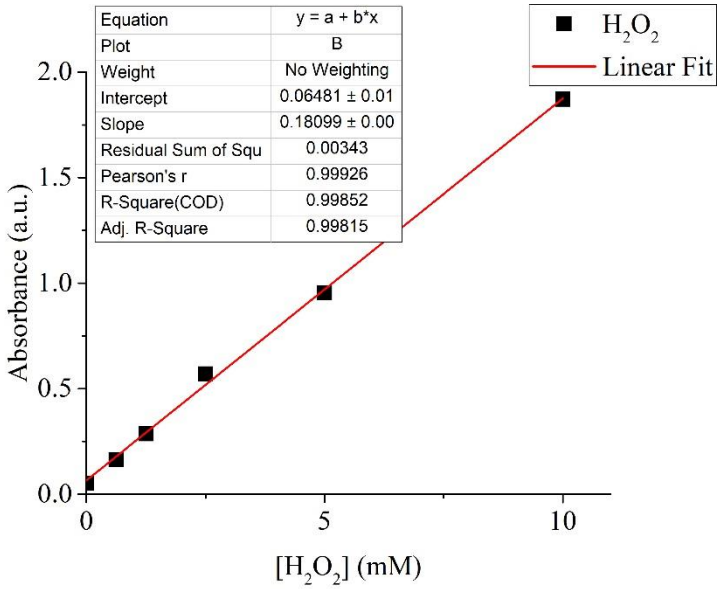

Figure 2.11 Measured absorbance at 407 nm for different known concentrations of H_2O_2.

The quantification of nitrite (NO_2^-) and nitrate (NO_3^-) was performed using the nitrate/nitrite colorimetric assay kit (Cayman) according to the suppliers' instructions. In Figure 2.12, the standard curves prepared for NO_2^- and NO_3^- quantification are presented. The absorbance was measured at 540 nm using the same spectrophotometric system as for H_2O_2.

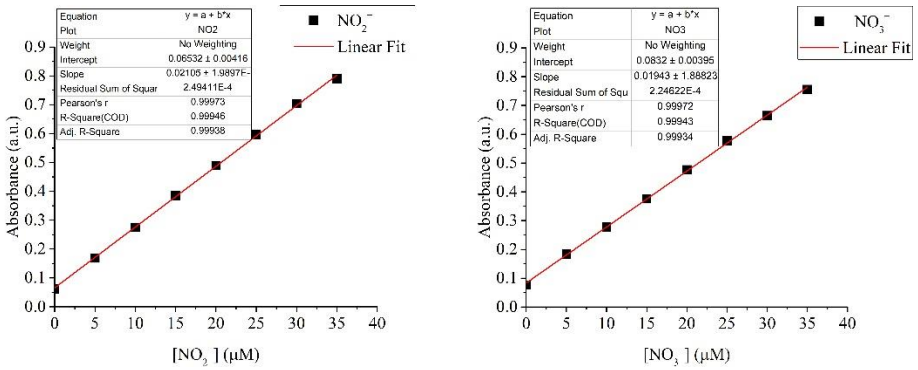

Figure 2.12 Measured absorbance at 540 nm for different known concentrations of NO_2^- and NO_3^-.

2.2.3.3 Conductivity measurements

The conductivity was measured in the pPBS using a SevenEasy pH/conductivity meter (Mettler Toledo, France). The conductivity meter was calibrated before each experiment with the calibration samples provided by Mettler Toledo.

2.2.3.4 Measurements of the solution temperature

The temperature of pPBS was measured (within 5 s after plasma treatment) with a thermocouple that was placed inside the solution.

2.2.3.5 H2DCFDA fluorescence assay

Detection of $ONOO^-$/ONOOH was performed by fluorescence spectrophotometry using the 2,7-dichlorodihydrofluorescein diacetate (2-(2,7-dichloro-3,6-diacetyloxy9H-xanthen-9-yl)-benzoic acid) (H2DCFDA) fluorescent dye (ThermoFisher Scientific). Briefly, H2DCFDA was diluted in ethanol and a working solution of 50 mM was obtained. Due to the possible light sensitivity, the dye was kept in the dark prior to and during the experiment. Just before the treatment, the working solution was diluted 25 times into PBS and, thus, a final solution of 2 mM H2DCFDA in PBS was treated by the plasma. The fluorescence measurements were performed using a spectrophotometer (Infinite 627® M200 PRO Tecan, France). The excitation wavelength was at 495 nm and the fluorescence was measured at 521 nm[141]. An important issue that we should underline here is the selectivity of H2DCFDA to other RONS. H2DCFDA has been reported to exhibit sensitivity also to hypochlorite anions/hypochlorous acid (ClO^- /HOCl), except to peroxynitrites. Also, for this fluorescence assay, a calibration curve, like those represented in Figures 2.11 and 2.12 for H_2O_2, NO_2^- and NO_3^-, could not be obtained as ad-hoc $ONOO^-$/ONOOH solutions were not available. Thus, in this Thesis' work, the dye was used for a rather qualitative study and especially for the detection of $ONOO^-$/ONOOH in the plasma-treated solutions.

2.2.3.6 Indigo reagent for detection of ozone

Ozone detection was achieved using potassium indigo trisulfonate (Sigma Aldrich). Indigo was diluted in PBS and a working solution of 10 mM was obtained. Just before the treatment, the solution was diluted 10 times into PBS and, thus, a final solution of 1 mM of indigo in PBS was treated by the plasma. The absorbance

measurements were performed using a spectrophotometer (Infinite 627® M200 PRO Tecan, France) at 600 nm. Due to the possible light sensitivity, the dye was kept in the dark prior to and during the experiment[142]. Unfortunately, indigo is not selectively sensitive to ozone. It can react also with other RONS, both short- and long-lived. In our own experimental conditions, we verified that it could react with H_2O_2 and singlet delta oxygen. For the first, it requires a high concentration of around 50 mM to decolorize the indigo, concentration 25-50 times higher than that measured in our plasma-treated solutions. On the other hand, for the latter, as it is presented in Chapter 4, experimental conditions where the MCSD reactor (R3) produces high fluxes of singlet delta oxygen and negligible concentrations of ozone were sufficient to significantly decolorize the indigo. Thus, as for peroxynitrites, this reagent cannot be used for a quantitative measurement of ozone but rather for a qualitative study.

2.2.3.7 Singlet delta oxygen sensor green (SOSG) for the detection of $O_2(a^1\Delta_g)$

Singlet delta oxygen ($O_2(a^1\Delta_g)$) detection was achieved using Singlet Oxygen Sensor Green (SOSG) (ThermoFisher Scientific). SOSG was diluted in 33 µL of methanol and a working solution of 5 mM was obtained. Just before the treatment, the solution was diluted 100 times in PBS and, thus, a final solution of 50 µM of SOSG in PBS was treated by the plasma. The fluorescence measurements were performed using a spectrophotometer (Infinite 627® M200 PRO Tecan, France). The excitation wavelength was at 504 nm and the fluorescence was measured at 525 nm. Due to the possible light sensitivity, the dye was kept in the dark prior to and during the experiment[143]. As the previously mentioned reactive species (except for hydrogen peroxide, nitrites and nitrates), also here we could not use ad-hoc $O_2(a^1\Delta_g)$ concentrations for the calibration of SOSG. Nevertheless, we used fluorescein that has the same excitation and emission wavelengths as the SOSG. The obtained calibration curve (see Figure 2.13) cannot be used for the absolute measurement of the $O_2(a^1\Delta g)$ concentration as the fluorescein and the endoperoxides (that are produced when the SOSG reacts with $O_2(a^1\Delta g)$) do not have the exact same quantum yield. Nevertheless, it can give a general image on the $O_2(a^1\Delta g)$ concentrations in the plasma-treated solution. Concerning the selectivity of SOSG towards $O_2(a^1\Delta g)$, we witnessed that SOSG can also react with other reactive oxygen species such as O_3 (see chapter 4).

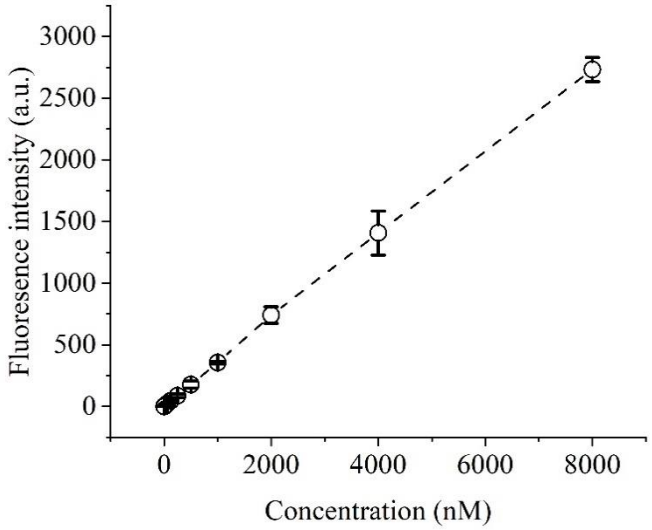

Figure 2.13 Fluorescein calibration curve while using Singlet delta oxygen sensor green (SOSG).

2.2.3.8 Terephthalic acid for the detection of •OH radicals

Detection of •OH radicals was performed by fluorescence spectrophotometry using terephthalic acid (ThermoFisher Scientific). Briefly, terephthalic acid was diluted in methanol and a working solution of 50 mM was obtained. Just before the treatment, the working solution was diluted 25 times in PBS and, thus, a final solution of 2 mM terephthalic acid in PBS was treated by the plasma. The fluorescence measurements were performed using a spectrophotometer (Infinite 627® M200 PRO Tecan, France). The excitation wavelength was at 310 nm and the fluorescence was measured at 425 nm. Due to the possible light sensitivity, the dye was kept in the dark prior to and during the experiment[144]. Also, for this fluorescence assay, a calibration curve, like in Figures 2.11 and 2.12 for H_2O_2, NO_2^- and NO_3^-, could not be obtained as ad-hoc •OH radical solutions were not available. Thus, in this Thesis' work, the dye was used for a rather qualitative study and especially for the detection of •OH radicals in the plasma-treated solutions.

2.2.3.9 pH detection with pH markers

For monitoring the pH during the freezing process, regardless if it was typically frozen at –20 or –80 °C, or slowly frozen (by using isopropanol-filled containers) towards –80 °C, or fast frozen (by using liquid nitrogen) and then stored at –20 °C, two different electrophoretic color markers were used as pH indicators: bromophenol blue and thymol blue. While the first color marker changes from blue at pH 4.6 to yellow at pH 3.0, the second transitions from

yellow at pH 2.8 to red at pH 1.2. Thymol blue was provided by Sigma-Aldrich, while Bromophenol blue was purchased from Bertin (France). The pH of the mimicking solutions was modified using hydrochloric acid. To estimate the pH of the frozen plasma-treated solutions from their colour, calibration samples were prepared containing untreated PBS with modified pH in which the pH markers were added. As we can see in Figure 2.14, for each pH value, a distinct colour of the solution containing the colour markers was obtained. Thus, the actual pH of the frozen treated solutions (presented in Chapter 4) was estimated by comparing the colours of the calibration samples with the colours of the treated samples with image processing. To be able to compare numerically the calibration samples with the treated ones, a weight was attributed to each sample which was the R+G–B. Thus, the calibration samples gave as a polynomial function, the solution of which, for a given value of R+G-B values, unveiled the pH of the treated solution.

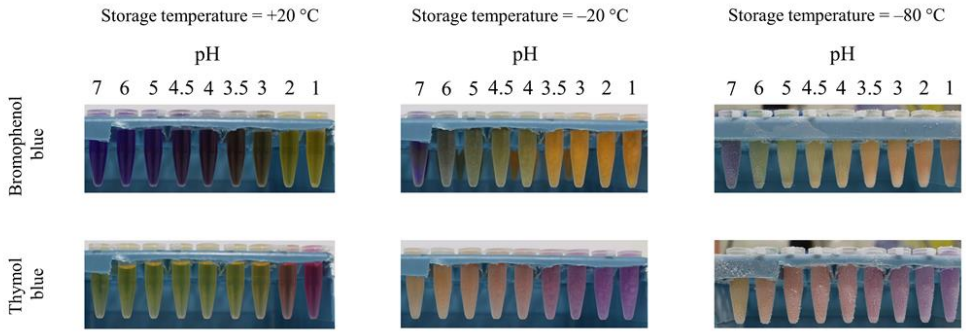

Figure 2.14 Photographs of Eppendorf tubes containing untreated PBS with adjusted pH values (from 1 to 7) and Bromophenol blue (top) or Thymol blue (bottom), after storage for 6 hours at +20 °C, –20 °C and –80 °C. On the top of the photographs is indicated the initial pH value of the solution before freezing (measured using a SevenEasy™ pH meter S20 fitted with an InLab® 639 Micro electrode).

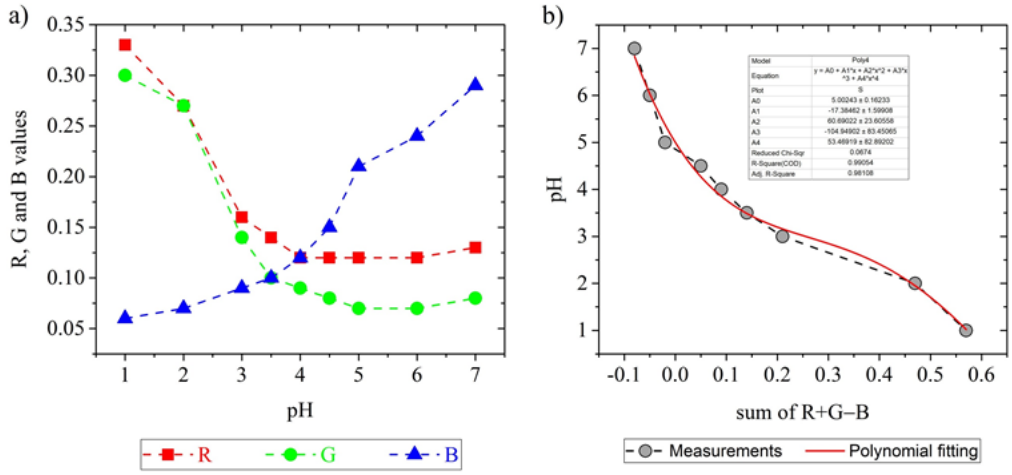

Figure 2.15 a) R, G and B values obtained from the photographs of the Eppendorf tubes containing untreated PBS with adjusted pH and bromophenol blue and stored at +20 °C for 6 hours (top left of Figure 2.14; mean values of a large area). b) Evolution of the sum of R+G–B as a function of the

pH, as well as the polynomial function used for the calculation of the pH values of the plasma-treated PBS (Figure 4.36), plotted in Figure 4.38.

2.2.3.10 Dismutation of H_2O_2 by pyruvate

To scavenge H_2O_2, we used sodium pyruvate (Thermo-Fischer Scientific, France), a known H_2O_2 scavenger. The pyruvate was added to pPBS after the plasma treatment. Sodium pyruvate was used in two different cases in this Thesis' work. Firstly, it was added in the plasma-treated solution to scavenge H_2O_2, and thus, quantify the cytotoxic effect of the solution on the cells that cannot be attributed to hydrogen peroxide (but rather to other reactive oxygen and nitrogen species). Secondly, it was added in the plasma-treated solution to validate our hypothesis that, in acidic environments, H_2O_2 can oxidize NO_2^-. For the first case, a pyruvate at a concentration of 5 mM was used, while, for the second case, concentrations of 5 and 50 mM of pyruvate were used.

2.2.3.11 Dismutation of H_2O_2 by catalase

A 10 mg/mL stock solution of catalase (Sigma-Aldrich, specific activity 2000–5000 units/mg of protein) was prepared in 50 mM potassium phosphate buffer. This solution was diluted 10 000 times in PBS or pPBS. Catalase was added to pPBS immediately after plasma treatment (for direct plasma treatment), and just before the addition of pPBS to the cells (for indirect plasma treatment), so it was present only during the incubation time.

2.2.3.12 Quenching of other ROS by DMSO, Taurine, NaN_3, or L-*Histidine*

Stock solutions of Taurine, NaN_3, and L-histidine at 500 mM were prepared in distilled water (Taurine and NaN_3) and PBS (L-histidine). The final concentration of Taurine was 5 mM, of NaN_3 1 mM, and of L-histidine 1 or 5 mM. DMSO was used at a final concentration of 1%. Normally a percentage of 0.5% of DMSO is proposed to ensure that it will not be toxic to the cells, but we verified that the percentage we used is not toxic to our cells (Figure 5.18 -> DMSO 1% -> Mocked column). Compounds were added to PBS either before or immediately (within 5 s) after plasma treatment. Mock-treated cells were handled the same way as treated cells.

2.2.4 Preparation, treatment, and analysis of all the biological targets

2.2.4.1 Experiments conducted with R1 – Cancer and normal cells treatment *in vitro*

2.2.4.1.1 Plasma treatment

In short-term *in vitro* experiments (incubation up to 24 h post-treatment), 5×10^4 to 2×10^5 cells were seeded per well in 24-well plates in 1 mL of complete medium and incubated for 24 to 72 h so that the cells were between 50% and 60% confluent at the time of plasma treatment. In long-term *in vitro* experiments (incubation from 48 h to 72 h posttreatment), 2×10^4 to 10^5 cells were seeded per well in 24-well plates in 1 mL of complete medium and incubated for 24 h. For direct plasma treatment, the cell culture medium was removed, the cells washed one time with phosphate-buffered saline containing 0.9 mM $CaCl_2$ and 0.49 mM $MgCl_2$ and 800 µL of PBS were added to each well. PBS covering the cells was then exposed to He/O_2 or He plasma. resulting in plasma-treated PBS (named pPBS for convenience in this Thesis). At the end of the plasma treatment (immediate effects), pPBS was either left in contact with cells at room temperature for 1 h (early effects) and then removed (direct plasma treatment) or immediately removed (only immediate effects). For indirect plasma treatment, 800 µL of PBS were added per empty well and treated with He/O_2 plasma, resulting also in pPBS. Thereafter, pPBS was put in contact with the cells for 1 h, after which it was removed. For reconstituted buffer, 800 µL of untreated PBS containing the same concentrations of H_2O_2, NO_2^- and NO_3^- and the same value of pH as in plasma-treated (for 12 min) PBS was put in contact with the cells for 1 h, after which it was removed. In all cases (direct and indirect plasma treatments, as well as reconstituted buffer), after removal of pPBS, 1 mL of complete medium was added to the cells, and the plates were incubated at 37 °C and 5% CO_2 in a humidified atmosphere for from 6 h to 72 h.

2.2.4.1.2 Cell viability assays

The cell viability was determined using MTT, CellTiterGlo®, and trypan blue assays. MTT assay is a colorimetric assay and CellTiterGlo® is a luminescent assay, both assessing the metabolic activity of the cells that is proportional to the number of viable cells under cytotoxic conditions. For the MTT assay, the cell culture medium was removed, and the cells were covered with 500 µL of complete medium containing 0.5 mg/mL thiazolyl blue tetrazolium bromide (MTT) (Sigma-Aldrich, Saint-Quentin Fallavier, France). The plates were incubated for 3–4 h at 37 ◦C until a purple precipitate was visible. The resulting intracellular purple formazan was then solubilized by adding 500 µL of isopropanol 95%/hydrochloric acid 1.5%. Spectrophotometric quantification was then performed at 570 nm using a well plate reader (Infinite® M200 PRO Tecan, Lyon, France). For the

CellTiterGlo® assay, the cell culture medium was removed, and the cells were covered with 300 µL of a solution 1/1 (vol/vol) of complete culture medium/CellTiterGlo® reagent. The plates were shaken for 15–20 min to allow complete lysis of cells and 100 µL of solution were transferred into 96-well white plates. Luminescence signal was recorded on a plate reader (VICTOR™X3, Perkin Elmer, Villebon-sur-Yvette, France). The trypan blue assay is a direct counting of living cells, which exclude the dye, and of dead cells, which incorporate the dye. To perform the assay, 6 h post-treatment, cell culture medium containing floating cells was transferred into 2 mL Eppendorf tubes, the tubes centrifuged for 5 min at 6000 rpm, after which the medium was discarded. 100 µL of fresh medium was added to each tube, and the cells were counted. In parallel, remaining adherent cells in each well were detached by trypsin, collected in 2 mL Eppendorf tubes, and further processed, as described above. Cell counting was performed on a LUNA-II automatic cell counter (Logos Biosystem, Villeneuve d'Ascq, France).

2.2.4.1.3 Measure of lipid peroxidation and intracellular ROS formation

Cells were seeded in 24-well plates and incubated in a humidified incubator at 37 ◦C / 5% CO_2 for 1 to 3 days depending on the number of seeded cells. When cells were about 80% confluent, the medium was removed and replaced by 0.25 mL of fresh DMEM high glucose, containing 5 µM BODIPY 581/591 C-11 (ref D3861, Invitrogen, Les Ulis, France) to assess for lipid peroxidation, or 5 µM H2DCFDA (ref C6827, Invitrogen) to assess for intracellular ROS production. The plates were further incubated for 30 min, after which the medium was discarded, the cells washed 1× with fresh complete medium, and 1× with PBS. Following 1 h incubation post direct and indirect plasma treatments or reconstituted buffer, the medium was removed, the cells washed 1× with PBS, and trypsinized. The cells were collected in FACS tube in 0.4 mL of MACS buffer (PBS containing 2% BSA, 1 mM EDTA, and 0.09% sodium azide, Miltenyi Biotec, Paris, France) and analyzed by flow cytometry (BD LSRFortessa™ X-20, BD, Le Pont de Claix, France), as per the manufacturer's instructions.

2.2.4.1.4 Flow cytometry analysis of RPE-hTERT cells using Propidium Iodide (PI)

RPE-hTERT cells were exposed to direct plasma treatment (12 min plasma treatment (immediate effects) followed by 1 h incubation (early effects)) and further incubated in a complete cell culture medium for 6 h. All cells were then collected into Falcon tubes. After centrifugation, cell pellets were either resuspended in MACS buffer containing 10 µg/mL of PI or resuspended in PBS and fixed in 70% EtOH. Fixed cells were then centrifuged, washed once in MACS buffer, and resuspended in MACS buffer containing 10 µg/mL of PI. The cells were analyzed by flow cytometry (BD LSRFortessa™ X-20, BD), as per the manufacturer's

instructions.

2.2.4.1.5 Apoptosis assay using caspase detection method

Caspase 3/7 activity was monitored 6 h after treatment using Caspase-Glo® 3/7 Assay System (Promega, Charbonnières-les-Bains, France).

2.2.4.1.6 Bovine serum albumin treatment

The same protocol used for cancer and normal cells treatment was also followed for the plasma treatment of BSA protein. The effect of plasma treatment on the proteins was assessed by Stain-free gel (trichloro-ethanol) and by SimplyBlue staining. The intensity of the decolorization of the sample (Figure 2.16) was quantified with image processing.

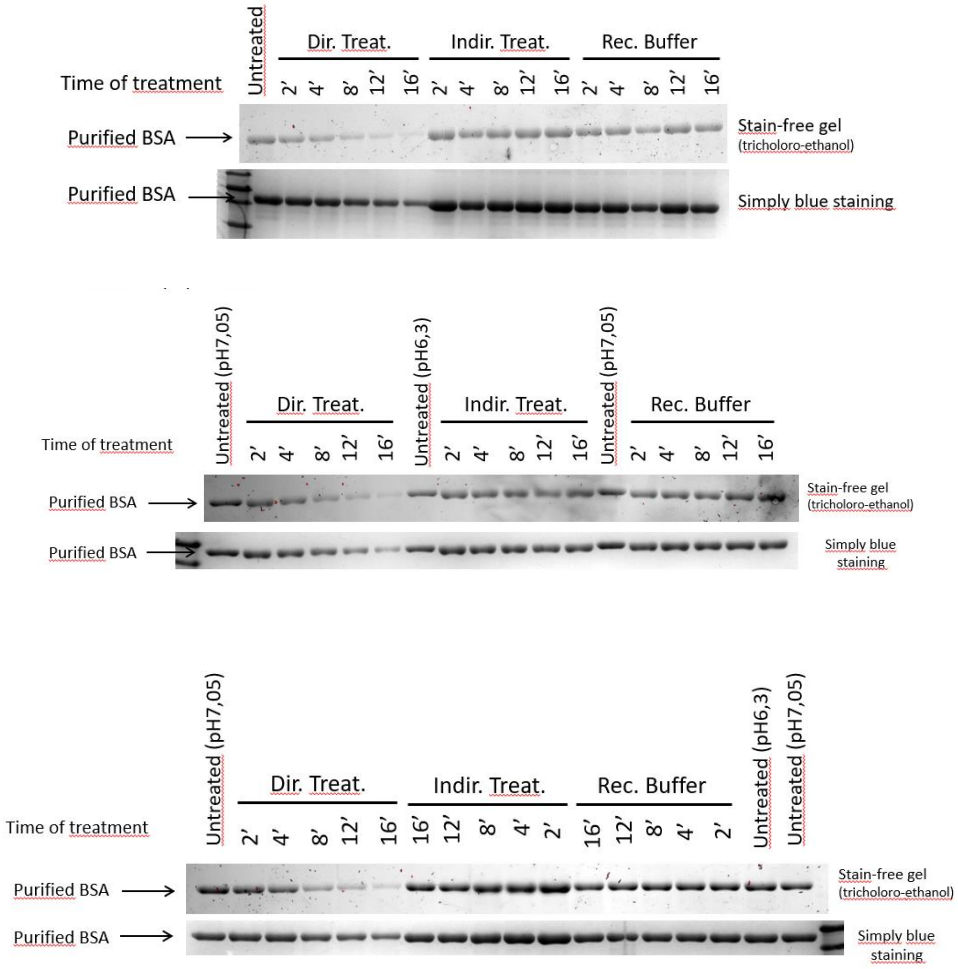

Figure 2.16 Photos of the BSA protein treated with direct plasma treatment, indirect plasma treatment and reconstituted buffer as analysed using SimplyBlue staining.

2.2.4.1.7 Statistical analyses

All the results are expressed as mean ± standard deviation (SD) of 2 to17 independent experiments, with each time point in duplicate. The significance level, or p-value, is calculated using the Student's t-test and displayed on the figure plots as NS: $p > 0.05$; *: $p \leq 0.05$; **: $p \leq 0.01$; ***: $p \leq 0.001$; ****: $p \leq 0.0001$.

2.2.4.2 Experiments conducted with R2 – Cancer and normal cells treatment *in vitro* and *in vivo*

2.2.4.2.1 pPBS production, mimicking solutions preparation, and their storage procedure for the *in vitro* experiments

The procedure followed to produce pPBS is depicted schematically in Figure 2.17. More precisely, 3 mL of Dulbecco's phosphate buffered saline (PBS) containing Ca^{2+} and Mg^{2+} (DPBS, Ca^{++}, Mg^{++}, 14040-133), named PBS(Ca^{2+}/Mg^{2+}), were placed in individual wells of 24-multiwell plates (Nunclon® Delta Surface, Thermo Fisher Scientific, DK, 142475, France) and treated by the plasma for 20 minutes (except if stated differently). Afterward, the amount of water evaporated during the plasma treatment (*ca.* 700 µL) was compensated by adding 700 µL of sterile water. Subsequently, the pPBS was divided and placed into several Eppendorf tubes (0.5 mL each). On the day of the plasma treatment (D0), and within 2 hours after the PBS treatment, the absolute concentrations of H_2O_2, NO_2^- and NO_3^- (Figure 2.17), as well as the pH value of the pPBS, were measured. Note that it has been verified that the RONS concentrations remain the same between immediately after (within 10 minutes) and a few hours after the plasma treatment if the pPBS is kept at +4 °C or + 20 °C. The remaining Eppendorf tubes were stored at different storage temperatures considered in this study: +20 °C, +4 °C, –20 °C, and –80 °C. For the preparation of mimicking solutions, we used untreated PBS(Ca^{2+}/Mg^{2+}), into which we added pure concentrations of H_2O_2, NO_2^- and NO_3^- as those measured in pPBS ($[H_2O_2]$ = 2.53 mM, $[NO_2^-]$ = 1.5 mM and $[NO_3^-]$ = 0.75 mM, see Figure 2.17). The pH of the mimicking solutions was adjusted to the same value as that measured in pPBS, using hydrochloric acid . The concentration of the reactive species (H_2O_2, NO_2^- and NO_3^-) and the value of the pH were measured, both in pPBS and in mimicking solutions, after 1 (24 hours after the treatment at D0), 7, 14, 21, and 75 days of storage (Figure 2.17 c). Finally, the degradation of the RONS and the modification of the pH due to the storage time or/and temperature were quantified in relation to the initial values measured on the day of the plasma treatment (for pPBS) or the day of preparation (for the mimicking solutions), within 2 hours after it (D0).

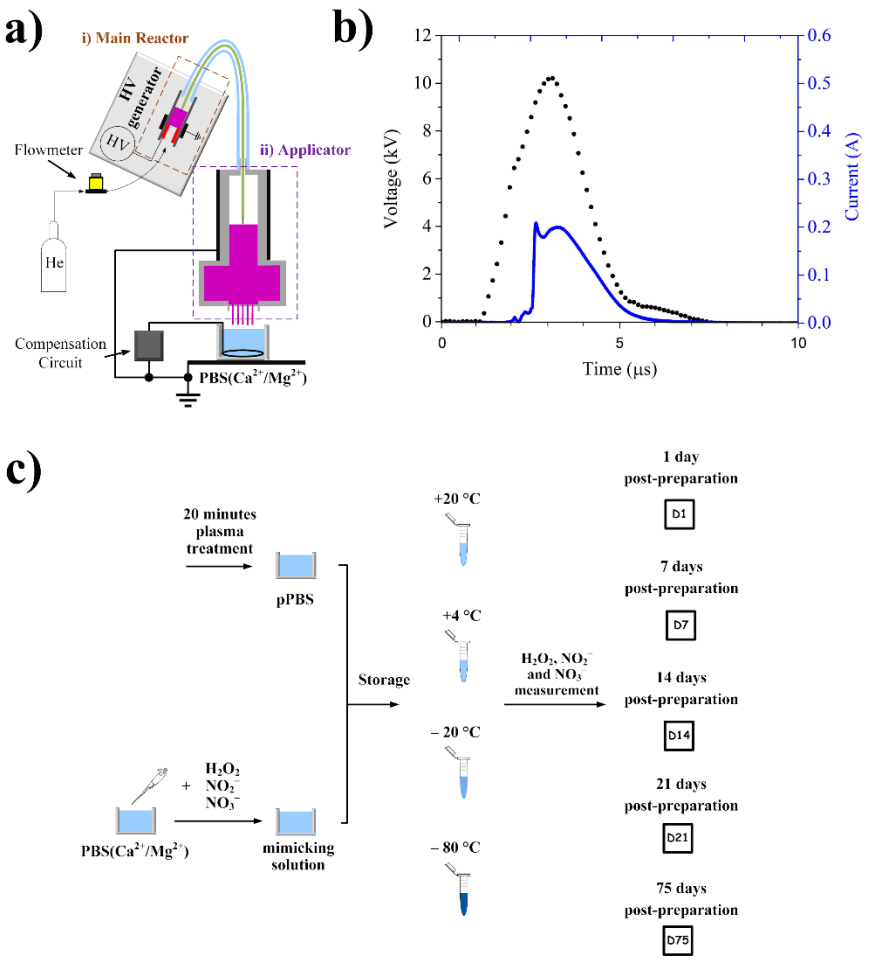

Figure 2.17 a) Conceptual view of the experimental setup and the two reactors used in this study i) for the plasma production and ii) for the solution treatment. b) Electrical characteristics of the multi-jet plasma source: high voltage measured on the power supply (black dots) and current measured on the compensation circuit (blue line). c) Conceptual view of the experimental procedure employed for the treatment, storage, and analysis of the pPBS samples.

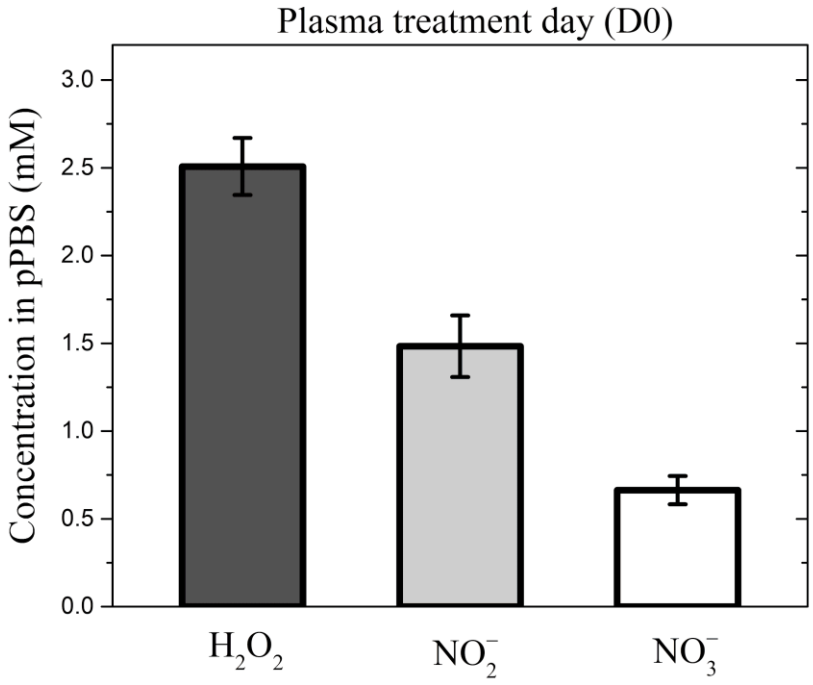

Figure 2.18 Concentration of H_2O_2, NO_2^- and NO_3^- in pPBS measured on the day of the plasma treatment (D0), within 2 hours after it. The data shown are the mean values ± SEM of 34 independent experiments for H_2O_2 and 30 independent experiments for NO_2^- and NO_3^-.

2.2.4.2.2 Cell culture

DC-3F Chinese hamster lung fibroblasts[33] and highly tumorigenic murine fibrosarcoma LPB cells[34], all mycoplasma-free, were cultured as adherent cells in Minimum Essential Medium (MEM, 31095-029) and Roswell Park Memorial Institute 1640 Medium (RPMI Medium, 21875-034), respectively. All media were supplemented with 10% fetal bovine serum (FBS, F7524), 100 $U.mL^{-1}$ penicillin, and 100 mg. mL^{-1} streptomycin (15140-122). Adherent cells were spread at 37 °C in a 95% humidity atmosphere containing 5% CO_2 (HERAcell 240i incubator CO_2, Thermo Scientific, France) and passaged upon confluency (every two days at a 1:10 dilution or every three days at a 1:30 dilution) using TrypLE™ Express Enzyme solution (12604-013). Short-term cell viability for routine sub-culturing was assessed by the trypan blue exclusion dye method (Trypan Blue Solution, T8154) with a Countess™ II FL Automated Cell Counter (Invitrogen, France), considering only viable cells. Cells were regularly checked for mycoplasma contamination *via* polymerase chain reaction (PCR) (not detailed).

For all assays on those cell lines (cytotoxicity and cell membrane permeabilization), 300 µL of cell suspension at a density of 1.80×10^5 $cells.mL^{-1}$ were used to seed each well of 48-well plates (Nunclon® Delta Surface, Thermo

Fisher Scientific, DK, 150687, France), 24 hours before the experiment (*i.e.* at D–1), allowing to reach *c.a.* 80 to 90% confluence of the cell layer on the day of the experiment (D0). Just before any assay, the medium above the cells was gently removed by aspiration, and the cell layer was washed twice with PBS(Ca^{2+}/Mg^{2+}). For sham conditions, all procedures remained identical to pPBS conditions, but untreated PBS, previously stored under the same storage conditions as the pPBS, was used instead.

2.2.4.2.3 Cell viability assessment by clonogenic assay

The cytotoxicity of pPBS, previously stored under different storage conditions, was determined by means of the clonogenic assay for DC-3F cells. LPB cells do not form colonies and, therefore, the assessment of their viability could not be performed using this precise test. Adherent DC-3F cells were incubated with 200 µL of pPBS per well for 10 minutes (note that the pPBS put in contact with the cells was always at room temperature and had just been unfrozen or warmed up a few minutes before, if applicable). Afterward, pPBS was gently removed from the cell layer and cells in each well were detached by 100 µL TrypLE™ Express and suspended in its culture medium. A serial dilution of the single-cell suspensions was performed for cell cloning as previously reported[31]. Concretely, based on the total number of cells counted in the single-cell suspension in untreated PBS (for D0) or in untreated PBS previously stored at +4 °C (for D1 and D21), the single-cell suspension of every sample was diluted in complete medium at a final concentration of 125 cells. mL^{-1} in a final volume of 8 mL. Cells were then distributed in 3 wells of a 6-multiwell plate (Nunclon® Delta Surface, Thermo Fisher Scientific, DK, 140675, France) by pouring 250 cells in 2 mL per well. This seeding allows individual (and surviving) cells to form discrete colonies over 5 days of cell culture at 37 °C in a 5% CO_2 humidified cell incubator. After 5 days of cell culture, colonies were fixed and stained with a solution of formaldehyde (3.7% vol/vol) containing crystal violet (0.2% wt/vol) in H_2O. The number of clones for each condition was counted. Colonies containing more than 50 cells were counted as “normal size colonies”, and those containing from *c.a.* 20 to fewer than 50 cells were counted as “small colonies”. The viability was then normalized to the number of clones in the corresponding sham sample.

2.2.4.2.4 Cell membrane permeability assessment by flow cytometry analysis

The eventual permeabilization of the cells treated by the pPBS was investigated by means of the fluorescent nucleic acids stain YO-PRO®-1 Iodide uptake (629.04 Da). The non-permeant YO-PRO®-1 dye is commonly used as an

indicator for cell membrane permeabilization. Indeed, YO-PRO®-1 can enter the cell only when the cell membrane is permeabilized, and, once in the cells, it intercalates with nucleic acids, resulting in a strong green fluorescence signal which is detectable by flow cytometry. On the day of the experiment, the medium above the cells was removed and the cell layer was washed twice with PBS(Ca^{2+}/Mg^{2+}). The two cell lines were then incubated for 1 hour with the mixture of pPBS (previously stored under different storage conditions) and YO-PRO®-1 Iodide at 2 µM (200 µL per well). After the treatment, the solution above the cell monolayer was gently removed and the cells were harvested using TrypLE™ Express Enzyme dissociation (200 µL per well). The cell suspension was immediately analyzed by flow cytometry (C6 flow cytometer, BD Accuri, San Jose, California, US) with 10 000 events recorded per sample within a selected gate that excludes cellular debris. The YO-PRO®-1 uptake (cell permeabilization) was evaluated using green fluorescence channels (excitation 488 nm, emission 530/30 nm). More precisely, we assessed the median of the fluorescence intensity per cell (an indication of the average level of permeabilization of the cells).

2.2.4.2.5 Adherent cells electropulsation setup

We used the system described in Ref. [145] for the electropulsation of the adherent cell monolayer. More precisely, as displayed in Figure 2.19, an in-house built mold of PDMS (polydimethylsiloxane, SYNGARD™ 184 Silicone Elastomer, DE) with an empty 2 cm^2 rectangle was inserted in a Ø 35 mm Petri dish (Nunclon® Delta Surface, Thermo Fisher Scientific, DK, 353001) to obtain a 2 cm^2 surface for cell growth. One day before the experiment, 600 µL of cell suspension were added to the defined area of each Petri dish at a density of 2.20×10^5 cells·mL^{-1} (i.e. 1.32×10^5 cells/600 µL) for DC-3F fibroblasts or 1.80×10^5 cells·mL^{-1} (i.e. 1.08×10^5 cells/600 µL) for B16-F10 melanoma cells, in respect to their growing speed and morphology (malignant B16-F10 murine melanoma cells grow much faster than DC-3F Chinese hamster lung fibroblasts). These seeding densities are based on our previous observation and experience, as they appear to be suitable for obtaining a homogenous cell layer at ca. 80% confluency (not entirely dense) after 24 h of cell culture. Different pre-treatment protocols were tested on the day of the experiment. Afterward, the electric pulses were applied on the cell layer by means of an in-house built electrode configuration consisting of two parallel stainless-steel plates (2 mm thick), fixed in the PDMS mold, and distant of 6 mm. The electrodes and the custom molding PDMS were designed to ensure the entire exposition of the cell monolayer to EPs. To generate microsecond pulsed electric fields (µsPEFs), the Cliniporator™ (IGEA, Carpi, IT) was used to deliver eight consecutive square-wave electric pulses of 100 µs duration, at a repetition frequency of 1 Hz, and different field strengths (500, 600, 1100, and 1400 V/cm)[12].

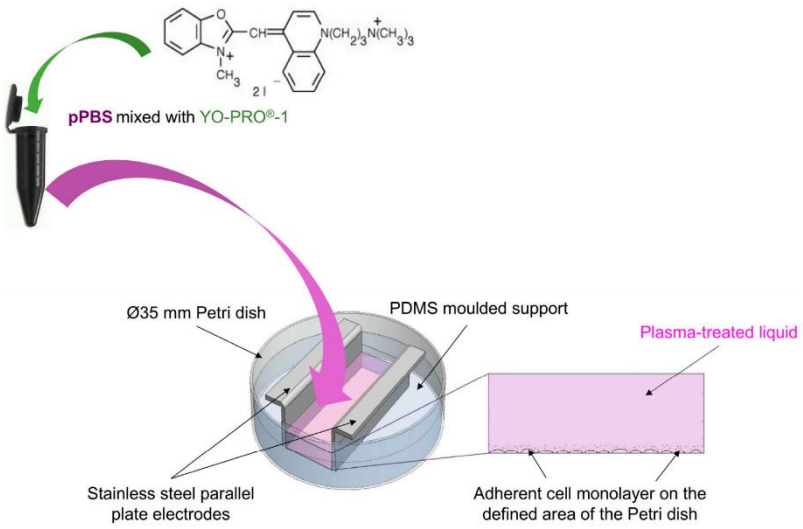

Figure 2.19 Schematic illustration of the electropulsation setup used in the combined treatment of µsPEFs and pPBS[12].

2.2.4.2.6 Combined treatment

The combined treatment associated µsPEFs and pPBS to treat cells. Untreated PBS was used as a control for all of the experiments. Before exposing the cells to the sham or the pPBS, YO-PRO®-1 Iodide (629.04 Da) (Life Technologies, Y3603) was added to these media at a final working concentration of 2 µM (unless otherwise specified). On the day of the experiment, the medium above the cells was removed and the cell layer was washed twice with PBS. 500 µL of the YO-PRO®-1-containing pre-treatment solution (sham or pPBS) was added to the cells for different incubation times (10 or 20 min), and then µsPEFs were delivered (strengths ranging between 500 and 1400 V/cm). Afterward, the electrodes were removed from the PDMS support, and the pre-treatment solution was then replaced by the YO-PRO®-1-containing post-treatment solution (sham or pPBS) for 10 min. In the absence of PEF (0 V/cm), the pre-treatment time was fixed at 20 min. In the presence of µsPEFs, the control condition (cells pre- and post-treated using Sham) was carried out with 20 min of pre-treatment[12].

2.2.4.7 Preparation of *in vivo* experiments

2.2.4.7.1 EP generator and electrodes

Electroporation was performed using the electric pulse generator Cliniporator™ (IGEA, Carpi, Italy) delivering HV pulses and LV pulses. Eight square-wave EPs of amplitude over distance ratio of 1000 V/cm, duration 100 µs at 1 Hz

were used. Non-invasive stainless-steel plate electrodes (P30-8B, IGEA, Carpi, Italy) consisting of 2 metallic plates of 1 mm thick and 4.7 mm apart were employed. Voltage was set up according to the distance between the 2 plates of the electrodes, thus 470 V for the plate electrodes distant 4.7 mm was used in this study.

2.2.4.7.2 Experimental procedure

Prior to treatment, mice were anesthetized with Isoflurane (Isoflurin® 1000 mg. g-1, Axience, FR) in an induction chamber. For all groups receiving pPBS, an i.t. administration of pPBS, either the 20-minutes-pPBS or the 1-hour-pPBS, was performed at 6 minutes prior to the administration of bleomycin, and the administered volume was half of the tumor volume which was individually measured during the randomization. Bleomycin (Roger Bellon SA, Neuilly-Sur-Seine, France) was i.v. administered in the retro-orbital sinus 4 min before the delivery of the EPs, at a dose of 10 µg per 100 µL per animal. For mice receiving EPs (groups 2, 4, and 5), their tumor was placed in-between the electrodes. To ensure a correct electric field distribution around the tumor volume, conductive gel (Asept Uni'Gel US, Aspet Inmed, France) was used to fill the space between electrodes and tumors (Ivorra, Al-Sakere, Rubinsky, & Mir, 2008).

2.2.4.8 Statistical analysis

Unless otherwise specified, all the results corresponding to the chemical composition of the pPBS are expressed as mean values ± standard deviation (SD) of three independent experiments. All the results corresponding to the effect of the pPBS on the cancer cells are expressed as mean values ± SD of three independent experiments, with each time point in at least four independent samples (quadruplicate). The significance level, or p-value, was calculated using the Student's t-test. Statistical significance levels found between the values of different groups were associated with p-values of > 0.05 (NS), < 0.05 (*), < 0.01 (**), < 0.001 (***) and < 0.0001 (****).

2.2.5 Experiments conducted with R3 – Treatment of different types of lipids

The MCSD was used in this study to treat different types of lipids. Thus, the lipids oxidation due to direct and indirect plasma treatment was studied. Although most measurements for this work have been conducted with the MCSD, we also treated, directly and indirectly, the lipids with the reactors R1 and R2 for comparison.

2.2.5.1 Chemicals

The unsaturated GPCs, 1-2 diacyl- sn3-glycerophosphocholines (POPC, DOPC, DLPC, DHAPC), and the saturated GPC, DSPC, were obtained from Avanti Polar Lipids (Alabaster, AL, USA). HEPES (4-(2-hydroxyethyl)1-piperazine-1 ethanesulfonic acid), $FeSO_4$ (ferrous sulfate solution in 1% acetic acid), hydrogen peroxide (H_2O_2 30%, w/v), and LC-MS grade solvents were provided by Sigma-Aldrich (Darmstadt, Germany).

2.2.5.2 Preparation of DOPC, DLPC, or DHAPC in giant unilamellar vesicles (GUVs)

DOPC, DLPC, and DHAPC vesicles were prepared from stock solutions of 1.0 $mg.ml^{-1}$ chloroform. Their concentration was then prepared at 30 $\mu g.ml^{-1}$ (40µM) in 10 mM ammonium bicarbonate for GUVs, which were prepared at 6°C according to a modified protocol[146]. Chemical oxidation was carried out with final concentrations of 20 µM DLPC, 10 mM H_2O_2, and 10 mM $FeSO_4$. This mixture was left to react for 2h at 60°C or 1h at 37°C. Controls were performed by replacing H_2O_2 and $FeSO_4$ with water. 100 aliquots of the incubation mixture were added with 100µL of IS solution (DSPC 2.5 $\mu g.ml^{-1}$ methanol) and extracted with 1000µL chloroform/methanol (2/1, v/v). After evaporation of the solvent, the dried extract was dissolved in 100 µL methanol and stored at 10°C until ESI-MS/MS analysis.

2.2.5.3 Preparation of POPC in liposomes unilamellar vesicles (LUVs)

Liposomes POPC vesicles (40 mg) were prepared from a stock solution of 8 $mg.ml^{-1}$ in 5mL chloroform, dried under vacuum, and then dissolved in 2mL methanol to prepare a 25 mM POPC concentration in HEPES buffer.

2.2.5.4 Incubation experiments of GPCs (POPC, DOPC, DLPC and DHPAC)

20µM GPCs were incubated at 37°C in buffer (PBS or ammonium bicarbonate pH 7,5) diluted twice with plasma-treated buffer (pT), which was prepared after 20 min exposition at room temperature using the multi-jet plasma source and stored at 4°C.

2.2.5.5 Liquid chromatography–tandem-mass spectrometry (MS/MS)

POPC, DOPC, DLPC, and DHPAC and their oxidized products were detected by LC MS/MS. 10 µL of the extracted sample was injected into the HPLC (Ultimate 3000, Dionex, USA), using the mobile phase consisting of acetonitrile/water (95:5, v/v) with 0.1% formic acid at a flow rate of 100 $\mu l.min^{-1}$. The LTQ-Orbitrap™ hybrid

mass spectrometer (Thermo Fischer Scientific Inc, Waltham, MA, USA), controlled by the Xcalibur™ software was operated in SAMM (IPSIT), using the positive electrospray ionization (ESI) mode with a capillary voltage of 3400 V and with the temperature of capillary and source set to 325°C and 100°C, respectively, and using nitrogen as sheath gas with a desolvation temperature of 300°C. ESI MS mass spectra were scanned over m/z 150–1200. MS/MS detection was performed using helium with a collision energy of 27%. Using MS/MS ion chromatograms, the ratio of their peak area over the IS area was calculated from parallel reaction monitoring transitions from precursor ions (M+H)+ to the same product ion, m/z 184, corresponding to the phosphatidylcholine group.

Chapter 3

Gaseous Phase Plasma Physics

Introduction

A short introduction on the physical mechanisms of atmospheric pressure plasma jets was presented in Chapter 1. Subsequently, the main diagnostic tools used for the investigation of the gaseous phase of plasmas generally in the field of plasma physics and especially in this work were depicted in Chapters 1 and 2, respectively. This Chapter is devoted to the presentation of the experimental results obtained on the gaseous plasma and plasma effluent, as well as the electrical and thermal characteristics of the cold atmospheric pressure plasma jets reactors used in this Thesis work.

This Chapter contains results only for the single-plasma jet (Reactor 1) and the multi-plasma jet (Reactor 2), as the gaseous phase and the electrical characteristics of the MCSD were previously studied by our group and were not part of this study[131,105].

In this Chapter, we examine several key characteristics of the produced cold atmospheric-pressure plasmas that are related with several applications in biomedicine. These characteristics are: a) the gas temperature and the temperature of the reactors' parts (when it is meant for them to be in touch with soft tissue) to ensure that there is no risk of thermal damage, b) the electrical characteristics of the reactor to avoid any possible electrical shock and c) the electric field and electron density in the front of the ionization wave as they might play a role on the efficiency of plasmas in different biomedical applications.

Table of contents

3.1 Thermal characteristics of the cold atmospheric-pressure reactors

Firstly, the temperature of the cold atmospheric pressure single-plasma jet (reactor 1) was measured (see Figure 3.1). The temperatures of the reactors' parts were measured with an infrared thermal camera. The hottest point of the reactor was found to be on the connection of the high voltage power supply and the reactor (cf. Figure 2.8). The temperature of the dielectric (quartz) remains relatively low (around 30 °C, harmless to a living tissue) during the 20 minutes of PBS treatment.

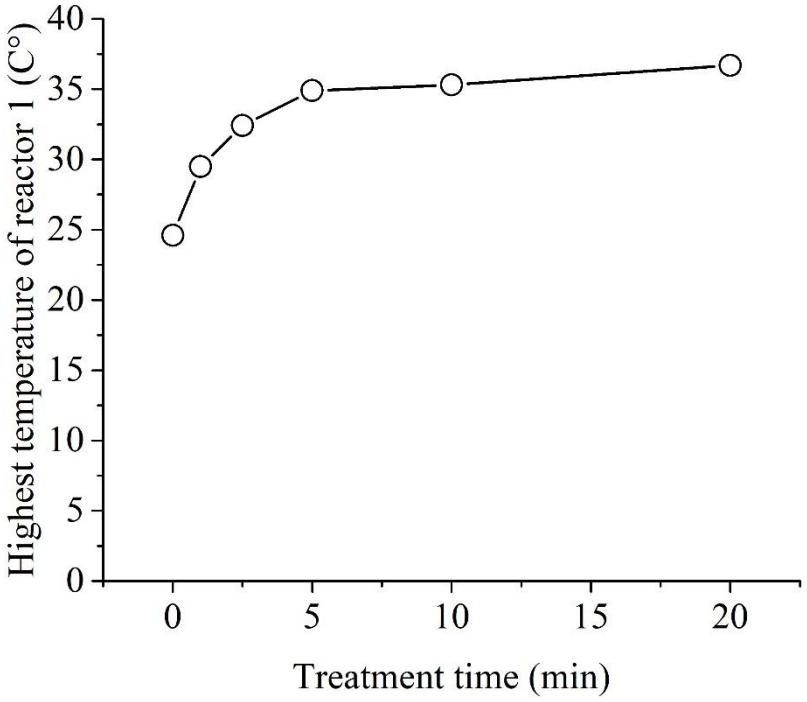

Figure 3.1 The temperature of reactor 1 as a function of the treatment time. The treated target is PBS, and the depicted temperature corresponds to the hottest point of the reactor (HV electrode) at the given treatment time (also marked with a red triangle in the photos of Figure 2.8 in Chapter 2). The infrared photos were obtained with an emissivity of 0.85.

The results obtained with the cold-atmospheric pressure multi-plasma jet (reactor 2) are presented in Figure 3.2. Our motivation for this work was dual. As mentioned in Chapter 1, this reactor is specially designed for an application *in vivo* against superficial tumors (skin cancer). For this reason, it is essential that not only the gas temperature but also the temperature of the reactor's parts, which will be in touch or close enough to a living organism, have a relatively low temperature to avoid any burns. Even if the reactor is designed and implemented in GREMI, Orléans, France, during this Ph.D Thesis we actively participated in its

amelioration. Part of this improvement was also the careful choice of the applicators' material (Chapter 2) in order to avoid its degradation due to localized heating. To do so, the study of the temperatures reached on the applicators during the plasma treatment was essential.

After 20 minutes of use, the hottest point of the applicator is located on the customized 3D-printed spacer that is in contact with the treated target, PBS in our case (cf. Figure 2.7). Even if its final absolute temperature could be worrying, as 57°C could cause discomfort or even burns to a living organism, we can see that the actual increase of the materials temperature is no more than 25 °C as the room temperature the day of the measurements was 32 °C (and thus, the reactor's temperature before the ignition of the plasma). Nevertheless, some modifications are required to the reactor or the experimental conditions to limit the final temperature of the applicator. These modifications could be a change of the applicator's material or an imposition of a lower initial temperature by air conditioning the room where the plasma treatment of the liquid is taking place. Also, the material of the 3D-printed spacer (plastic) does not degrade at such moderate temperatures.

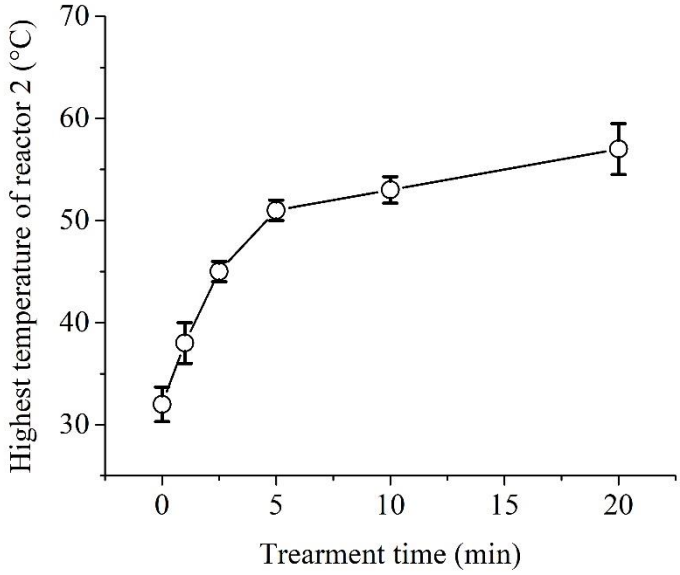

Figure 3.2 The temperature of the applicator of reactor 2 as a function of the treatment time. The treated target is PBS and the depicted temperature corresponds to the hottest point of the reactor at the given treatment time (also marked with a red triangle in the photos of Figure 2.7 in Chapter 2). The infrared photos were obtained with an emissivity of 0.85.

In Chapter 2, we mentioned the use of a thermocouple for the measurement of the temperature of the plasma-treated liquid after the plasma-

treatment. The temperature of the PBS treated both by the single-plasma jet and the multi-plasma jet was found to be relatively low. More specifically, after 12 minutes of treatment with the single-plasma jet, the liquid temperature was 22 °C (the temperature before the plasma ignition was 23 °C), while after 20 minutes of treatment with the multi-plasma jet, the liquid temperature was 36 °C (the temperature before the plasma ignition was 26 °C). Both temperatures are safe against cells and tissues.

3.2 Electrical characteristics of the single- and multi-plasma jets

The applied high voltage, as well as the DBD current were measured for different experimental conditions in the case of R1 (single-jet), while in the case of R2 (multi-jet), as the experimental conditions were fixed, its electrical characteristics were monitored only for that specific set of operating conditions. Subsequently, the energy consumption of the reactors was calculated from the aforementioned data. Here, we must specify that for R1, the measured current corresponds to the current of the DBD, while for R2 it is the total current of the system, as it is measured in the compensation circuit (cf. Figure 2.1). The high voltage probe is located on the high voltage cable that connects the power supply and the high voltage electrode for both cases. Hence, for none of the reactors, the current in the plasma jet was measured. For R1, the presented current is the conductive current of the main discharge – DBD (Chapter 1), after the subtraction of the capacitive current from the total current. For R2, it is not possible to distinguish these two, as the plasma is not produced in the applicator (Chapter 2).

The frequency of the high voltage power supply that drove the single-plasma jet was 10 kHz and the calculated energy dissipation for each square pulse was approximately 0.2 mJ. In the frame of this work, the electric characteristics of the single-plasma jet were studied for different experimental conditions. More specifically, the treatment distance was varied from 2 to 20 mm (with a step of 2 mm), two different gas flow rates were tested, i.e., 0.5 and 1 slm, and 2 different gas compositions were studied, i.e. 100% He and 99.8% He/ 0.2% O_2. The data are not presented here for all the cases as no significant difference was found between them. More precisely, if we average all the values obtained from the different experimental conditions, we obtain a mean value of 0.2 mJ with a ±SD of 3.4E-3 mJ. Indicatively, in Figure 3.3, we provide the instantaneous power measured in the DBD (black line) and the cumulative energy consumed in the DBD (blue line). These data were acquired at a treatment distance of 8 mm, with a gas flow rate of 1 slm and a gas composition of 100% He. If we observe closely Figure

3.3 we can see that an important part of the calculated energy is due to oscillations between the 2 pulses. Thus, we should underline here that the energy consumed during the two current pulses is around 75 Mj (50 μJ from the first pulse and 25 μJ from the second). Nevertheless, as stated also before, the signals are almost identical for the other experimental conditions. This was expected as the current that we study refers to the DBD current and not to the plasma plume current. On top of that, whenever oxygen is added into the feeding gas, its percentage is relatively low (0.2%) to affect the electrical characteristics of the DBD discharge. Finally, we observe that both the current waveform as well as the energy consumption on the DBD are similar during the rising and the falling of the high voltage pulse (cf. Figure 2.5). This was also observed in already published reports[147] and is due to the accumulation of charged species on the dielectrics during the positive discharge[148].

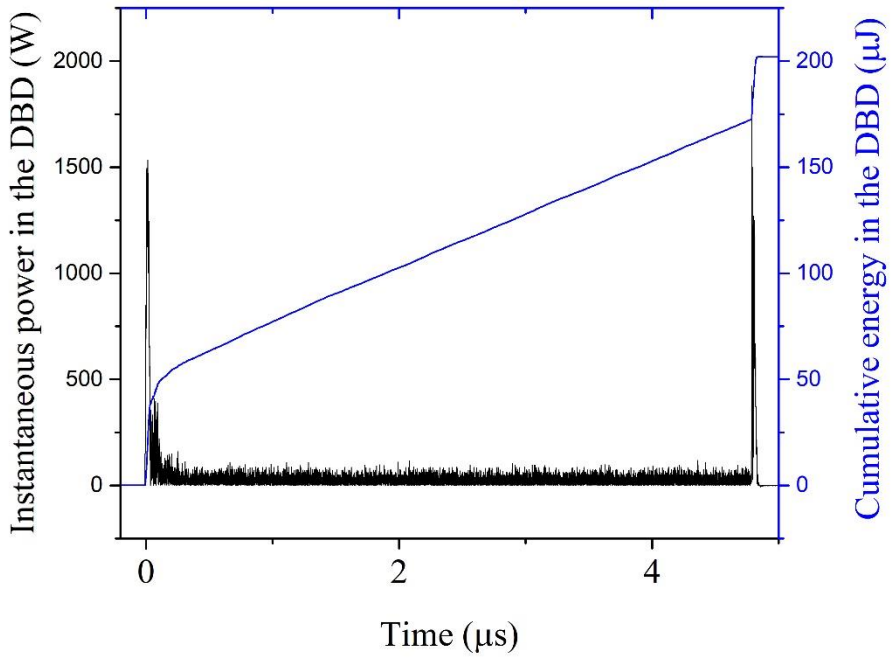

Figure 3.3 Instantaneous power and cumulative energy measured in the DBD of reactor 1 (single-jet) at a treatment distance of 8 mm, with a gas flow rate of 1 slm and a gas composition of 100% He.

The frequency of the high voltage power supply that drove the multi-plasma jet was 2 kHz and the calculated energy dissipation for each pulse was approximately of 2.7 mJ (when the discharge was driven by 11 kV).

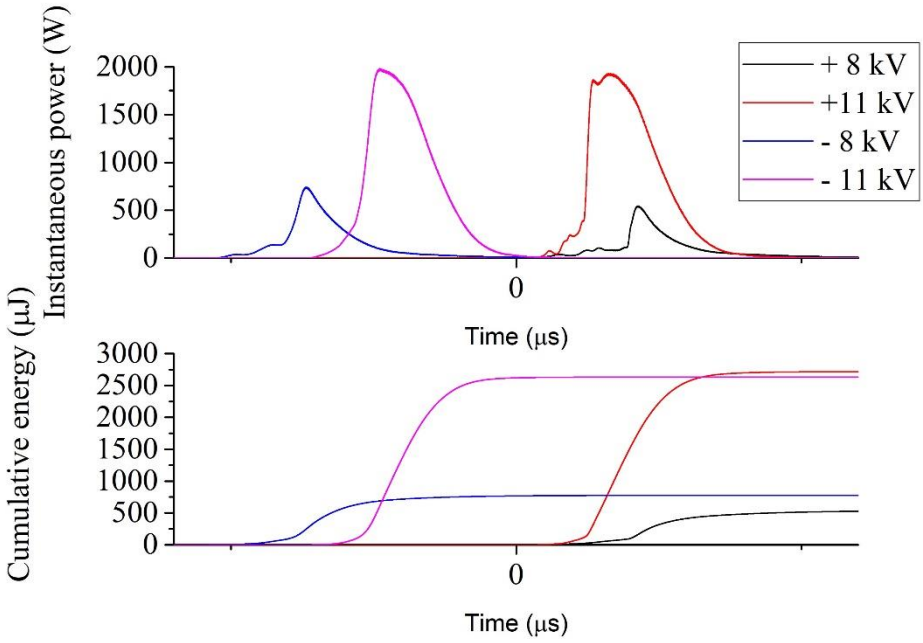

Figure 3.4 Instantaneous power and cumulative energy measured in the system of reactor 2 (multi-jet).

In Figure 3.4, the instantaneous power and the cumulative energy measured in the system are provided for two different voltage amplitudes and two different voltage polarities. The negative polarity is shown here as it was used in experiments presented in Chaper 4 (cf. Figures 4.8 and 4.9). As we can observe, the energy consumption of the system is higher when negative pulses are used, for the case of 8 kV.

3.3 Localized electric field

In Figure 3.5, a global spectrum (300-900 nm) of the emission of the single-plasma jet is presented. When needed, in this Chapter, we will refer to this figure to identify the different atoms and molecules that were studied.

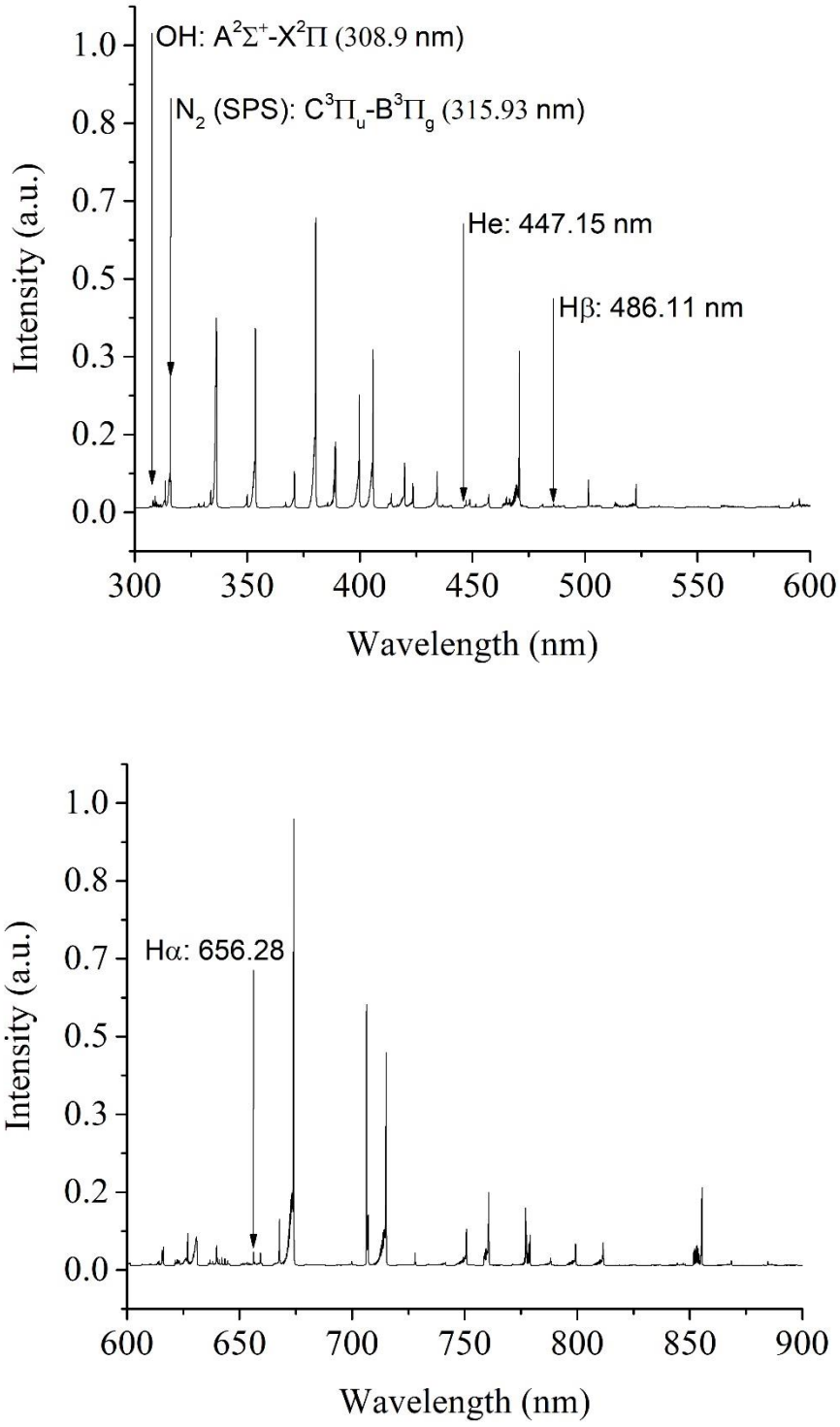

Figure 3.5 Global spectrum (300-900 nm) showing the emissions of the excited species produced by the single-plasma jet that are studied in this chapter. As working conditions, we used a gas flow rate of 1 slm, a gas composition of 100% He, a treatment distance of 8 mm and high voltage amplitude of 6 kV.

As mentioned in Chapter 2, for the measurement of the axial localized electric field of the ionization wave, the method of polarized Stark shifting was used. In this work, we mainly used the He line at 447.1 nm. In order to fix the gate duration as well as the gate delay of the iCCD camera, the speed of the ionization wave (streamer) propagating into the ambient air had to be determined. Regarding the gate duration this is essential in order to be certain that for a given time period, the light detected by the camera corresponds to the front of the ionization wave. In Figure 3.6, we can see the location of the front of the ionization (axial position) wave as a function of the iCCD camera gate delay. As front of the ionization wave, we always considered the brightest spot detected on the camera for a given camera gate delay. Here, we must underline that each 50 pixel of the camera (y axis in Figure 3.6) correspond to 1 mm in the axial direction. Thus, the mean velocity is calculated to be 3.2×10^6 cm/s. It is also interesting to note that while for the first 200 pixel (that correspond to 4 mm) the velocity of the streamer is rather constant (Figure 3.7), then the streamer accelerates, and this acceleration is even more profound as it approaches the liquid (Figure 3.7).

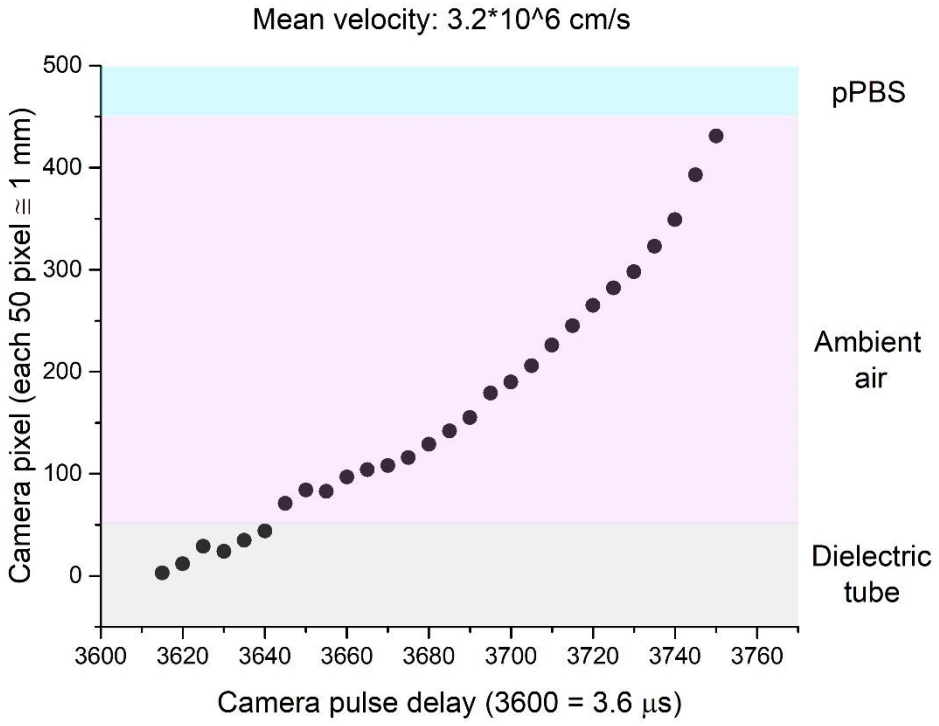

Figure 3.6 Position of the ionization front as a function of the time.

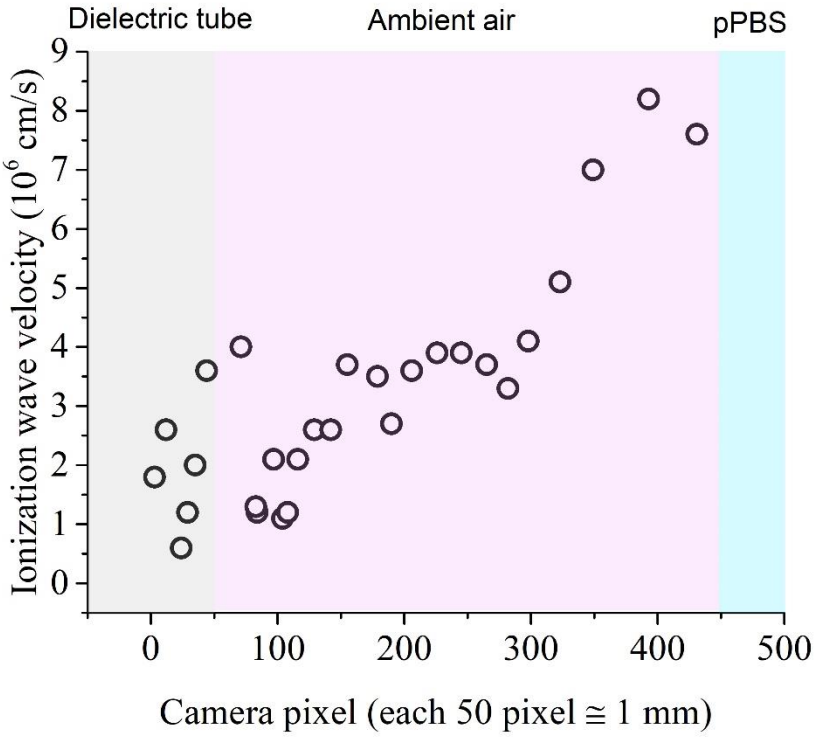

Figure 3.7 Instantaneous velocity of the ionization wave as a function of the position.

In Figure 3.8, the electric field over 13 mm, starting from inside the dielectric tube (quartz) and finishing at the surface of the liquid, is shown. The treatment distance is 8 mm, as this was the distance mainly used for the treatment of normal and cancer cells (Chapter 5). Therefore, the electric field is measured over 5 mm before the plasma exits the dielectric tube (grey shade in Figure 3.6), and over 8 mm when it propagates through the ambient air (pink shade in Figure 3.6). As we can see, the electric field in the front of the ionization wave remains relatively stable alongside the dielectric tube and its value was found to be 11-12 kV/cm. On the other hand, when the plasma exits the tube and propagates through the ambient air towards the plasma-treated liquid, the value of the localized electric field increases, reaching its maximum measured value (17.44 kV/cm) just before touching the liquid. Similar results were obtained also by Hofmans *et al.*, when they did not ground the saline solution that they used as a target[112]. In the literature it is reported that pulses of an amplitude of around 1-2 kV/cm are capable of permeabilizing the cellular membrane[12,149]. Thus, the electric field in the front of the ionization wave is a parameter of our single-plasma jet that could play a role in its efficiency against tumours that is presented in Chapter 4.

Here we should underline the clear connection between electric field strength in the bullet head and bullet velocity as mentioned previously also by

Stretenovic *et al.*[150]. If we observe Figure 3.7, we can see that the velocity of the plasma bullet is stable for the positions inside the capillary. For the same positions, the electric field in the front of the ionization wave is also stable and it is even slightly decreasing. For the following positions (outside the capillary tube and towards the liquid), the ionization wave accelerates, and the electric field also increases. This increase of the electric field is also observed by others even when the plasma jet is not in contact with a target[151]. To explain the observed phenomenon, we will study the behaviour of the electric field and therefore the velocity of the ionization wave in two different phases. First, we have the slight decrease of the electric field towards the orifice of the capillary tube (positions -4 to 0 mm) which is explained by the electric potential screening because of the surface charging of the inner walls of the capillary (quartz in our case)[152–154]. The electric field then increases as the ionization wave exit the capillary. This effect is attributed to the contraction of the ionization waves as they are moving away from the capillary, which strengthens the electric field by focusing the charge density into a smaller volume[152], leading to an increase in the ionization wave propagation speed[151,152,155].

The numbers presented in Table 3.1 correspond to the camera gating delay, with which the front of the ionization wave was recorded. The three individual experiments that were conducted are presented separately but also as the mean ± SD. With this table, we want to point out that the time at which the ionization wave appears in a certain position is not fixed and can differ from one day to another. That might be linked to exterior factors that could affect the speed of the ionization wave such as the ambient temperature or the humidity. Here we must underline that the rise of the high voltage pulse corresponds to a delay of 3.20 μs.

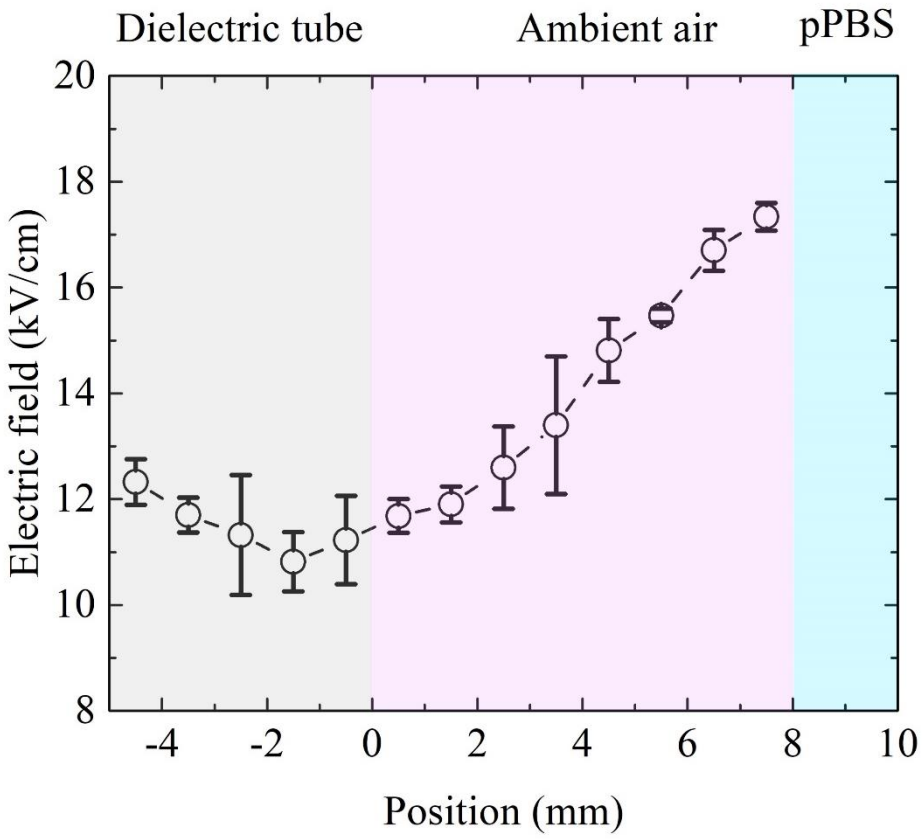

Figure 3.8 Calculated electric field value with a spatial resolution of 1 mm. The camera gate duration was set to 20 ns and the gate delay was varied to obtain for each position the maximum electric field value (head of the streamer). The treatment distance was fixed at 8 mm. The values presented in this Figure are the mean ± SD of three independent experiments.

	-4.5 mm	-3.5 mm	-2.5 mm	-1.5 mm	-0.5 Mm	0.5 mm	1.5 mm	2.5 mm	3.5 mm	4.5 mm	5.5 mm	6.5 mm	7.5 mm
Set 1	3.52	3.58	3.60	3.66	3.68	3.66	3.68	3.72	3.76	3.78	3.78	3.78	3.80
Set 2	3.50	3.54	3.54	3.60	3.62	3.62	3.64	3.70	3.74	3.74	3.74	3.76	3.78
Set 3	3.52	3.54	3.54	3.56	3.56	3.56	3.58	3.62	3.62	3.64	3.68	3.74	3.80
Mean +/- SD	3.51 0.01	3.55 0.02	3.56 0.03	3.60 0.05	3.62 0.06	3.61 0.05	3.63 0.05	3.72 0.03	3.70 0.08	3.72 0.07	3.73 0.05	3.76 0.02	3.79 0.01

Table 3.1 Delay of the camera gate with which the front of the ionization wave was recorded. The numbers correspond to μs.

In Figure 3.9, similar results to those of Figure to 3.8 are presented, but this time the treatment distance is fixed at 20 mm. As we can observe, the values of the electric field obtained inside the capillary tube are like those of Figure 3.8. On top of that, again the electric field in the front of the ionization wave increases when at positions outside the tube and towards the liquid. The difference between the two Figures concerns the actual value of the electric field outside the capillary tube: when a treatment distance of 20 mm is used, it is significantly lower

(-X% on average). However, it should be underlined that, even if the plasma is in contact with the liquid, here we did not measure the electric field close to the contact point, which is located 12 mm away from our last measured point.

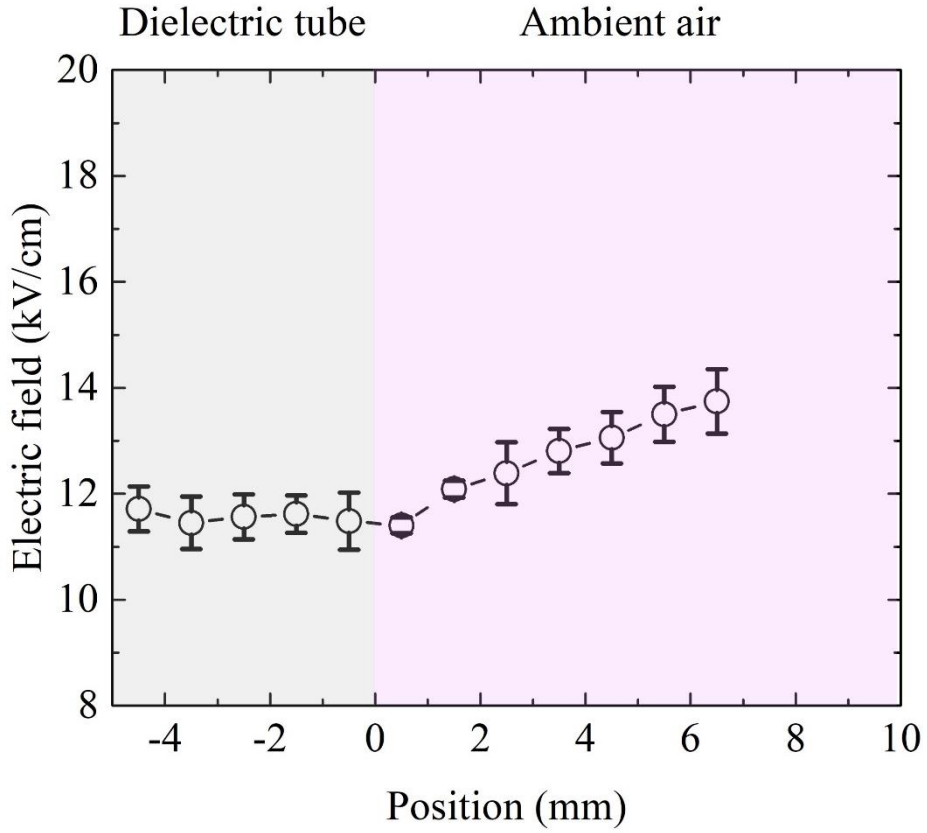

Figure 3.9 Calculated electric field value with a spatial resolution of 1 mm. The camera gate duration was set to 20 ns and the gate delay was varied to obtain for each position the maximum electric field value (head of the streamer). The treatment distance was fixed at 20 mm. The values presented in this Figure are the mean ± SD of three independent experiments.

3.4 Gas temperature

As it is described in Chapter 1, it is possible to estimate the temperature of the gas by studying the rotational distributions of certain probe molecules. To do so, we compared two different probe molecules in this Thesis' work, i.e., the OH: $A^2\Sigma^+$-$X^2\Pi$ at 308.9 nm and the N_2 (SPS): $C^3\Pi_u$-$B^3\Pi_g$ at 315.93 nm.

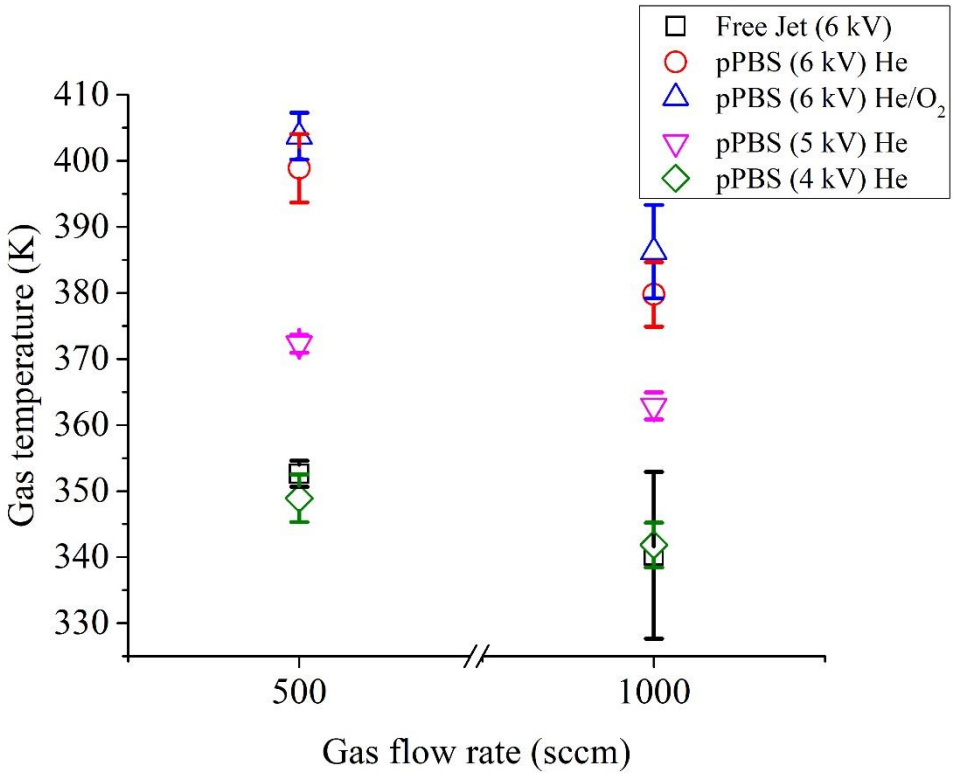

Figure 3.10 Gas temperature as estimated from the rotational distribution of OH: $A^2\Sigma^+$-$X^2\Pi$. The values presented in this Figure are the mean ± SD of two independent experiments and correspond to the average value of the Trot over 5 mm above the surface of the PBS. These results were acquired for a treatment distance of 8 mm, except for the Free Jet case, when no target was placed in front of the single plasma jet.

In Figure 3.10, the estimated gas temperature is presented as a function of the applied high voltage amplitude and the gas flow rate. On top of that, and for 6 kV, the estimated gas temperature is also provided when the jet is not in contact with a target – Free Jet – (recall that PBS is placed at a distance of 8 mm for all the other cases) and for a gas composition of 99.8 % He / 0.2 % O_2 (100% He for all the other cases). As we can see, for all the cases studied here we have a slightly higher gas temperature when a gas flow rate of 0.5 slm is used. This phenomenon has also been previously observed[119], where it was shown that the gas along the plasma jet is mainly heated due to heat convection from the dielectric. When a higher gas flow rate is applied, the cooling of the reactor's dielectric is higher, and, thus, the temperature of the reactor's material is lower, and, as a result, the heat convection to the gas is lower. Besides that, in Figure 3.10, we can also observe that the increase of the amplitude of the applied voltage leads to an increase of the gas temperature. This is due to the higher energy that is delivered to the gas. Finally, when the plasma is not in contact with a target, the gas temperature is significantly lower. As we saw in Figure 3.9, when the treatment distance is increased, the electric field of the front of the ionization wave is decreased. Even if the data of Figure 3.9 do not correspond to the Free Jet case (given that the plasma is still in contact with the liquid), it represents an intermediate situation.

The lower localized electric field for large treatment distances could be an explanation for the lower gas temperature in the Free Jet. This hypothesis should be verified in the future by measuring the localized electric field also for a Free Jet.

In Figure 3.11, the rotational temperature of the two different probe molecules used in this Thesis is presented as a function of the position alongside the axis of the plasma jet. The plasma-treated solution was PBS and the experimental conditions were 6 kV, 1 slm of pure He and the distance between the nozzle of the reactor and the PBS was fixed at 8 mm. As we can see, the rotational temperature $N_2(C)$ is always slightly higher than that of OH, even if this difference is not statistically significant. On top of that, the rotational temperature increases with the increase of the position, being the highest the closest to the liquid. Having already seen that the electric field increases for positions closer to the liquid, a proportional increase of the gas temperature was expected.

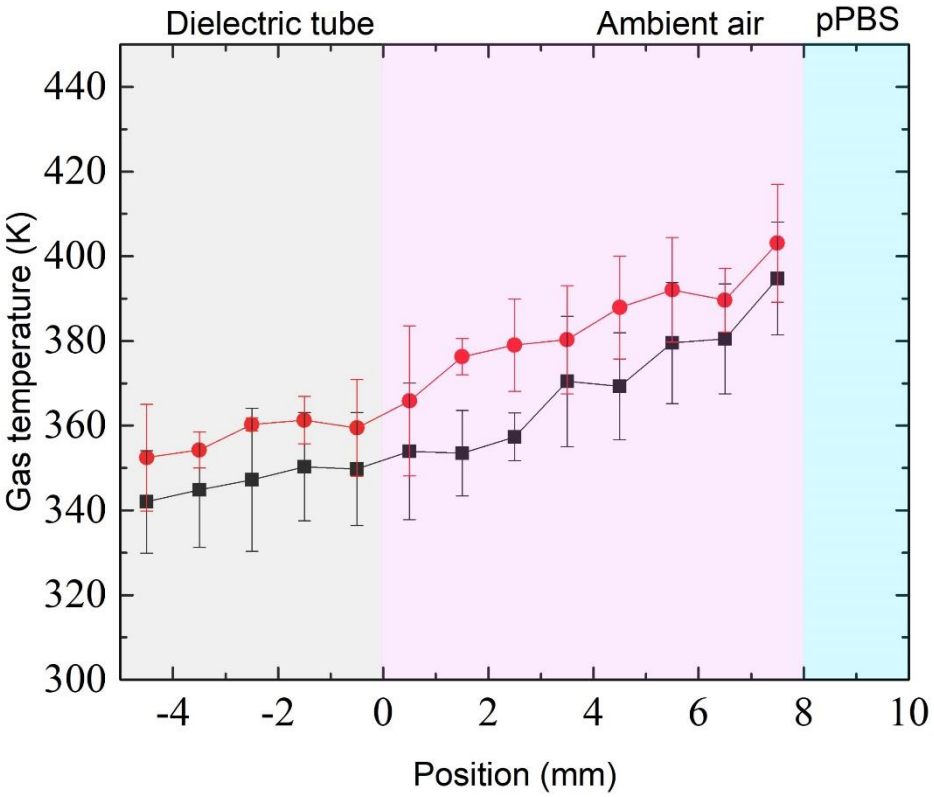

Figure 3.11 Rotational temperature of OH: $A^2\Sigma^+$-$X^2\Pi$ (black points) and N_2 (SPS): $C^3\Pi u$-$B^3\Pi g$ (red points). The values presented in this Figure are the mean ± SD of three independent experiments. These results were acquired for a treatment distance of 8 mm.

In Figure 3.12, the gas temperature, as estimated from the rotational distribution of OH, is presented. This time the treatment distance is fixed at 20 mm. Again, we observe the same tendency as in Figures 3.6, 3.8 and 3.9. The

electric field and gas temperature are stable or even slightly decreasing in the positions inside the capillary tube and increasing afterwards for positions towards the target, PBS in our case.

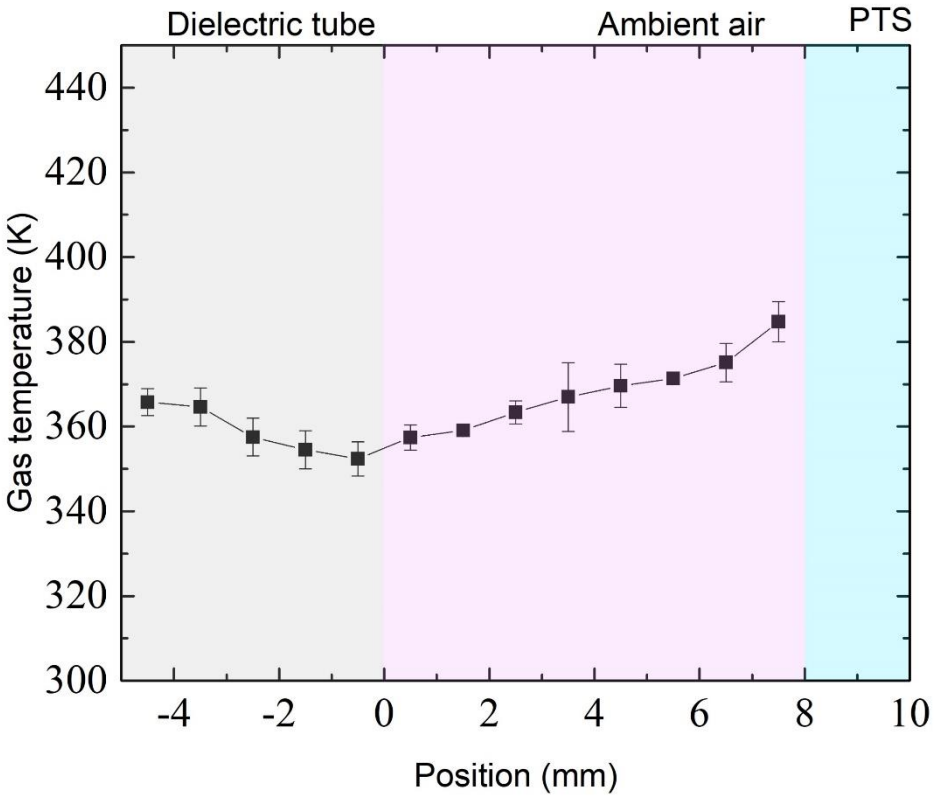

Figure 3.12 Gas temperature as estimated from the rotational distribution of OH: $A^2\Sigma^+$-$X^2\Pi$. The values presented in this Figure are the mean ± SD of TWO independent experiments. These results were acquired for a treatment distance of 20 mm.

3.5 Electron density

As a final step for the characterization of the gaseous phase plasma, the electron density was calculated. To do so, two different Balmer spectral lines were used, i.e. the H_α and the H_β.

In Figure 3.13, we present the electron density of the ionization front, as estimated from the H_α and H_β lines. From this Figure, we can observe that for both probe atoms, as we approach the liquid target, the electron density increases. As also shown before, this probably is not linked to the target itself but to the fact

that the electric field (and as a result the electron density and gas temperature) increases at positions outside the capillary tube towards the liquid. The same tendency, in a more moderate way is observed also for a distance of 20 mm between the reactor's nozzle and the surface of the PBS (Figure 3.14).

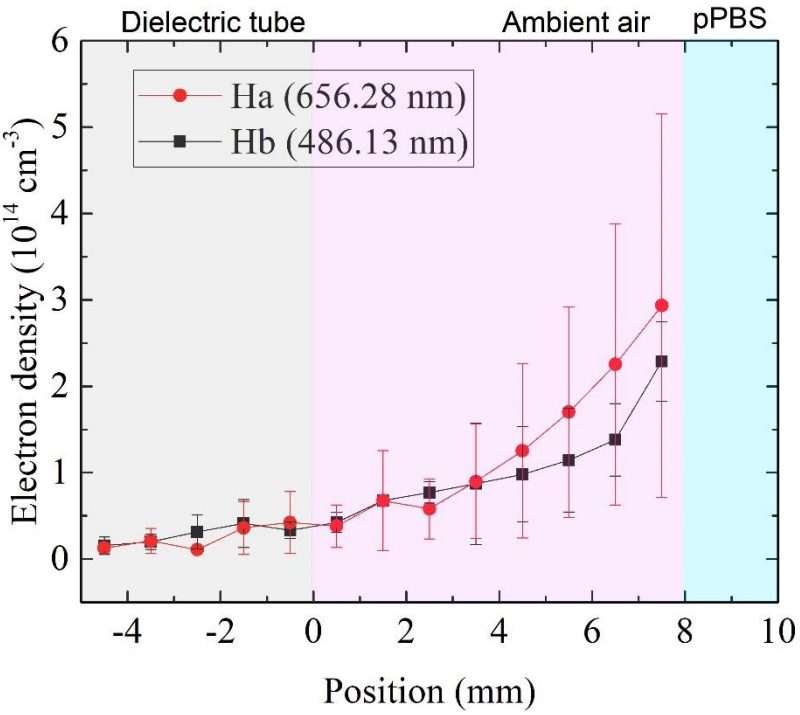

Figure 3.13 Calculated electron densities as a function of the axial position. The values presented in this Figure are the mean ± SD of three independent experiments and were obtained for a treatment distance of 8 mm.

More specifically, we can see that the electron density inside the capillary is similar for both treatment distances. When the ionization wave exits the dielectric tube, the electron density slightly increases, reaching values that are significantly lower than those obtained for a treatment distance of 8 mm. As for the electric field, we should also underline here that the positions closer to the liquid are not studied.

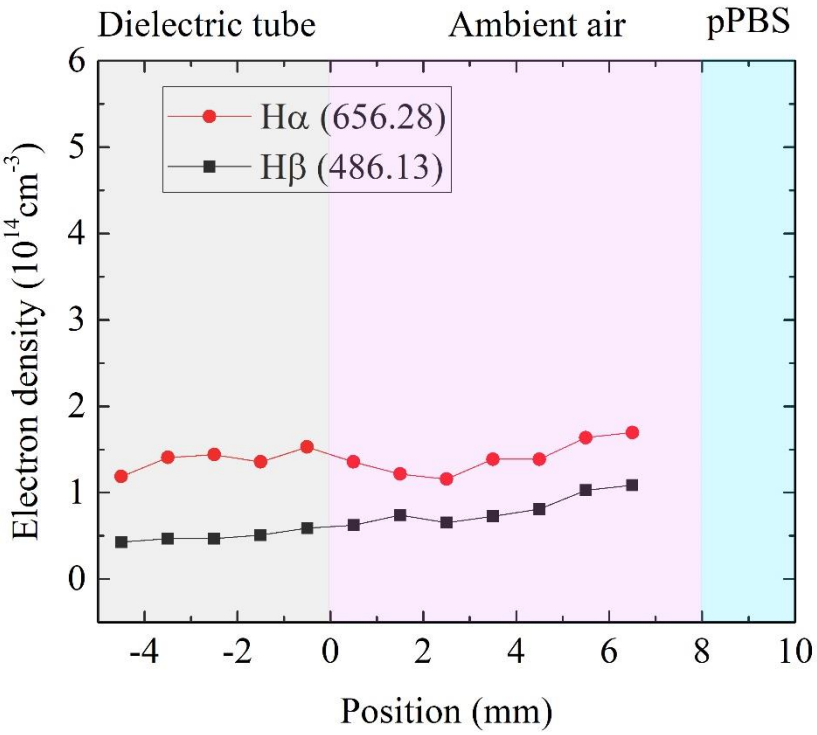

Figure 3.14 Calculated electron densities as a function of the axial position. The values presented in this Figure are the mean value of one independent experiment and were obtained for a treatment distance of 20 mm.

Conclusions

Except from our keen interest to study the physical processes of the plasma produced mainly by the single-plasma jet, our main motivation for the experiments presented in this Chapter was the investigation of those characteristics of the gaseous plasma phase that could play a role during its application to biomedicine. Thus, we saw in this Chapter that both the gas temperature and the temperature of the materials of the reactors studied remain relatively low. This is the first step to even consider the application of these types of plasmas in biomedicine. Nevertheless, it is possible, the method we use here overestimates the gas temperature. We want to underline that because especially the plasma produced by the single-plasma jet does not cause any burns when in touch with a soft tissue. This fact indicates that its temperature is not superior to 45-50 C°. Then, the Stark polarizing method that we used here unveiled that the electric field in the front of the ionization wave remain stable, or even slightly decreasing, for positions inside the dielectric tube and as we are moving towards the tube orifice. When the ionization wave exits the capillary, the electric field increases with the increase of the axial position. Its final value, just before the liquid, can be up to 17-18 kV/cm , which is more than enough to permeabilize the cellular membrane. Coherent results were obtained also for the velocity of the ionization wave, confirming the link between these two parameters. More specifically, the ionization wave has a constant speed inside the quartz, and then it increases for positions outside the capillary tube. In parallel, and because of the enhanced electric field when the ionization wave propagates outside the capillary, we also observed an increased gas temperature and a higher electron density. For all the physical quantities studied here, the values that were obtained for a treatment distance of 20 mm are lower compared to those obtained with a treatment distance of 8 mm. Collectively, our results show that the single-plasma jet could be a safe if we consider its materials temperature and efficient (high electric field in the front of the ionization wave) solution against cancer therapy considering its physical properties. On the other hand, more experiments are needed to verify the gas temperature as we think that our method overestimates it. The plasma treatment distance should be chosen carefully to achieve the highest efficiency of the plasma towards biological targets. Finally, the impact of the plasma-liquid contact should be studied in detail in the future in order to understand how this interaction can affect the physical properties of the produced plasma.

Chapter 4

Liquid Phase Chemistry

In this chapter, an in-depth investigation of the reactive oxygen and nitrogen species (RONS) presence and concentration in plasma-treated solutions, mainly plasma-treated PBS (pPBS), is presented. These RONS can be divided in three different categories, when characterized from their lifetime in the liquid, namely, short-lived, intermediate-lived, and long-lived. Their detection and mostly the determination of their concentration in the plasma-treated solutions is a great challenge due to their very short lifetime (for short-lived reactive species) and the high difficulty of using methods such as emission and absorption spectroscopy in a liquid medium. More specifically, and compared to the gaseous phase, the first problem that arises when spectroscopy is used is the absorption of the liquid itself and, thus, the weakening of the signal. On top of that, there are numerous reactive species whose absorption spectra overlap each other, like for instance ozone and hydrogen peroxide. Thus, to selectively detect these reactive species, different methods should be employed as much as possible. In this Thesis' work, these reactive species were detected by colorimetry, coupled with absorption and/or fluorescence spectrophotometry. The reactive species that were studied are reported in the literature as key drivers of the anti-cancer capacity of plasma-treated solutions. On top of that, the possibility of preserving the concentration of certain long-lived reactive species (H_2O_2, NO_2^- and NO_3^-) for a long period of time, i.e. several weeks or months, if stored at the proper temperature, was also studied. Finally, the pH, conductivity and temperature of the plasma-treated solutions were determined, not only because they can also play a direct role in the anti-cancer capacity of these solutions, but also because their values have a direct impact on the RONS concentration and conservation over time.

Table of contents

Introduction

As we know from the literature, by treating a liquid with plasma we drastically change its chemical properties[156]. This is mainly due to short-, intermediate- and/or long-lived reactive species that are formed in the gaseous phase and transferred into the liquid or that are formed directly in the liquid phase, constituting the secondary products of certain chemical reactions. The presence of these reactive species in the liquid phase results also in the modification of some other characteristics of the liquid such as its pH or its conductivity.

Most of the applications of plasmas in medicine are performed in an open-air environment and, thus, copious reactive oxygen and nitrogen species can be produced[156–158]. Depending on the working conditions that are used for the production of the plasma, different plasma-treated liquid chemistries can be induced[122,159]. Khlyustova *et al.* provided a rather detailed review on the importance of the different plasma working conditions in the final plasma-treated liquid chemistry, especially when it comes to hydrogen peroxide production[123]. The full characterization of a cold atmospheric pressure plasma reactor, in terms of reactive species production and as a function of the different experimental conditions, such as high voltage amplitude and frequency, gas composition and flow rate, and treatment distance, among others, is of high importance for its future application.

Besides the production of the reactive species in the liquid, in plasma pharmacy it is essential that these reactive species conserve their concentrations over long time periods. For the short- and intermediate-lived reactive species, this is not possible due to their high reactivity in aqueous environments. On the other hand, this is feasible for the long-lived reactive species, only if stored properly[12,64,66].

Thus, in this chapter, we characterized all the three reactors that were then used in different biomedical applications in this Ph.D. Thesis (see Chapter 5), in terms of short-, intermediate- and long-lived reactive species concentrations in the plasma-treated liquids for different experimental conditions. We also assessed the storage conditions (storage temperature) and the maximum period over which these solutions can retain their chemical composition.

This chapter is divided in two different parts. The first part is devoted to an in-depth analysis of the chemical characteristics of plasma-treated liquids, mainly pPBS (Chapter 2, section 2.1) in our case. Nevertheless, in some cases, we also studied the chemistry modification, due to plasma treatment, of water (sterile

water containing NaCl to simulate the conductivity of PBS), cell culture medium (Dulbecco's Modified Eagle Medium) and NH_4HCO_3. Hence, the absolute concentrations of H_2O_2, NO_2^- and NO_3^- were measured, and the concentrations of $O_2(a^1\Delta g)$, O_3, and $ONOO^-$ and •OH were estimated in pPBS. In parallel, the pH, the conductivity, and the temperature of the pPBS were monitored. The second part of this chapter is devoted to the investigation of the conservation of the long-lived reactive species concentration (H_2O_2, NO_2^- and NO_3^-) in pPBS as a function of the storage time and temperature.

4.1 Absolute measurement of H_2O_2, NO_2^- and NO_3^- in plasma-treated liquids

4.1.1 The concentration of long-lived reactive oxygen and nitrogen species in plasma-treated solutions

4.1.1.1 Cold atmospheric pressure single plasma jet (reactor 1)

As mentioned before, H_2O_2 and NO_2^- are mainly responsible for the cytotoxic effect of plasma-treated liquids. Given that the cold atmospheric pressure single jet (reactor 1) was mainly used for the application on cancer cells, a parametric study of this reactor in terms of H_2O_2, NO_2^- and NO_3^- concentrations was implemented. Even if in most of the cancer treatment cases, NO_3^- does not seem to be toxic against the cells, we included it in our study as its concentration is directly linked to the concentration of NO_2^-. The different parameters studied here are graphically presented in Figure 4.1. Besides the experimental conditions mentioned in Figure 4.1, our group has varied in the past also the high voltage amplitude and the high voltage pulse width, and a high voltage amplitude of 6 kV with a pulse width of 4.8 µs was chosen. The choice of the pulse duration was based on previous studies of this reactor, which showed that with this value (4.8 µs) the production of RONS (H_2O_2, NO_2^- and NO_3^-) is maximized[160].

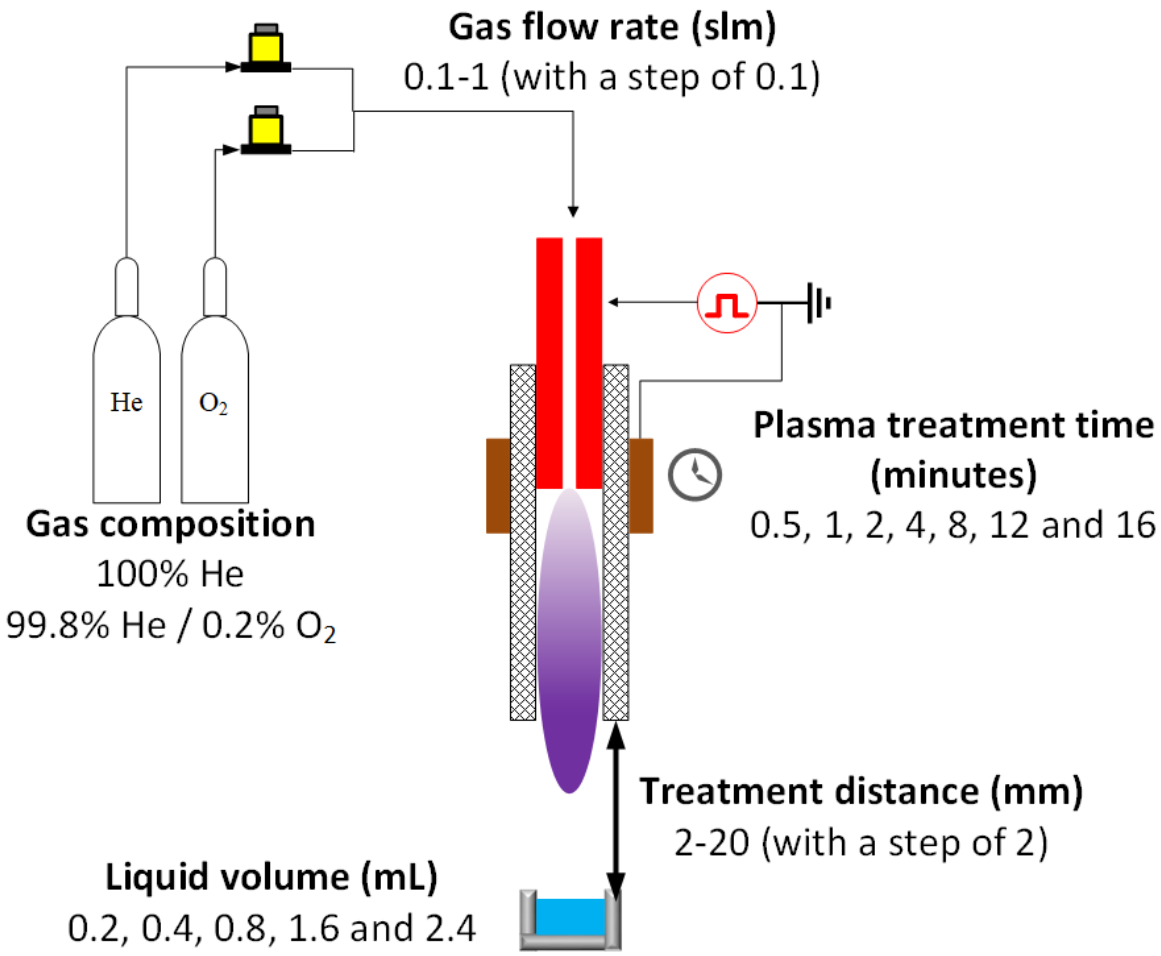

Figure 4.1 Schematic overview of the different experimental conditions varied in this study.

Before the presentation of our results concerning the liquid phase chemistry of the pPBS, we have to underline that for all the treatment distances studied here (2-20 mm), the plasma touches the liquid.

We started our study by determining the liquid volume that we should use. As we can see in Figure 4.2, the concentration of the three RONS studied here decreases almost linearly with the increase of the liquid volume (especially for the three first initial volumes, i.e. 0.2, 0.4 and 0.8 mL). This was expected as the plasma produces the same number of reactive species for each treatment time, and, thus, by increasing the liquid volume we also increase proportionally the dilution of these reactive species.

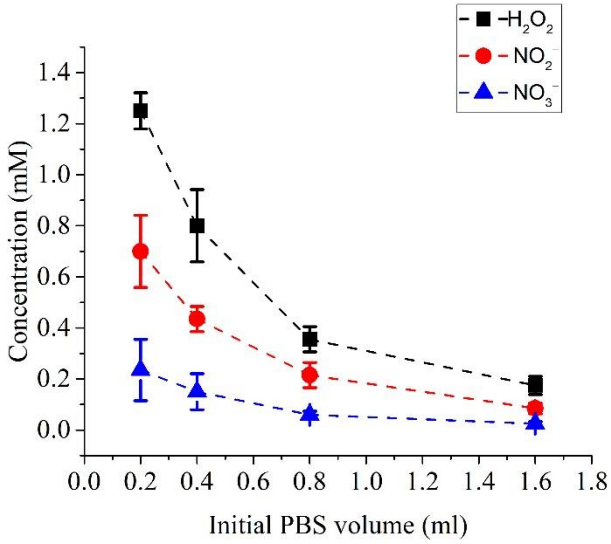

Figure 4.2 H_2O_2, NO_2^- and NO_3^- concentrations as a function of the initial liquid volume. The gas flow rate was 1 slm and the gas composition 100% He. The treatment distance is kept at 8 mm. The data are the mean values ± SD of 2 independent experiments.

We continued our study by varying the treatment distance (Figure 4.3).

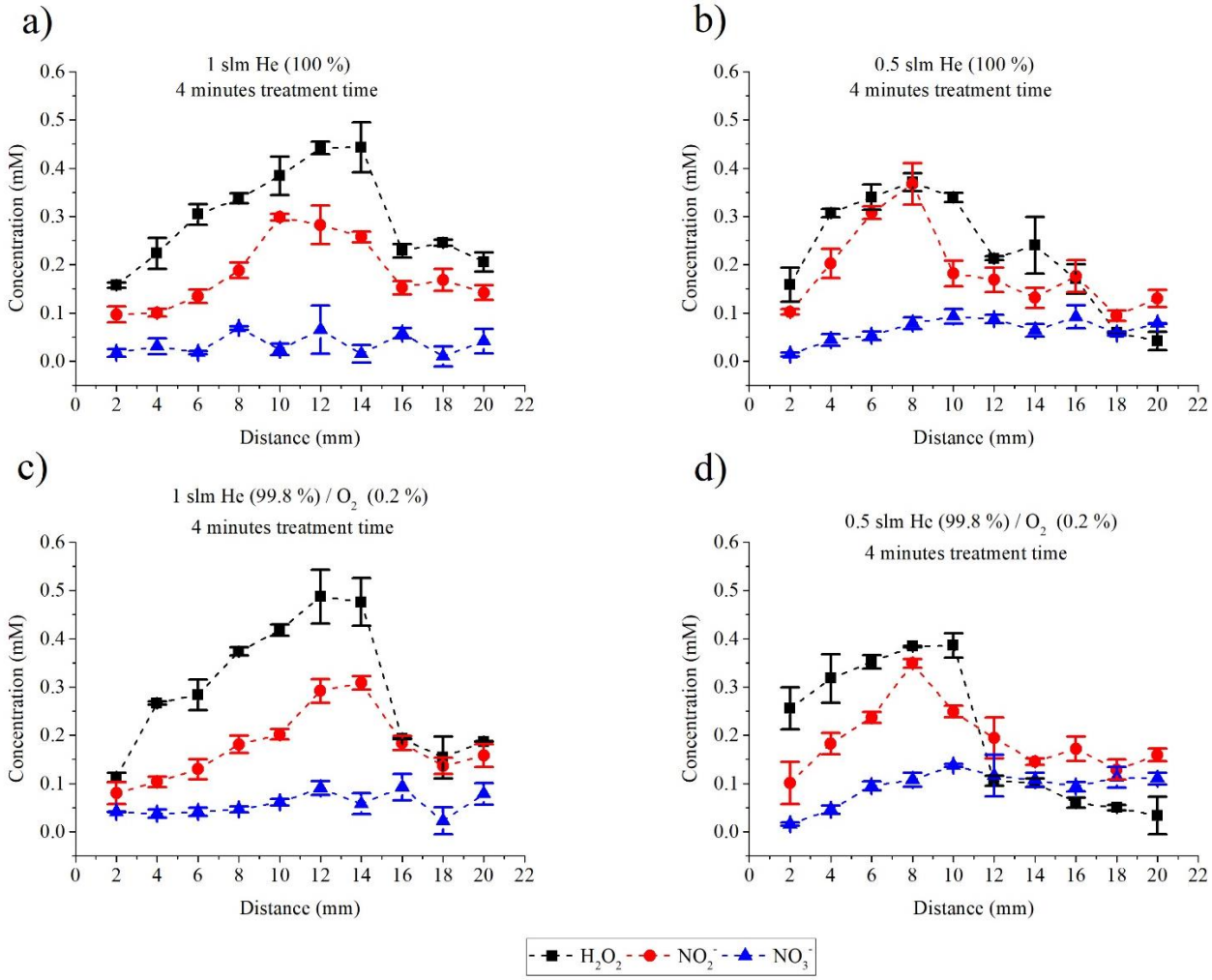

Figure 4.3 H_2O_2, NO_2^- and NO_3^- concentrations as a function of the distance between the tube orifice and the surface of the liquid for two different gas flow rates, i.e. 1 and 0.5 slm, and two different gas compositions, i.e. 100% He and 99.8% He / 0.2% O_2. The data are the mean values ± SD of 3 independent experiments.

As it is shown in Figure 4.3, the concentration of both H_2O_2 and NO_2^- reaches its maximum value for a range of treatment distances between 8 and 12 mm. The concentration of NO_3^- is relatively low to lead to any conclusions, even if it seems to follow for most of the cases studied here the same pattern as H_2O_2 and NO_2^-. This evolution of the reactive species concentration as a function of the treatment distance was expected. Here we should underline that the depth of the liquid was 4.4 mm. As it is analysed in Chapter 1 (section 1.4.1), if the time required for the plasma or the plasma effluent to reach the solution is short (i.e. short gap and high gas flow rate), •OH radicals that are transported into the gas-solution interface (where they recombine) are the main source for aqueous H_2O_2. For longer distances between the tube orifice and the surface of the solution and/or lower flow rates, aqueous H_2O_2 mainly originates from gaseous H_2O_2, which is generated by •OH radical recombination in the gas phase. For very big treatment distances, we have enough time to produce gaseous H_2O_2 but due to the big distance a significant part of its concentration is then diffused into the surrounding air. Thus, a lot of the reactive species produced do not end up in the liquid. A similar explanation should be given also for the evolution of the NO_2^- concentration. At lower gas flow rates, ambient air species can easily diffuse into the plasma jet, and, thus, the HNO_2 concentration highly increases in the gas phase. Upon increasing the gas flow rate, it becomes more difficult for ambient air species to diffuse into the plasma effluent. Except from that, by increasing the treatment distance (as for H_2O_2), the species have more time to recombine in the gaseous phase before reaching the liquid, while at very big treatment distances only a small part of them reaches the liquid and the rest are diffused in the ambient air. Regarding these results, we should always consider at the same time the treatment distance and another pivotal parameter, the gas flow rate.

As we can see in Figure 4.4, for a given treatment distance (8 mm), the concentration of H_2O_2 increases rapidly with the increase of the gas flow rate from 0.2 to 0.4 slm and it stabilizes after that. On the contrary, the concentrations of both NO_2^- and NO_3^- initially increase, and, after reaching a maximum value at 0.4-0.5 slm, they decrease. Thus, we can conclude that the formation of NO_2^- and NO_3^- is a slower process than the formation of H_2O_2. Considering our last results (Figures 4.3 and 4.4), we cannot find the optimal treatment distance, in terms of the highest concentrations of reactive species in the treated liquid, if we do not know the gas flow rate, and vice-versa we cannot conclude on the optimal gas flow rate without having determined before the treatment distance.

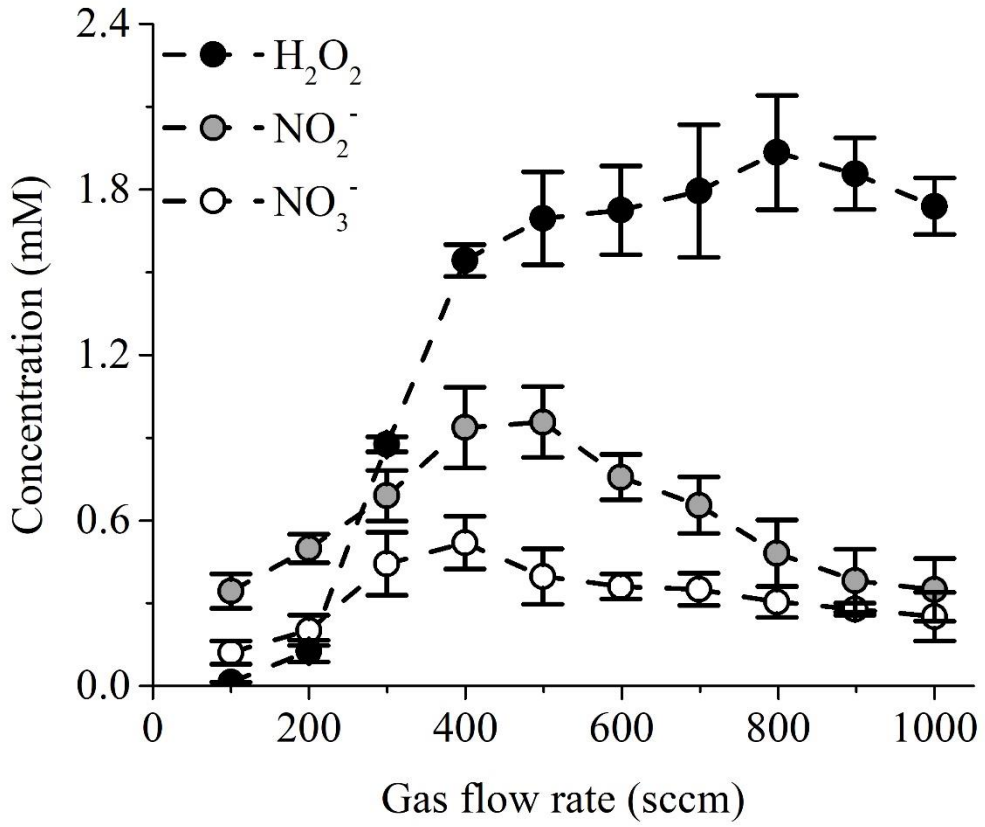

Figure 4.4 H_2O_2, NO_2^- and NO_3^- concentrations as a function of the gas flow rate for a treatment distance of 8 mm, a gas composition of 99.8% He/ 0.2% O_2 and a treatment time of 12 minutes. The data are the mean values ± SD of 2 independent experiments.

Finally, the exact dose of the reactive species that is needed for each application can be controlled by altering the plasma treatment time. As it is shown in Figure 4.5, the concentration of all three reactive species increases with the increase of treatment time in the time range that we studied here (0-16 minutes). This is because of the accumulation during the plasma treatment of reactive species in the liquid.

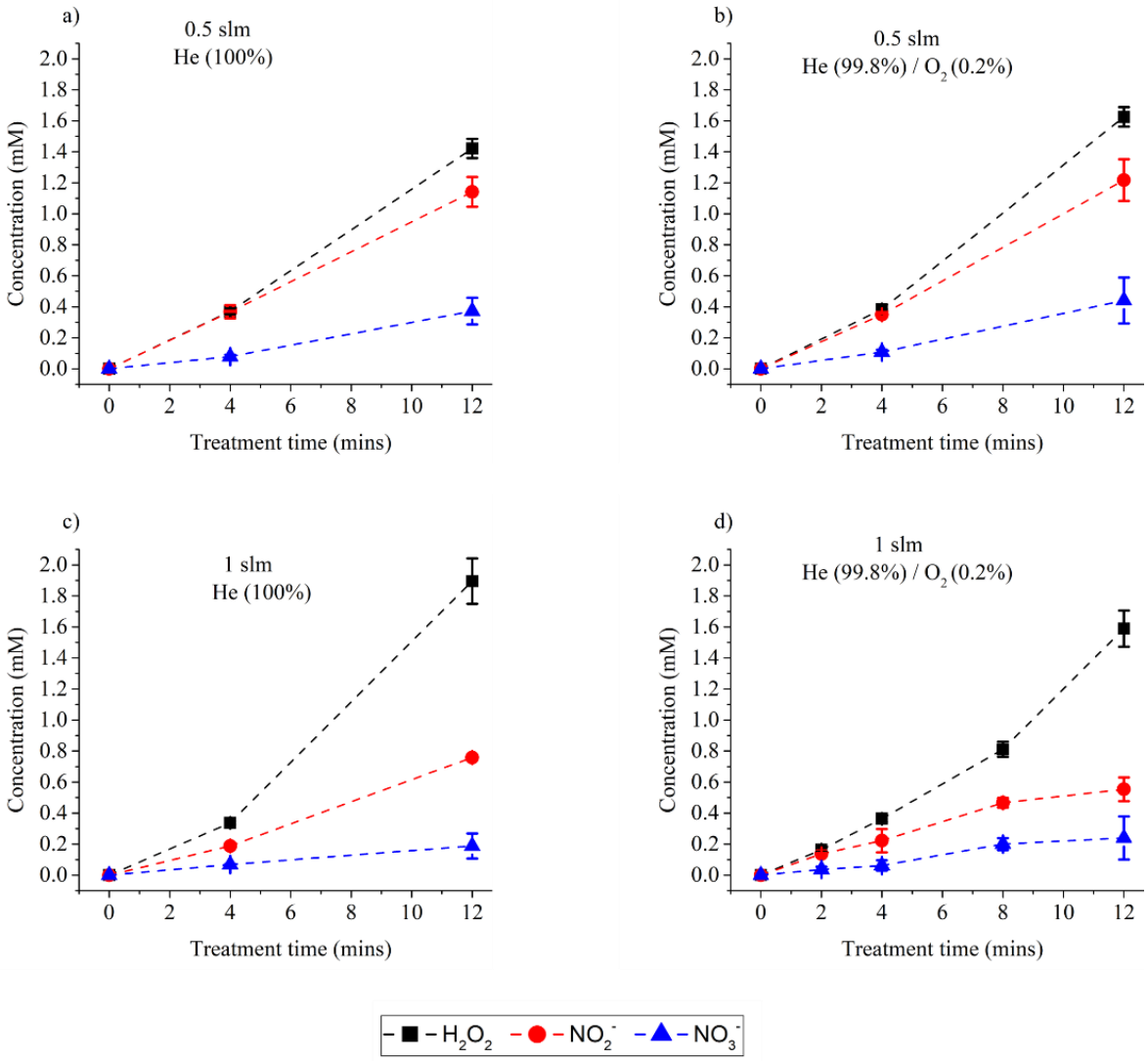

Figure 4.5 H_2O_2, NO_2^- and NO_3^- concentrations as a function of the plasma treatment time for two different gas flow rates, i.e. 1 and 0.5 slm and two different gas compositions, i.e. 100% He and 99.8% He/ 0.2% O_2. The treatment distance is set at 8 mm. The data are the mean values ± SD of 3 independent experiments.

Nevertheless, one should be aware that after longer periods of treatment, the chemical characteristics of pPBS are not the same. For example, besides the numerous reactive species produced in the pPBS, its conductivity, pH and temperature at the end of the treatment might also vary as a function of the plasma treatment time. Thus, different chemical interactions in the liquid might be favored. One of these reactions could be the oxidation of NO_2^- by H_2O_2, which takes place essentialy in acid environments. A lot of attention is required when different liquids (and not tampon solutions) like salty water are used. In our case, when water was treated instead of PBS, its pH rapidly decreased and, therefore, the concentration of NO_2^- was found to be much lower than in PBS, for the same experimental conditions. At the same time the concentration of H_2O_2 also decreases while the concentration of NO_3^- increases if salty water is treated

compared to PBS. Indicatively, after 10 minutes of treatment time, the pH and NO_2^-, H_2O_2 and NO_3^- concentrations of pPBS prepared with the multi-plasma jet were 5.9 and 1.1 mM, 2 mM, and 0.75 mM respectively, while, when salty water was used (we used salty and not sterile water to have the same initial conductivity as in PBS), they were found to be 2.3 and 0.1 mM, 1.3 mM, and 1.75 mM respectively. This phenomenon is explained in detail later in this chapter (section 4.3). Except for long-lived reactive species it has been reported that the pH of the solution can have an effect also on short-lived reactive species such as OH radicals[161]. Moreover, it is known that during the treatment of liquids with plasma, evaporation occurs[162–164]. To investigate the possibility of the PBS acidification due to plasma treatment, we measured its pH when treated by the plasma. Alongside, the conductivity of the pPBS was also monitored. In Figure 4.6, the evolution, as a function of the plasma treatment time, of the solutions pH (black color) and conductivity (blue color) are plotted. As we can see, the increase of the plasma treatment time leads to an almost linear decrease of the solution's pH, while it increases the liquids' conductivity. The pH of the pPBS is decreased due to the production of several different acids, like nitric/nitrous acid[165], while the accumulation of charged species produced and/or transferred in the liquid phase from the plasma result in the increase of its conductivity[166].

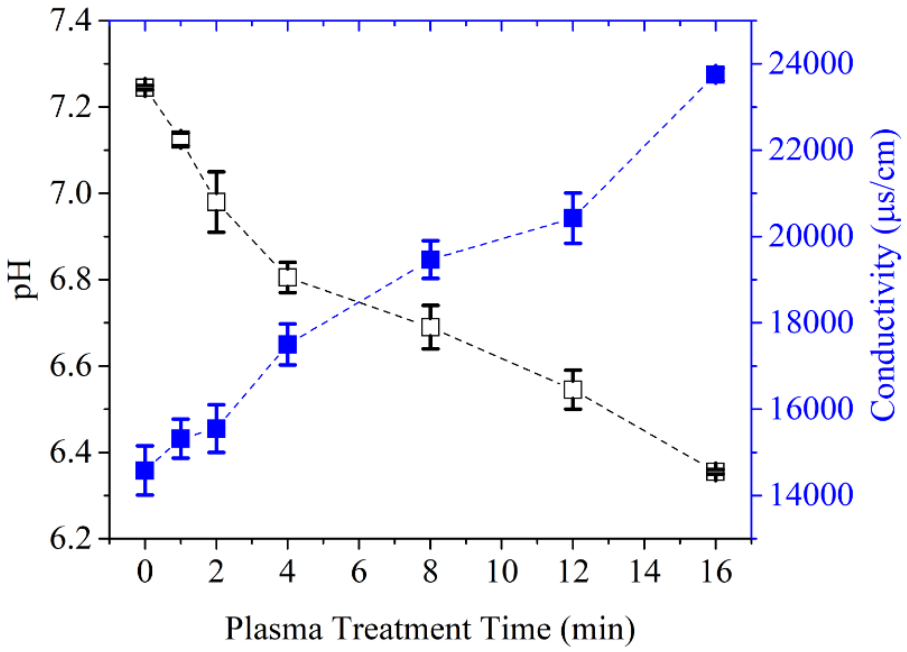

Figure 4.6 pH (black) and conductivity (blue) of the pPBS as a function of the plasma treatment time. The data are the mean values ± SD of 2 independent experiments.

4.1.2.2 Cold atmospheric pressure multi-plasma jet (reactor 2) and MCSD (reactor 3)

With the multi-plasma jet (reactor 2) we could not vary as many different experimental conditions as we did with the single plasma jet, as it is designed to operate at fixed conditions. Thus, we have only varied the high voltage amplitude (7-11 kV), the voltage polarity and the plasma treatment time (1, 2, 5, 10, 15 and 20 minutes). For the case of a high voltage amplitude of 7 kV, only the concentration of the H_2O_2 was measured and it also increased almost linearly with the increase of the treatment time, and it was always around 30% of the H_2O_2 concentration measured when the applied voltage was of 11 kV. The results obtained for 11 kV are presented in Figure 4.7. Here, we must point out that a gas flow rate of 1 slm with a gas composition of 100% He was used. The distance between the reactor orifice and the surface of the liquid was fixed at 4 mm while for this reactor the distance between the surface of the PBS and the bottom of the well was 16.5 mm. As we can observe in Figure 4.7, also with this reactor, we have an almost linear increase of the reactive species concentration with the treatment time (especially up to 10 minutes of treatment), even if their concentration shows a slight tendency to saturate after 10 minutes of treatment, especially for H_2O_2 and NO_3^-. Any comparison between the plasma multi-jet and the plasma single-jet, reactors 2 and 1 respectively, should be made considering that the working conditions and the experimental setups differ.

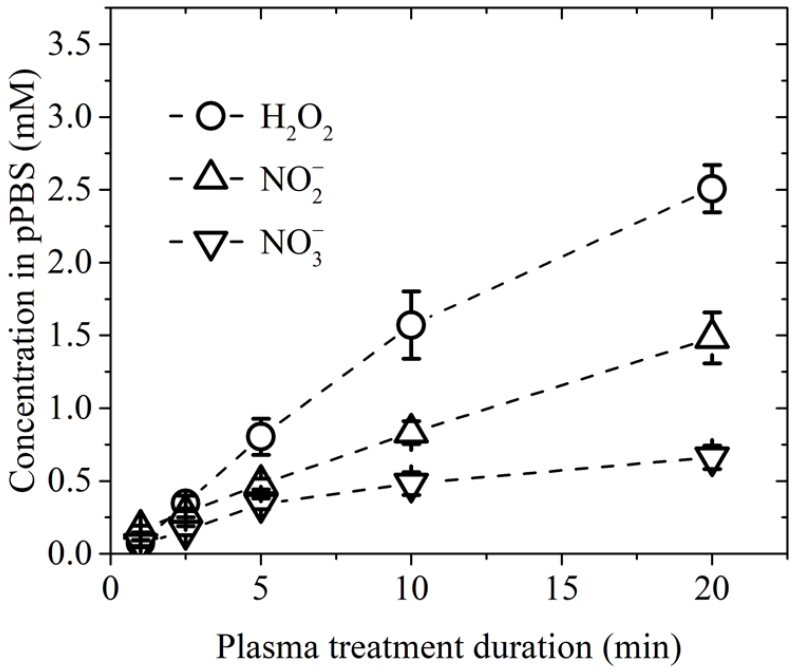

Figure 4.7 H_2O_2, NO_2^- and NO_3^- absolute concentrations as a function of the plasma treatment time. The data for the H_2O_2 are the mean values ± SEM of 18 (for the 20 minutes treatment time) or 10 (for the 10 minutes treatment time) or 5 (for the 5, 2.5 and 1 minutes treatment time) independent experiments. For NO_2^- and NO_3^-, the data are the mean values ± SEM of 6 independent experiments.

Then, we tested the effect of the high voltage polarity on the concentration of these three reactive species in the plasma-treated liquid. To our knowledge, there are only a few studies[167–169] studying the different impact of positive and negative voltage polarity on the final concentration of the reactive species in the plasma-treated liquid.

As depicted in Figure 4.8, the concentration of the reactive nitrogen species studied here, NO_2^- and NO_3^-, is not considerably affected by the high voltage polarity. Nevertheless, they follow the general rule, which we have also observed previously, that the increase of the high voltage absolute amplitude leads to an increase of the reactive species concentration. On the other hand, the production of H_2O_2 by the plasma is significantly affected by the high voltage polarity. We can see that, with negative polarities, the production of H_2O_2 is much lower than with positive polarities. On top of that, when the polarity is negative, the H_2O_2 does not follow the above-mentioned rule and it decreases with the increase of the absolute value of the high voltage amplitude.

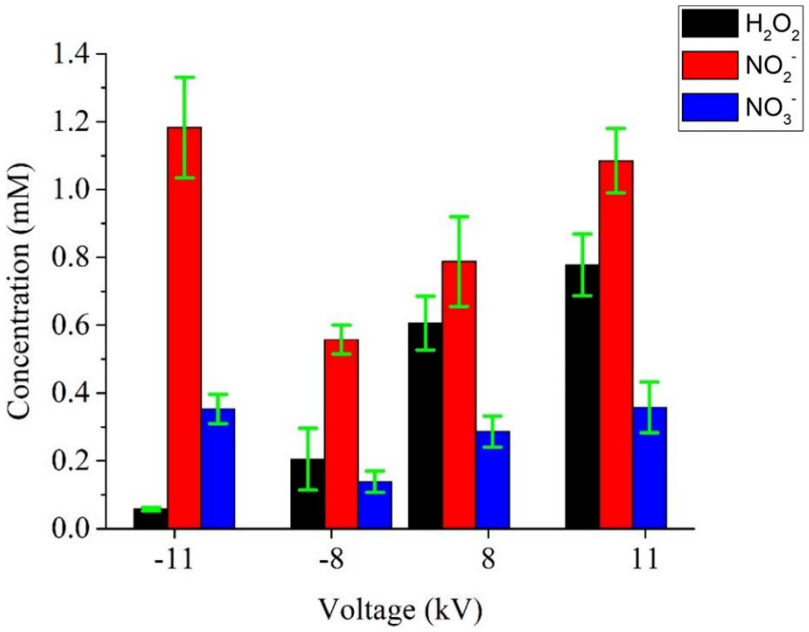

Figure 4.8 H_2O_2, NO_2^- and NO_3^- absolute concentrations as a function of the high voltage amplitude and polarity. The data are the mean values ± SD of 2 independent experiments.

There are limited works that report on the impact of the voltage polarity on the hydrogen peroxide concentration in plasma-treated liquids[167,168]. Most of them have similar results to ours: when negative polarity high voltage is applied, the concentration of H_2O_2 in the plasma-treated liquid is significantly lower than when positive polarity high voltage is applied. Mededovic *et al*. proposed that the electrons originating from the high voltage electrode are drawn towards the

positive ground electrode (liquid surface), and, a large voltage drop in the surface of the liquid, takes place. Due to the low voltage drop at the boundary, water cations that are formed and are still far from the gas–liquid boundary, cannot be significantly accelerated towards it[170]. Therefore, water cations that collide with the neutral water molecules have much lower energy than the same cations formed in the positive polarity discharge. Thus, the concentration of the radicals formed at the gas liquid surface will also be lower[167]. This is probably why there is a lower production of H_2O_2 in the negative polarity discharge than in the positive polarity discharge. Nevertheless, their reactor is not a plasma jet but they form their discharge directly between the high voltage electrode (pin) and the grounded electrode. But even if a much-detailed study is needed to conclude for the nature of this difference between negative and positive polarity on the concentration of H_2O_2, produced by an atmospheric pressure plasma jet, their hypothesis could also apply to our case.

Given the previous results, we wanted to investigate whether the lower concentration of hydrogen peroxide in the plasma treated liquid, when negative polarity is used, could be due to its lower production in the gaseous phase, or to a degradation in the liquid phase, possibly by other reactive species whose production is favored with a negative high voltage polarity. Thus, as presented in Figure 4.9, we treated the liquid again for 20 minutes but this time, for half of the time (10 minutes), we used a negative polarity, and, for the other half of the time (10 minutes), a positive polarity. As we can see in Figure 4.9, if in half of the treatment time a negative polarity is used, we measure almost half of the hydrogen peroxide that is produced with 20 minutes of treatment with a positive polarity. This means that when a negative polarity high voltage is applied, we do not degrade the existing hydrogen peroxide, but we rather do not produce any additional hydrogen peroxide. Also, there was no significant difference between the concentration of hydrogen peroxide when negative polarity is used during the first or the second half time (10 minutes) of the treatment. Finally, for all the cases studied here, the high voltage polarity did not significantly affect the concentration of the nitrogen species.

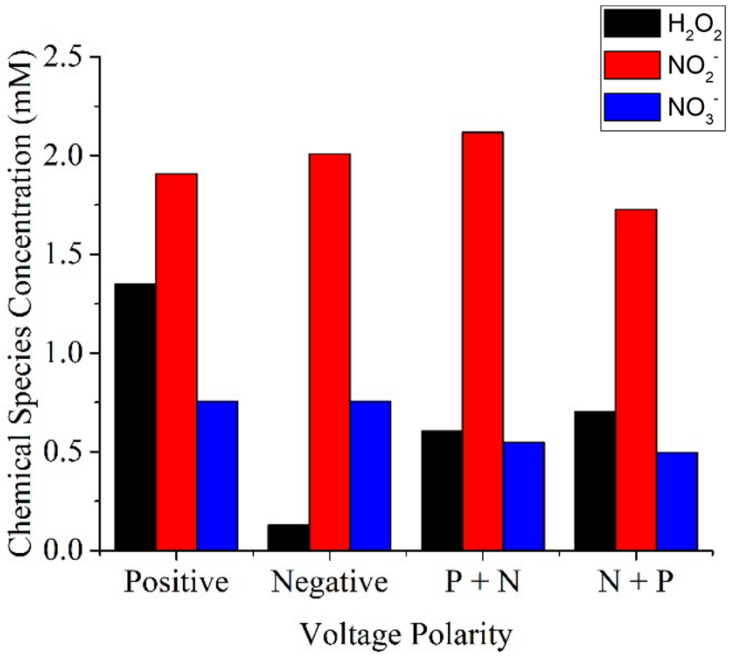

Figure 4.9 Concentration of the 3 reactive species (H_2O_2, NO_2^-, NO_3^-) as a function of the voltage polarity for an absolute amplitude corresponding to 11 kV. The cases studied here correspond to a) Positive = positive voltage for 20 minutes, b) Negative = negative voltage for 20 minutes, c) P + N = positive voltage for 10 minutes and, subsequently, negative voltage for another 10 minutes, and d) N + P = negative voltage for 10 minutes and, subsequently, positive voltage for another 10 minutes.

Regarding the MCSD, we did not detect any H_2O_2 in the treated solution, even with very big treatment times of 10 minutes, and we detected only traces of nitrites and nitrated that correspond to nM concentrations. This was expected as the discharge is not in contact with ambient air.

4.2 Short and intermediate-lived reactive species concentration in plasma-treated solutions

As mentioned before, long-lived reactive species are the main drivers of plasma anti-cancer efficiency[39,122]. Nevertheless, the transfer from the gaseous phase to the liquid or the formation in the liquid of short- and intermediate-lived reactive species is of great importance for plasma medical applications. As analysed in detail in Chapter 1, reactive oxygen species such as singlet delta oxygen or ozone are widely known for their potential to induce cell's death.

Thus, to further characterize the plasma-treated liquid chemistry, the concentrations of several reactive species that are present in the plasma-treated liquid and have a short- or intermediate lifetime were estimated. The short- and intermediated-lived reactive species considered in this study are presented in

Figure 4.10, where are also designated the colorimetric assays used for the detection of each species as well as their approximate lifetime in water. Nevertheless, we should underline here that these values can differ by orders of magnitude, depending on the conditions, i.e., temperature of liquid, pH, presence of other components, etc.

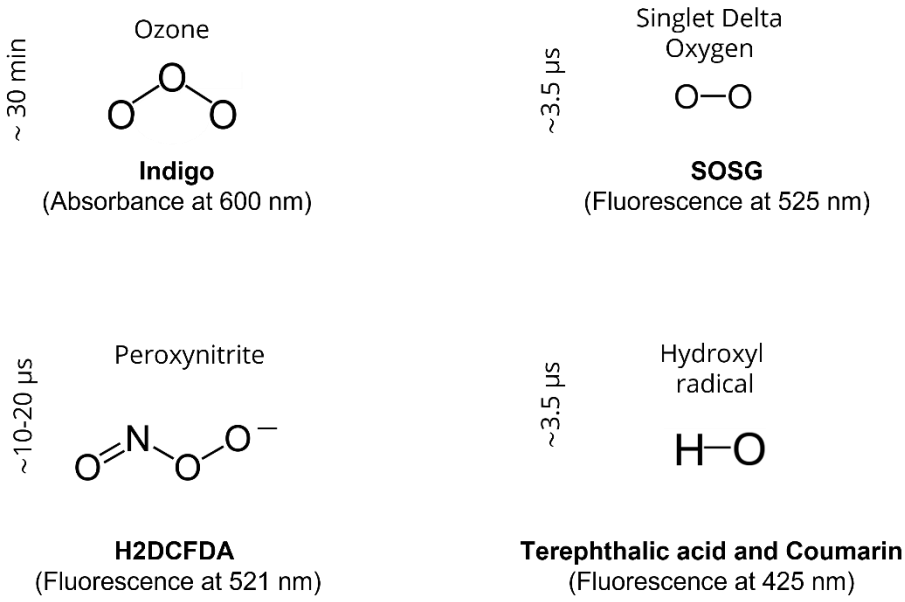

Figure 4.10 The short- and intermediate-lived reactive species present in the plasma-treated liquids considered in this study. The chemical used for the detection of each species is indicated in bold, as well as the wavelength considered in the absorption spectroscopy measurements. By the side of each species, vertically, the half-life of the species in water is indicated.

These reactive species were measured in PBS, treated by the single plasma jet (reactor 1) and the MCSD (reactor 3). Reactor 2 (multi-plasma jet) was not included in this study as it was used in this Ph.D Thesis only to produce pPBS and it was never included in direct plasma treatments. Thus, even if for research purposes, it would be very interesting to perform in the future the short- and intermediate-lived reactive species measurements also for this reactor (R2).

4.2.1 Ozone measurements

One of the reactive oxygen species studied in this Thesis' work was O_3. Ozone, among other species, might also play a role in plasma cancer treatment due to two reasons. Firstly, it is previously reported to be an efficient complementary therapy against certain types of tumours[171]. On top of that, it has an intermediate lifetime of several minutes, a fact that indicates that it could play a role at killing cancer cells both during direct plasma treatment and indirect plasma treatment. As indicated in Figures 4.10 and 4.11, the concentration of

ozone is determined with the help of indigo trisulfonate. Unfortunately, indigo is not selectively decolorized by O_3. In aqueous solutions that contain only O_3, prepared by an ozonator for example, it can be proven very useful for the estimation of O_3. Nevertheless, in a plasma-treated solution that has a much more complex chemistry, it can easily and rapidly react with other reactive oxygen species, giving finally a wrong estimation of O_3 concentration. On the other hand, as described in chapter 2, the liquids treated by the MCSD reactor (R3) exhibit a much simpler chemistry containing principally O_3 and singlet delta oxygen. Unfortunately, also in the case of the MCSD reactor, we have some indications that the indigo reacts with other reactive oxygen species. The reaction of O_3 with indigo is considered to be stochiometric (Figure 4.11). Thus, by calculating the concentration of the decolorized indigo, we are able to estimate the concentration of O_3 produced in the PBS treated by the MCSD. Before presenting our experiments, we must underline that from the reactive oxygen species that could react with the indigo and, thus, interfere with our measurements of O_3, we can exclude hydrogen peroxide as we verified that it can only decolorize indigo if found in much higher concentrations (>50 mM) than those produced by our plasma reactors. Indeed, our reactors produce much smaller concentrations of hydrogen peroxide (~1-2 mM) and, thus, we can exclude its interference on the measurements of O_3.

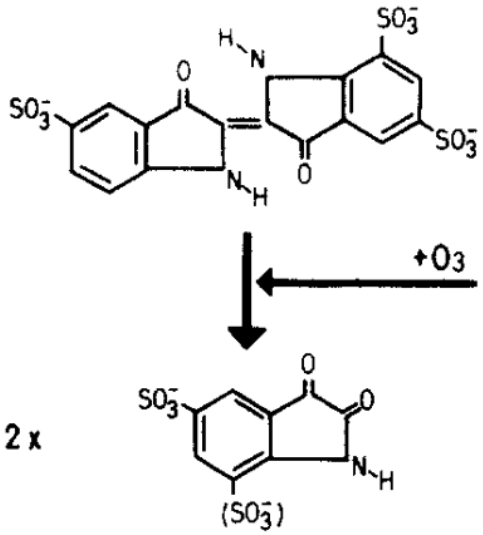

Figure 4.11 Indigo trisulfonate and its ozonation product. Figure taken unchanged from [142].

In Figures 4.12 and 4.13, the concentration of O_3 in PBS treated by the single-plasma jet and the MCSD, respectively, is presented. Here, any comparison between the two reactors should be done carefully as the treatment times with the single-plasma jet are up to almost one order of magnitude longer. Generally, the MCSD produces much higher concentrations of O_3 if the pertinent experimental conditions are used (8 slm, 97% He and 3% O_2 in the feeding gas).

In Figure 4.12, we can observe that when the treatment time is doubled (from 4 to 8 minutes), we have an almost twofold increase of the O_3 concentration. Also, when higher gas flow rates are used, the decolorization of indigo is more intense. Finally, when a small percentage of O_2 (0.2%) is added into the feeding gas, we furtherly increase the concentration of O_3 in the plasma-treated liquid. These results were expected as the O_3 concentration in the plasma-treated liquid should increase with O_2 admixture in the feeding gas and with higher gas flow rate. On the other hand, as we can see in the columns with the green shades, if sodium azide (NaN_3) is added to the solution prior the treatment, the measured O_3 concentrations are lower for the same experimental conditions. NaN_3 is a known scavenger of singlet delta oxygen (rate constant = 2.2×10^9 $M^{-1}s^{-1}$) and hydroxyl radicals (rate constant = 1.1×10^{10} $M^{-1}s^{-1}$)[172]. Thus, this is a first but rather solid indication that the indigo is not selectively decolorized by O_3, but it can also react with other reactive oxygen species. In order to better estimate the actual concentration of the O_3 in the liquid, the concentrations measured in the presence of NaN_3 can be subtracted from the concentrations measured without, but again this would exclude only two of the possible reactive species that might interfere with the measurement. Thus, from this measurement, we will keep only the comparison between the different experimental conditions and the estimation of the order of magnitude of the indigo decolorization in the pPBS, which is found to be in the range of 0.2 – 0.9 mM.

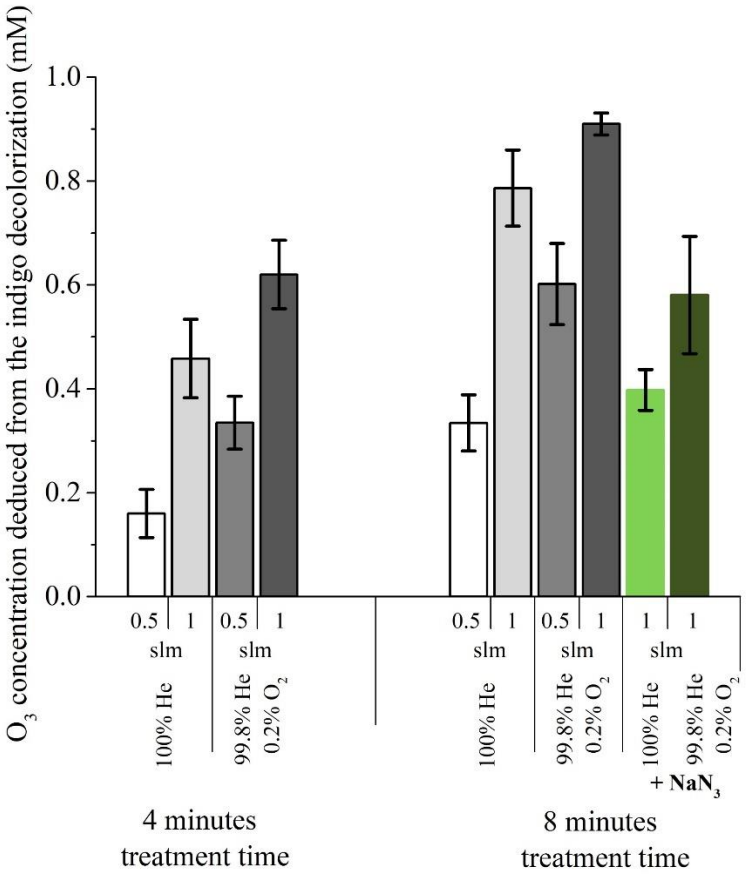

Figure 4.12 O_3 concentration measurement when PBS is treated by the single-plasma jet with a treatment distance of 8 mm. The data are the mean values ± SD of 2 independent experiments.

Similarly, in Figure 4.13, we can see that the MCSD produces concentrations of O_3 in the plasma-treated liquid of the same order of magnitude as the single-plasma jet. Nevertheless, we have to underline that if the treatment time with the MCSD was 12 minutes (as with the single-plasma jet), as the MCSD can produce higher fluxes of O_3, the O_3 concentrations in the pPBS would be much higher, especially for gas admixtures with 3% of O_2.

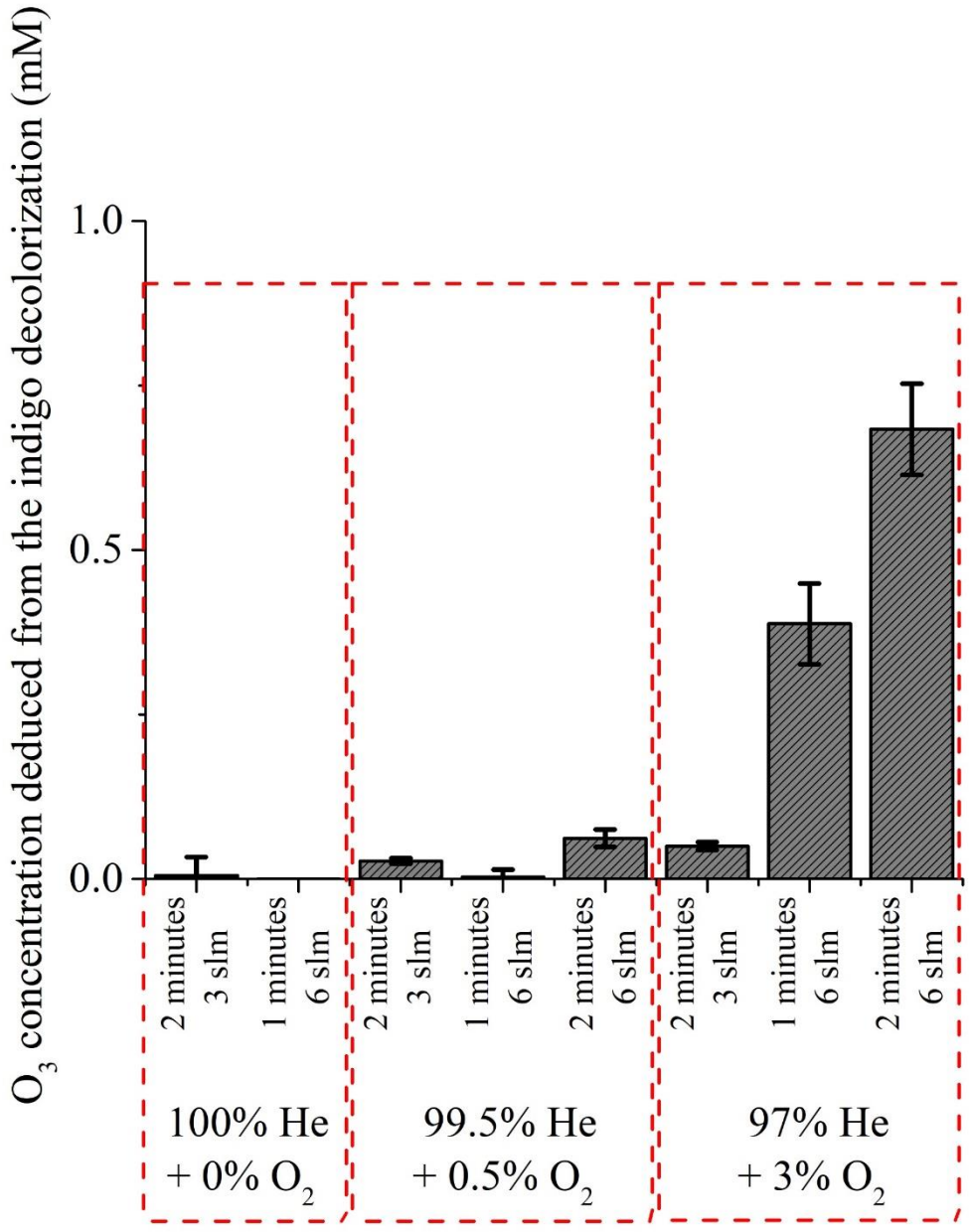

Figure 4.13 O_3 concentration measurement when PBS is treated by the MCSD. The data are the mean values ± SD of 2 independent experiments.

As we can see in Figure 4.13, we do not detect almost any ozone when the feeding gas is composed only of He, while a small concentration of O_3 is detected when we add 0.5% O_2 into the feeding gas, and the O_3 concentration becomes much more significant with 3% O_2. This phenomenon is described in detail in the Ph.D. Thesis of João Santos Sousa[105]. Briefly, when pure Helium is used as the working gas, the produced concentrations of both O_3 and singlet delta oxygen are very low. If we add in the gas mixture O_2 the produced concentration of singlet

delta oxygen increases. For a percentage of up to 1-2% of O_2 in the working gas, the concentration of singlet delta oxygen increases with the increase of that percentage. For higher percentages of molecular oxygen in the working gas, the concentration of singlet delta oxygen will start to decrease due to insufficient energy deposition per oxygen molecule[105]. This will have an immediate effect on the concentration of the ozone. Given that the molecular oxygen of the gas cannot be used to produce singlet delta oxygen (for higher O_2 percentages in the working gas), the singlet delta oxygen will no longer react with the ozone to form molecular oxygen. That will lead to an increase of the ozone concentration. On the top of that, as expected, we can see that with the increase of the plasma treatment time we have again proportional increase of the O_3 concentration. Finally, we can also observe that the increase of the gas flow rate leads to an increase of the ozone measured in the liquid.

Given that, *in vitro*, in most of the cases, the biological target is covered by a liquid, it is very important for the reactive oxygen and nitrogen species to be able to reach the target. Thus, their dissolution in the liquid is of high importance. As mentioned in Figure 4.10, the half-life of O_3 in aqueous solutions is about 30 minutes. To investigate the dissolution of O_3 in the liquid we repeated the experiment with the indigo but, this time, the indigo was added in the solution just after the treatment by the plasma (within 5 seconds).

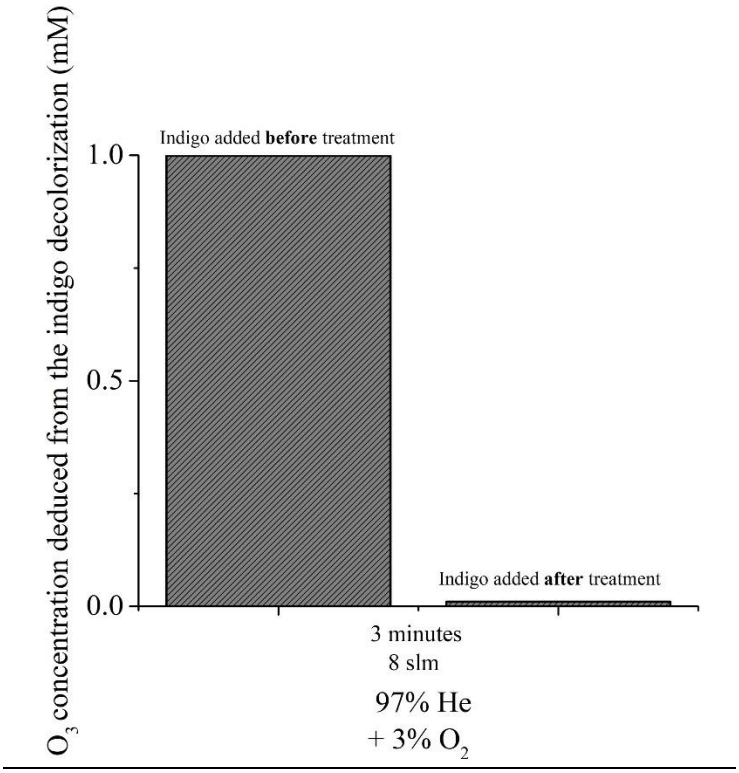

Figure 4.14 Indigo decolorization when present during the treatment time and when added just

after the treatment. The PBS was treated by the MCSD.

As we can see in Figure 4.14, if the indigo is added just when the plasma is turned off, there is almost no O_3 detected in the solution. This fact is unfortunate for the biomedical applications that require a liquid layer covering the biological target as it suggests that O_3 will not be able to reach and oxidize the biological target. Thus, O_3 should maybe be excluded from the reactive oxygen species that contribute to cell's death, *in vitro*. These targets can therefore be oxidized only by other reactive oxygen and nitrogen species produced in or transferred to the liquid by the plasma treatment or by secondary products of chemical reactions with O_3. Here, we should underline that the same results were obtained also with the single-plasma jet (no decolorization of indigo if added after the treatment). On top of that, preliminary experiments on the gaseous phase of the MCSD showed a significant O_3 concentration when the gas composition was 97% He and 3% O_2, while we detected only a very small amount of O_3 for the other two gas compositions studied here. That in combination with the difficulty of O_3 to dissolve into pPBS might indicate the decolorization of indigo by other oxygen species of a shorter lifetime like singlet delta oxygen. Hence, indigo is not sufficiently selective to be considered as an appropriate probe for measuring the concentration of O_3 in plasma-treated solutions.

4.2.2 Singlet delta oxygen measurements

Recently, Bauer *et al.* showed that the formation of primary singlet delta oxygen ($O_2(a^1\Delta_g)$) through the complex interaction between NO_2^- and H_2O_2 resulted in the inactivation of membrane-associated catalase, secondary $O_2(a^1\Delta_g)$ generation, further catalase inactivation, intracellular glutathione depletion, and intercellular RONS-mediated apoptosis signaling[26,29]. Thus, $O_2(a^1\Delta_g)$ is one of the short-lived reactive species that could possibly contribute to the anti-cancer action of direct plasma-treatment. Singlet delta oxygen measurements or even only its detection in aqueous solutions is a very challenging task due to its very short lifetime (few microseconds). For the measurement of singlet delta oxygen concentration in pPBS, we used Singlet Oxygen Sensor Green (SOSG), which is a singlet delta oxygen fluorescent probe. The details of the singlet delta oxygen concentration measurement with the sensor green are explained in detail in Chapter 2.

It is reported in the literature that singlet oxygen sensor green reacts selectively with singlet delta oxygen[173] and, therefore, it has been used in plasma-treated solutions for the estimation of $O_2(a^1\Delta_g)$ concentration. Nevertheless, we found that this is not true, at least in our experimental conditions. In order to verify the selectivity of this $O_2(a^1\Delta_g)$ detection method, we first plasma-treated PBS

containing SOSG and NaN_3. Sodium Azide, as mentioned in Chapter 2, is a well-known scavenger of $O_2(a^1\Delta_g)$ and •OH. As it can be seen in Figure 4.15, the addition of NaN_3 in the solution prior to the treatment leads to a significant reduction of the singlet oxygen sensor green fluorescence after plasma treatment, but the production of endoperoxides (when SOSG reacts with singlet delta oxygen, endoperoxides are produced that are fluorescent) is still very high. This leads us to the conclusion that there are other reactive oxygen species that also react with the singlet oxygen sensor green forming, thus, endoperoxides.

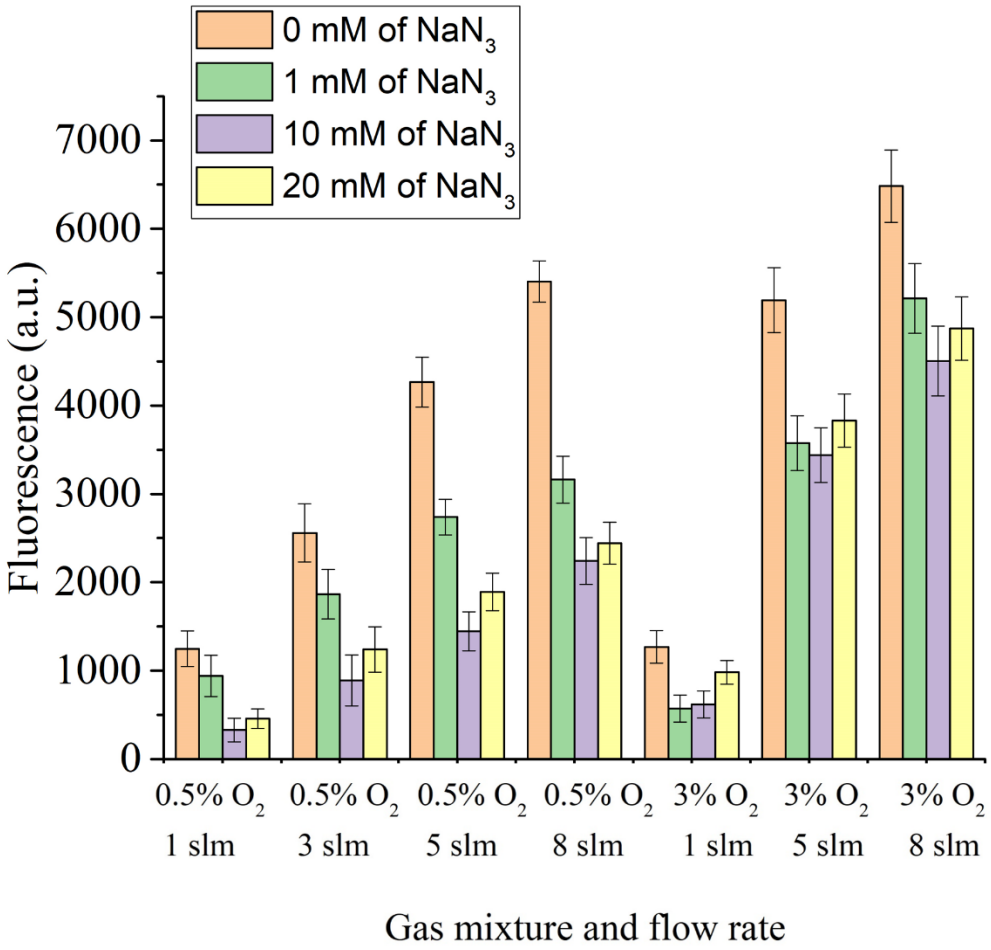

Figure 4.15 Detection of singlet delta oxygen in PBS treated by the MCSD for different experimental conditions. The treatment time was 2 minutes. The data are the mean values ± SD of 2 independent experiments.

As we can see in Figure 4.16, also when the single-plasma jet is used for the PBS treatment, the addition of sodium azide does not totally prevent the production of endoperoxides and, thus, we must assume that also in this case the SOSG does not react only with singlet delta oxygen in the solution. On top of that, it has been previously reported that the reaction rate of SOSG with singlet delta oxygen is around 3.8 10^8 $M^{-1}s^{-1}$ [174], which is a much slower reaction than that of

sodium azide with singlet delta oxygen (2.2×10^9 $M^{-1}s^{-1}$)[172]. Nevertheless, these measurements could be used for a qualitative comparison between the different experimental conditions studied here. Again, as for all the RONS studied until this point, we observe a proportional increase of the singlet delta oxygen concentration with the increase of the treatment time. Also, as in the gaseous phase[30,105], a higher concentration of $O_2(a^1\Delta_g)$ in the pPBS can be estimated when a small percentage of molecular oxygen is added into the feeding gas. On the other hand, the concentration of singlet delta oxygen does not fluctuate significantly with the increase of the gas flow rate.

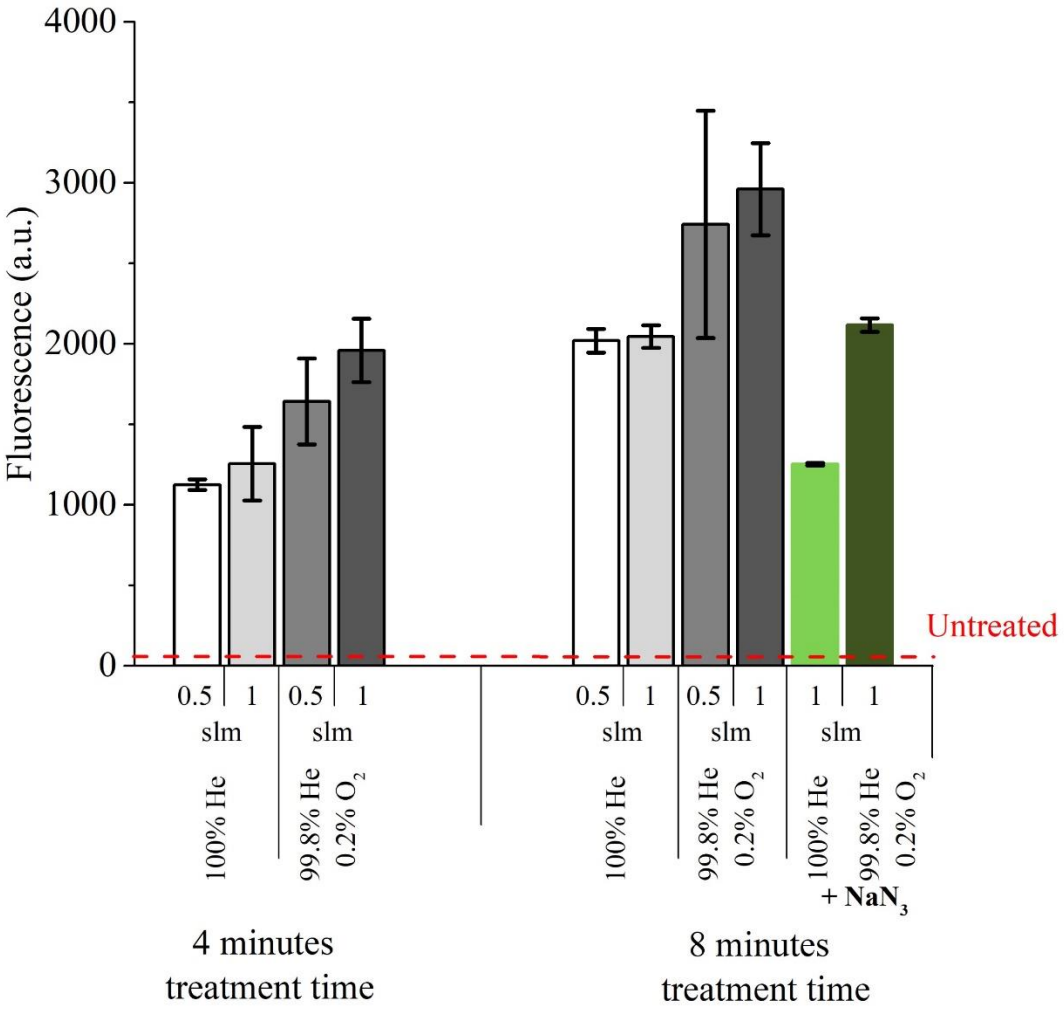

Figure 4.16 Detection of singlet delta oxygen in PBS treated by the single-plasma jet for different experimental conditions at a treatment distance of 8 mm. The data are the mean values ± SD of 2 independent experiments.

4.2.3 Peroxynitrite measurements

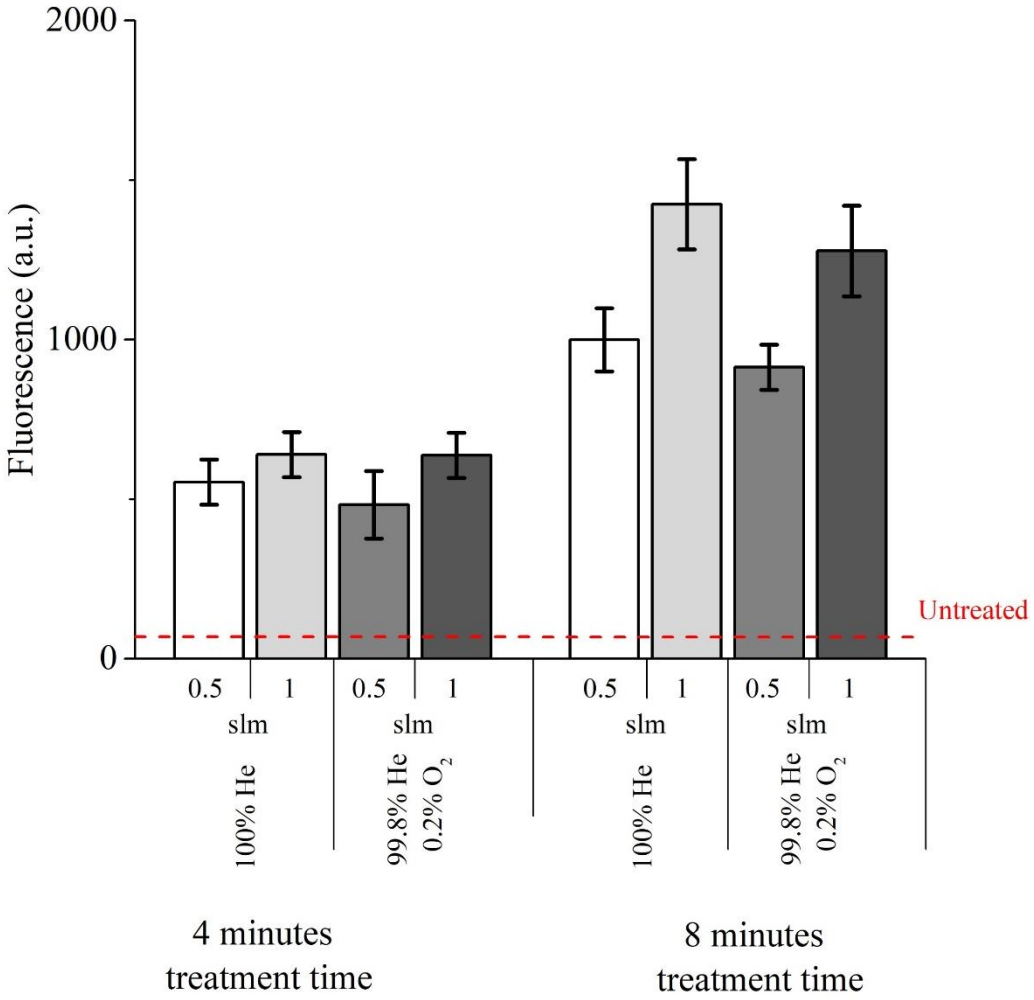

Figure 4.17 Detection of peroxynitrites in PBS treated by the single-plasma jet for different experimental conditions at a treatment distance of 8 mm. The data are the mean values ± SD of 2 independent experiments.

Peroxynitrites were also detected in the plasma-treated solution. Peroxynitrites decay into hydroxyl radicals and nitrites. Both these reactive species could induce cytotoxic effects and with a significantly acidic pH they are also assumed to be responsible for the strong bactericidal effect of plasma treatment[141]. As we can see in Figure 4.17, the concentration of peroxynitrites does not follow exactly the same tendency as those of the other reactive oxygen species studied here. More specifically, we have an almost twofold increase of its concentration when the treatment time is doubled. On the other hand, it seems that the production of peroxynitrites is less related to the gas composition and more related to the gas

flow rate. Even if we cannot measure the absolute concentration of peroxynitrites, others who have used the same method to detect it in plasma-treated solutions ended-up with similar fluorescence values[141]. As we saw in Chapter 1 (Eq. 18), the formation of peroxynitrites is due to the reaction of H_2O_2 and NO_2^-. Given that the concentration of these reactive species is not affected by the gas compositions but only by the gas flow rate (Figure 4.3) the concentration of peroxynitrites is logical to follow the same pattern.

4.2.4 Hydroxyl radical measurements

Finally, we also studied the concentration of hydroxyl radicals in the plasma-treated (by the single-plasma jet) solution. Hydroxyl radicals are probably the most important short-lived reactive species produced in pPBS. They efficiently oxidize the majority of organic compounds they come in contact with, such as cancer cells, proteins and lipids, and, by radical recombination, they are the main source of the hydrogen peroxide produced by the plasma[161]. Our results unveil that hydroxyl radicals exhibit a similar behavior to the other short-lived reactive species studied here. More specifically, even if our results are for only two treatment times, it seems that, the increase of the plasma treatment time leads to a proportional increase of the species concentration. Also, as for ozone and peroxynitrites, when the gas flow rate increases, the concentration of hydroxyl radicals also increases, and the addition of molecular oxygen into the feeding gas increases the concentration of hydroxyl radicals that were detected in the plasma-treated PBS (pPBS). The increase of hydroxyl radicals with the addition of O_2 in the gas mixture can be explained by the contribution $O_2^{\bullet -}$ to its production (Eq. 21, Chapter 2), the concentration of which is also increased when a gas composition of He/O_2 is used.

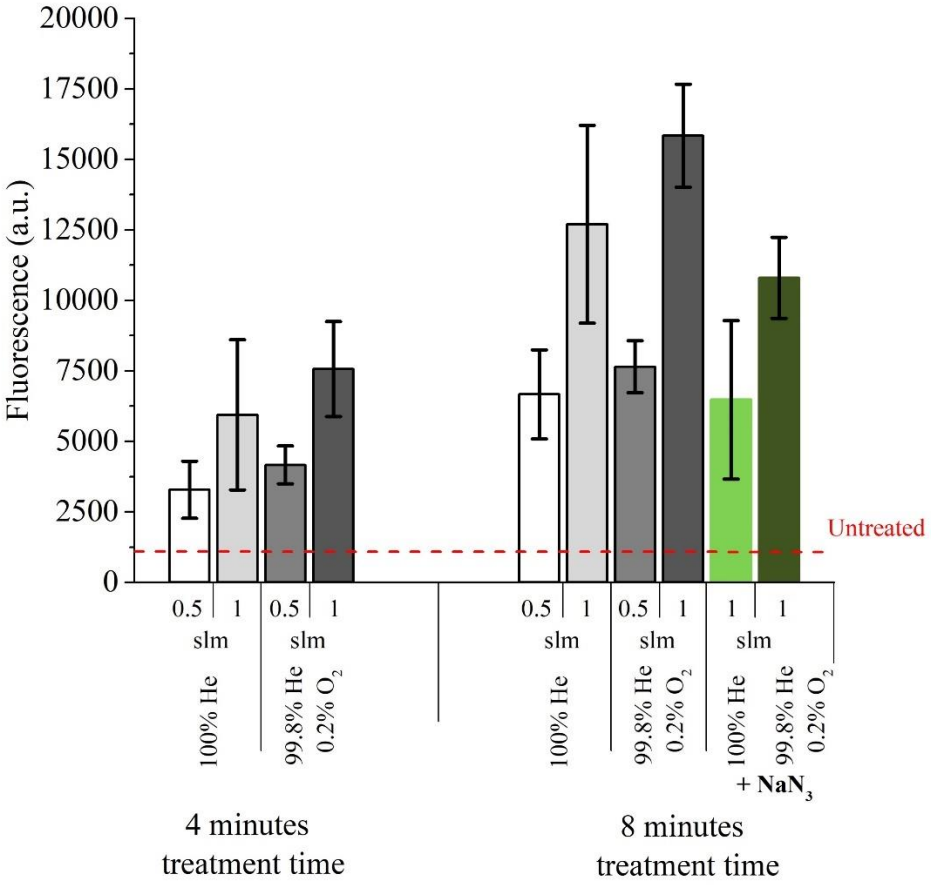

Figure 4.18 Detection of •OH in PBS treated by the single-plasma jet for different experimental conditions at a treatment distance of 8 mm. The data are the mean values ± SD of 2 independent experiments.

Conclusions

As mentioned before, the measurement of the absolute concentrations of short-lived reactive species in the plasma-treated liquid is a rather challenging task. In this work, we managed to detect in the pPBS three of the short-lived reactive oxygen and nitrogen species that are reported to contribute to the anti-cancer capacity of plasma-treated solutions: •OH, $^1O_2$, and ONOO–. We have also estimated the concentration of another important intermediate-lived reactive oxygen species: O_3. Generally, we observed that the increase of the plasma treatment time leads to a rather proportional increase of the reactive species concentration in the liquid phase, that the increase of the gas flow rate results in an increase of the concentration of most of them and that the addition of a small percentage of O_2 into the gas also increases their concentrations. The previous results helped us define the experimental conditions that we used afterwards for

the treatment of cancer and normal cells. As an example, we can mention that the addition of 0.2% of O_2 into the feeding gas did not have a significant impact on the concentration of the long-lived reactive species in the liquid, while it significantly increased the presence of short- and intermediated-lived reactive species, like singlet delta oxygen. Thus, we decided to perform most of our *in vitro* experiments with a gas mixture of He with 0.2% of O_2 (see Chapter 5).

4.3 Preserving the anti-cancer efficacy of plasma-treated solutions over time: a prerequisite for their clinical application

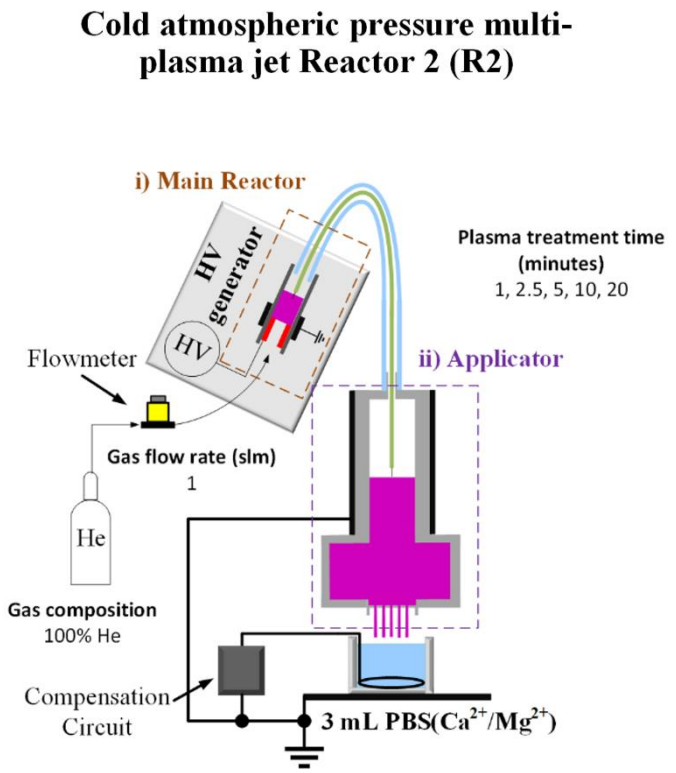

Figure 4.19 Schematic overview of the reactor and the experimental conditions used in this study.

Over the last decades, plasma pharmacy has been an emerging research field within plasma medicine, especially when it comes to cancer treatment. Numerous publications show that plasma-treated solutions can be an effective anti-cancer agent against different types of tumour cells, including ovarian cancer, cervical cancer, pancreatic cancer, glioblastoma, colon cancer and melanoma, both *in vitro* and *in vivo*[175–177].

As it was underlined in Chapter 1, the anti-cancer properties of such plasma-treated solutions are mainly due to the delivery of long-lived reactive oxygen and nitrogen species (RONS) that can be generated in or transferred into

the liquid phase. It is now widely accepted that hydrogen peroxide (H_2O_2) is the main species responsible for their cytotoxic effects[12,40]. However, synergistic effects with nitrite (NO_2^-), nitrate (NO_3^-) and the pH of the pPBS have also been reported[12,39,122].

To be considered as effective anti-cancer agents, it is essential that these plasma-treated solutions maintain their anti-cancer properties over time. One key parameter for the conservation of plasma-treated solutions, as well as of any other agent, is the storage temperature. Shen *et al.* investigated the evolution of plasma-treated water (PTW) when stored at 4 different temperatures (+25, +4, −20 and −80 °C) over 30 days in terms of H_2O_2, NO_2^- and NO_3^- concentrations as well as its bactericidal activity[64]. They found that the bactericidal ability of PTW increased with decreasing storage temperature. Besides, they also found that the concentrations of H_2O_2, NO_2^- and NO_3^- decreased over time for all storage temperatures except for –80 °C. Contrariwise, Judée *et al.*, who used plasma-activated medium (PAM) to treat colon adenocarcinoma multicellular tumor spheroid (MCTS), found that, when the PAM was stored at +4 °C or –80 °C, it retained its genotoxic activity, which was not the case for the PAM stored at +37 °C or –20 °C[178]. Thus, they suggested that H_2O_2 concentration in PAM remained stable during at least 7 days of storage at +4 °C and −80 °C, while a storage at +37 °C and −20 °C certainly decomposed H_2O_2. Yan *et al.* showed that while the H_2O_2 was stable in plasma-treated PBS stored at +8 °C and –25 °C for up to 3 days, its concentration was reduced as a function of storage time (and for the same storage conditions) when the PTS was cell culture medium[66]. These discrepancies between reports can be attributed to both the different types of plasmas used for the treatment of the solutions and to the different treated solutions. Indeed, as it was also partially presented earlier in Chapter 4, different working conditions such as gas flow rate, gas composition, treatment distance, room conditions (e.g. humidity and temperature) and high voltage amplitude result in the production/transfer of different reactive species in/into the liquid[67,68]. Besides the fluctuation of the RONS concentration, the chemical reactivity of plasma-treated solutions is also highly dependent on the final pH of the solution after plasma treatment. In fact, the pH of the plasma-treated solutions could be one of the crucial parameters that may explain the choice of the different storage temperatures proposed by the aforementioned authors. Indeed, not only the acidic pH of plasma-treated solutions may contribute alongside RONS to their cytotoxic capacity, but it is also an important parameter for the stability of RONS[39,69].

The work presented in this section is devoted to the determination of pertinent storage conditions to preserve the cytotoxic effects of pPBS. Thus, the chemical stability of pPBS was assessed here, in terms of the H_2O_2, NO_2^- and NO_3^-

concentrations as a function of storage time and temperature for up to 75 days after production by plasma treatment. The chemical mechanisms leading to the degradation of these RONS in certain storage conditions of the pPBS and the catalytic role of the acidic pH were also investigated.

4.3.1 RONS (H_2O_2, NO_2^- and NO_3^-) degradation as a function of storage time and temperature

As previously reported[122], the anti-cancer properties of pPBS are mainly due to the combined action of H_2O_2 and NO_2^- and, in some cases, with also the acidic pH[39]. Thus, the chemical stability of these RONS, produced by the multi-plasma jet (R2) in pPBS, was assessed as a function of the storage time and temperature. Their concentration in pPBS within 2h from plasma treatment (D0) is depicted in Figure 4.7. At first, the degradation of H_2O_2 in the pPBS was investigated (see Figure 4.20). When the pPBS was stored at room temperature (around +20 °C) or at +4 °C, no significant degradation of H_2O_2 was observed for up to 75 days of storage in relation to the initial concentration obtained just after the plasma treatment (at D0, Figure 4.7). Also, no significant difference was observed between these two storage temperatures, in terms of H_2O_2 stability over time. On the contrary, when the pPBS was stored at –20 °C or –80 °C, the concentration of H_2O_2 decreased over time, even after just 1 day of storage (24 hours after the treatment at D0). The maximum degradation was measured after 7 days of storage, when the concentration of H_2O_2 was found to be about 20% and 30% lower than its initial concentration when stored at –80 °C and –20 °C, respectively. No further significant degradation was observed after this period of storage (>D7). However, it must be stressed that the difference (about 10% points) between these two storage temperatures (–20 °C and –80 °C) is statistically significant, except at day 75 (D75).

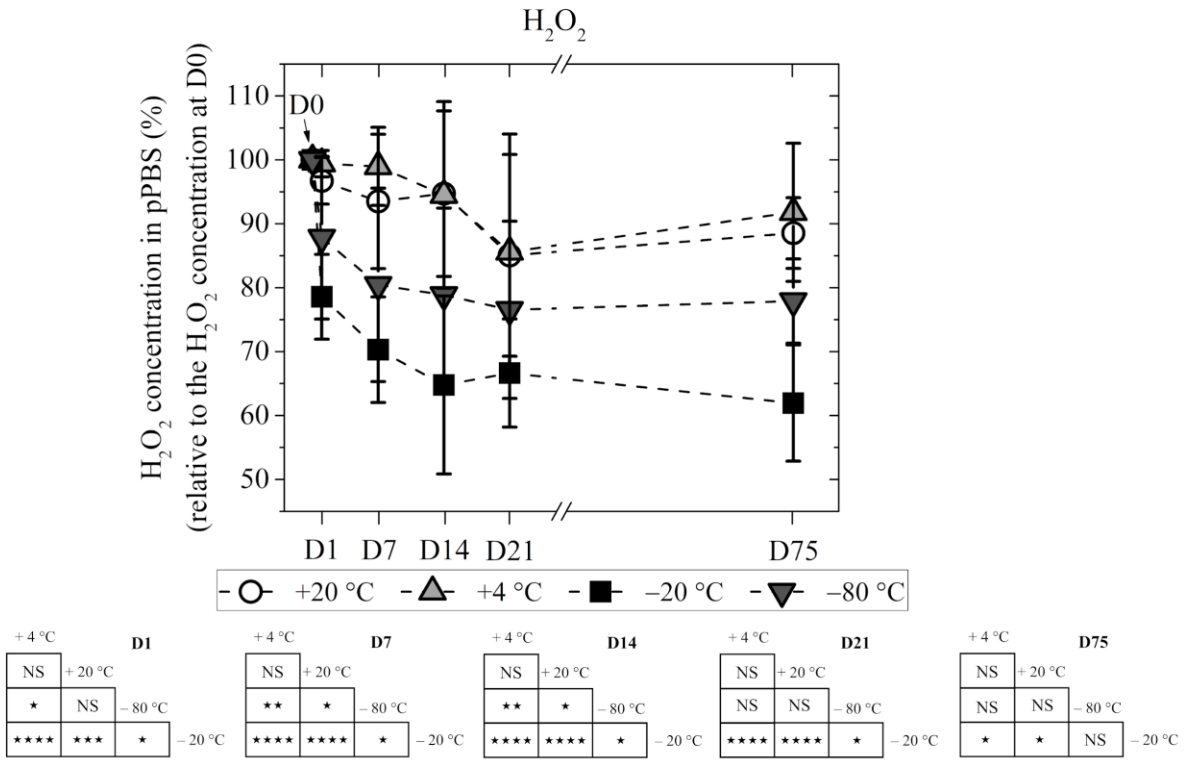

Figure 4.20 The concentration of H_2O_2 in the pPBS as a function of the storage time, when stored at four different temperatures: +20, +4, –20 and –80 °C. The concentration of H_2O_2 in % is calculated in relation to the initial concentration measured on the day of plasma treatment (D0), within 2 hours from it. For up to 21 days of storage (D21), the data are the mean values ± SD of 9, 9, 18 and 9 independent experiments for +20, +4, –20 and –80 °C, respectively. For 75 days of storage (D75), the data are the mean values ± SD of 3 independent experiments for all the storage temperatures. Statistical significance NS: $p > 0.05$; *: $p \leq 0.05$; **: $p \leq 0.01$; ***: $p \leq 0.001$; ****: $p \leq 0.0001$ (t-test).

As previously reported[12], and as we also found in our work (Figure 4.7), the concentration of RONS (H_2O_2, NO_2^- and NO_3^-) in the pPBS increases proportionally with the duration of the plasma treatment. To evaluate the effect of the total concentration of these reactive species on the degradation of H_2O_2, PBS(Ca^+/Mg^+) was plasma-treated for 1, 2.5, 5, 10 and 20 minutes and then stored at +4 °C and –20 °C (see Figure 4.22). These two storage temperatures were chosen because they induce the lowest and the highest degradation of H_2O_2 over storage time, respectively (see Figure 4.20). The ratio of the concentrations of H_2O_2 and NO_2^- varied between 0.5 and 2 for the plasma treatment times considered here (see Figure 4.21). As one can see in Figure 4.22, our results unveiled, on the one hand, that, independently of the plasma treatment time, and, thus, of the initial concentrations of the RONS studied here, H_2O_2 was always significantly degraded when the pPBS was stored at –20 °C (about 20-35% degradation, as compared to the initial concentration of H_2O_2 measured at D0), except in some cases for only one day of storage (D1), for which there was no degradation. In fact, this

degradation was more pronounced after 7 days (D7) than during the first 24 hours of storage (D1). On the other hand, when the pPBS was stored at +4 °C, the concentration of H_2O_2 was stable (>85% in relation to the H_2O_2 concentration at D0) over 21 days (D21).

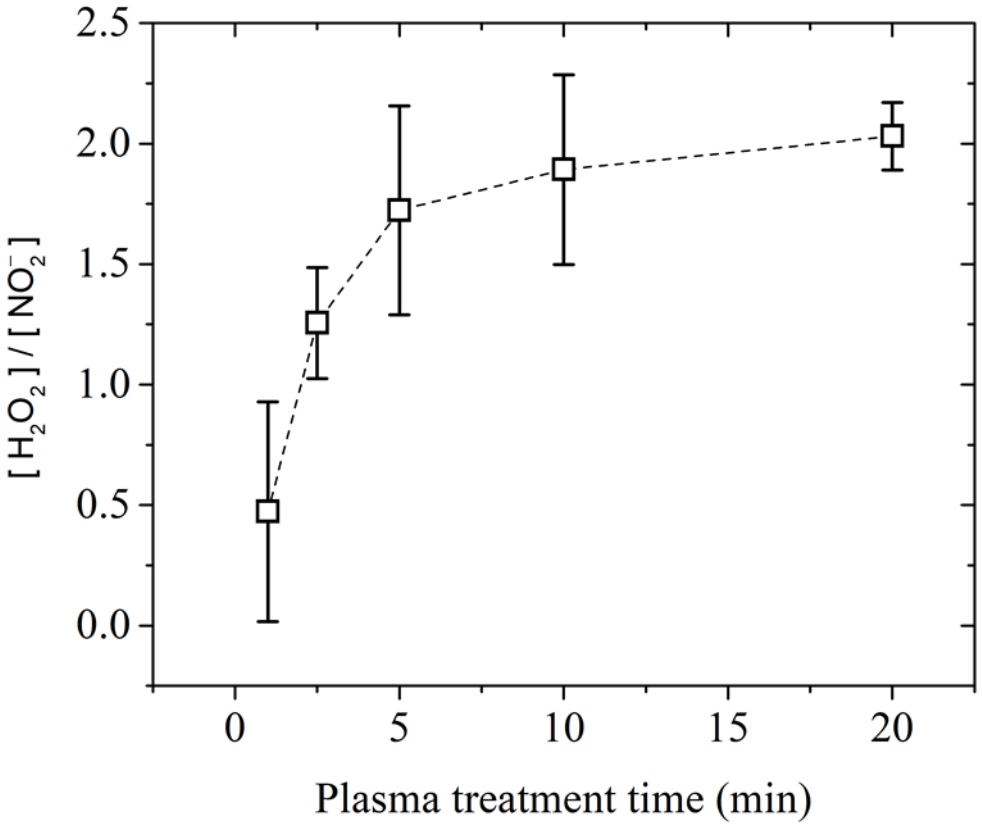

Figure 4.21 The $[H_2O_2]/[NO_2^-]$ ratio was calculated for every independent experiment of Figure 4.7 and the mean value ± SD of 5 independent experiments is presented as a function of the plasma treatment time.

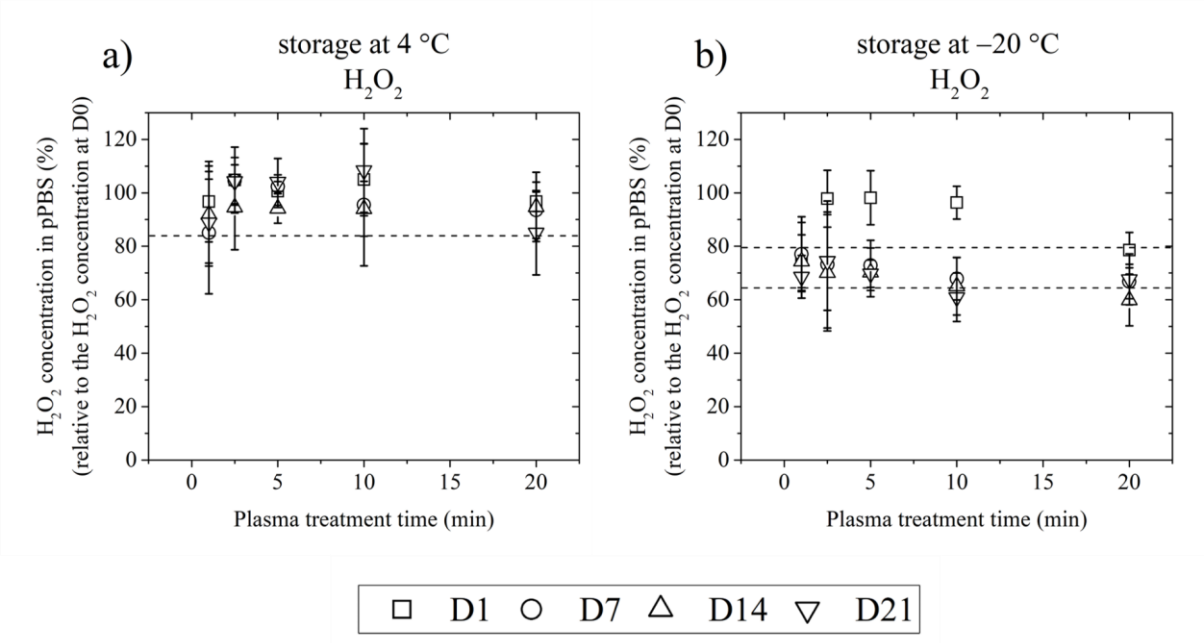

Figure 4.22 Concentration of H_2O_2 in the pPBS as a function of the plasma treatment time, when stored at a) +4 °C and b) –20 °C for 1 day (D1), 7 days (D7), 14 days (D14) and 21 days (D21). The concentration of H_2O_2 in % is calculated in relation to the initial concentration of H_2O_2 measured on the day of the plasma treatment (D0), within 2 hours from it. For the 20 minutes plasma treatment time, the data are the mean values ± SD of 9 (for +4 °C) and 17 to 18 independent experiments (for –20 °C), while for 10 minutes plasma treatment time, of 7 to 10 independent experiments (for both storage temperatures). For all the other plasma treatment times (1, 2.5 and 5 minutes), the data are the mean values ± SD of 2 to 5 independent experiments (for both storage temperatures).

Although H_2O_2 has been described as a key player in pPBS-induced reduction of cancer cells viability[33], its synergistic effect with reactive nitrogen species such as NO_2^- has also been reported[39,122]. To conclude on the overall degradation of the pPBS as a function of the storage time and temperature, the concentration of these reactive nitrogen species was also monitored (see Figure 4.23). We found that both NO_2^- and NO_3^- were stable for up to 21 days when the pPBS was stored at +4 °C or +20 °C. For longer storage times (75 days), the concentration of NO_2^- decreased by about 35-40% at these storage temperatures. As for H_2O_2, there was no significant difference between storing at room temperature (around +20 °C) or in the fridge (+4 °C). When the pPBS was stored at –20 °C, we observed a massive degradation of NO_2^-, over about 90%, occurring even from the first day of storage. The degradation at –80 °C was also significant (about 70%). On the contrary, the concentration of NO_3^- increased when the pPBS was stored at –20 °C or –80 °C, showing an inversely proportional behavior to that of NO_2^-. Even if the study on the reactive species conservation as a function of storage time is mainly conducted with the multi-plasma jet (R2), we should mention that also when the single-plasma jet (R1) was used for the production of these three reactive species, their concentrations were stable for several days if

stored at +4 or +20 °C (other temperatures that include freezing were not tested with this reactor).

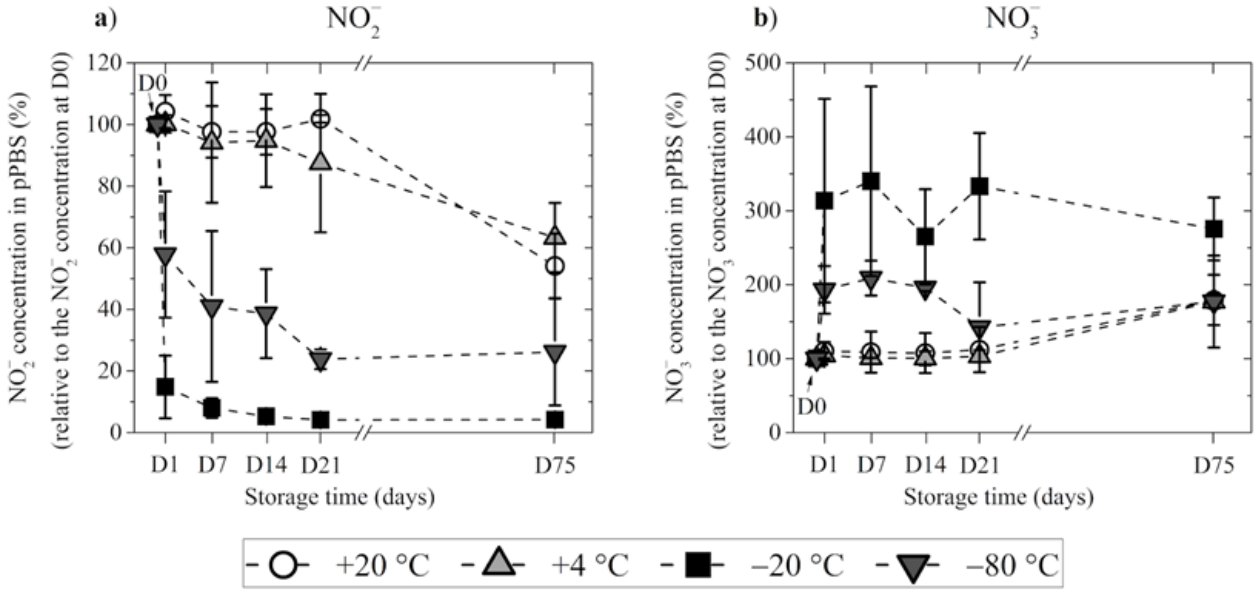

Figure 4.23 Concentration of a) NO_2^- and b) NO_3^- in the pPBS as a function of the storage time, when stored at four different temperatures: +20, +4, –20 and –80 °C. The concentration in % is calculated in relation to the initial concentration of a) NO_2^- or b) NO_3^- measured on the day of the plasma treatment (D0), within 2 hours from it. For NO_2^-, the data are the mean values ± SD of 8 and 3 independent experiments for up to 21 (D21) and for 75 days of storage (D75), respectively. For NO_3^-, the data are the mean values ± SD of 6 and 2 independent experiments for up to 21 (D21) and for 75 days of storage (D75), respectively.

4.3.2 Impact on the RONS degradation of their initial concentration and the pH of the solution

To understand the mechanisms of the pPBS degradation due to storage time or/and temperature, we first isolated the reactive species considered in this work (H_2O_2, NO_2^- and NO_3^-) by preparing mimicking solutions of those species in PBS with concentrations equivalent to those produced by a 20-minute plasma treatment ([H_2O_2] = 3 mM, [NO_2^-] = 1.5 mM and [NO_3^-] = 0.75 mM). Two different mimicking solutions were prepared: the first contained these reactive species concentrations in PBS(Ca^+/Mg^+) of pH = 7.1, while the second contained the same reactive species concentrations in PBS(Ca^+/Mg^+) of pH = 6.1 (equal to that of pPBS). For the following cases, there was no degradation over 21 days of storage at any of the storage temperatures studied here: 1) H_2O_2 alone, 2) NO_2^- alone, 3) NO_3^- alone, 4) NO_2^- + NO_3^-, 5) H_2O_2 + NO_3^- in mimicking solutions of both pH = 7.1 and pH = 6.1 (see Figures 4.23 (for 1), 2) and 3)), 4.24 (for 4)) and 4.25 (for 5))). In the case of H_2O_2 + NO_2^- in mimicking solutions of pH = 7.1, presented in Figure 4.27, the evolution over storage time at different storage temperatures of the reactive

species is like the case of H_2O_2 + NO_2^- + NO_3^- also at pH = 7.1 (see Figure 4.28). For these cases, the degradation over storage time of H_2O_2 in the mimicking solutions simulates its degradation in pPBS with a slightly delayed evolution, i.e. about –30% after 21 days instead of only 7 days of storage (see Figure 4.21). This time-shift is even more pronounced for the NO_2^- degradation, as the effect of the storage temperature observed after the first day of storage for the pPBS is only observed after 75 days of storage for the mimicking solutions (compare Figures 4.22 a) and 4.27). As so, the degradation of both H_2O_2 and NO_2^- is similar in pPBS or mimicking solutions after 75 days of storage. Contrariwise, the degradation of the solutions containing H_2O_2 + NO_2^- or H_2O_2 + NO_2^- + NO_3^-, but at a pH = 6.1, simulates closely the degradation of the pPBS, as shown in Figures 4.26 and 4.28, respectively.

Finally, mimicking PBS(Ca^+/Mg^+) solutions with different concentrations of H_2O_2 or of NO_2^- and pH = 7.1 were also investigated (see blue and red points in Figure 4.28), to study the effect of these RONS initial concentrations on their degradation. On the one hand, we observed that for a doubled concentration of H_2O_2, the degradation of H_2O_2 was slightly smaller and the degradation of NO_2^- slightly higher. On the other hand, with twice the concentration of NO_2^-, the degradation of H_2O_2 was significantly higher and that of NO_2^- significantly lower, especially when the solution was stored at –80 °C. This means that the stoichiometry of the reaction between H_2O_2 and NO_2^- inducing their degradation should be of 1:1, as, after a 20 min plasma treatment, the concentration of H_2O_2 in pPBS was about the double of that of NO_2^-. These experiments highlight the great importance of both the RONS concentration and the pH of the solution on the degradation over time of these RONS in pPBS.

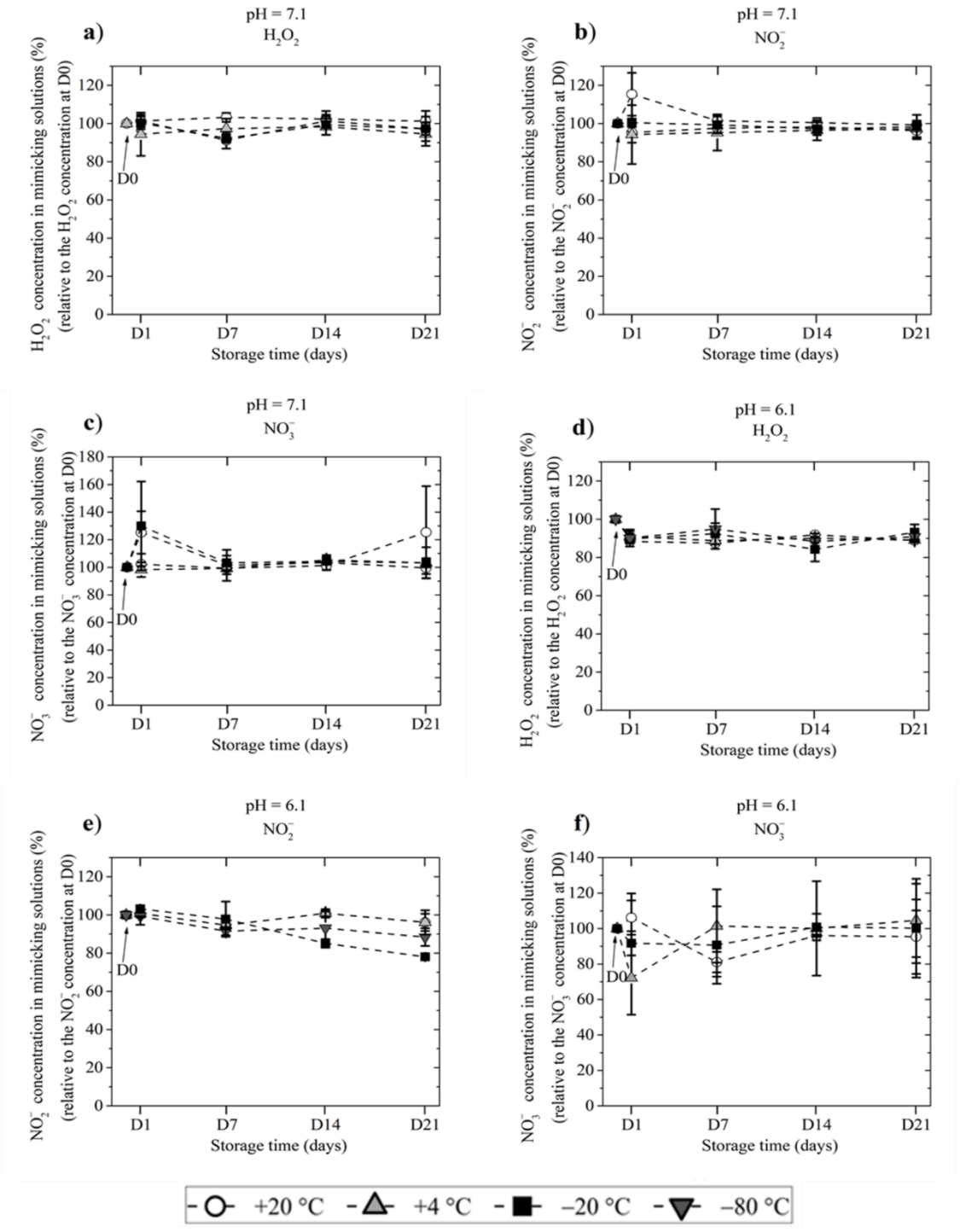

Figure 4.24 RONS alone for pH = 7.1 (a), b) and c)) and for pH = 6.1 (d), e) and f)). Concentration over storage time of H_2O_2 (a) and d)), NO_2^- (b) and e)) and NO_3^- (c) and f)) in mimicking solutions of pH = 7.1 and pH = 6.1 stored at +4, +20, –20 and –80 °C. Pure mimicking solutions were prepared containing only H_2O_2 (a) and d)) or NO_2^- (b) and e)) or NO_3^- (c) and f)). The data are the mean ± SD of 2 independent experiments. The differences between the curves are not statistically significant (p-values > 0.05), except in e) for D14 between +20 °C and –20 °C, and +4 °C and –20 °C, and for D21 between +20 °C and –20 °C, where the p-values are < 0.05 but > 0.01 (*).

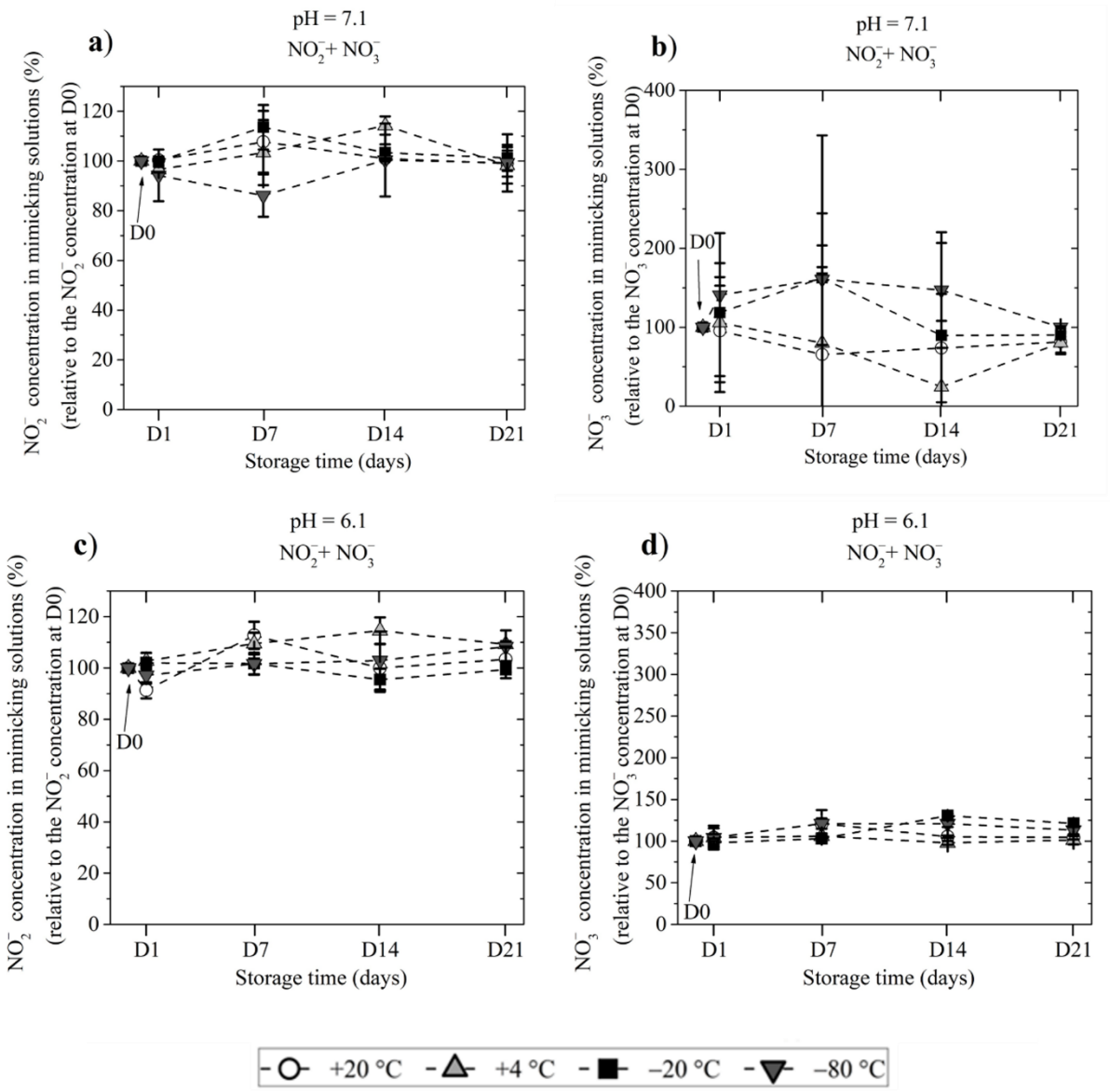

Figure 4.25 NO_2^- + NO_3^- for pH = 7.1 (a) and b)) and pH = 6.1 (c) and d)). Concentration over storage time of NO_2^- (a) and c)) and NO_3^- (b) and d)) in mimicking solutions of pH = 7.1 and pH = 6.1 stored at +4, +20, –20 and –80 °C. Pure mimicking solutions were prepared containing only NO_2^- and NO_3^-. The data are the mean ± SD of 2 independent experiments. The differences between the curves are not statistically significant (p-values > 0.05), except in d) for D14 between +20 °C and –20 °C, +20 °C and –80 °C, +4 °C and –20 °C, and +4 °C and –80 °C, where the p-values are < 0.05 but > 0.01 (*).

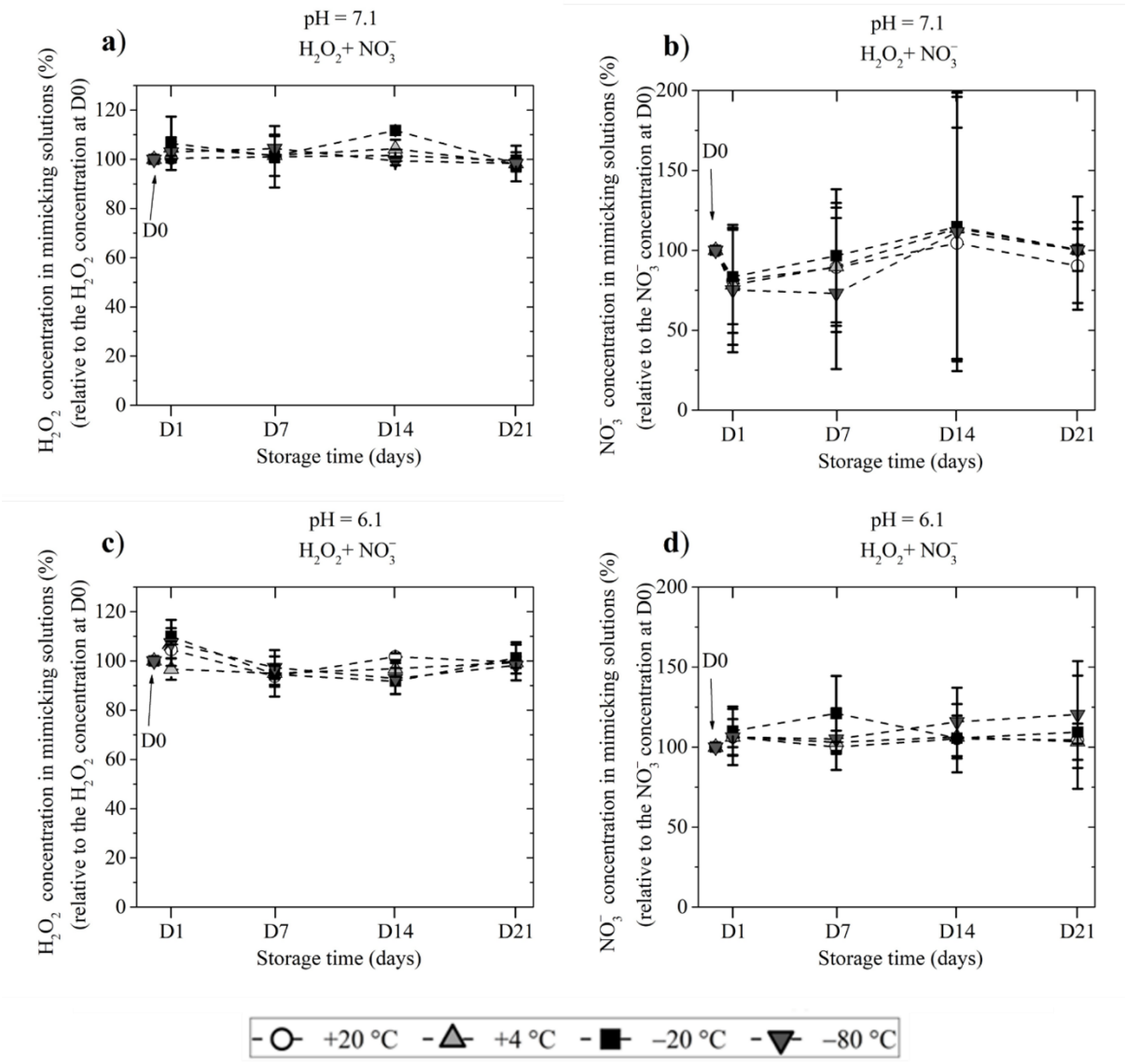

Figure 4.26 H_2O_2 + NO_3^- for pH = 7.1 (a) and b)) and pH = 6.1 (c) and d)). Concentration over storage time of H_2O_2 (a) and c)) and NO_3^- (b) and d)) in mimicking solutions of pH = 7.1 and pH = 6.1 stored at +4, +20, –20 and –80 °C. Pure mimicking solutions were prepared containing only H_2O_2 and NO_3^-. The data are the mean ± SD of 2 independent experiments. The differences between the curves are not statistically significant (p-values > 0.05), except in a) for D14 between +20 °C and –20 °C, and –80 °C and –20 °C, where the p-values are < 0.05 but > 0.01 (*).

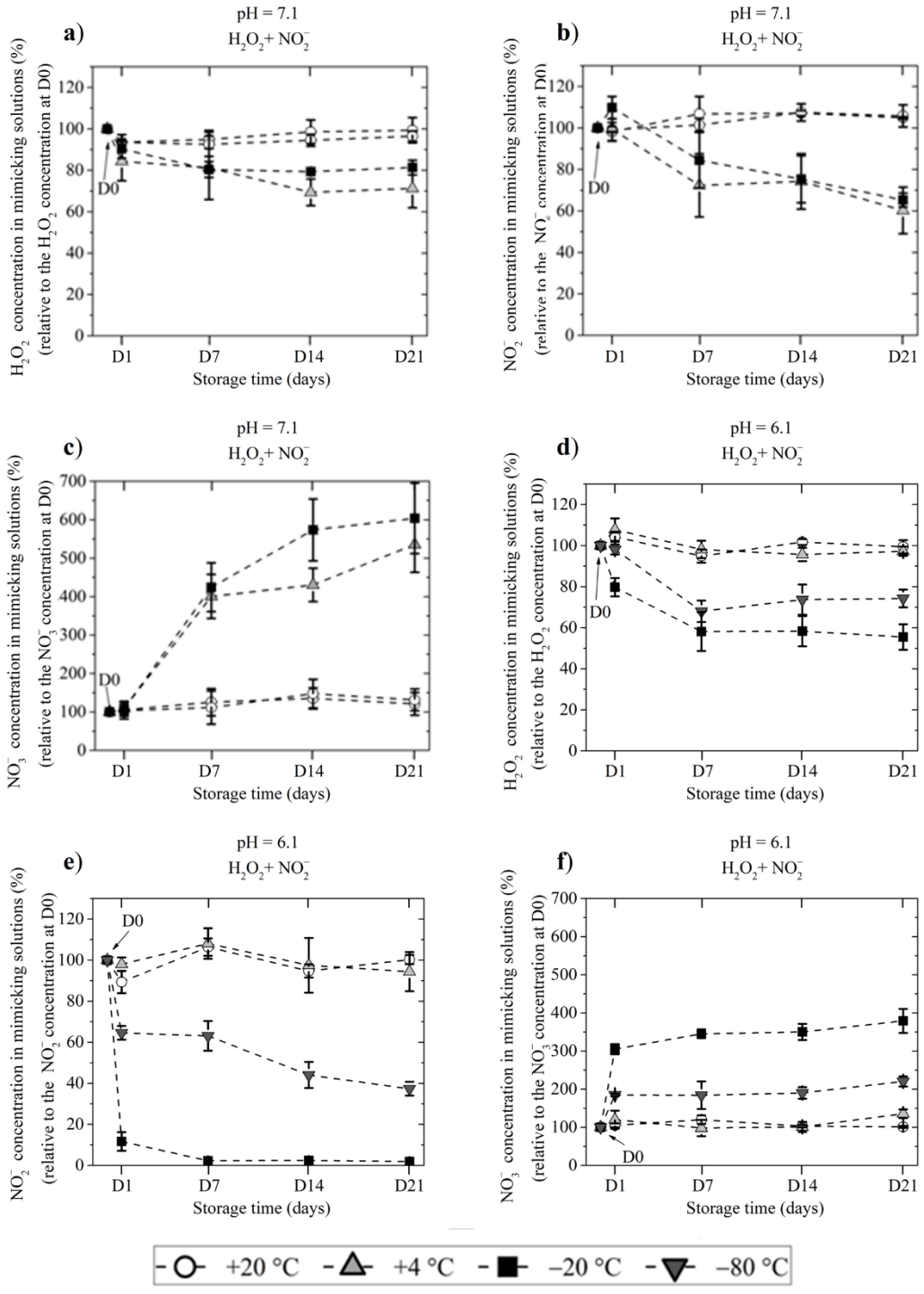

Figure 4.27 H_2O_2 + NO_2^- for pH = 7.1 (a), b) and c)) and for pH = 6.1 (d), e) and f)). Concentration over storage time of H_2O_2 (a) and d)), NO_2^- (b) and e)) and NO_3^- (c) and f)) in mimicking solutions of pH = 7.1 and pH = 6.1 stored at +4, +20, –20 and –80 °C. Pure mimicking solutions were prepared containing only H_2O_2 and NO_2^-. The data are the mean ± SD of 2 independent experiments.

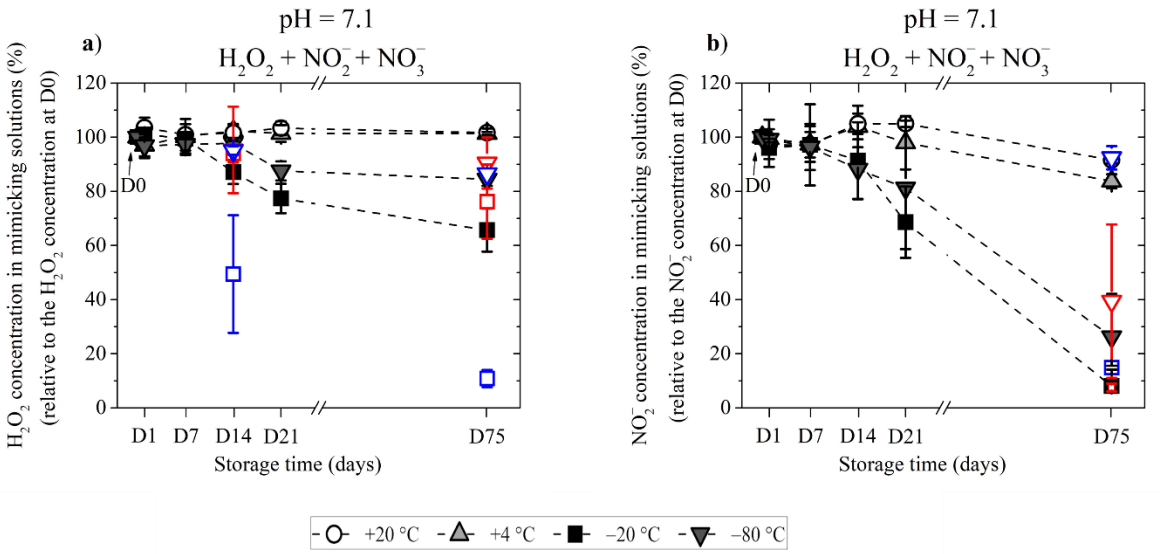

Figure 4.28 Concentration of a) H_2O_2 and b) NO_2^- in mimicking solutions of H_2O_2, NO_2^- and NO_3^- and of pH = 7.1, as a function of the storage time, when stored at four different temperatures: +20, +4, –20 and –80 °C. The blue and red points correspond to mimicking solutions containing 2*[NO_2^-] and 2*[H_2O_2], respectively, stored at –20 °C (squares) or –80 °C (down triangles). The concentration in % is calculated in relation to the initial concentration of a) H_2O_2 or b) NO_2^- measured on the day of preparation of the solutions (D0). The data are the mean values ± SD of 4 independent experiments for all experimental conditions, except for mimicking solutions containing 2*[NO_2^-] and 2*[H_2O_2] (2 independent experiments) and mimicking solutions containing 1*[NO_2^-] and 1*[H_2O_2] and stored for 75 days (D75) (3 independent experiments).

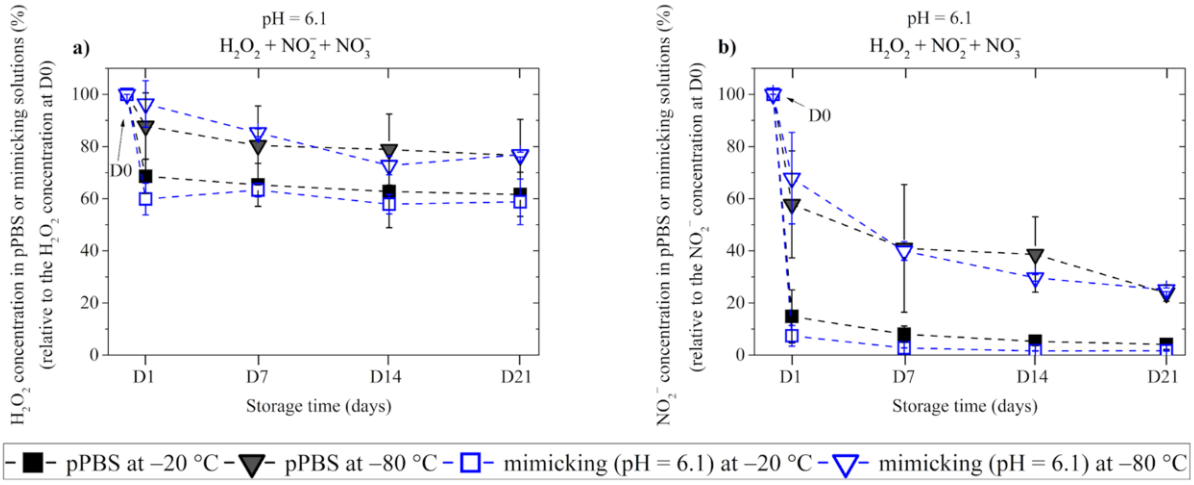

Figure 4.29 Concentration of a) H_2O_2 and b) NO_2^- in pPBS (black symbols; same data as in Figures 4.18 and 4.21) and in mimicking solutions of H_2O_2, NO_2^- and NO_3^- and of pH = 6.1 (blue symbols), as a function of the storage time, when stored at –20 °C (squares) and –80 °C (down triangles). The concentration in % is calculated in relation to the initial concentration of a) H_2O_2 or b) NO_2^- measured on the day of preparation of the solutions (D0). For the mimicking solutions stored at –20 °C and –80 °C, the data are the mean values ± SD of 3 and 2 independent experiments, respectively.

To underline the essential role of H_2O_2 on the oxidation of NO_2^- in pPBS,

due to storage time and/or storage temperature, sodium pyruvate, a known H_2O_2 scavenger, was used. The reaction of sodium pyruvate and of another also known H_2O_2 scavenger, catalase, are reported to be 1:1 with the H_2O_2, meaning that to scavenge for example 5 mM of H_2O_2 we also need 5 mM of sodium pyruvate (or catalase). To verify this in our own experimental conditions, 2.5 mM of these two H_2O_2 scavengers were added, separately, in pPBS just after the plasma treatment and the reduction of the H_2O_2 concentration was monitored as a function of the incubation time. In this case, pPBS was produced with R1, because this is the only plasma reactor that was used for direct plasma treatment. The results show that both scavengers totally quench the H_2O_2 if they are incubated with it for more than 10 minutes (Figure 4.30). Here we must mention that the scavengers were added in the solution after the treatment with the plasma. For sodium pyruvate, it is possible to add it before the treatment and in this case similar results are obtained, as if it was added after treatment. For catalase, it is not possible for it to be present during the plasma treatment as it is degraded by the treatment, making it not able to efficiently scavenge H_2O_2.

Hence, pPBS containing or not 5 mM or 50 mM of sodium pyruvate (added after the plasma treatment) were stored at –20 °C and the concentration of H_2O_2, NO_2^- and NO_3^- was measured after 1, 7, 14 and 21 days of storage (see Figures 4.32 for NO_2^- and NO_3^- and 4.30 for H_2O_2). By adding sodium pyruvate, we were able to scavenge most (5 mM, 90% reduction) or virtually all (50 mM, below the detection limit) of the H_2O_2 in pPBS and, thus, to reduce its concentration by at least 90% (Figure 4.30). As depicted in Figure 4.33, the addition of sodium pyruvate partially prevents the degradation of NO_2^-. More specifically, the quenching of 90% of the H_2O_2 present in pPBS resulting from the addition of 5 mM sodium pyruvate led to a decrease of the degradation of NO_2^- from about 85-95% (without sodium pyruvate) to about 35-50% (with 5 mM sodium pyruvate) upon storage at –20 °C. This NO_2^- degradation that is still observed when pPBS with 5 mM sodium pyruvate is stored at –20 °C is due to the remaining concentration of H_2O_2. Indeed, according to Figure 4.32, even such small concentrations of H_2O_2 can oxidize about 20-30% of the NO_2^-. From Figure 4.32, it can also be concluded that the reaction between H_2O_2 and NO_2^- is not catalytic and, again, that its stoichiometry is 1:1. Collectively, the results with the mimicking solutions at pH = 6.1 (Figure 4.29) and those with the addition of sodium pyruvate (Figure 4.33) suggest that H_2O_2 is by far the main oxidizer of NO_2^- in our experimental conditions of very low pH (about 2-3, see section 4.39), confirming previously published results on the nitrous acid oxidation in aqueous aerosols[179]. Finally, as shown in Figure 4.32, the concentration of NO_3^- increased inversely proportional to the decrease of the concentration of NO_2^-, both with and without sodium pyruvate, highlighting that NO_3^- is a product of the oxidation of NO_2^-.

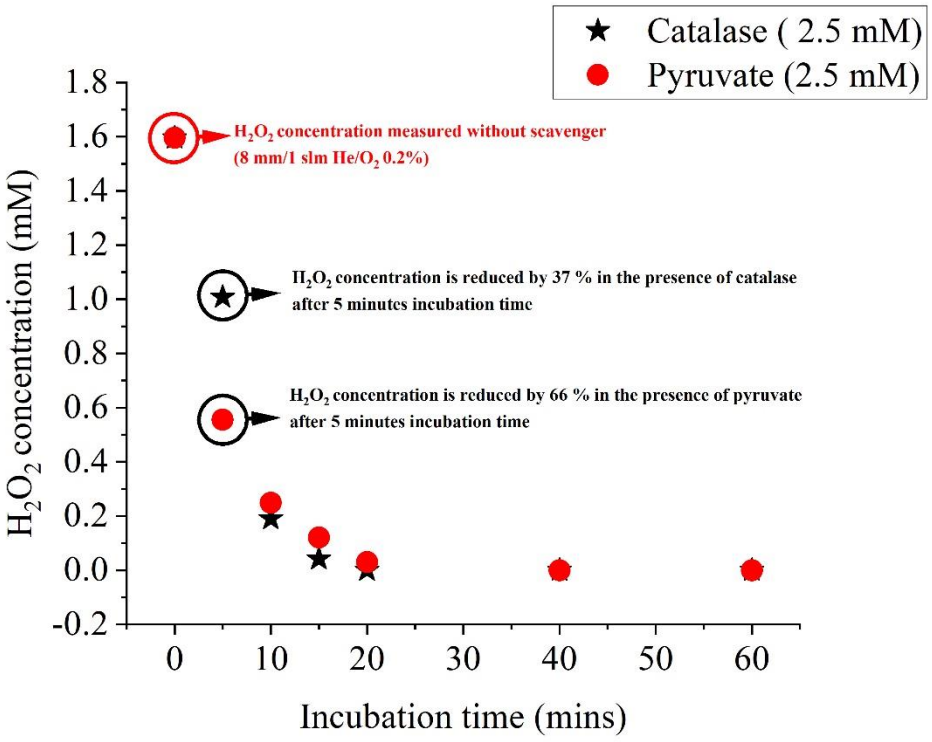

Figure 4.30 H_2O_2 concentration in pPBS as a function of incubation time with catalase (black symbols) or sodium pyruvate (red symbols).

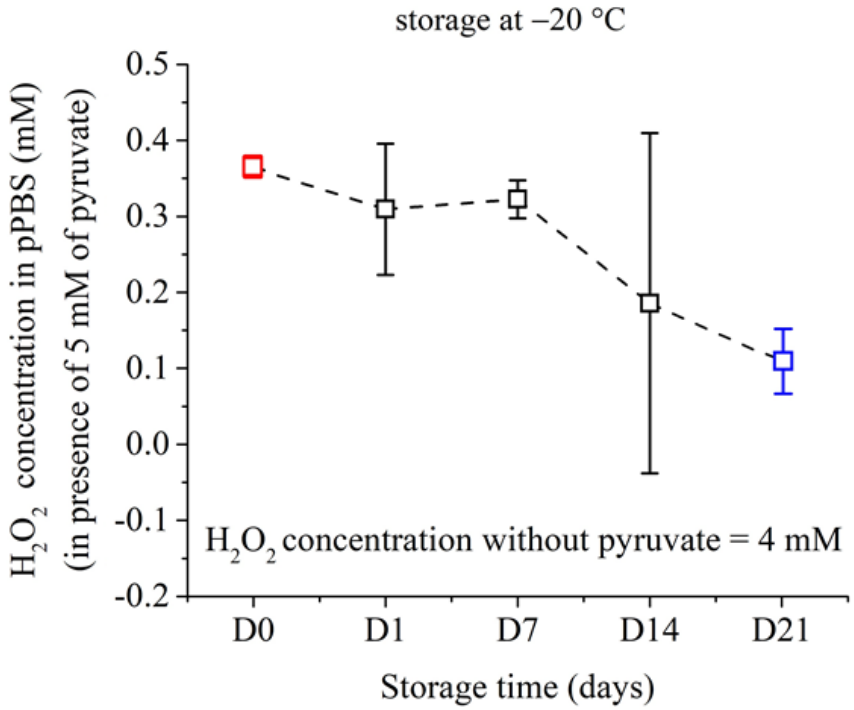

Figure 4.31 Concentration over storage time at –20 °C of H_2O_2 in plasma-treated PBS containing 5 mM of sodium pyruvate. The H_2O_2 initial concentration, before the addition of sodium pyruvate, was 4 mM (>90% reduction of H_2O_2 due to sodium pyruvate). The data are the mean ± SD of 3

independent experiments.

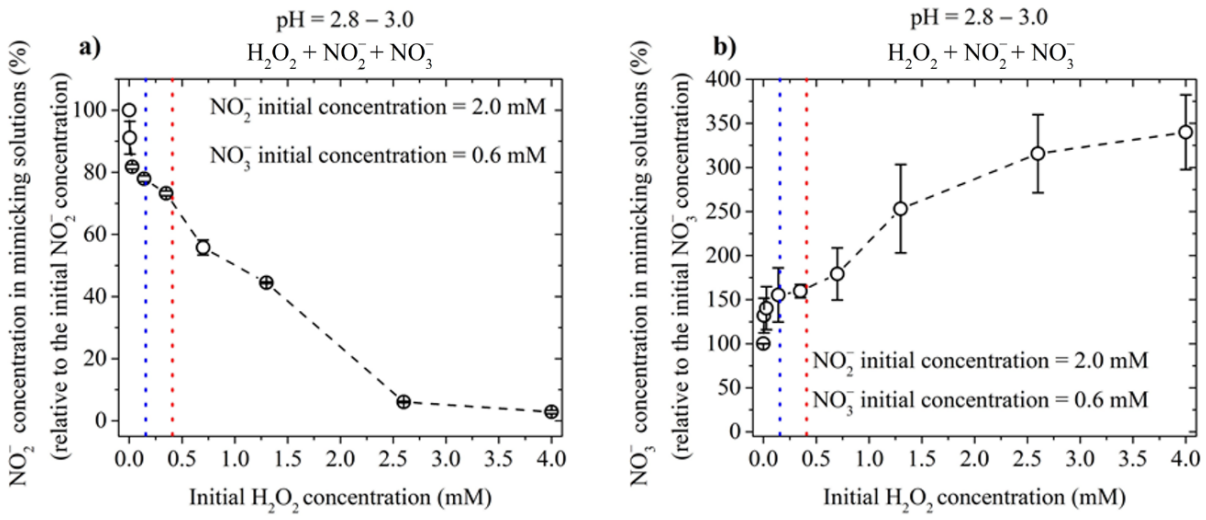

Figure 4.32 Concentration of a) NO_2^- and b) NO_3^- in mimicking solutions of pH = 2.8-3.0 in the presence of different H_2O_2 concentrations. The blue and red vertical lines correspond to the minimum and maximum values of H_2O_2 concentration measured in plasma-treated PBS in the presence of 5 mM pyruvate (Figure 4.32). The data are the mean ± SD of 3-4 independent experiments.

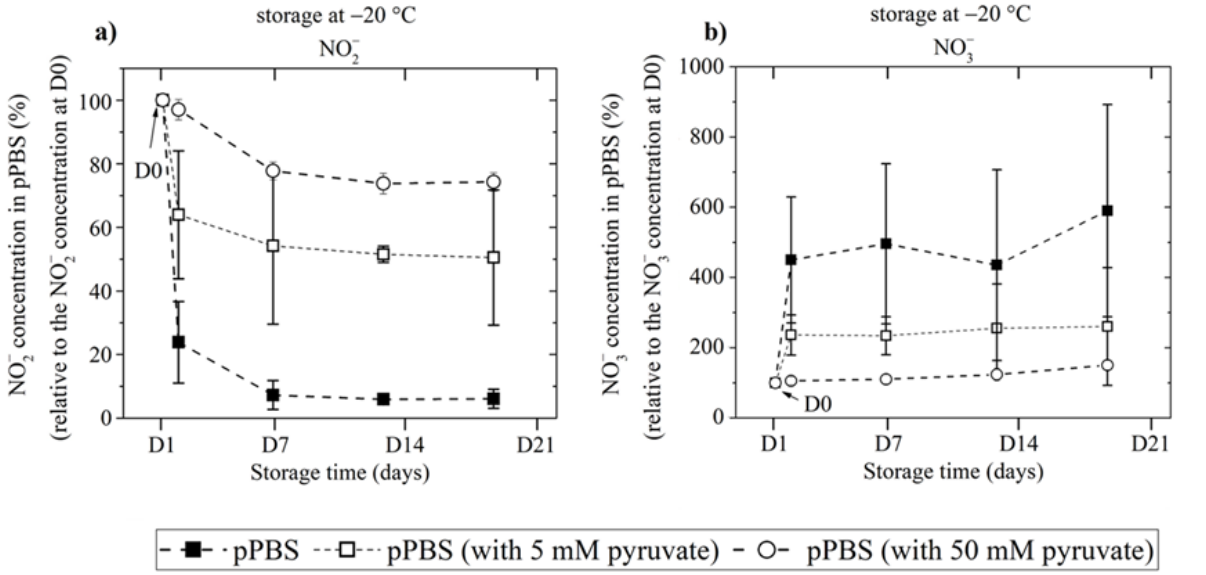

Figure 4.33 Concentration of a) NO_2^- and b) NO_3^- in pPBS containing or not 5 mM or 50 mM of sodium pyruvate, as a function of the storage time, when stored at –20 °C. The concentration in % is calculated in relation to the initial concentrations of NO_2^- and NO_3^-, measured on the day of the plasma treatment (D0), within 2 hours from it. The data are the mean values ± SD of 2, 3 and 8 independent experiments for the pPBS + 50 mM sodium pyruvate, pPBS + 5 mM sodium pyruvate and the pPBS alone, respectively.

4.3.3 Impact of the freezing rate on the degradation of RONS

As stated before, the degradation of the RONS studied here (H_2O_2, NO_2^- and NO_3^-) occurs mainly for storage temperatures requiring the freezing of the pPBS (–20 °C and –80 °C). To better understand the impact of the freezing process, the degradation of the chemical components of the solution as a function of its freezing rate was studied. As so, pPBS were fast frozen in liquid nitrogen and then stored at –20 °C (see open squares in Figure 4.34), or slowly frozen in isopropanol-filled containers when stored at –80 °C (see full circles in Figure 4.35), or normally frozen when just stored at –20 °C or –80 °C. As depicted in Figures 4.34 and 4.35, the freezing rate of the solution has almost no impact on the degradation of H_2O_2 and NO_2^-. It seems that the evolution over storage time of the reactive species concentration at –20 °C and –80 °C depends only on the final storage temperature of the solution.

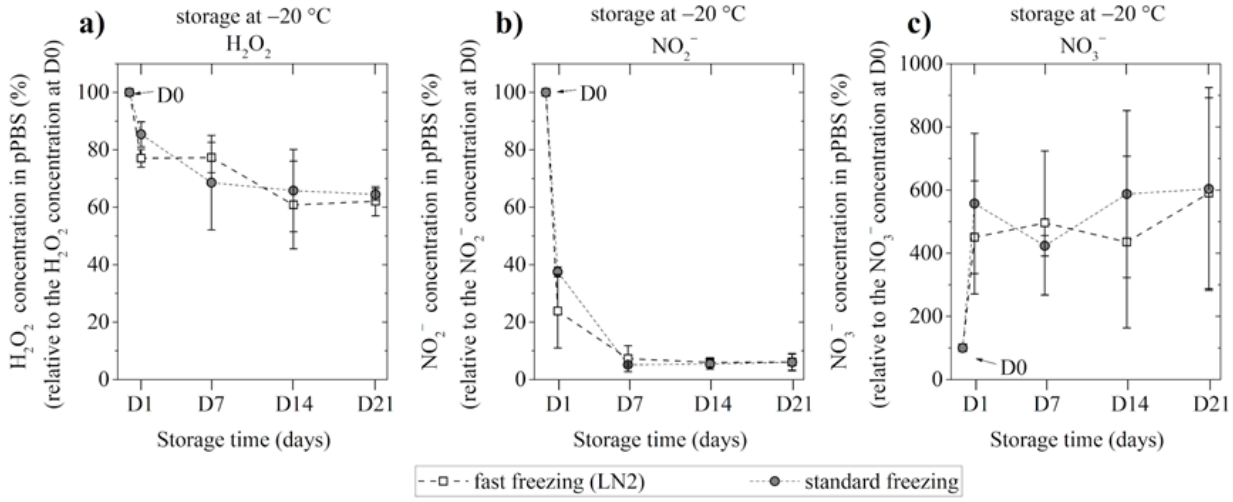

Figure 4.34 Concentration of a) H_2O_2, b) NO_2^- and c) NO_3^- in pPBS as a function of the storage time, when stored at –20 °C, but frozen at two different freezing rates: standard as a consequence of storage at –20 °C or fast by liquid nitrogen (LN2) before immediate storage at –20 °C. The concentration in % is calculated in relation to the initial concentration of a) H_2O_2, b) NO_2^- and c) NO_3^- measured on the day of the plasma treatment (D0), within 2 hours from it. The data are the mean values ± SD of 5 independent experiments.

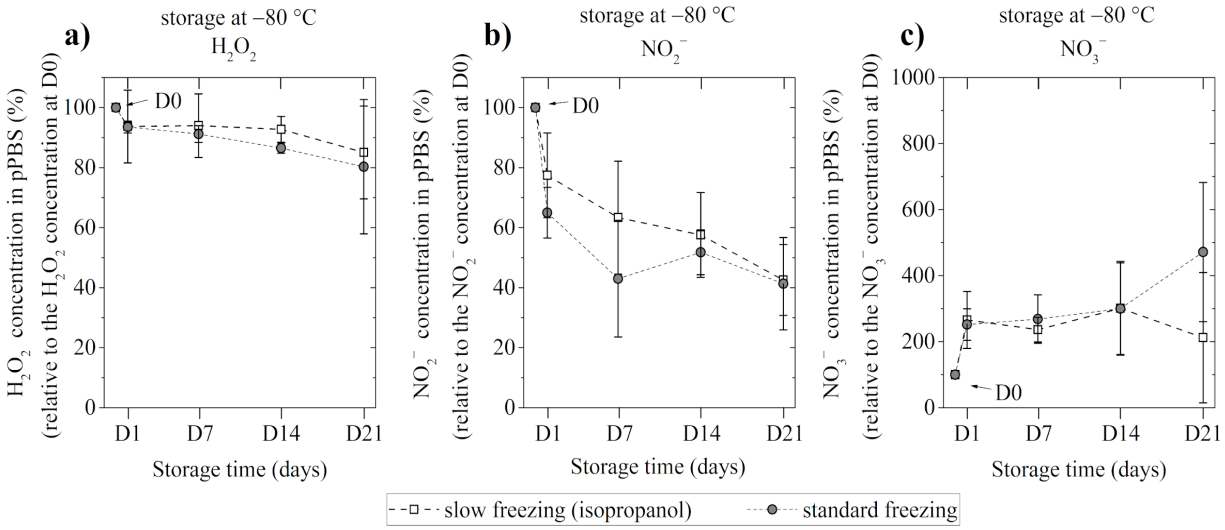

Figure 4.35 Concentration of a) H_2O_2, b) NO_2^- and c) NO_3^- in pPBS as a function of the storage time, when stored at –80 °C, but frozen at two different freezing rates: standard as a consequence of storage at –80 °C or slow by using isopropanol-filled containers when storing at –80 °C. The concentration in % is calculated in relation to the initial concentration of a) H_2O_2, b) NO_2^- and c) NO_3^- measured on the day of the plasma treatment (D0), within 2 hours from it. The data are the mean values ± SD of 5 independent experiments.

4.3.4 Acidification of the solution during its freezing

The pH of pPBS was also monitored as a function of the storage time and temperature. We found that the plasma treatment results in an acidification of the PBS(Ca^+/Mg^+), from an initial pH of 7.1 (± 0.1) to a pH of 6.2 (± 0.5). This pH value stays relatively stable (± 0.3, see Table 1) independently of the storage time or temperature (note that for the cases of a storage at –20 °C and –80 °C, the pH was measured after unfreezing the pPBS). Nevertheless, as previously reported[36], the pH value of the solutions is affected during the freezing process. Thus, the variation of the pH of the pPBS during the freezing towards –20 °C and –80 °C was also monitored. As depicted in Figure 4.38, the pH of the still unfrozen solution changes throughout the first hour of freezing. Using two different pH indicators (bromophenol blue and thymol blue), the final pH value of the frozen pPBS is estimated to be around 3.5-2.5 and 2.5-1.5 for storage at –20 °C and –80 °C, respectively. The pH reaches values lower than 3 in less than 1 hour. Figure 4.39 shows the acidification of untreated PBS with different initial pH values (from 1 to 7), as a result of the freezing of the solutions. Both pH color markers indicate that freezing of untreated PBS (uPBS), when its initial pH is around 6 or less, results in a substantial acidification of the solution. Moreover, the acidification, due to freezing, is rather similar for the uPBS with an initial pH of 6 and for the pPBS (compare Figures 4.35 and 4.36). Finally, the acidification of both uPBS for all the initial pH values considered here and pPBS is similar when stored at –20 °C or –80 °C. It is interesting to note that, after unfreezing the solutions, both pH color

markers indicate that the initial pH is retrieved (Figure 4.36), confirming the pH values measured with the pH meter (Table 1).

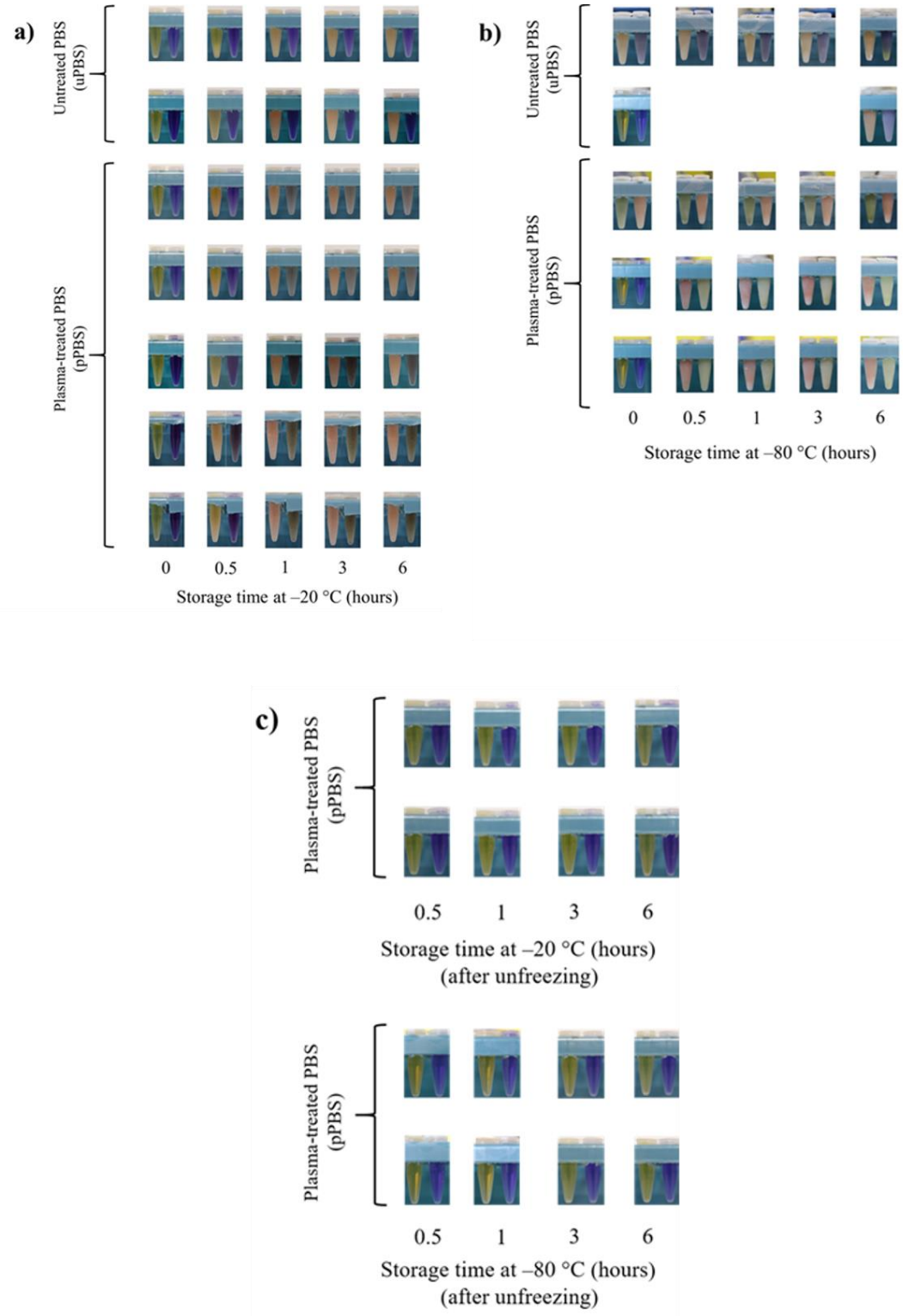

Figure 4.36 Photographs of Eppendorf tubes containing untreated and plasma-treated PBS after storage for 30 minutes, 1, 3 and 6 hours at a) –20 °C and b) –80 °C, and c) after unfreezing. The initial pH of the untreated PBS (before freezing) is 7.1 ± 0.1 while of the plasma-treated PBS is 6.15 ± 0.52 (measured using a SevenEasy™ pH meter S20 fitted with an InLab® 639 Micro electrode).

For every photograph, the Eppendorf tube on the left contains Thymol Blue, while that on right, Bromophenol Blue.

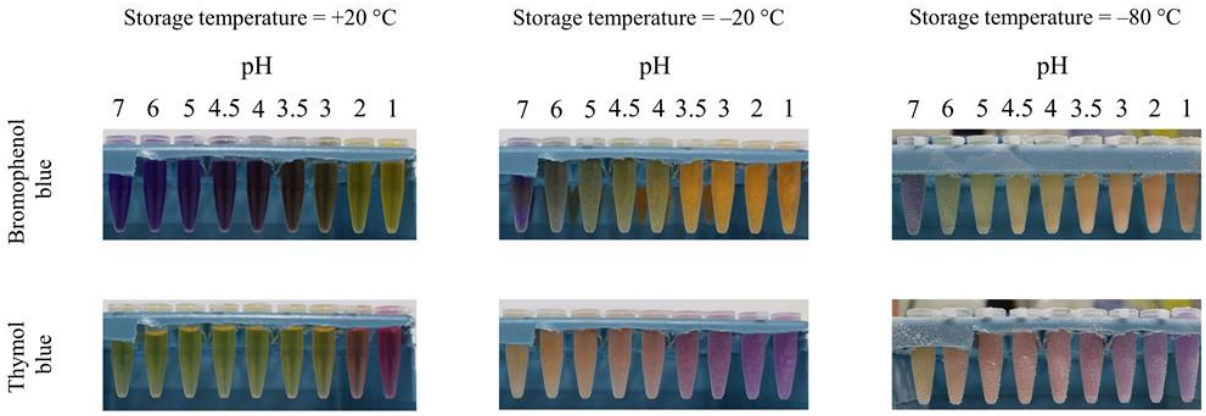

Figure 4.37 Photographs of Eppendorf tubes containing untreated PBS with adjusted pH values (from 1 to 7) and Bromophenol blue (top) or Thymol blue (bottom), after storage for 6 hours at +20 °C, –20 °C and –80 °C. On the top of the photographs is indicated the initial pH value of the solution before freezing (measured using a SevenEasy™ pH meter S20 fitted with an InLab® 639 Micro electrode).

pH at D0 = 6.15 ± 0.52

pH	D1	D7	D14	D21	D75
+20 °C	6.29 ± 0.23	6.27 ± 0.32	6.31 ± 0.25	6.44 ± 0.23	6.23 ± 0.21
+4 °C	6.39 ± 0.16	6.44 ± 0.17	6.44 ± 0.13	6.31 ± 0.14	6.29 ± 0.10
–20 °C	6.44 ± 0.31	6.42 ± 0.11	6.44 ± 0.19	6.39 ± 0.19	6.35 ± 0.17
–80 °C	6.41 ± 0.32	6.19 ± 0.41	6.47 ± 0.21	6.35 ± 0.20	6.33 ± 0.25

Table 1. pH of the pPBS measured on the day of the plasma treatment (D0), within 2 hours from it, and after storage at different temperatures (+20, +4, –20 and –80 °C) for different periods of time (1, 7, 14, 21 and 75 days). The data are the mean values ± SD of 3 (for D1, D7, D14 and D21) or 2 (for D75) independent experiments.

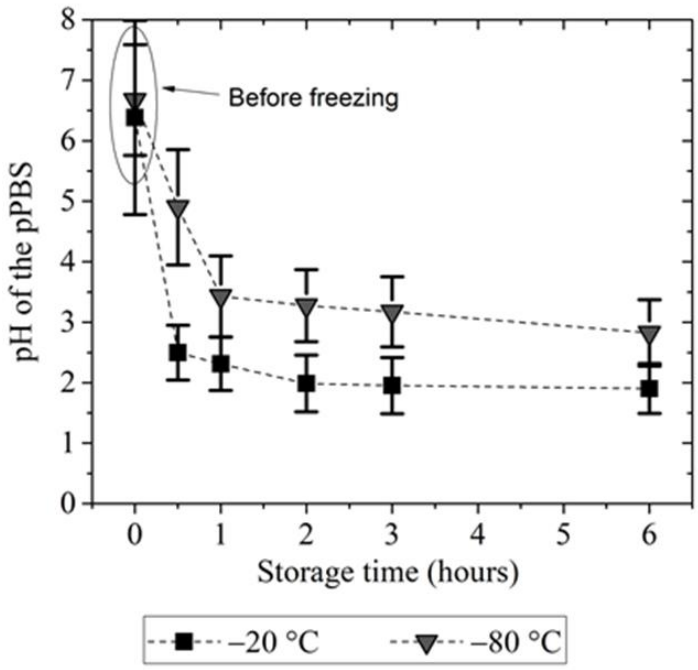

Figure 4.38 pH values of pPBS as a function of the storage time at –20 °C and –80 °C. The pH was evaluated by using bromophenol blue as a pH indicator and the polynomial function relating the sum of R+G–B values and the pH value determined in Figure 2.15. The RGB values used are the mean values of a large area of the photographs of the Eppendorf tubes containing pPBS and bromophenol blue after storage for 30 minutes, 1, 3 and 6 hours at –20 °C and –80 °C (Figure 4.36). The data are the mean values ± SD of 5 and 3 independent experiments for storage at –20 °C and at –80 °C, respectively.

Having established that the freezing of the solution decreases its pH, regardless of if it is uPBS or pPBS, we then studied the effect of this acidification on the concentration of the three RONS considered here. Figure 4.39 shows the concentration of H_2O_2, NO_2^- and NO_3^- 6 hours after the preparation of mimicking solutions of PBS(Ca^+/Mg^+) with different pH values and maintained at room temperature. As it can be seen in Figure 4.39, we should consider a pH value of 5 as a lower threshold for the stability of these reactive species. For pH values lower than 5, the acidic environment of the solution results in the degradation of H_2O_2 and favours the oxidation of NO_2^- and its partial transformation into NO_3^-. These data are coherent with both the calculated pH values of the frozen pPBS solutions determined with the help of the pH indicators (about 2-3) and our measurements of the concentration of the reactive species in pPBS stored at –20 °C or –80 °C. Indeed, similarly to after storage at –20 °C or –80 °C, at a pH of about 2-3 we observe a massive degradation of NO_2^- and a modest degradation of H_2O_2. As a matter of fact, the degradation of NO_2^- presented in Figure 4.39 is even greater than after storing at –20 °C or –80 °C (see Figure 4.23). This might be due to the higher temperature of the solutions considered in Figure 4.39 (room temperature), which could favor the reactions of degradation of H_2O_2 and NO_2^-.

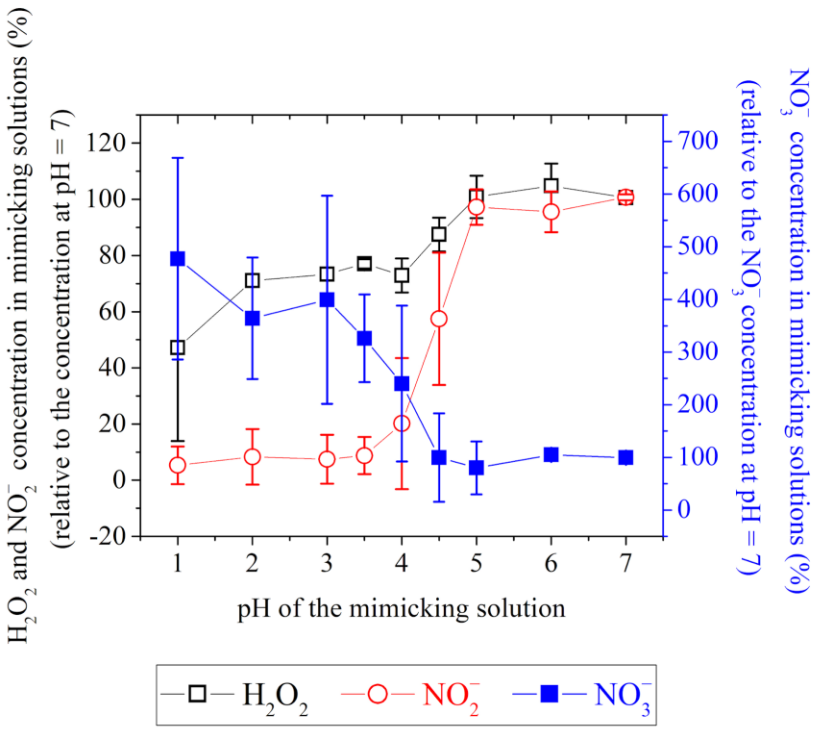

Figure 4.39 Concentration of H_2O_2, NO_2^- and NO_3^- 6 hours after the preparation of mimicking solutions with different pH values, maintained at room temperature. The concentration in % is calculated in relation to the concentration of H_2O_2, NO_2^- or NO_3^- measured in the solution with pH = 7 6 hours after preparation. The data are the mean values ± SD of 6 independent experiments.

4.3.5 Discussion

The application of cold atmospheric-pressure plasmas (CAPPs) in cancer therapy has been lately one of the central research topics in the domain of plasma medicine. Two methods of plasma cancer treatment have mainly been used: direct and indirect plasma treatments[45,122], each one with its own advantages and drawbacks[39]. One of the main advantages of indirect plasma treatment is the possibility of production and storage of extensive quantities of plasma-treated solutions, minimizing the time and equipment constraints that direct plasma treatment requires. However, in order to be considered as efficient anti-cancer agents, these plasma-treated solutions should retain their anti-cancer effects over time. The aim of this study was to bring new insights on the chemical stability of plasma-treated PBS(Ca^+/Mg^+), pPBS, when stored for a considerable period of time at different temperatures, and to determine whether the pPBS can preserve its anti-cancer properties over storage.

At first, the reactive oxygen and nitrogen species (RONS) that are mainly

responsible for the anti-cancer effects of pPBS, i.e. H_2O_2, NO_2^- and NO_3^-[39], were monitored as a function of storage time and temperature. On one hand, we found that these three reactive species are relatively stable both at around +20 °C (room temperature) and +4 °C (fridge) for a significant period of storage (up to 75 days). Contrariwise, when stored at –20 °C and –80 °C, the absolute concentration of both H_2O_2 and NO_2^- decreases significantly. This degradation is much more pronounced for NO_2^-, and at –20 °C for both reactive species. On the other hand, we witnessed an increase of the concentration of NO_3^- when the pPBS was stored at –20 °C or –80 °C. Regardless of the storage conditions, the total concentration of the reactive nitrogen species studied here, i.e. [NO_2^- + NO_3^-], remains nearly constant. Thus, when the concentration of NO_2^- decreases, that of NO_3^- increases almost inversely proportionally. A similar behavior of the concentration of each of these three reactive species was also observed when, instead of pPBS, untreated PBS(Ca^+/Mg^+), uPBS, containing the same concentrations of H_2O_2, NO_2^- and NO_3^- and the same pH as in pPBS (named mimicking solution), was stored at –20 °C and –80 °C (Figure 4.29). Interestingly, when the initial pH of the mimicking solution was not altered (pH of uPBS = 7.1, while pH of pPBS = 6.1), the degradation of H_2O_2 and NO_2^- and the increase of NO_3^- was much less profound (Figure 4.28). Additionally, excessive concentrations of H_2O_2 or NO_2^- in the mimicking solution further degraded the NO_2^- or H_2O_2, respectively. Finally, the addition of 5 mM or 50 mM of sodium pyruvate, a known H_2O_2 scavenger, in pPBS after the plasma treatment partially prevented the degradation of NO_2^- (Figure 4.33). Collectively, these results show that the main driver of the NO_2^- degradation when the pPBS is stored at –20 °C or –80 °C is the H_2O_2 (which is also degraded), while a key role in that degradation is also played by the pH of the solution before its storage.

To investigate the role of the pH on the chemical stability of the pPBS, mimicking solutions were prepared containing the same concentrations of reactive species as in pPBS, but with different pH values, from highly acidic (pH = 1) to neutral (pH = 7). We found that the three reactive species studied here are stable for 6 hours for a pH greater than 5, while in more acidic environments, their concentration either decreases (strongly for NO_2^- and moderately for H_2O_2) or increases (strongly for NO_3^-). Similarly, Lukes *et al.* showed that, under acidic conditions (pH = 3.3), the concentration of H_2O_2 and NO_2^- decreases during the post-treatment period (300 minutes), while the concentration of NO_3^- increases[156,180]. As reported by Anbar in 1954[69], the oxidation of nitrite (NO_2^-) to nitrate (NO_3^-), in the presence of H_2O_2, takes place rapidly when the pH of the solution is highly acidic (see equation 1). Another chemical reaction that could degrade NO_2^- is its oxidation by dissolved oxygen that takes place also in acidic environments[181]. Nevertheless, we can consider that dissolved oxygen does not play an important role in our experimental conditions as uPBS containing only NO_2^- (without H_2O_2) did not exhibit any degradation upon storage at –20 °C or –

80 °C, and uPBS containing both species and an adequate initial pH (6.1) simulate well the chemical evolution of pPBS. Interestingly, the pH of our pPBS, is much higher than that required for the NO_2^- oxidation to take place. On top of that, as reported in other works, the pH appears also in our case to remain stable regardless of the storage period or temperature of the solution (Table 1)[182]. Given that the degradation of H_2O_2 and NO_2^- is only observed, in our case, at the storage temperatures of –20 °C or –80 °C, one can wonder what are the mechanisms that are triggered by the freezing of the solution.

As it was previously reported, freezing of phosphate buffer solutions can result in the gradual decrease of the pH of the part of the solution that remains in the liquid state during the freezing process[183–185]. These pH variations in partially frozen solutions are dependent upon the eutectic temperatures and the concentration and solubility of its various components. Thus, as water is removed from the liquid phase (during freezing), the concentration of the various salts increases in the remaining solution. In order to verify these observations in our own experimental conditions, two pH indicators (bromophenol blue and thymol blue) were added to uPBS of different pH values. Subsequently, these solutions (uPBS + pH indicators) were stored at –20 °C or –80 °C. Photographs of the Eppendorf tubes containing these solutions unveiled the gradual acidification of the uPBS when stored at both –20 °C and –80 °C (Figure 4.36). The final pH value of the frozen solutions was estimated to be around 2-3 for solutions of initial pH of 6 or less. When mimicking solutions of initial pH = 7 were frozen, their acidification was less significant (Figures 4.26 and 4.27). Similar results were obtained when pPBS containing the pH indicators were frozen (Figures 4.35 and 4.36). Additionally, it is interesting to notice that no significant difference was observed regarding the solution acidification between storage at –20 °C and –80 °C, even if the acidification is more pronounced at –80 °C. Collectively, our results confirm that, when frozen, even uPBS becomes highly acidic. This acidification, that is related only to uPBS composition and to the storage temperature and is likely not affected by the enriched chemistry of pPBS due to plasma treatment, favours, as previously discussed, the subsequent oxidation of NO_2^- by H_2O_2 into NO_3^- (see equation 1).

$$H_2O_2 + NO_2^- + H^+ \rightarrow NO_3^- + H^+ + H_2O \qquad \text{(Eq. 1)}$$

Having established that the storage of the solutions (uPBS or pPBS) at –20 °C or –80 °C leads to the degradation of H_2O_2 and NO_2^- due to their acidification during freezing, we tried to explain the difference on this degradation observed between these two storage temperatures. Indeed, our results showed that, for all the cases studied here (both pPBS and mimicking solutions), the degradation of the solution is less significant when the freezing temperature is lower (–80 °C). It

was previously reported that an important factor of the pPBS freezing that affects the concentration of the reactive species studied here (H_2O_2, NO_2^- and NO_3^-) is the freezing rate of the solution[181,186]. However, in our case, that degradation is not affected by the freezing rate (Figures 4.33 and 4.34). Recently, though, Alpana *et al.* reported that the eutectic temperature of Dulbecco's PBS is −23.7 ± 0.3 °C (similar values were also found by Han *et al.*[187]). This means that when stored at –20 °C, the storage temperature at which the most considerable degradation of H_2O_2 and NO_2^- is observed, the temperature of the solutions is above the eutectic point of the saline buffer solutions used in this work. Contrariwise, when the solutions are stored at –80 °C, their temperature is far below this point. Taking this into consideration and that the freezing of the solution results in an acidic pH (either at –20 °C or –80 °C), we propose that the oxidation of NO_2^- by H_2O_2, and, thus, their mutual degradation, is favored at –20 °C compared to –80 °C, because these reactive species co-exist for a longer period of time in an acidic pH in a solution partially frozen when stored at –20 °C than at –80 °C. Besides that, it has been determined that the rate constant of the reaction described in equation 2 decreases with decreasing temperature at low pH (around 2)[188]. Equation 2 also highlights that, as discussed before, the conversion of NO_2^- into NO_3^- by oxidation by H_2O_2 increases with the increase of the concentration of the reactants and the decrease of the pH. It is worth noting that both occur during the freezing of the pPBS.

$$-\frac{d[H_2O_2]}{dt} = -\frac{d[NO_2^-]}{dt} = +\frac{d[NO_3^-]}{dt} = k[H^+][H_2O_2][NO_2^-] \qquad \text{(Eq. 2)}$$

Conclusions

In this chapter, an in-depth analysis of the chemical properties of plasma-treated liquids, produced by three different plasma reactor configurations was attempted. As a first step, the measurement of the absolute concentrations of three long-lived reactive oxygen and nitrogen species, i.e. H_2O_2, NO_2^- and NO_3^-, for various plasma working conditions was conducted. In parallel, the conductivity, the liquid temperature and its pH were monitored. As a second step, short- and intermediate-lived reactive species such as $O_2(a^1\Delta_g)$, O_3, $ONOO^-$ and •OH were detected and measured in the plasma-treated liquid again as a function of different experimental conditions. Finally, as a third step, the possibility of conserving the long-lived reactive species for a long storage time was investigated. As a result, the three different plasma reactors were significantly characterized in terms of reactive oxygen and nitrogen species that can be found in the pPBS.

In general, this chapter is of great importance for understanding the plasma-treated liquid chemistry. All the reactive species studied here have been

previously reported to play a role on the cytotoxic capacity of pPBS. Thus, the work of this chapter was essential and a prerequisite for the investigation of the mechanisms leading to cancer cells death both with direct and indirect plasma treatments, which can be found in Chapter 5.

Chapter 5

Application of plasmas in cancer therapy

The use of cold plasmas in oncology is limited by the accessibility of the tumor. As such, we must consider two types of plasma application modalities that are currently used to treat cancer cells: the direct and indirect treatments. Direct treatment involves direct exposure of the biological target to plasma in the presence of a liquid (e.g., cancer cells *in vitro*) or not (e.g., superficial tumors *in vivo*), and can be divided into 2 different phases, phase I and phase II. As phase I we consider the plasma treatment itself; more specifically, the time over which the plasma is on and in contact with the liquid. As phase II we consider the period of time from the moment that the plasma is turned off and during which the target is incubated with the plasma-treated liquid. Indirect treatment, which consists only of phase II, involves the treatment of a liquid (e.g., saline solution like PBS, or cell culture medium), and subsequent application of these plasma-activated solutions onto the biological target, *in vitro* or *in vivo*. *In vivo*, the treatment of superficial tumors such as skin tumors and head and neck tumors can be achieved by direct treatment. However, the big challenge for the plasma oncology community is the treatment of non-superficial cancers. One approach is surgery. Nevertheless, surgery has the disadvantage of causing post-operation discomfort to the patient. Another approach is endoscopy, which has a much lower risk of bleeding and infection than open surgery and causes less discomfort, in the long-term, to the patient. Finally, the delivery of "plasma species" to deep tissues could be achieved via plasma-activated solutions.

The type of plasma application has several implications in what regards the nature of the physicochemical parameters that interact with the biological target. In the case of direct treatment, physical factors (ultraviolet, heat, and electromagnetic field) and chemical factors (long- and short-lived ROS/RNS) are present during the treatment, while only chemical factors, and among them essentially long-lived species such as H_2O_2 and NO_2^-, should be considered in indirect treatment. While several groups have shown that, *in vitro*, both treatments were equivalent in inducing cancer cell death, in altering cell surface adhesion molecules or in inactivating enzymatic functions[40,47–49], others have reported that direct treatment is more effective than indirect treatment at killing tumor cells[50,52,189]. As so, there is still a debate regarding the selectivity of cold plasma at inducing cell death preferentially in tumor cells over healthy cells. These discrepancies between reports can be attributed to the fact that the anti-cancer capacity of a plasma-activated solution depends on several factors such as the size of the wells in which cells are seeded, the volume of the treated liquid, the

liquid composition (e.g., PBS versus culture medium), the gap between the plasma source and the liquid, the gas flow rate, the gas admixture, and the plasma device itself[42,61–63].

This chapter is divided in three parts. The chapter is organized that way for two main reasons. Firstly, even if all the experiments, both *in vivo* and *in vitro* served the general purpose of the investigation of the mechanisms leading to cell death during the plasma treatment, each of them was part of a different research project and, thus, the specific purpose of each study was different. Secondly, the plasma system used for the biological targets' treatment was not the same for every work as well as the biological targets themselves (for example different cellular models were used).

In the **first** part, we thoroughly studied *in vitro* these two treatment modalities (direct and indirect plasma treatment) to bring new insights into the potential use of plasmas for cancer treatment. We used two models of head and neck cancer cells, CAL27 and FaDu, and three models of normal cells (1Br3, NHK, and RPE-hTERT). PBS was used as the liquid of interest, and the concentration of plasma-induced H_2O_2, NO_2^- and NO_3^-, as well as pH change, were measured (presented in Chapter 4, Figures 4.3 and 4.6). Cells were exposed to direct plasma treatment, indirect plasma treatment or reconstituted buffer (PBS adjusted with plasma-induced concentrations of H_2O_2, NO_2^-, NO_3^- and pH). Metabolic cell activity, cell viability, lipid peroxidation, intracellular ROS production, caspase 3/7 induction and cellular membrane permeabilization were quantified. If we showed that direct plasma treatment is slightly more efficient than indirect plasma treatment and reconstituted buffer at inducing lipid peroxidation, intracellular increase of ROS and cancer cell death in tumor cells, our data also revealed that reconstituted buffer is equivalent to indirect plasma treatment. In contrast, normal cells are quite insensitive to these two last treatment modalities. However, they are extremely sensitive to direct plasma treatment. Indeed, we found that phase I, i.e. plasma treatment, and phase II, i.e. incubation time, act in synergy to trigger cell death in normal cells and are additive concerning tumor cell death. Our data also highlight the presence in plasma-treated PBS of yet unidentified short-lived reactive species that contribute to cell death. In this study, we provide strong evidence that, *in vitro*, the concentration of RONS (H_2O_2, NO_2^- and NO_3^-) in combination with the acidic pH are the main drivers of plasma-induced PBS toxicity in tumor cells but not in normal cells, which makes ad-hoc reconstituted solutions powerful anti-tumor treatments. In marked contrast, direct plasma treatment is deleterious for normal cells *in vitro* and should be avoided. Based on our results, we discuss the limitations to the use of pPBS for cancer treatments. For this study, we used the atmospheric pressure single plasma jet (reactor 1).

In the second part, we investigated the impact of the conservation over long periods of time (several weeks) of pPBS on its anti-cancer efficacy on human cancer cells *in vitro*, by quantifying the viability and the membrane permeabilization of the cells following treatment with those solutions. The cytotoxic efficiency of the pPBS was conserved when stored at conditions that did not degrade the three aforementioned long-lived reactive species, i.e., at 4 ^{o}C. Contrariwise, when the pPBS was stored at -20^{o}C, it was less efficient at killing the cancer cells even after the first day of storage. Indeed, understanding the physicochemical properties and the anti-tumor activity of pPBS before and after storage is crucial for their practical application as anti-cancer drugs. For this study, we used the atmospheric pressure multi-plasma jet (reactor 2), based on the plasma GUN that was previously developed at GREMI[190]. This reactor was designed and implemented at the GREMI laboratory in Orleans, France, and it was optimized in the frame of this work. On top of that, in this second part, the study of the efficiency of all three plasma reactors, i.e. cold atmospheric pressure single- and multi-jet (reactors 1 and 2) and MCSD (reactor 3), at oxidizing different types of lipids is also presented. For this study, we treated the lipids both directly and indirectly. Lipid peroxidation has been highlighted due to its involvement in the pathogenesis of age-related diseases and, on the top of that, as presented in the first and third part of this chapter, because it might play a key role on the anti-cancer capacity of plasma treatment due to the oxidation of the cellular membrane. The monitoring by mass spectrometry of the lipid oxidation products in glycerol-phosphocholines (GPCs) formed under oxidative stress conditions, such as pulsed electric fields in electro-permeabilization, may provide signaling markers. In this work, three different types of lipids were treated: a) 1,2-Dioleoyl-sn-glycero-3-phosphocholine (DOPC), b) 1,2-dilauroyl-sn-glycero-3-phosphocholine (DLPC) and c) 1,2-Didocosahexaenoyl-sn-glycero-3-phosphocholine. Besides the direct and indirect plasma treatments, we also treated the lipids with ad-hoc concentrations of hydrogen peroxide. For the experimental conditions where we have established an increased production of reactive oxygen species, especially ozone and singlet delta oxygen, we observed a high oxidation rate of the lipids, while for the working conditions for which the production of these reactive species is lower the oxidation of the lipids is comparable to the error bars and, thus, our results are not conclusive.

In the third part, we investigated the potential capabilities of the combined application of indirect non-thermal plasma treatment (plasma-activated solutions) and microsecond Pulsed Electric Fields (μsPEFs) to outperform *in vitro* cell electro-permeabilization, the basis of electrochemotherapy (ECT). Thus, PBS was plasma-treated (pPBS) and used afterwards to explore the effects of its combination with μsPEFs. Analysis of two different cell lines (DC-3F Chinese hamster lung fibroblasts and malignant B16-F10 murine melanoma cells), by flow

cytometry, revealed that this combination resulted in significant increases of the level of cell membrane electro-permeabilization, even at very low electric field amplitude. The B16-F10 cells were more sensitive to the combined treatment than DC-3F cells. Importantly, the percentage of permeabilized cells reached values like those of cells exposed to classical electroporation field amplitude (1100 V/cm) when the cells were treated with pPBS before and after being exposed only to very low PEF amplitude (600 V/cm). Although the level of permeabilization of the cells that are treated by the pPBS and the PEFs at 600 V/cm is lower than the level reached after the exposure to μsPEFs alone at 1100 V/cm, the combined treatment opens the possibility to reduce the amplitude of the EPs used in ECT, potentially allowing for a novel ECT with reduced side-effects. Finally, we conducted *in vivo* studies on inbred female immunocompetent C57Bl/6J mice. Here, we treated the mice with plasma-treated liquid by using treatment times of 20 minutes and 1 hour. The treatment of the mice with the liquid was followed by an ECT treatment or by a treatment with bleomycin, an anti-cancer drug. The purpose of this study was the achievement of the same level of permeabilization of tumor cells (and therefore the same efficacy of ECT) with less intense and therefore more "comfortable" electrical pulses. We showed that indeed, the most efficient tool against this type of cancer, *in vivo*, is the combination of ECT with pPBS (20 minutes plasma treated PBS) treatment.

All these works were the result of different fruitful collaborations. Thus, it is necessary to state below my contribution to each one of these works:

For the first part: This work was done in close collaboration with Dr. Pierre-Marie Girard from the Institute Curie in France. My contribution to this work includes the characterization of the plasma-treated liquids, the treatments with the plasma (both directly and indirectly) of the cancer and normal cells and the participation on the analysis of the effect of the plasma on the cells in what concerns the cells metabolic activity and viability. More advanced diagnostics such us those regarding the lipid peroxidation, intracellular ROS production, caspase 3/7 induction were conducted by Dr. Pierre-Marie Girard, with my assistance.

For the second and third parts: This work was done in close collaboration with Dr. Thai-Hoa Chung, Dr. Lluis M. Mir and Dr. Alain Deroussent from the Institute Gustave Roussy (IGR) in France and with Dr. Augusto Stancampiano, Dr. Eric Robert, and Dr. Jean-Michel Pouvesle from the laboratory GREMI. My contribution to these works was the characterization of the reactor, which led to its amelioration, the characterization of the plasma-treated liquids, the investigation of their conservation, and the production and chemical characterization of the plasma-treated liquids used for the treatment of the cancer cells and/or the mice. On top of that, I conducted the treatment of all the

lipids both directly and indirectly by the plasma. All the biological analysis both for the *in vivo* and the *in vitro* experiments were conducted in IGR by Dr. Thai-Hoa Chung and Dr. Lluis M. Mir, while the design and implementation of the experimental setup took place in GREMI by Dr. Augusto Stancampiano, Dr. Eric Robert and Dr. Jean-Michel Pouvesle. The analysis of the effect of the plasma treatment on the lipids was conducted by Dr. Alain Deroussent.

Table of Contents

First part: Role of Short- and Long-Lived Reactive Species on the Selectivity and Anti-Cancer Action of Plasma Treatment *In Vitro*

As mentioned before, the treatment of cancer cells by plasma can be achieved in two different ways: with direct and indirect treatments. In Figure 5.1, the treatment modalities used in this study are depicted. We should underline that this wording will remain the same across the whole chapter. As we can see, direct plasma treatment is divided in two parts: Immediate effects and Early effects. The immediate effects correspond to the effects of the plasma and the plasma treated liquid on the cells during the plasma treatment. The early effects correspond to the 1-hour incubation of the cells with the pPBS, but only when this follows the Immediate effects. In fact, when the pPBS is added for 1 hour onto cells that were not present during the plasma treatment, it is called indirect plasma treatment. When mimicking solutions of H_2O_2, NO_2^-, NO_3^- and acidic pH are added for 1 hour onto cells that were not present during the plasma treatment, it is called Reconstituted Buffer.

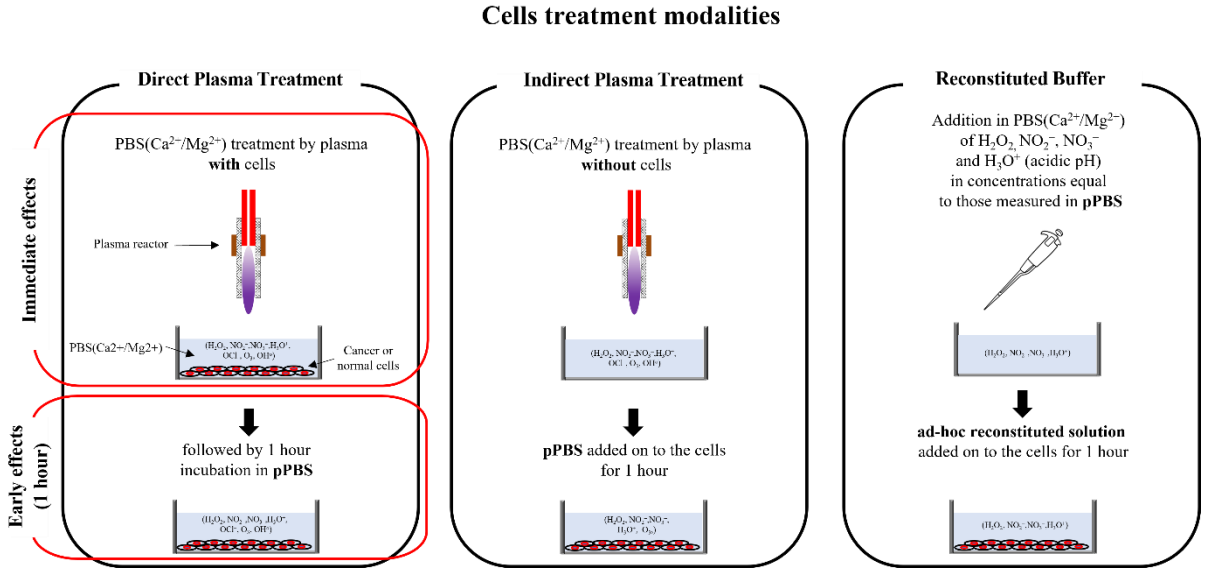

Figure 5.1 Schematic illustration of the different modalities used for cell treatment.

5.1 Influence of Plasma Treatment Time, Gas Flow Rate, Gas Composition and Treatment Distance on Cancer Cell Death after Indirect Plasma Treatment

The plasma treatment time is a key parameter that determines the extent of the cellular response to plasma treatment. To determine the difference between direct and indirect treatments, the reduction of cancer cell's viability of two different cancer cell lines, CAL27 and FaDu, was studied as a function of the plasma treatment time at a gas flow rate of 1 slm and at a treatment distance of

8 mm. Each plasma treatment time was followed by an incubation time of 1 h.

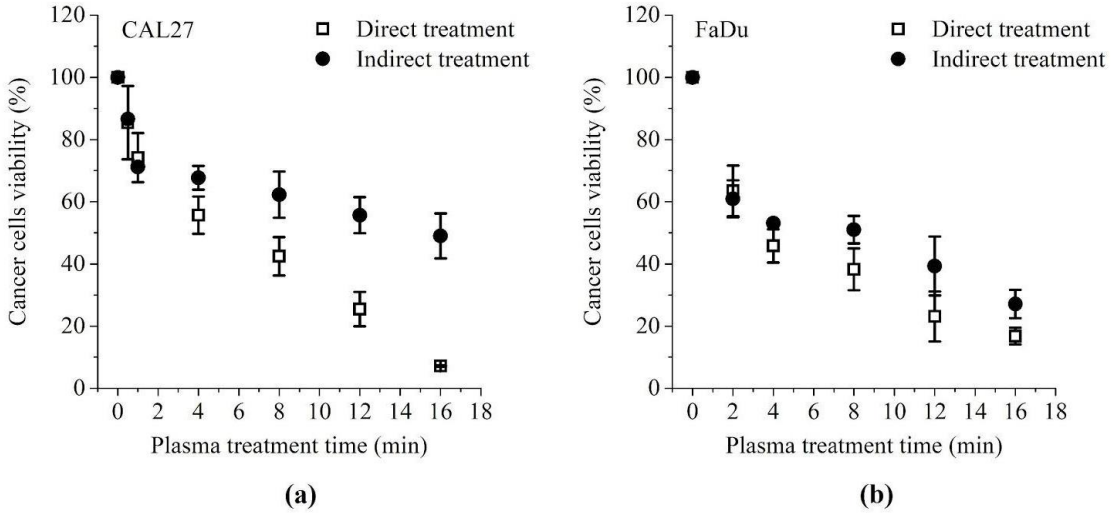

Figure 5.2 Comparison of direct and indirect treatments for (a) CAL27 and (b) FaDu as a function of the plasma treatment time. Cell viability was monitored 24 h post treatment. The results were obtained for a gas flow rate of 1 slm, a gas composition of 99.8% He/ 0.2% O_2 and a treatment distance of 8 mm. The data are the mean +- SD of 6 independent experiments.

Our results showed a plasma treatment time-dependent decrease of the cell viability for both cell lines after direct and indirect treatments (Figure 5.2). However, for CAL27, the direct treatment was more effective than the indirect treatment, while, for FaDu, the difference between the two types of treatment was less significant. We also observed that the reduction of the cell's viability follows two different phases. For short plasma treatments, the cells viability dropped drastically by 30% for CAL27 (1 minute plasma treatment) and by 40% for FaDu (2 minutes plasma treatment), irrespective of the type of treatment (direct or indirect). For longer plasma treatments, the loss of viability continues to decrease almost linearly but the slope of the curve is softer. Indeed, for indirect treatment, the cell viability for CAL27 diminished only by 20% points between 1 and 16 min of plasma treatment (from 70% to 50% of viability), and for FaDu by 30% points between 2 and 16 min of plasma treatment (from 60% to 30% of viability). For direct treatment, the loss of viability is around 60% points for CAL27 and 40% points for FaDu for the same time frame. Taken together, these results suggest that for plasma treatment times between 1 and 2 min, indirect treatment is as efficient as direct treatment to induce loss of cell viability, at least for these two cancer cell lines, while, for longer plasma treatment times, direct treatment is more effective, especially for CAL27. Given that the main purpose of this work is to study the mechanisms leading to cell death upon plasma treatment, a plasma treatment time of 12 minutes was chosen and applied to most of the treatments in the first part of this chapter. The main reason was that we wanted to study the contribution of the different components of the plasma and the pPBS to the

reduction of the cell viability. To do so, and to be able to compare the efficiency of the plasma when different working conditions were used, we wanted to have a reduction of the cell's viability in the range 20-70%.

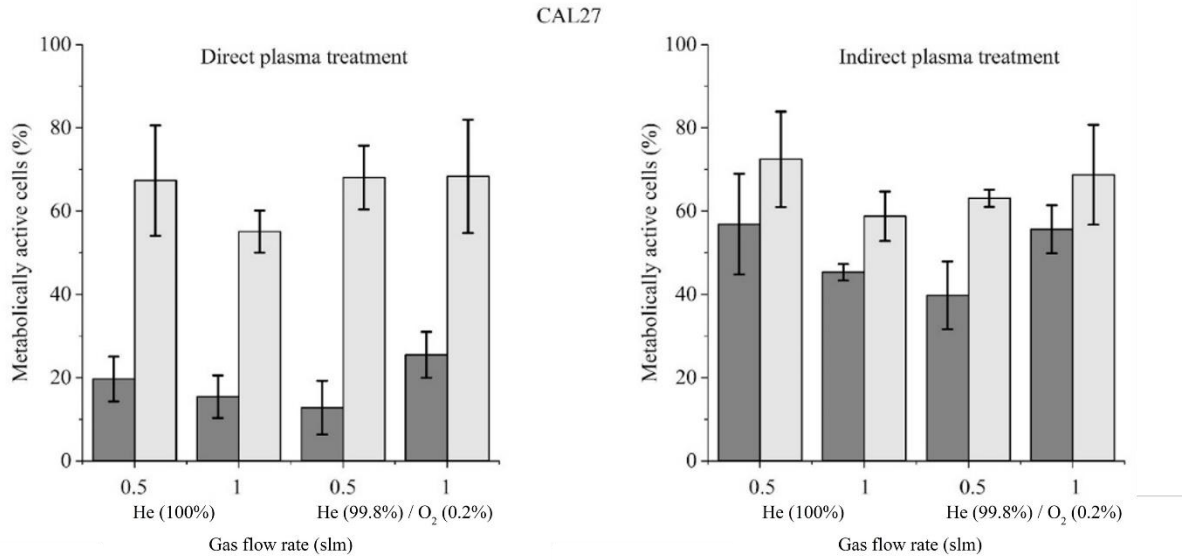

Figure 5.3. Comparison of direct and indirect treatments for CAL27 as a function of the gas flow rate, the gas composition, and the treatment distance. The columns that are in light grey represent a treatment distance of 20 mm, while the columns that are in dark grey represent a treatment distance of 8 mm. Cell viability was monitored 24 h post treatment. The data are the mean +- SD of 3 independent experiments.

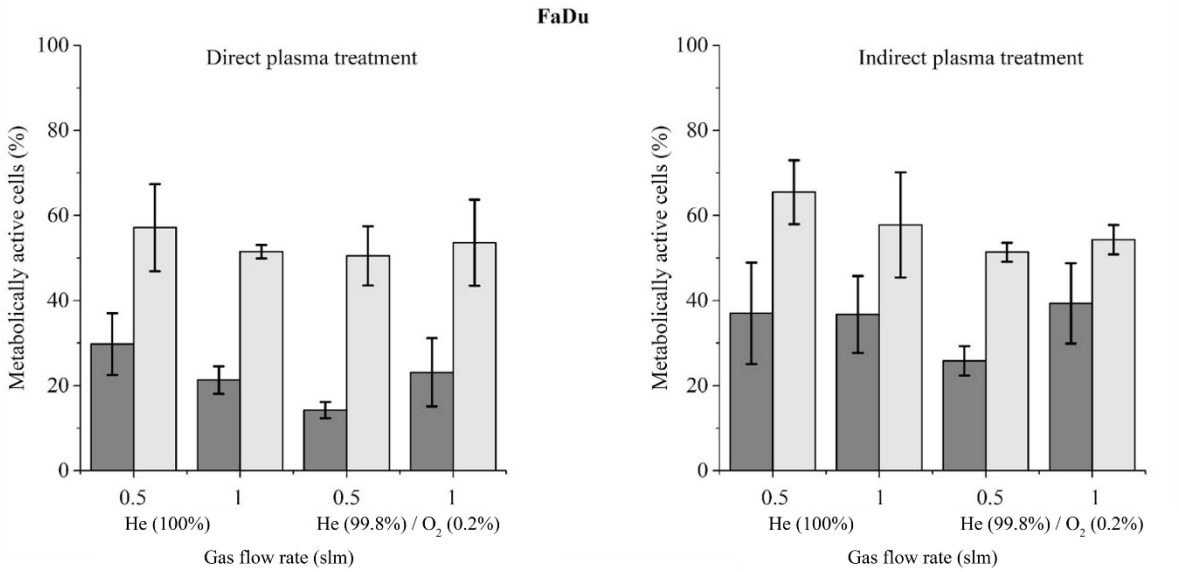

Figure 5.4 Comparison of direct and indirect treatments for FaDu as a function of the gas flow rate, the gas composition, and the treatment distance. Cell viability was monitored 24 h post treatment. The columns that are in light grey represent a treatment distance of 20 mm, while the columns that are in dark grey represent a treatment distance of 8 mm. The data are the mean +- SD of 3 independent experiments.

Having defined the plasma treatment time (12 minutes), we wanted to investigate the effect of different working parameters on the cancer cells' viability in an attempt to correlate our results on the cancer cells with the chemical analysis of the pPBS that was presented in chapter 4. In figures 5.3 and 5.4, we present our results on the reduction of the cancer cells viability upon direct or indirect plasma treatments for 2 different gas flow rates (0.5 and 1 slm), 2 gas compositions (100% He and 99.8% He/ 0.2% O_2) and 2 different treatment distances (8 and 20 mm). Firstly, the reduction of the cancer cells viability is always higher when the treatment distance is of 8 mm, compared to 20 mm. This is more intense for direct plasma treatment, but it is also true for indirect plasma treatment. This observation agrees with our previous results on the production of RONS when the treatment distances of 8 and 20 mm were compared (Figure 4.3). Secondly, we can see that the cells (especially CAL27) are more sensitive towards direct plasma treatment for the treatment distance of 8 mm, while, for the treatment distance of 20 mm, direct and indirect plasma treatments have almost the same effect. From this result, we can conclude that, at least for CAL27, other physical facftors such as the electric field and the ultraviolet radiation or chemical factors such as short-lived reactive species do also contribute to the reduction of the cells viability during the plasma treatment time (12 minutes), besides the long-lived reactive species. On the other hand, the similarity of direct and indirect treatments on FaDu cells unveil that, for this particular cell line, it is mainly the long-lived reactive species that reduce their viability. Finally, for both cancer cell lines and for both direct and indirect plasma treatments, we could notice that the condition of 0.5 slm of He (99.8%) + O_2 (0.2%) is slightly more effective. Interestingly, this is the working condition where the maximum concentration of H_2O_2 + NO_2^- was measured (Figure 4.3), as, even if the concentration of H_2O_2 does not significantly change with the gas flow rate, the concentration of NO_2^- is almost the double at 0.5 slm. This fact points to the same direction as previous reports[39,122], that these RONS are the main anti-cancer drivers of the plasma-activated solutions. Nevertheless, most of our *in vitro* experiments with this reactor on the normal and cancer cells were conducted with a gas flow rate of 1 slm. With this gas flow rate, even if it is less efficient at killing the cells, the discharge is visually more stable as it is not perturbed by external factors such as our movement in the room. This was the reason why 1 slm was used for most of our experiments.

5.2 Role of RONS on Cancer Cell Death

Since H_2O_2 and NO_2^- act in synergy to induce cancer cell death[43,122], we investigated their inter-dependence in promoting cancer cell death. To do that, FaDu and CAL27 cells were exposed to two concentrations of H_2O_2 in PBS (0.8 mM and 1.6 mM), while the concentration of NO_2^- was gradually increased up to 1.6

mM. At first, we observed that these two cell lines demonstrate a different sensitivity to H_2O_2 in standalone, with CAL27 being more resistant than FaDu (Figure 5.5). Similar results (FaDu more sensitive than CAL27) were published by Ianelli *et al.* when these two different cancer cell lines were treated with anti-cancer drugs, and more specifically with VPA, CDDP, and CX [191]. To our knowledge there is no comparative study of these two cancer cell lines treated by plasma or plasma-treated liquid. While NO_2^-, NO_3^- or a combination of NO_2^-/ NO_3^- have virtually no toxic effect on the cell lines in the range of concentrations used in this study (cf. insets in Figure 5.5), increasing the concentration of NO_2^- in the presence of H_2O_2 led to a concentration-dependent decrease of cell viability (Figure 5.5). The synergistic effect of these two reactive species on the viability of the cancer cells was calculated using Combenefit software (https://www.cruk.cam.ac.uk/research-groups/jodrell-group/combenefit) with Bliss, HAS, and Loewe models[192]. All models gave the same results (see Table 1), strongly confirming that H_2O_2 and NO_2^- act synergistically in inducing cancer cells death. As presented in Table 1, this synergistic effect becomes more conspicuous for higher NO_2^- concentrations. Here, we have to underline that the positive numbers in Table 1 indicate a synergistic effect, while negative values would have indicated antagonism. Moreover, the higher the absolute value, the higher the synergy or the antagonism (there is no upper or lower limits).

Collectively, the results demonstrate that optimum cancer cell death can be achieved at a well-defined concentration of H_2O_2 by adding the appropriate concentration of NO_2^-. For example, 60% cell viability for CAL27 is observed following incubation in H_2O_2 1.6 mM or a combination of H_2O_2 0.8 mM + NO_2^- 0.2 mM (Figure 5.5 a)). Similarly, 30% cell viability for FaDu is observed following incubation in H_2O_2 1.6 mM or a combination of H_2O_2 0.8 mM + NO_2^- 0.8 mM (Figure 5.5 b)). Among the long-lived species present in pPBS, H_2O_2 has been described as a master player in pPBS-induced loss of cancer cell viability[33]. To further demonstrate that this is also true in our experimental conditions, cancer cells were incubated for 1 h in pPBS containing or not catalase, which decomposes H_2O_2 into H_2O and O_2. Our results showed that the presence of catalase during pPBS treatment completely prevents the toxicity of pPBS (Figure 5.6 a)), and this fully correlates with a complete loss of H_2O_2 in pPBS resulting from the addition of catalase (Figure 5.6 b)). These results underline the fact that H_2O_2 is an essential factor in pPBS leading to cancer cell death.

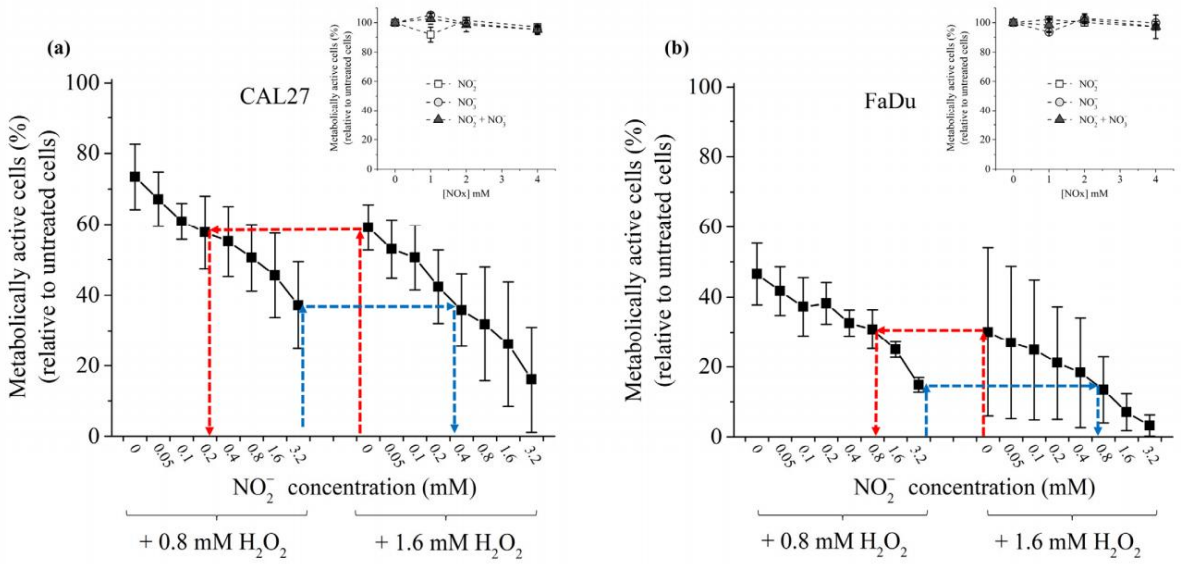

Figure 5.5 Synergistic effect of H_2O_2 and NO_2^- in inducing cancer cell death. CAL27 (a) and FaDu (b) were incubated in PBS containing H_2O_2 at 0.8 or 1.6 mM and increasing concentrations of NO_2^- from 0 to 3.2 mM. The red and blue dashed arrows highlight the fact that the same % of cell viability can be reached using the appropriate combination of H_2O_2 + NO_2^-. Insets: cell viability of CAL27 (a) and FaDu (b) in the presence of increasing concentrations of NO_2^-, NO_3^- and NO_2^- + NO_3^-. The data are the mean ± SD of 2 to 4 independent experiments.

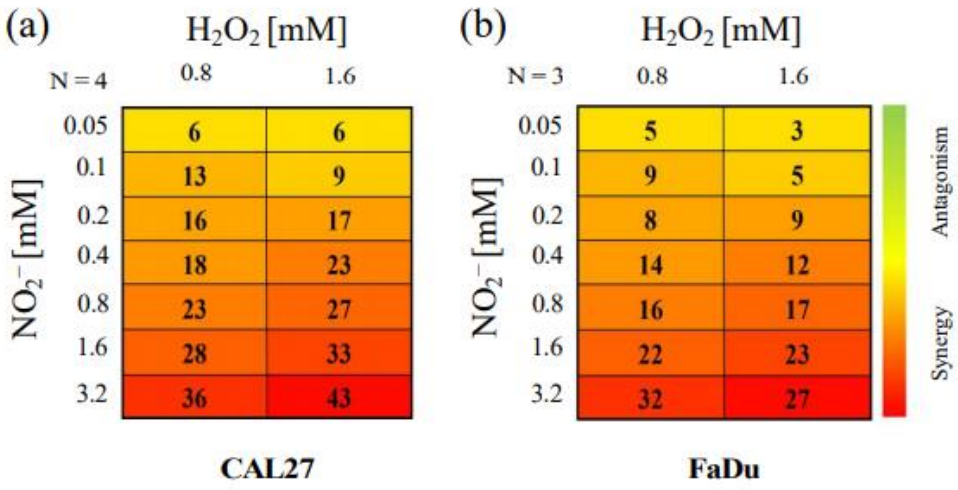

Table 1. H_2O_2 and NO_2^- act synergistically in inducing cancer cells death. Synergy analysis for a) CAL27 and b) FaDu. Identical results were obtained with all three models used (Loewe, Bliss and HAS). The numbers in bold correspond to the synergy/antagonism score for each dose combination of H_2O_2 and NO_2^-. The number of independent experiments implemented for this analysis is reported in the top left corner as N.

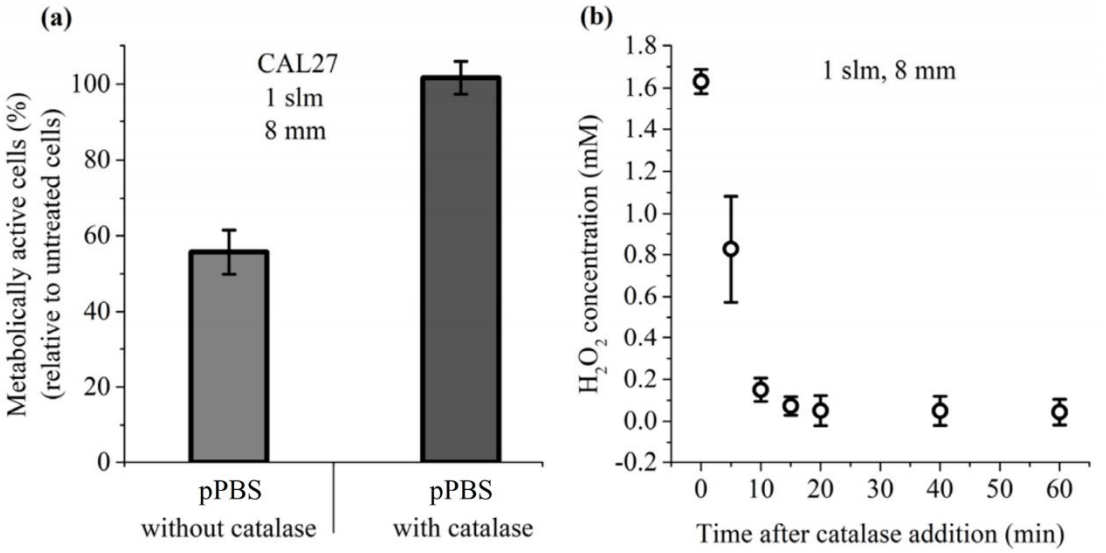

Figure 5.6 Catalase prevents the toxicity of pPBS. (a) CAL27 cells were incubated for 1 h in pPBS alone or pPBS with catalase. Catalase was added after plasma treatment. Cell viability was monitored 24 h post-treatment. (b) Concentration of H_2O_2 in pPBS as a function of the time elapsed after the addition of catalase. The data are the mean ± SD of 3 to 6 independent experiments.

5.3 Effect of Acidic pH in Combination with RONS on Cancer Cell Death

Having established that cancer cell death can be induced by a combination of H_2O_2 and NO_2^-, we then added another parameter to this cocktail of reactive species: the pH of PBS, whose value changes upon plasma treatment. For this study, we first considered a plasma treatment performed for 12 min at a gas flow rate of 0.5 slm (99.8 % He/ 0.2 % O_2) and at a treatment distance of 8 mm, which are the conditions resulting in the highest production of RONS (Figure 4.3), the highest loss of viability for CAL27 and FaDu cell lines (Figures 5.3 and 5.4) and the strongest reduction in pH (–0.55 to pH 6.5). We therefore compared the cell viability of both cell lines after 1 h incubation in PBS pH 7.05 (untreated condition), 1 h incubation in PBS pH 6.5, 1 h incubation in pPBS (plasma-treated PBS for 12 min at a distance of 8 mm and a gas flow rate at 0.5 slm), and 1 h incubation in a reconstituted buffer (PBS pH 7.05 or pH 6.5, containing 1.6 mM H_2O_2, 1.5 mM NO_2^- and 0.55 mM NO_3^-). We found that the acidic environment of PBS alone does not affect cell viability, while the reconstituted buffer (RB) at pH 7.05 has a strong effect, although not as strong as pPBS (Figure 5.7). Finally, the combined effects of the acidic pH and the concentration of reactive species (RB at pH 6.5) recapitulate the effect of pPBS on the viability of cancer cells (Figure 5.7). We also performed the same analysis for a treatment distance of 20 mm, for which fewer RONS, less loss of cell viability, and less pH reduction were measured. Again, the reconstituted buffer (RONS in PBS plus adjusted pH) recapitulates the effect of pPBS on the viability of cancer cells (Figure 5.8). Together, these results demonstrate that, in addition to the concentration of RONS, the pH must be

considered to fully explain the toxicity of pPBS during indirect plasma treatment. Most importantly, they also demonstrate that *in vitro* a reconstituted buffer is as efficient as indirect plasma treatment (pPBS). The concentration of the previously mentioned RONS and the pH value were measured as a function of the storage time of pPBS. More specifically, the stability of H_2O_2, NO_2^-, NO_3^-, and pH in the treated solution was assessed 1, 3, 6, 12, 24 and 72 h after the plasma treatment. Concerning the concentrations measured immediately after the plasma treatment, no significant degradation (<10%) of these reactive species was observed for up to 3 days of storage at room temperature (23 °C) and the pH was also stable over time. For the same time period and storage temperature, H_2O_2, NO_2^- and NO_3^-, and pH were also stable in ad-hoc solutions (RB).

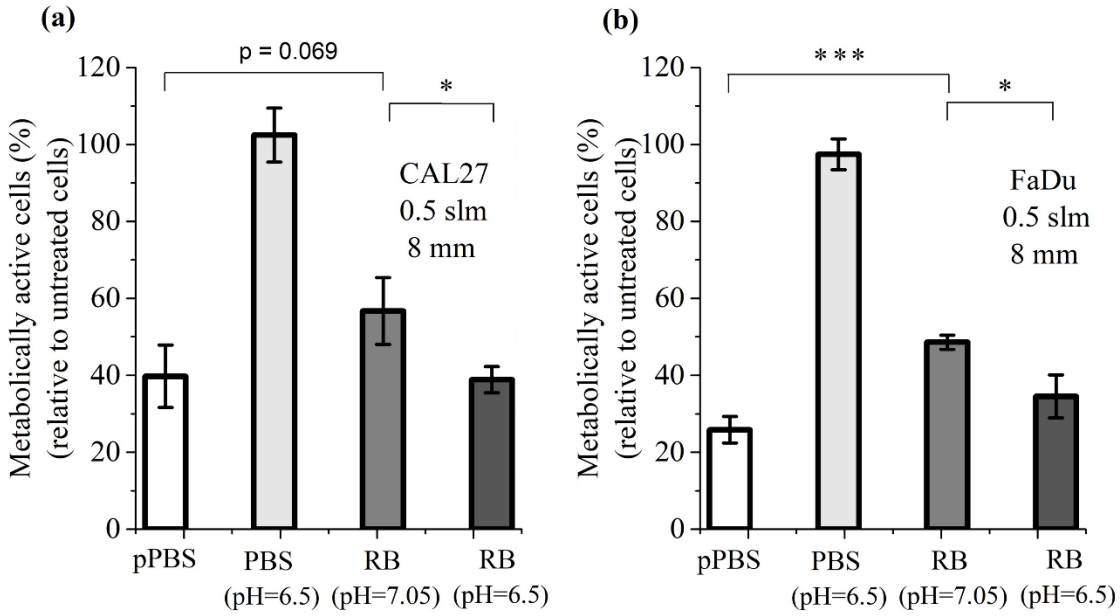

Figure 5.7 Combined effect of pH and RONS on the cell viability of CAL27 (a) and FaDu (b) cell lines. Cell viability was assessed 24 h after 1 h incubation in pPBS, in PBS pH 6.5, and in reconstituted buffer (RB) pH 7.05 or pH 6.5. RB consists of 1.6 mM H_2O_2, 1.5 mM NO_2^- and 0.55 mM NO_3^-. The results presented here correspond to a gas flow rate of 0.5 slm (99.8% He/0.2% O_2), a treatment distance of 8 mm and a treatment time of 12 min. The data are the mean ± SD of 3 independent experiments. Statistical significance NS: $p > 0.05$; *: $p \leq 0.05$; ***: $p \leq 0.001$ (t-test).

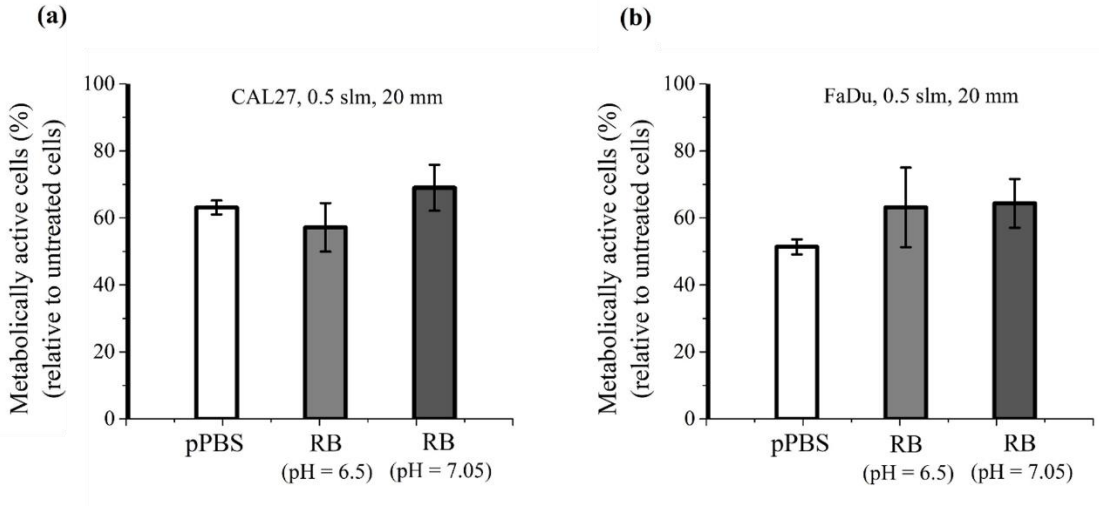

Figure 5.8 Combined effect of pH and RONS on the cell viability of CAL27 (a) and FaDu (b) cell lines. Cell viability was assessed 24 h after 1 h incubation in pPBS, in PBS pH 6.5, and in reconstituted buffer (RB) pH 7.05 or pH 6.5. RB consists of 0.45 mM H_2O_2, 0.4 mM NO_2^- and 0.15 mM NO_3^-. The results presented here correspond to a gas flow rate of 0.5 slm (99.8% He/0.2% O_2), a treatment distance of 20 mm and a treatment time of 12 min. The data are the mean ± SD of 3 independent experiments. The differences of the data presented here are not statistically significant.

5.4 Reconstituted Buffer Is as Efficient as pPBS to Induce Lipid Peroxidation, Intracellular ROS Formation, Caspase 3/7 Activity and Cell Death

To further support our conclusion that reconstituted buffer (RB) recapitulates most, if not all, of the effects induced by pPBS on cells *in vitro*, we analyzed lipid peroxidation, intracellular ROS formation, caspase 3/7 activation, and cell death. Caspase-3 and Caspase-7 are essential regulators of the apoptotic cascade[193]. To do so, CAL27 and FaDu were incubated for 1 h in RB or pPBS. Lipid peroxidation and ROS formation were analyzed immediately after incubation, while caspase 3/7 activation was analyzed 6 h after incubation, and cell death was evaluated 6 h and 72 h post-incubation. Examples of flow cytometry dot plots (forward scatter vs fluorescence for lipid peroxidation) are shown in Figures 5.9, 5.10 and 5.11. We found that both treatments are equivalent for all endpoints analyzed (Figure 5.12). Indeed, in response to either RB or pPBS, we observed around a 1.5-fold increase of lipid peroxidation both in CAL27 and FaDu (Figure 5.12 a)), around a 3-fold and 2-fold increase of intracellular ROS levels in CAL27 and FaDu, respectively (Figure 5.12 b)), around an 8-fold increase in caspase 3/7 activity in CAL27, while no increased activity was detected in FaDu (Figure 5.12 c)), and progressive cell death from 6 to 72 h post-treatment, both in CAL27 and FaDu (Figure 5.12 d)). Here we should remind that for all the experiments that are presented in this Chapter, the incubation of the cells with the pPBS was 1 hour. After that, the pPBS was replaced by fresh culture medium that remained with the

cells until the measurement of their viability.

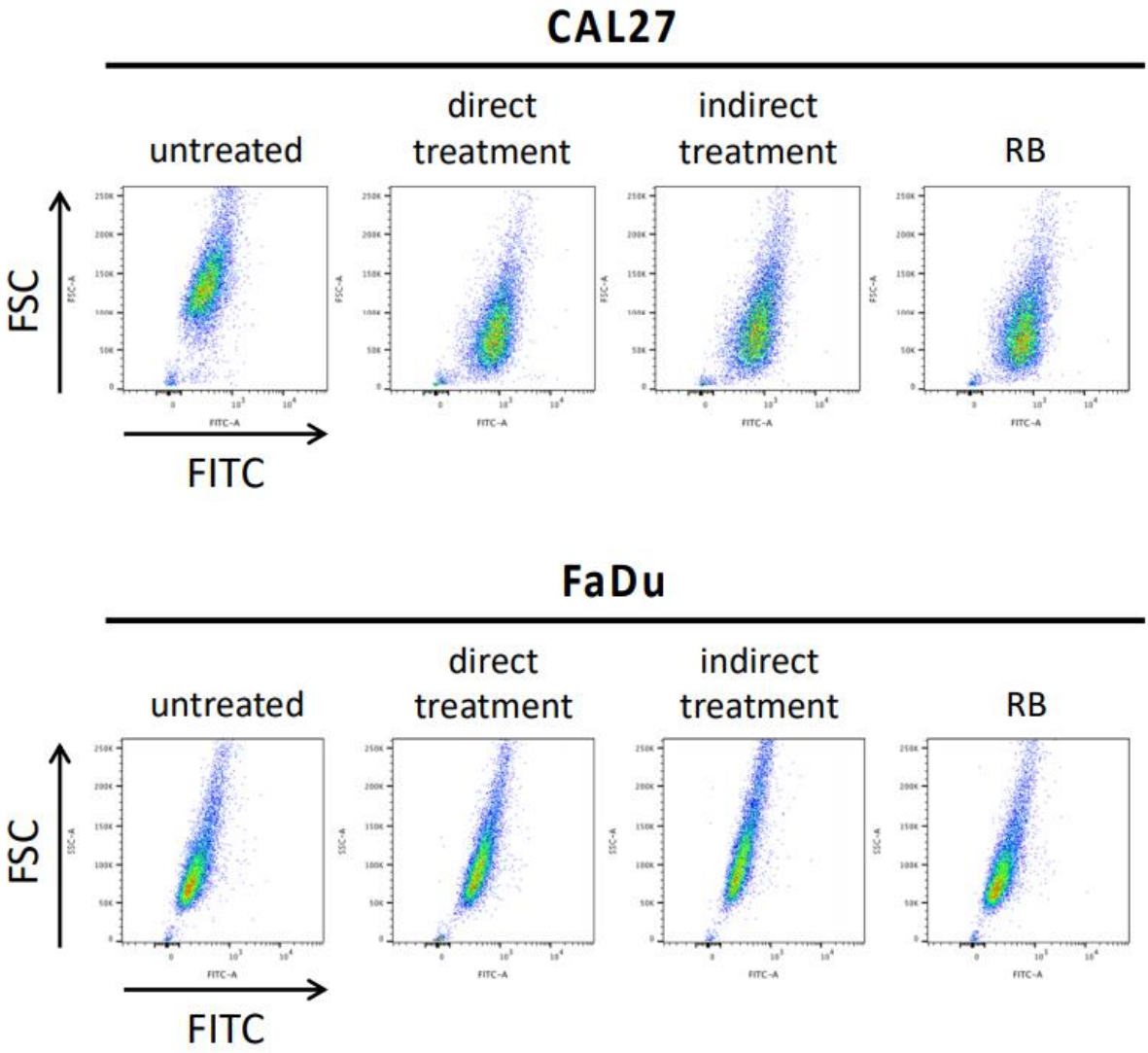

Figure 5.9 Oxidation of BODIPY 581/591 C-11 after treatment of CAL27 and FaDu cells. The cells were incubated for ½ h with 5 µM BODIPY 581/591 C-11, after which the cells were left untreated or treated in PBS by direct and indirect plasma treatments or reconstituted buffer (RB). After 1 h incubation in untreated or treated PBS, the cells were further incubated for 5 to 6 h in complete cell culture medium, and then collected for FACS analysis. Cells were analyzed by flow cytometry (BD LSRFortessa™ X-20, BD), as per manufacturer instructions. Shown is a representative experiment of the forward scatter versus fluorescence (FITC) for CAL27 and FaDu.

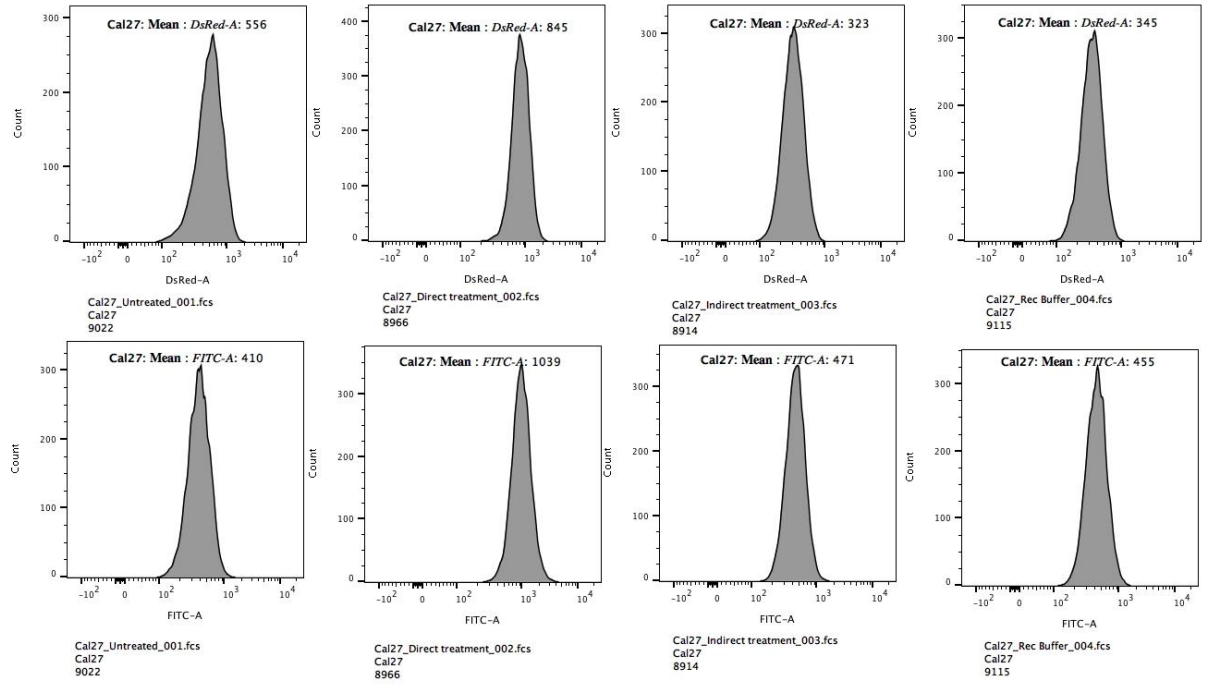

Figure 5.10 Oxidation of BODIPY 581/591 C-11 after treatment of CAL27. The cells were incubated for ½ h with 5 µM BODIPY 581/591 C-11, after which the cells were left untreated or treated in PBS by direct and indirect plasma treatments or reconstituted buffer (RB). After 1 h incubation in untreated or treated PBS, the cells were further incubated for 5 to 6 h in complete cell culture medium, and then collected for FACS analysis. Cells were analyzed by flow cytometry (BD LSRFortessa™ X-20, BD), as per manufacturer instructions. Shown is a representative experiment of the cells count versus fluorescence (FITC) for CAL27.

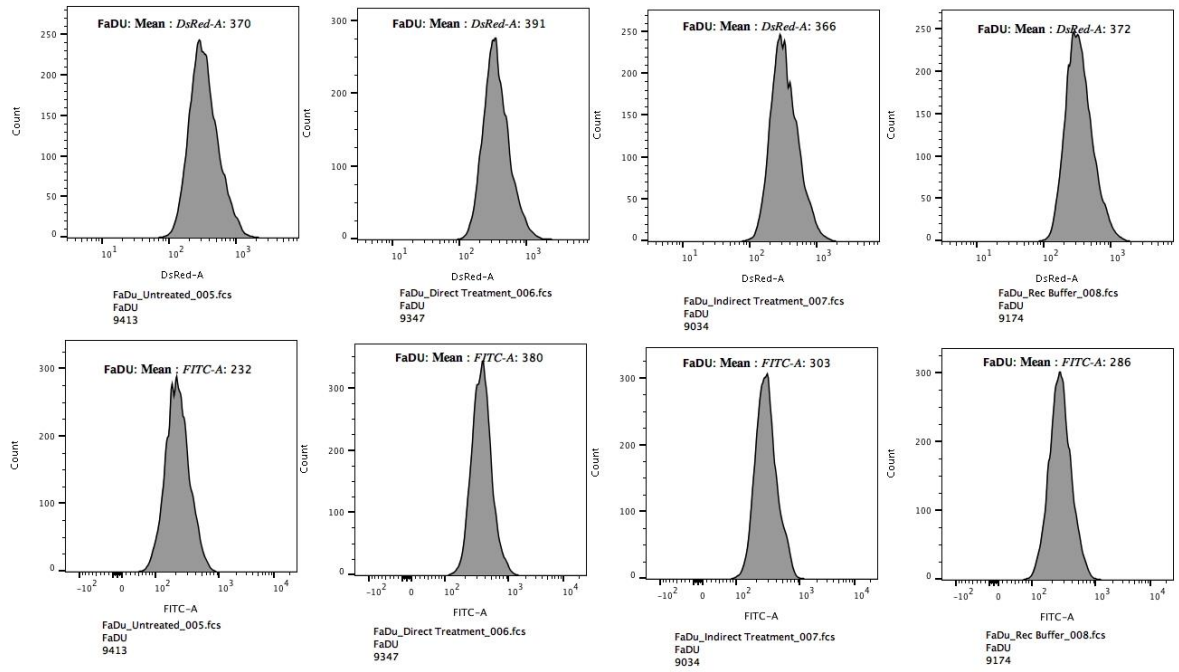

Figure 5.11 Oxidation of BODIPY 581/591 C-11 after treatment of FaDu. The cells were incubated for ½ h with 5 µM BODIPY 581/591 C-11, after which the cells were left untreated or treated in PBS by direct and indirect plasma treatments or reconstituted buffer (RB). After 1 h incubation in untreated or treated PBS, the cells were further incubated for 5 to 6 h in complete cell culture medium, and then collected for FACS analysis. Cells were analyzed by flow cytometry (BD LSRFortessa™ X-20, BD), as per manufacturer instructions. Shown is a representative experiment of the cells count versus fluorescence (FITC) for FaDu.

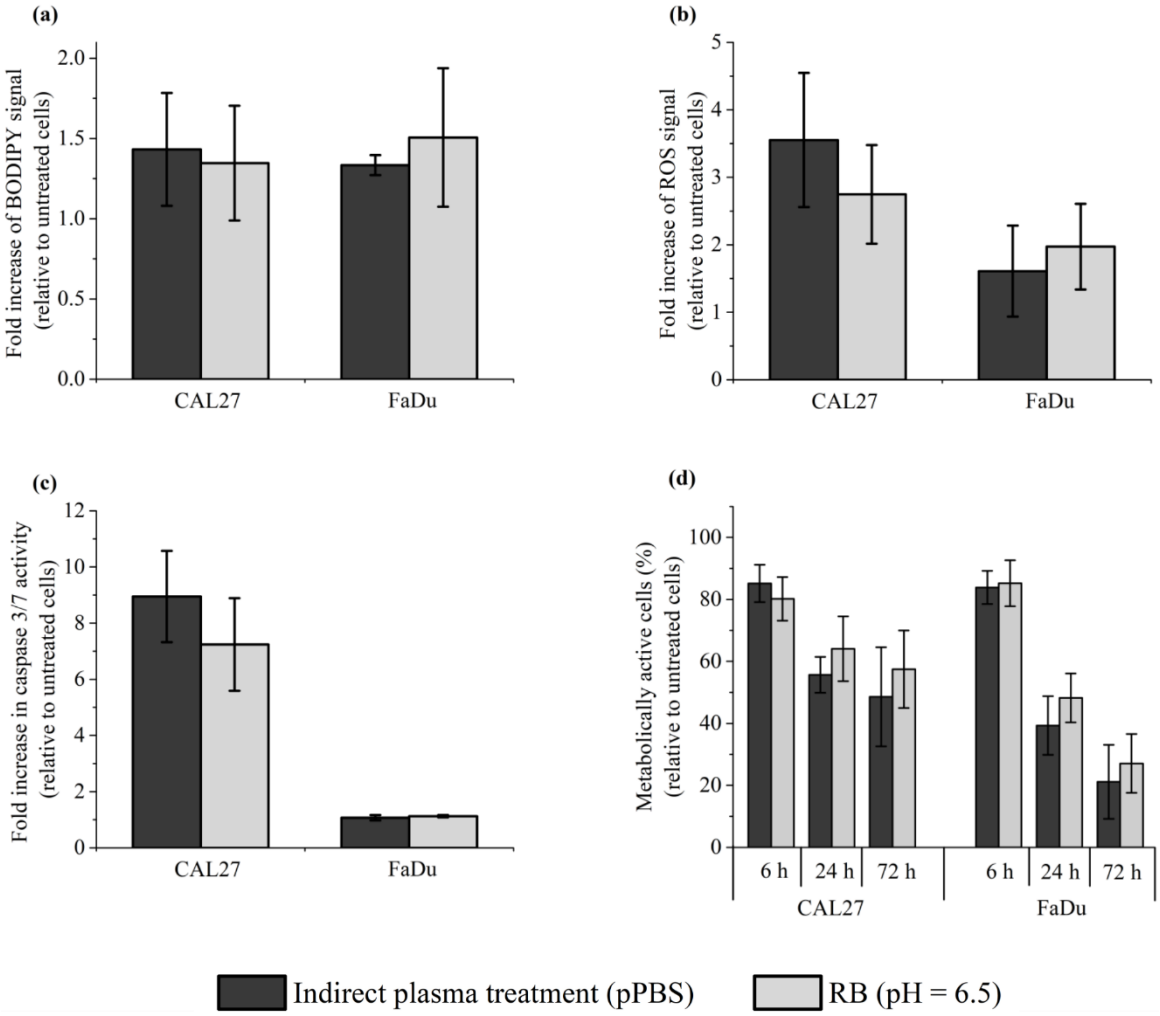

Figure 5.12 Reconstituted buffer (RB) and pPBS are equivalent in inducing lipid peroxidation, an intracellular increase of ROS, caspase 3/7 activation, and cell death. CAL27 and FaDu cells were exposed to pPBS (indirect plasma treatment) or RB for 1 h, and then the cells were either immediately collected for evaluation of lipid peroxidation (**a**) and intracellular ROS formation (**b**), or further incubated in a fresh cell culture medium for 6 h to evaluate caspase 3/7 activation (**c**) or for 6 h, 24 h and 72 h to evaluate cell death (**d**). The results presented here correspond to a gas flow rate of 1 slm (99.8% He/0.2% O_2), a treatment distance of 8 mm, and a treatment time of 12 min. The data are the mean ± SD of 4 to 7 independent experiments for (**a**,**b**), 2 independent experiments for (**c**), and 3 to 4 independent experiments for (**d**).

5.5 Effect of Direct Plasma Treatment on Lipid Peroxidation, Intracellular ROS Production, Caspase 3/7 Activation and Cancer Cell Viability

In the previous sections, we demonstrated that a reconstituted buffer composed of adequate concentrations of H_2O_2 and NO_2^-, and adequate pH, is as efficient as the corresponding pPBS at triggering cell death by long-lived RONS-dependent processes. As the plasma is composed of ions, electrons, photons, radicals, as well as excited atoms and molecules, and an electric field, we then

focused on the effect of direct plasma treatment on lipid peroxidation, intracellular ROS production, caspase 3/7 activation, and cell viability in CAL27 and FaDu cells to compare it with the effect of indirect plasma treatment. We found that the level of lipid peroxidation was significantly, although moderately, increased after direct plasma treatment compared to indirect plasma treatment (Figure 5.13 a)), while the level of intracellular ROS production (Figure 5.13 b)) and caspase 3/7 activation (Figure 5.13 c)) was similar after both treatments. Despite these moderate effects between direct and indirect plasma treatments, the direct plasma treatment was more efficient than the indirect plasma treatment at inducing cell death in CAL27 and FaDu, insofar as cell viability at 72 h post-treatment was about 28% and 54% in CAL27, and 13% and 20% in FaDu, respectively (Figure 5.13 d)). These results suggest that other chemical species and/or plasma physical factors contribute alongside long-lived species to the toxicity of direct plasma treatment.

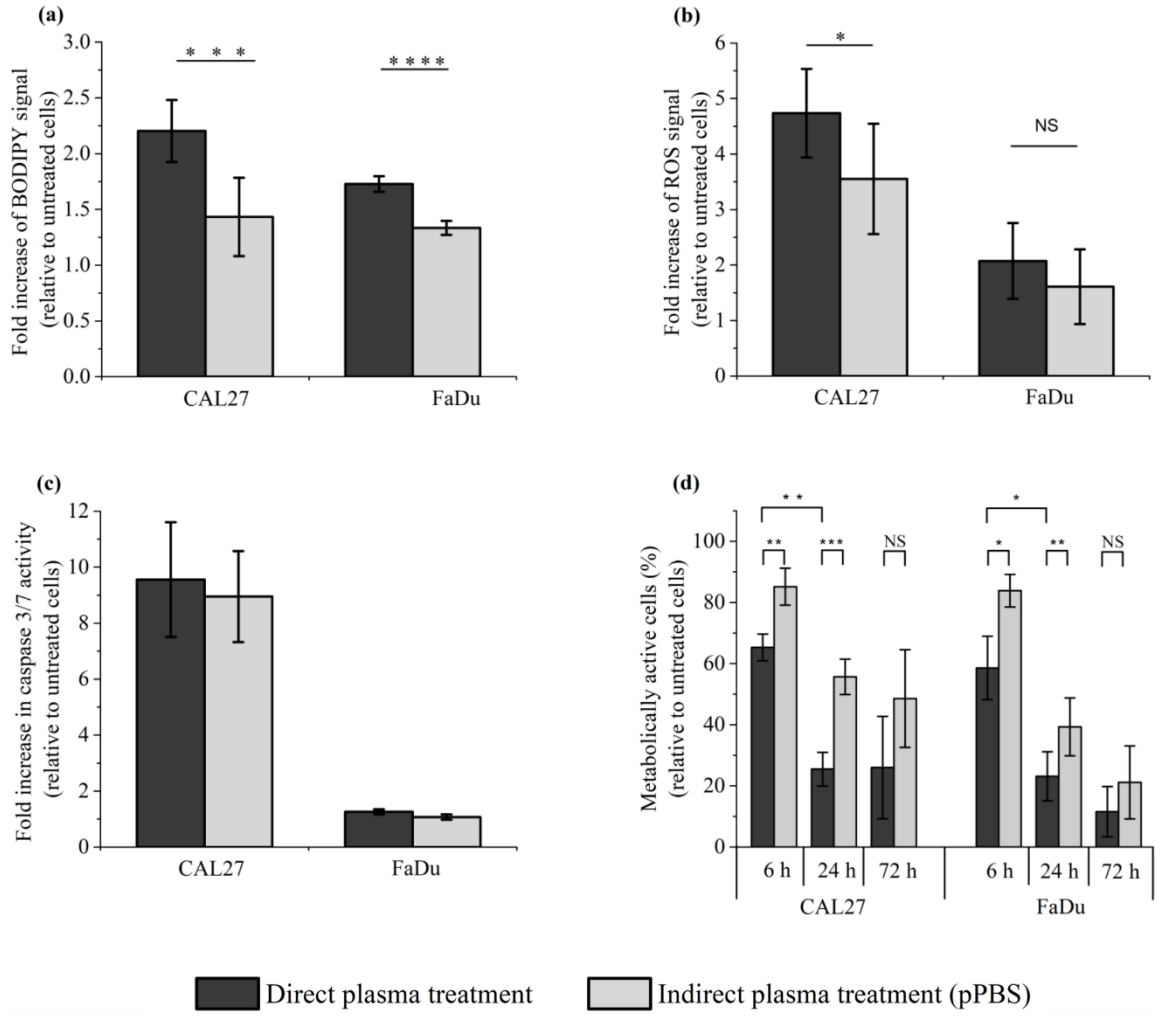

Figure 5.13 Direct plasma treatment is slightly more efficient than indirect plasma treatment (pPBS) at inducing lipid peroxidation, an intracellular increase of ROS, and cancer cell death, while no significant difference was observed between these two treatment methods at inducing caspase

3/7 activation. CAL27 and FaDu cells were exposed to direct and indirect (pPBS) plasma treatments, and then the cells were either immediately collected for the evaluation of lipid peroxidation (**a**) and intracellular ROS formation (**b**), or further incubated for 6 h to evaluate caspase 3/7 activation (**c**) or for 6 h, 24 h and 72 h to evaluate cell death (**d**). The results presented here correspond to a gas flow rate of 1 slm (99.8% He/0.2% O_2), a treatment distance of 8 mm and a treatment time of 12 min. The data are the mean ± SD of 4 to 7 independent experiments for (**a**), 4 independent experiments for (**b**), 2 independent experiments for (**c**), and 3 to 4 independent experiments for (**d**). Statistical significance NS: $p > 0.05$; *: $p \leq 0.05$; **: $p \leq 0.01$; ***: $p \leq 0.001$; ****: $p \leq 0.0001$ (t-test).

5.6 Contribution of Plasma Treatment Time (Immediate Effects) versus Incubation Time (Early Effects) to the Toxicity of Direct Plasma Treatment

Direct plasma treatment consists of two phases: the period of plasma treatment (immediate effects), which corresponds to the time during which cells covered by PBS are exposed to the plasma, and the period of incubation, which corresponds to the time during which the cells are further incubated in pPBS (early effects). Indirect plasma treatment consists only of the second phase. Here, we attempted to better characterize the key drivers of pPBS toxicity during direct plasma treatment, and more specifically during the first phase. Foremost, we evaluated the contribution of long-lived species (i.e. H_2O_2, NO_2^- and NO_3^-) to pPBS toxicity during the plasma treatment time (immediate effects). For that, we determined the average concentration of each of these species present in the PBS during the plasma treatment (at a gas flow rate of 1 slm and a treatment distance of 8 mm) from the first second ($[H_2O_2]_i = [NO_2^-]_i = [NO_3^-]_I \sim 0$ mM, i standing for initial) to the last second of the 12 min of treatment ($[H_2O_2]_f$ = 1.6 mM, $[NO_2^-]_f$ = 0.63 mM, $[NO_3^-]_f$ = 0.26 mM, f standing for final). In fact, the concentration of each of these species increases almost linearly as a function of the plasma treatment time (Figure 5.14 a) and Figure 4.5). Therefore, PBS was treated for 12 min and then CAL27 cells were incubated in this pPBS for 6 min, considering that this condition exposes the cancer cells to the same number of long-lived species as a plasma treatment of 12 min. In parallel, CAL27 cells were exposed to plasma treatment for 12 min without further incubation time (condition i, immediate effects), to plasma treatment for 12 min followed by 1 h incubation time (condition ii, direct plasma treatment), or to pPBS (PBS exposed to 12 min of plasma treatment) for 1 h (condition iii, indirect plasma treatment). Our results showed that the reduction of CAL27 cell viability exposed directly to plasma, followed by 1 h incubation time (condition ii, direct plasma treatment), is the sum of the reduction of cell viability induced only by plasma treatment (condition i, immediate effects), and the reduction of cell viability induced only by 1 h incubation in pPBS (condition iii, indirect plasma treatment) (Figure 5.14 b)). Indeed, the reduction of cell viability is ~75% in condition ii, ~30% in condition i and ~45% in condition iii (Figure 5.14b). Furthermore, as the reduction of cell

viability after 6 min of incubation in pPBS is ~10% (Figure 5.14b), this suggests that long-lived species cannot, on their own, account for the totality of cell death induced during plasma treatment (immediate effects), and that short-lived reactive chemical species and/or physical parameters (such as electric field, high energy photons, heat) can also contribute to the reduction of cell viability during the plasma treatment.

Recently, Bauer *et al.* showed that the formation of primary singlet delta oxygen ($O_2(a^1\Delta_g)$) through the complex interaction between NO_2^- and H_2O_2 resulted in the inactivation of membrane-associated catalase, secondary $O_2(a^1\Delta_g)$ generation, further catalase inactivation, intracellular glutathione depletion, and intercellular RONS-mediated apoptosis signaling[28,60,194,195]. Therefore, we examined the role of $O_2(a^1\Delta_g)$ in the reduction of viability during 12 min of plasma treatment (immediate effects). To do so, cells were exposed to plasma in PBS containing either L-histidine or sodium azide (NaN_3), two well-known $O_2(a^1\Delta_g)$ quenchers/scavengers[196–198]. Our results showed that the presence of L-histidine or NaN_3 did not prevent the loss of cell viability induced by the 12 min plasma treatment (Figure 5.14c)), thus suggesting that singlet delta oxygen does not play a role in the induction of cancer cell death during plasma treatment (immediate effects).

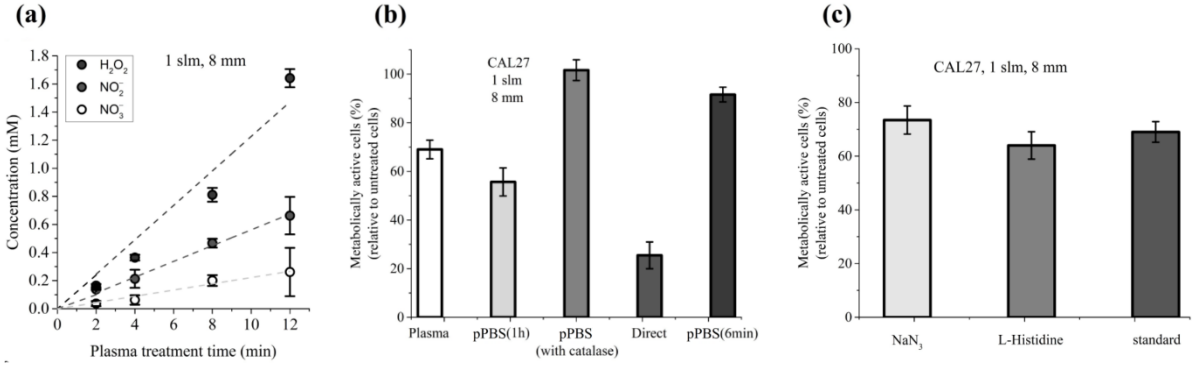

Figure 5.14 Cumulative contribution of plasma treatment time (immediate effects) and incubation time (early effects) in the reduction of cell viability induced by direct plasma treatment. (**a**) The concentrations of H_2O_2, NO_2^-, and NO_3^- were measured as a function of the plasma treatment time. (**b**) CAL27 cells were exposed to 12 min of plasma treatment (plasma, immediate effects), to indirect plasma treatment for 1 h without (pPBS 1 h) or with catalase (pPBS with catalase), for 6 min (pPBS 6 min), or to direct plasma treatment (direct). (**c**) CAL27 were exposed to 12 min of plasma treatment in PBS only (standard) or in PBS containing 1 mM L-histidine or 1 mM NaN_3. Cell viability was measured 24 h post-treatment using MTT assay. The experiments were performed at a gas flow rate of 1 slm (99.8% He/0.2% O_2) and a treatment distance of 8 mm. The data are the mean ± SD of 3 to 6 independent experiments.

5.7 Normal Cells are very Sensitive to Direct Plasma Treatment

Thus far, our experiments were conducted using two head and neck tumor cell lines. We then studied the sensitivity of normal cells to direct plasma treatment, indirect plasma treatment, and reconstituted buffer. At first, we used primary gingival keratinocytes (PGK), since these cells are non-cancerous counterparts of CAL27 and FaDu tumor cells. To perform such experiments with normal cells, we used a luminescent-based assay (CellTiter-Glo® assay), which is more sensitive than a colorimetric assay (e.g., MTT assay). The luminescent-based assay determines the number of viable cells in culture by quantitating the amount of Adenosine 5'-triphosphate (ATP) present, which indicates the presence of metabolically active cells. We found that the percentage of metabolically active cells dropped to 6%, 33%, and 57% 24 h post direct plasma treatment, indirect plasma treatment, and reconstituted buffer, respectively (Figure 5.15). Further incubation up to 72 h post-treatment revealed even a higher loss of activity after direct plasma treatment, while it remained unchanged after indirect plasma treatment and reconstituted buffer (5.13). Since these cells were grown in a very specific cell culture medium (see chapter 2), had a very limited number of cell divisions, and a slow division time, we also conducted the same experiments using two other normal cell lines, 1Br3 and RPE-hTERT (see chapter 2 for more details on the cancer and normal cells). Interestingly, we found that these two cell lines are also very sensitive to direct plasma treatment (Figure 5.16). Indeed, metabolic activity was reduced to 10% (1Br3) and 30% (RPE-hTERT) 6 h post direct plasma treatment, while it was at least 90% in both cell lines after indirect plasma treatment and reconstituted buffer (Figure 5.16). Longer incubation times up to 72 h post-treatment led to a further, strong reduction of metabolic activity after direct plasma treatment in 1Br3 (metabolic activity ~1%) and RPE-hTERT (metabolic activity ~2%) (Figure 5.16).

In marked contrast, metabolic viability after indirect plasma treatment and reconstituted buffer was almost unchanged from 6 h up to 72 h post-treatment in 1Br3 (from ~90% to ~80%) and moderately decreased in RPE-hTERT (from ~90% to ~60%) (Figure 5.16). These unexpected results suggest that normal cells (either primary cells or immortalized with hTERT) are relatively insensitive to the cocktail of long-lived RONS, while they are very sensitive to another type of reactive species, likely short-lived species, or to a physical parameter like UV photons, electromagnetic field or heat. As the treatment of PBS with the plasma does not affect its temperature, which remains at around 23 °C, the role of heat in cell death can be ruled out. Moreover, as the UV-C radiation emitted from the plasma measured at a distance of 8 mm from the reactor's nozzle is lower than 10^{-4} J/m² (detection limit of the detector used), the contribution of high-energy photons to the toxicity of the plasma should be negligible. Besides the conditions used for

the treatment of the cells (8 mm treatment distance and 0.8 mL of PBS, which corresponds to approximately 5 mm of PBS depth, i.e. 13 mm of distance between the cells and the reactor's nozzle), we tried to further approach the detector to the reactor's nozzle. Nevertheless, we did not detect any UV-C radiation, a result that indicates a very low UV-C emission from our plasma.

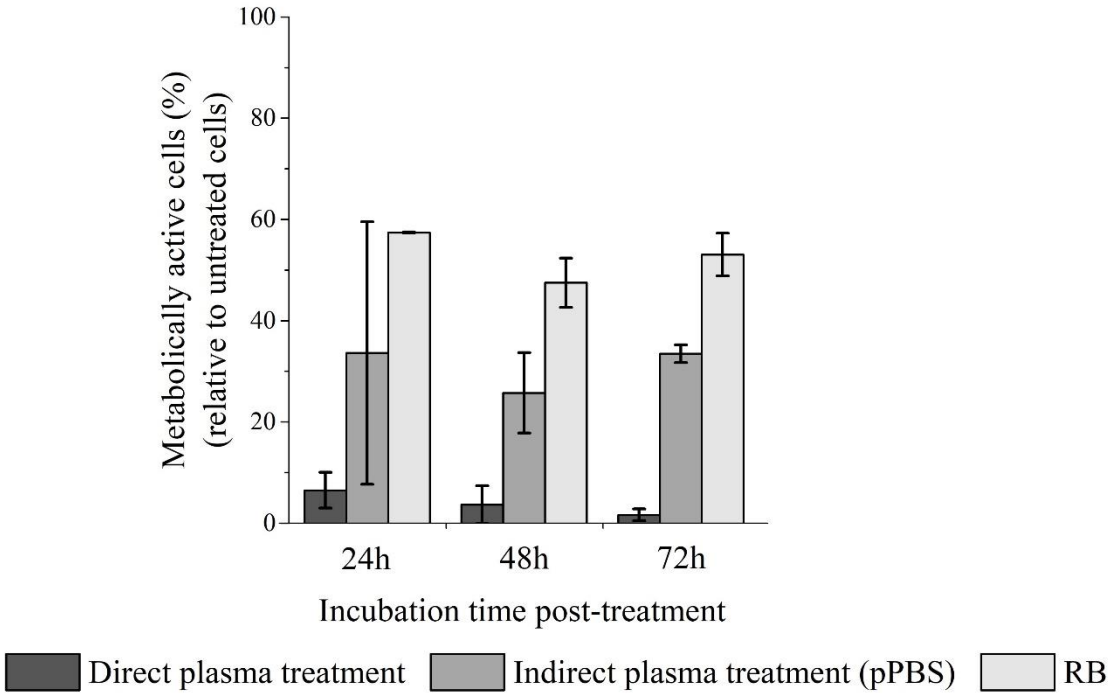

Figure 5.15 Primary human keratinocytes were exposed to direct plasma treatment (12 minutes plasma treatment + 1 hour incubation with pPBS), indirect plasma treatment (1 hour incubation with pPBS) and reconstituted buffer (1 hour incubation with RB). At 24 h, 48 h, and 72 h post-treatment, cell viability was quantified using CellTiter-Glo® luminescent assay (Promega). Conditions used were those corresponding to a gas flow rate of 1 slm (99.8% He / 0.2% O_2), a treatment distance of 8 mm and a treatment time of 12 min. The data are the mean ± SD of 2 independent experiments.

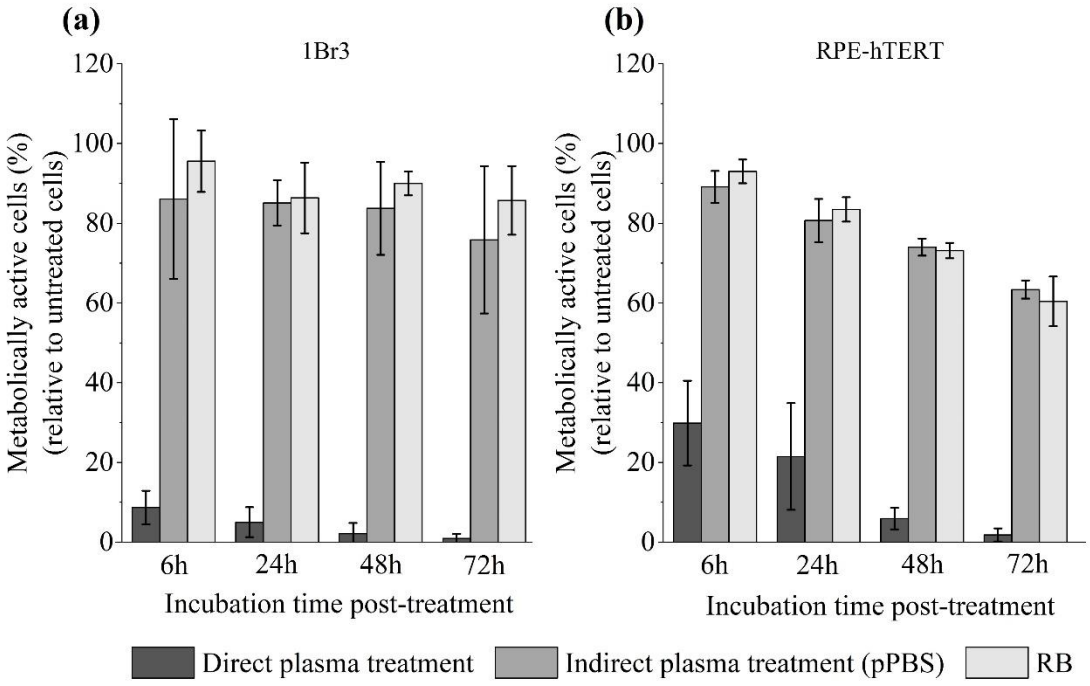

Figure 5.16 Severe loss of metabolic activity of normal cells after direct plasma treatment. Primary human fibroblasts (1Br3) and normal epithelial cells (RPE-hTERT) were exposed to direct plasma treatment, indirect plasma treatment (pPBS), and reconstituted buffer (RB). At 6 h, 24 h, 48 h, and 72 h post-treatment, metabolic activity was quantified using CellTiter-Glo® luminescent assay. Conditions used were those corresponding to a gas flow rate of 1 slm (99.8% He/0.2% O_2), a treatment distance of 8 mm, and a treatment time of 12 min. The data are the mean ± SD of 3 to 17 independent experiments.

5.8 Direct Plasma Treatment Triggers Strong Cell Detachment and Cell Death Few Hours Post-Treatment in RPE-hTERT Cells

To further decipher the precise nature of these chemical and/or physical factors, RPE-hTERT and CAL27 cells were exposed to direct plasma treatment, and treated PBS was either left on the cells for 1 h (immediate and early effects) or immediately removed (immediate effects only). When removed, treated PBS was replaced by a fresh cell culture medium and the cells were incubated for 6 and 24 h. At these time points, images were taken to visualize the effects of plasma treatment on cell morphology (see Figure 5.17). For RPE-hTERT cells, the most striking finding was observed after plasma treatment followed by 1 h incubation (direct plasma treatment) insofar as a considerable number of cells were already detached at 6 h post-treatment (Figure 5.17 a), direct treatment with incubation), and were generally forming clusters (Figure 5.17 a) and Figure 5.18 a)). Importantly, cell detachment was not observed in the absence of 1 h incubation following plasma treatment (Figure 5.17 a, direct treatment no incubation).

We then quantified, at 6 h post direct plasma treatment, the number of floating cells, and of the remaining adherent cells by trypan blue cell counting. On the one hand, we found that cells in suspension represent 22 ± 8% of the total cells, and among them 59 ± 13% are still alive at this time point (n = 8). However, these cells were unable to re-attach into 24-well plates when seeded in fresh medium (data not shown). On the other hand, we found that remaining adherent cells represent 26 ± 11% of the total cells, with a cell viability of 89 ± 9% (n = 8). It is to highlight that the percentage of living cells measured by trypan blue cell counting is in good agreement with the cell's metabolic activity determined by the luminescent-based assay (see Figure 5.16 b)).

Furthermore, since 6 h post direct plasma treatment, the sum of suspension cells plus remaining adherent cells is about 50% of the total cells. This strongly suggests that about 50% of the cells have already gone through cell lysis at this time point, and, therefore, cannot be detected either by cell counting or by flow cytometry (5.18 b)). Finally, we did not observe cell cycle arrests 6 h post direct plasma treatment (see Figure 5.18 c)).

For CAL27 cells, the most striking observation was a change in cell morphology (more rounded cells) at 6 h post plasma treatment, whether there was 1 h incubation or not (see Figure 5.17 b)). However, this change was less apparent at 24 h post-treatment when there was no incubation (Figure 5.17 b), direct treatment no incubation, T24 h). Together, these observations suggest that CAL27 cells better recover than RPE cells from direct plasma treatment.

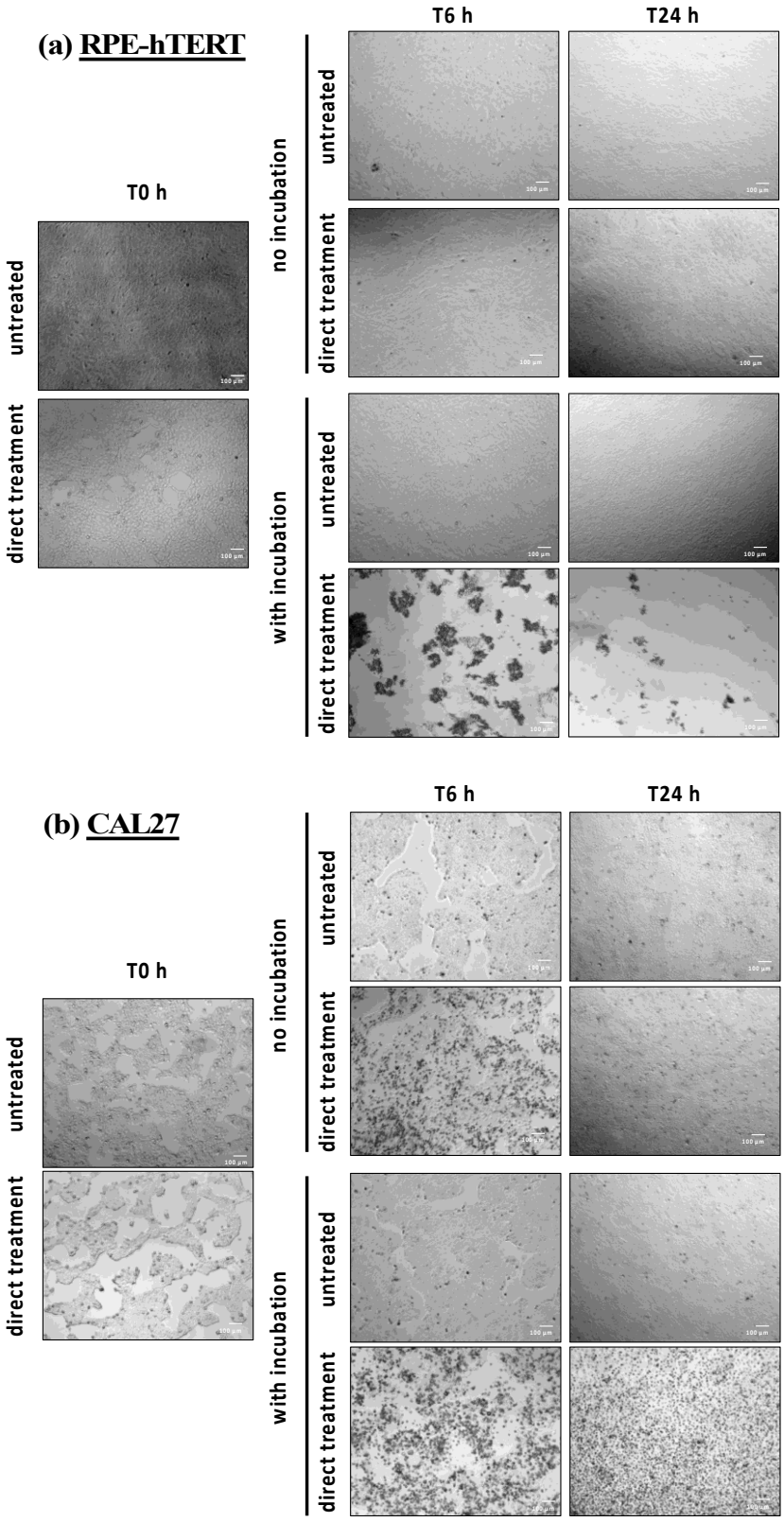

Figure 5.17 Change in cell shape and cell number after direct plasma treatment. (**a**) RPE-hTERT and (**b**) CAL27 cells were exposed in PBS to plasma treatment and further incubated (with incubation – early effects) or not (no incubation – immediate effects) in pPBS. Photographs were taken immediately (T0 h), 6 h (T6 h) or 24 h (T24 h) after plasma treatment, performed at a gas flow rate of 1 slm (99.8% He/0.2% O_2), a treatment distance of 8 mm and a treatment time of 12

min. Photographs were recorded on a Celena® S digital imaging system (Logos biosystem, Villeneuve-d'Ascq, France) at 4× magnification. Photographs are representative of two independent experiments.

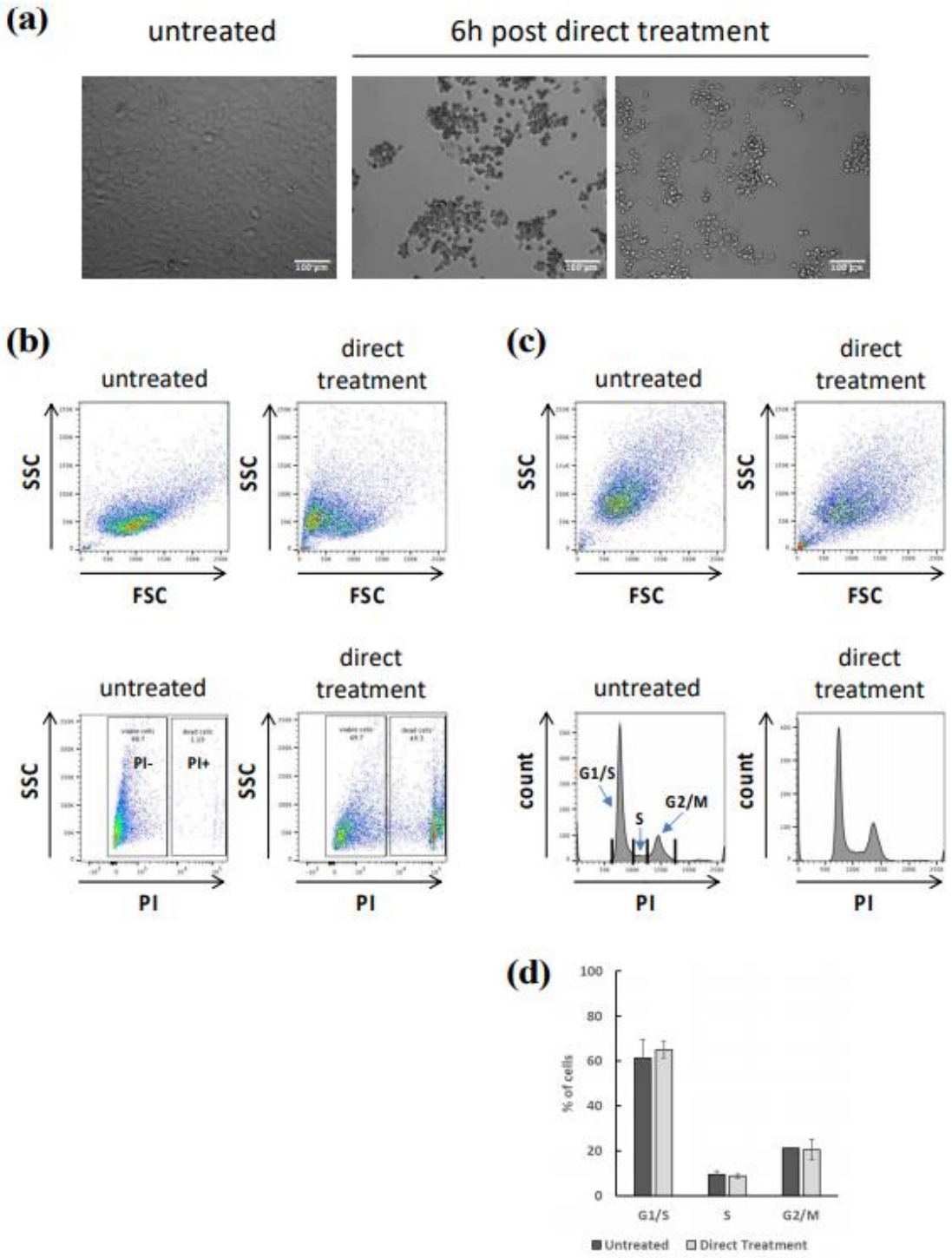

Figure 5.18 Cell death induced in RPE-hTERT cells by direct plasma treatment. RPE-hTERT cells were exposed to plasma treatment for 12 min and further incubated for 1 h in treated PBS (PAP). After removal of PAP, cells were incubated in complete cell culture medium for 6 h. (a) Photographs of untreated and treated cells were taken 6 h after direct plasma treatment. Photographs were

recorded on a Celena® S digital imaging system (Logos biosystem, France) at 10x magnification and are representative of 4 independent experiments. Note that the rounded cells are floating. Thereafter, all cells were collected and analyzed by flow cytometry. (b) Living and dead cells were stained with propidium iodide (PI). Dead cells (PI positive) represent 39 ± 10 % of the total cells (n = 4). Note that with this technic, cells that were lysed due to plasma treatment are not detected. (c) Cells were fixed in 70 % EtOH and stained with PI. (d) Quantification of cells in G1/S, S, and G2/M of the cell cycle 6 h after direct plasma treatment (n = 4). Conditions used were those corresponding to a gas flow rate of 1 slm (99.8% He / 0.2% O2) and a treatment distance of 8 mm.

5.9 Transient Reactive Species, produced in or Transferred to the Liquid Phase during the Plasma Treatment (Immediate Effects), Sensitize Normal but Not Tumor Cells to pPBS

Quantification of the metabolic activity of RPE-hTERT and CAL27 cells at 24 h post-treatment showed that plasma treatment (immediate effects, i.e. no incubation time) has a moderate effect on its own on metabolic activity for both RPE-hTERT and CAL27 (~80% of cell viability), and that the incubation time (early effects) is required to further increase cell death, moderately for CAL27 (~60% of cell viability), but more drastically for RPE-hTERT (~20% of cell viability) – compare “Direct” versus “Plasma” in Figure 5.19. Since pPBS treatment also has a moderate effect on metabolic activity for both RPE-hTER and CAL27 (~80% of cell viability; Figure 5.19), these data strongly suggest that plasma treatment (immediate effects) and incubation time (early effects) have a synergistic effect on the mortality of RPE-hTERT and confirm an additive effect on the mortality of CAL27.

To further investigate the potential that plasma treatment (immediate effects) “sensitizes” normal, but not tumor cells, to pPBS, cells were sequentially exposed to (1) plasma treatment for 12 min (immediate effects), after which pPBS was removed, and subsequently, (2) untreated PBS or pPBS was added for 1 h. We found that untreated PBS added immediately after plasma treatment was not (CAL27) or was moderately (RPE-hTERT) toxic to the cells, while the addition of pPBS strongly impinged cell viability to a level similar to that observed for each cell line after direct plasma treatment (compare “Direct” and “Plasma + pPBS 1h” in Figure 5.19). Collectively, these results support our hypothesis that plasma treatment (immediate effects) potentiates the toxic effect of long-lived RONS on normal cells.

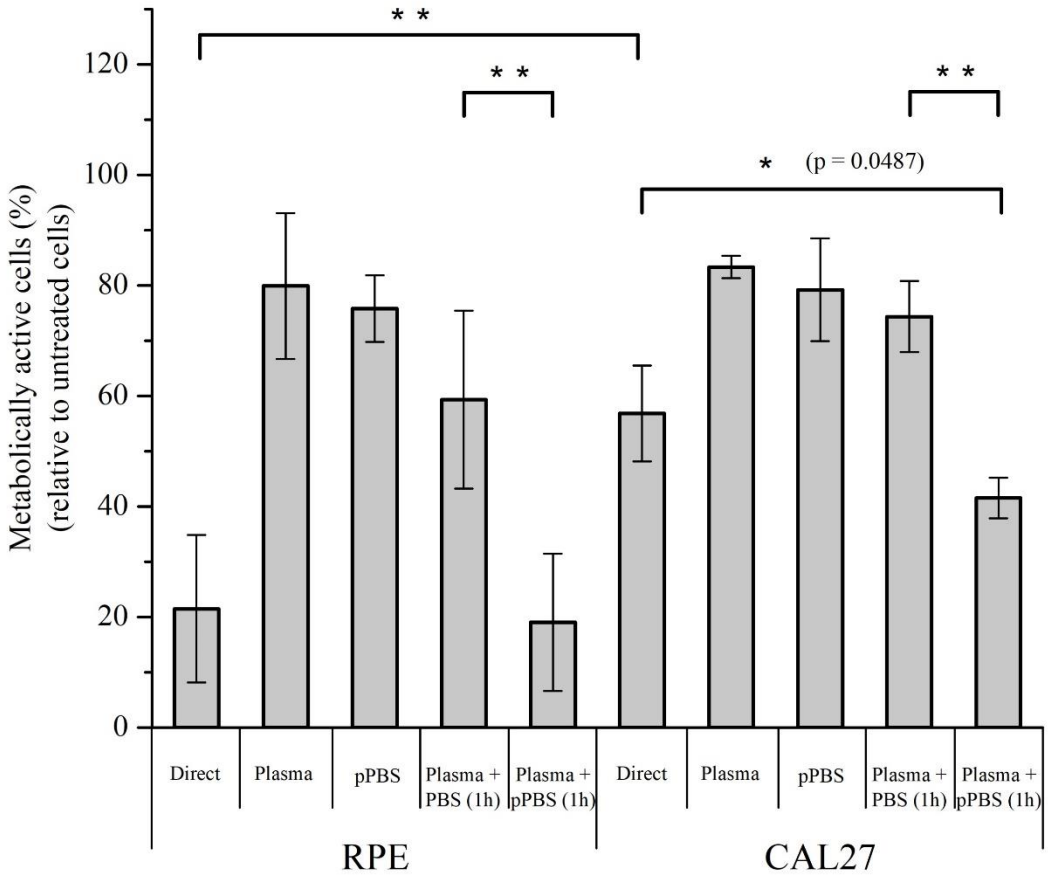

Figure 5.19 The incubation time (early effects) following plasma treatment (immediate effects) is required to achieve efficient cell killing after direct plasma treatment. RPE-hTERT and CAL27 cells were exposed to plasma treatment for 12 min and pPBS was either left on the cells for 1 h (Direct) or immediately removed (Plasma, immediate effects). Alternatively, cells were exposed to plasma-treated PBS for 1 h (pPBS), or to plasma treatment for 12 min followed by incubation in untreated PBS (Plasma + PBS) or in another pPBS (Plasma + pPBS) for 1 h. Metabolic cell activity was quantified using a CellTiter-Glo® luminescent assay 24 h post-treatment. Plasma treatments were performed at a gas flow rate of 1 slm (99.8% He/0.2% O_2) and a treatment distance of 8 mm. The data are the mean ± SD of 3 to 17 independent experiments. Statistical significance NS: $p > 0.05$; *: $p \leq 0.05$; **: $p \leq 0.01$; (t-test).

5.10 Characterization of Transient Reactive Species Present in pPBS

Thus far, we cannot exclude that the electric field rather than transient reactive species present during plasma treatment is responsible for the effective killing of normal cells after direct plasma treatment or plasma treatment (immediate effects) + pPBS (see above Figure 5.19). To challenge this hypothesis, RPE-hTERT cells were exposed to direct plasma treatment or to indirect plasma treatment for 1h, in which pPBS was added to the cells either immediately (T0 min)

or 5 min (T5 min), 10 min (T10 min), 20 min (T20 min), 30 min (T30 min), 45 min (T45 min) or >60 min (>T60 min) after plasma treatment. We observed a time-dependent response showing that, if pPBS was added immediately (T0 min) after plasma treatment, then the cell viability was close to that resulting from a direct plasma treatment, while, if pPBS was added 45 min after plasma treatment (T45 min), then the cell viability was similar to that resulting from an indirect plasma treatment with pPBS stored for several hours on the bench (>T60 min) (Figure 5.20). These results demonstrate that transient reactive species (short-lived species), and not the electric field, contribute mostly to the overall toxicity of plasma on normal cells. Furthermore, since the toxic activity of pPBS stored for 10 min (T10 min) on the bench is similar to that of the pPBS stored for >60 min (>T60 min), this means that the lifetime of the active species is short (<10 min). Based on the results shown in Figure 5.20, we estimated the lifetime of the active species to be of a few tens of seconds to a few minutes, therefore excluding plasma-derived very short-lived RONS such as free radicals or singlet delta oxygen ($O_2(a^1\Delta_g)$). We also excluded the role of $O_2(a^1\Delta_g)$ derived through the interaction of long-lived species in pPBS[28] since L-histidine, a quencher of $O_2(a^1\Delta_g)$, was unable to prevent plasma-induced cell death (Figure 5.20).

Among the reactive species, ozone (O_3) and chlorine species (Cl_2^-, ClO^-) are good candidates since they are both generated by cold atmospheric plasmas and their lifetime in liquids is in the range of seconds to hours, depending on the nature of the liquid[108,124,199]. We attempted to detect ozone production in pPBS by two spectroscopic methods: directly by its UV absorption at 258–260 nm and indirectly by the absorption detection at 600 nm of the decolorization of potassium indigo trisulfonate dye by ozone[200]. The first method failed since the high production of H_2O_2 and NO_2^- also generates an absorption peak at 258–260 nm and the second (that is presented in chapter 2) is not selective to ozone as we demonstrated in Chapter 4 (Figure 4.11). Since hydroxyl radicals are the main oxidants formed in the decomposition of ozone in water[142], we used dimethylsulfoxide (DMSO) to trap hydroxyl radicals[201,202]. Adding DMSO to pPBS immediately after plasma treatment strongly prevented cell death (Figure 5.20). However, insofar as DMSO is also oxidized by hypochlorite[203,204], we used taurine, a well-known hypochlorite scavenger[205,206], to assess the role of this species in plasma-induced cell death. As shown in Figure 5.20, adding taurine immediately after plasma treatment also strongly prevented cell death, but not to the same extent as with DMSO. Collectively, these results demonstrate that reactive species other than long-lived reactive species (likely •OH through O_3 decomposition and/or ClO^-) are produced by the plasma and are toxic to normal cells.

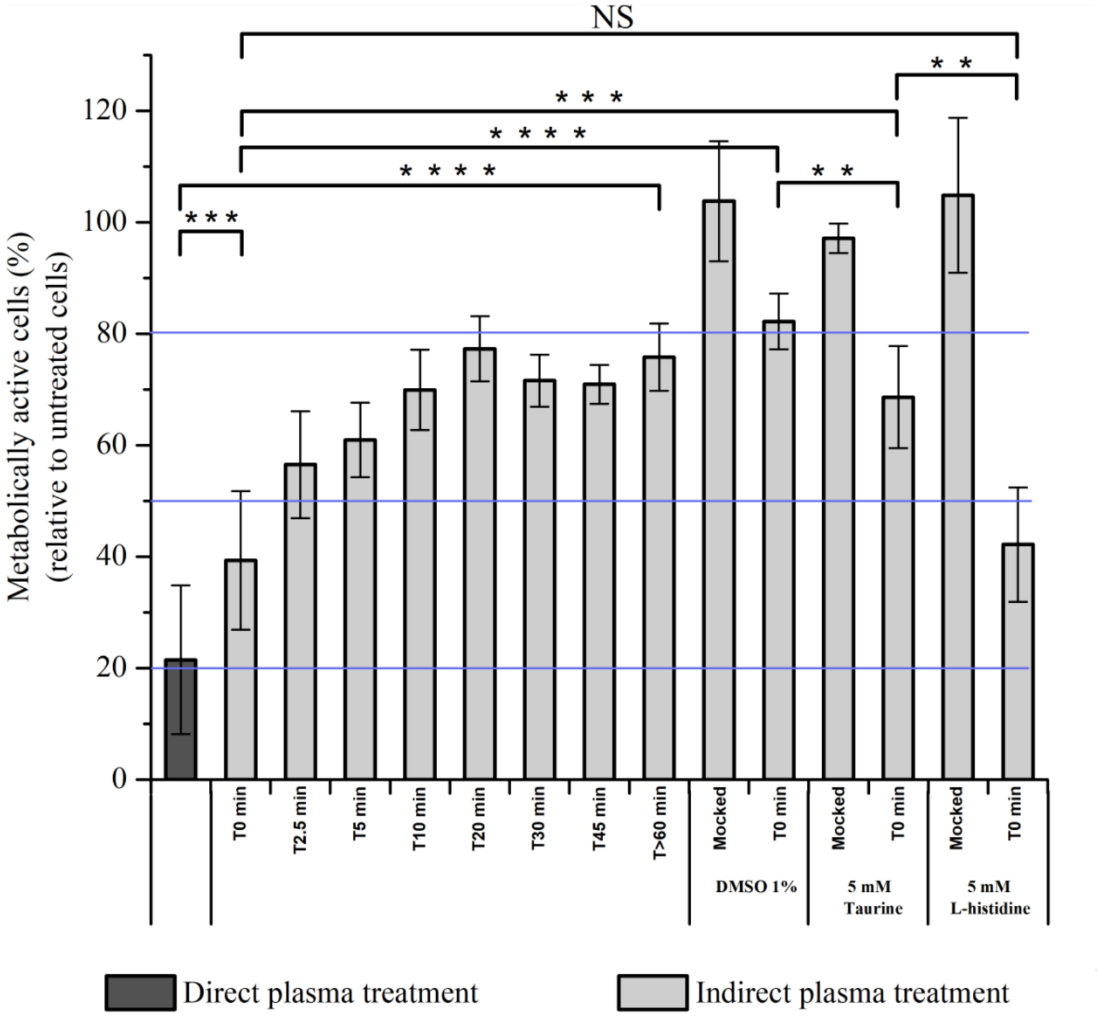

Figure 5.20 Full pPBS toxicity depends on transient reactive species. RPE-hTERT cells were exposed to direct plasma treatment in PBS or pPBS (indirect plasma treatment) either not stored (T0 min) or stored for various time periods on the bench (from 0 min to >60 min) after plasma treatment, before being added onto the cells for 1 h. Alternatively, DMSO at a final concentration of 1%, and Taurine and L-histidine at 5 mM were added immediately after plasma treatment to pPBS, which was immediately added to the cells for 1 h. Cell viability was quantified at 24 h post-treatment using CellTiter-Glo® luminescent assay. Solid blue lines indicate the average cell viability after direct plasma treatment (around 20%, minimum of cell viability and maximum concentration of transient reactive species), the average cell viability after indirect plasma treatment (pPBS, around 80%, maximum of cell viability and no transient reactive species), and the EC50 (around 50%). Plasma treatments were performed at a gas flow rate of 1 slm (99.8% He/0.2% O_2), a treatment distance of 8 mm, and a treatment time of 12 min. The data are the mean ± SD of 3 to 17 independent experiments. Statistical significance NS: $p > 0.05$; *: $p \leq 0.05$; **: $p \leq 0.01$; ***: $p \leq 0.001$; ****: $p \leq 0.0001$ (t-test).

5.11 Investigation of the cells permeabilization and of BSA protein disruption due to plasma treatment

Our findings, when comparing direct and indirect plasma treatments of a cancerous (CAL27) and a normal (RPE-hTERT) cell lines, suggest that the

hypersensitivity of normal cells to direct plasma treatment is due to an activation state that they undergo during the 12 minutes of plasma treatment (immediate effects). This activation makes them more vulnerable for the long-lived reactive species to act during the 1 hour of incubation time with the pPBS (early effects). We propose that during this activation, the cellular membrane is oxidized by the aforementioned short- and/or intermediate-lived reactive species, which facilitate the penetration into the cells of long-lived reactive species. To test our hypothesis, we firstly studied the capability of direct and indirect plasma treatment to permeabilize these two cell lines. Secondly, BSA protein was also treated by the plasma (both directly and indirectly), as they are proteins yielded from blood, which function as binding and transport proteins in blood circulation, and they are a good model to simulate the proteinic behavior to plasma treatment. This study should be taken into account when the plasma is used in *in-vivo* applications.

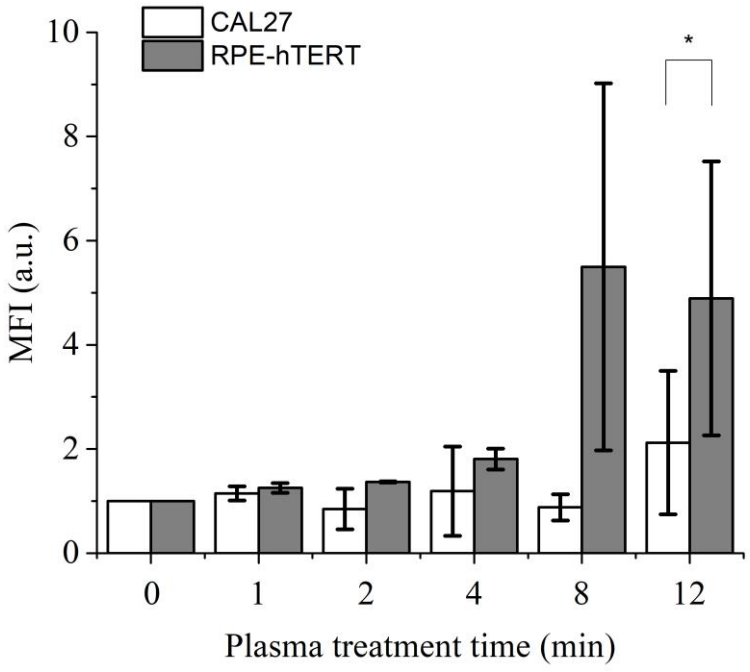

Figure 5.21 Mean fluorescence intensity (MFI) of propidium iodide (PI) indicating the permeabilization of both CAL and RPE cells when they undergo direct plasma treatment. The data are the mean ± SD of 2 independent experiments for all the treatment times except for the 12 minutes, where the data are the mean ± SD of 8 independent experiments. Statistical significance NS: $p > 0.05$; *: $p \leq 0.05$; **: $p \leq 0.01$; ***: $p \leq 0.001$; ****: $p \leq 0.0001$ (t-test).

As we can see in Figure 5.21, we have, indeed, a stronger permeabilization of the normal cells, even if for most of the treatment times the difference on permeabilization between normal and cancer cells is not statistically significant. Especially for the case of 12 minutes of plasma treatment, for which more

experiments were conducted, we have a significant difference between the two cell lines. This is a first important verification of our hypothesis regarding the oxidation of the cellular membrane of the normal cells during direct plasma treatment. For these experiments, a Propidium Iodide (PI) marker was used, whose size is relatively big, which makes its penetration through the cellular membrane more complicated. Thus, we propose that, in the future, these experiments should be repeated with a marker of smaller size that would allow us to detect less significant differences on the permeabilization of the cellular membrane of these two cells (CAL27 and RPE). An alternative for propidium iodide could be the DHR123 flow cytometry probe. It has half the molecular weight of propidium iodide (346.4 instead of 668.4 respectively). The problem with DHR123 is that to be detected during flow cytometry it must be oxidized. Thus, its efficiency should be verified before used.

Finally, the effect of direct and indirect plasma treatment on the cancer and normal cells was also further studied by treating BSA protein. For the assessment of the three plasma modalities on the proteins, stain free gel and simply blue staining were used. The acquired photos of the proteins were analyzed with image processing and the relative luminance of each one of them was calculated. Higher relative luminance means less color intensity and, thus, more significant effects of the plasma on the proteins. As we can see in Figures 5.20 and 5.21, the direct plasma treatment highly oxidizes the BSA protein, while the indirect plasma treatment exhibits a moderate effect. Here we need to underline that again the indirect plasma treatment has the exact same effect on the BSA protein as the reconstituted buffer. This means that also for the BSA oxidation during the indirect plasma treatment, we can hold responsible mainly the H_2O_2, NO_2^- and NO_3^- in combination with a slightly acidic pH. The quantification of the BSA protein oxidation (Figures 5.20 and 5.21) unveils a similar behavior to that of the normal cells, a fact that could be argued as a preliminary verification of our prior hypothesis: we activate the normal cells during the 12 minutes plasma treatments by damaging their membrane, enabling then the reactive oxygen and nitrogen species to penetrate into the cell during the incubation time.

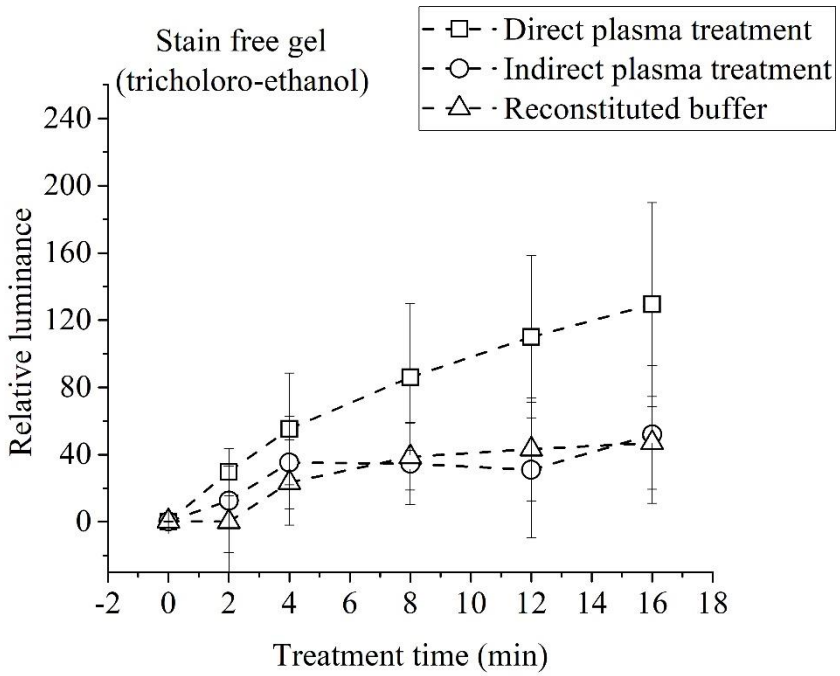

Figure 5.22 Relative luminance of BSA protein samples treated with the three plasma treatment modalities used in this work. The proteins were analyzed with Stain free gel and the data are the mean ± SD of 3 independent experiments. The data are obtained with image processing from the photos presented in Chapter 2.

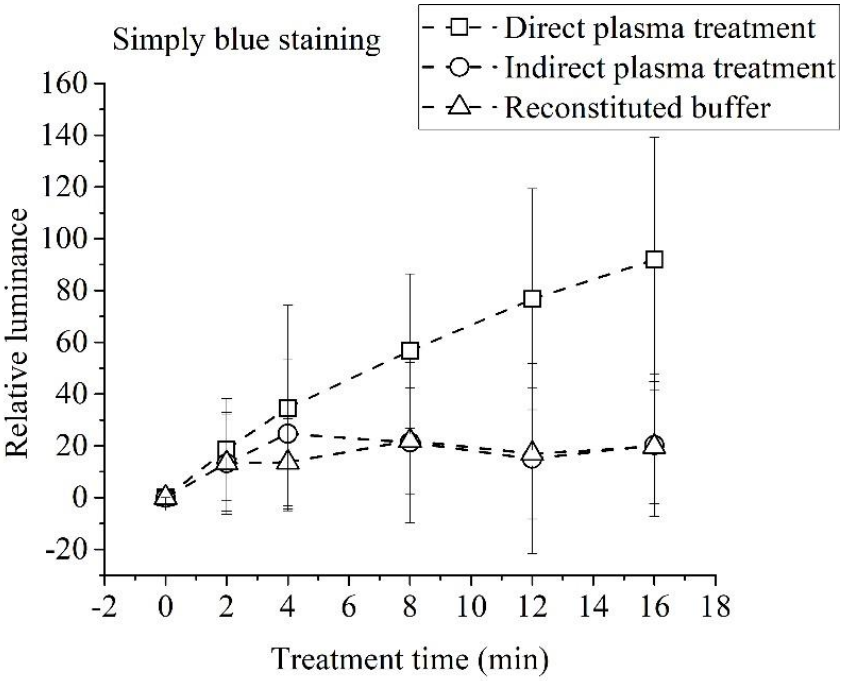

Figure 5.23 Relative luminance of BSA protein samples treated with the three plasma treatment modalities used in this work. The proteins were analyzed with Simply blue staining and the data are the mean ± SD of 3 independent experiments. The data are obtained with image processing from the photos presented in Chapter 2.

For the cells, we found that indirect plasma treatment has always the same effect as reconstituted buffer for all the cases studied in this work, both for normal

and cancer cells. Then, we observed that direct plasma treatment is highly toxic for cancer cells and equally or even more toxic towards normal cells, exhibiting thus an anti-selectivity. On the other hand, indirect plasma treatment and reconstituted buffer have a moderate effect against cancer cells and a slight effect on normal cells, exhibiting, thus, a selectivity towards killing the cancer cells instead of normal cells. Very similar results were obtained with the treatment of the BSA protein, as direct plasma treatment damages more the protein than indirect plasma treatment and reconstituted buffer, which have both a more moderate effect. On top of that, the effect of indirect plasma treatment and reconstituted buffer on the protein is very similar as it was for the cells.

5.12 Conclusions

Our investigation on the effects *in vitro* of plasma treatment on the cells (both cancer and normal cells) in this first part of chapter 5 unveiled that normal cells are relatively resistant to reconstituted buffer and indirect plasma treatment (phase II), i.e. to a mixture of H_2O_2 + NO_2^- + NO_3^- + acidic pH, and also to plasma treatment (phase I, immediate effects). Taken separately, each phase has little effect on the viability of normal cells, while direct plasma treatment (phases I and II) is very toxic to normal cells. These results reveal that these two phases act in synergy on the death of normal cells (unlike the case of tumor cells, where the effect of these two phases is additive). Furthermore, the cell death process is extremely fast, since at 6 h post direct plasma treatment, most of the normal cells, but not of the tumor cells, have already died. These observations paved the way to numerous questions: why are normal cells resistant to indirect plasma treatment, but not tumor cells? Why is there such a big difference in the response to direct plasma treatment between normal and tumor cells? Why is there an additive effect of plasma treatment (immediate effects) and incubation in pPBS (early effects) in tumor cells and a synergistic effect of those treatments in normal cells? Additionally, what reactive species contribute to this phenomenon?

It is well described that normal and tumor cells have different redox balances. Many reports have shown that tumor cells counterbalance intrinsic oxidative stress by upregulating antioxidant defense[207,208]. This increase in basal ROS generation renders cancer cells highly dependent on antioxidant systems and more vulnerable to agents that abrogate the antioxidant system and/or increase the ROS level[209,210]. Furthermore, it has also been proposed that tumor cells express more aquaporins at their cytoplasmic membranes than homologous normal tissues, speeding up the uptake of H_2O_2 inside their cytosol[211,212]. These features of cancer cells could explain the sensitivity of tumor cells, but not that of normal cells, to indirect plasma treatment or reconstituted buffer, whose toxicity relies essentially on H_2O_2[33,39]. Recently, Bauer *et al.* have demonstrated that

singlet delta oxygen, $O_2(a^1\Delta_g)$, which is generated through the interaction between plasma-derived H_2O_2 and NO_2^-, is at the origin of a cascade reaction in tumor cells, but not in normal cells, leading to inactivation of membrane-associated catalase, which in turns favors H_2O_2 uptake and triggers cell death[29,196]. This model could in fact fully explain reconstituted buffer being as effective as indirect plasma treatment regarding the biological response of CAL27 and FaDu to these two treatment modalities, even if this model has been very recently questioned[213]. The striking finding in our work comes from the hypersensitivity of normal cells to direct plasma treatment that cannot be explained only by long-lived reactive species, but that also requires the participation of short/intermediate-lived reactive species. The synergy that we observed between phase I (plasma ON) and phase II (plasma OFF, incubation in pPBS) on the death of normal cells strongly suggests that, during phase I, normal cells, but not tumor cells, are "activated", rendering them very sensitive to phase II. Indeed, we demonstrated that normal cells exposed to plasma treatment (phase I only, immediate effects) followed immediately by incubation in another plasma-activated PBS (indirect plasma treatment) exhibit similar sensitivity as if they have been exposed to direct plasma treatment (phase I + phase II). Interestingly, the cell activation phenomenon was previously described by Yan *et al.* to explain why tumor cells are more sensitive to direct plasma treatment than indirect plasma treatment[189].

In our study, we propose that this activation state plays a minor role in the vulnerability of tumor cells to direct plasma treatment, since the toxicity of phase I and phase II is additive rather than synergic, and although direct plasma treatment remains more efficient than indirect plasma treatment, this difference is less pronounced in tumor cells than in normal cells. Yan *et al.* showed that, in the tumor pancreatic adeno carcinoma cell line PA-TU-8988T, the desensitization of activation takes 5 h after the plasma treatment[189]. It is possible that, in our experimental conditions, the deactivation is extremely fast in tumor cells compared to normal cells. We showed that this "activation state" is triggered by short/intermediate-lived reactive species present in the liquid phase, even after the plasma is switched OFF. The liquid chemistry induced by cold atmospheric pressure plasma is rather complex[23,27]. Here, we showed that DMSO (•OH and ClO^- scavenger) or Taurine (ClO^- scavenger) can prevent completely (DMSO) or partially (Taurine) plasma-induced "activation state" in normal cells, suggesting that both chlorine species and hydroxyl radicals are the major reactive species that induce the "activation state". However, knowing that the lifetime of hydroxyl radicals in solution is of few µs[214], this means that, to interact with the cells, they have to be produced in their vicinity, originating from a more stable species. We propose that this more stable species is ozone (O_3). Ozone has a lifetime in water at 25°C and pH 7 of about 200 s, but this value depends on several factors including the chemical composition of the solution. Ozone is produced during

plasma treatment (phase I, plasma ON, immediate effects), and can undergo decomposition via a chain reaction mechanism resulting in the production of free hydroxyl radicals (•OH)[108]. Unfortunately, we have not been able to measure the absolute concentration of O_3 in pPBS (by absorption spectroscopy in solution) due to interference with the high concentration of H_2O_2 and NO_2^- produced in our experimental conditions. Therefore, further experiments need to be set to validate this hypothesis. Nevertheless, our previous experiments with indigo showed that the solubility of ozone in pPBS is very low. Thus, we might have to look for other short- and/or intermediate-lived reactive species that could be toxic to the cells. It remains unclear how short/intermediate and long-lived reactive species cooperate to induce cell death preferentially in normal cells over tumor cells. It is important to keep in mind that the cellular membrane is the first line of defense towards exogenous stress, such as chemically reactive species, and it is well documented that the membrane composition is different between normal and tumor cells[215–217]. Membrane composition is essential for cell survival as lipids are used for energy storage, compartmentalization and signaling[218]. We propose that lipids undergo oxidation upon plasma treatment, leading to lipid peroxidation, which in turn increases membrane permeability[212,219], likely due to transient pore formation[219], thus allowing for more extracellular compounds, such as long-lived RONS, to enter into the cells. Our results on the cells permeabilization and BSA protein oxidation could be used as a first verification of this hypothesis even if a more detailed investigation is necessary. Moreover, since lipid peroxidation increases membrane fluidity and decreases the electric field threshold needed for transient pore formation[212], we cannot rule out a role, albeit modest, of the electric field in the toxicity of direct plasma treatment, especially towards normal cells. In conclusion, we have shown that normal and tumor cells respond differently to plasma-treated liquid, whether we consider the direct or indirect plasma treatments. Indeed, we described, in this study, a synergistic effect of short/intermediate-lived species and long-lived species to trigger important cell death in normal cells, while these cells are relatively resistant to long-lived species alone. In contrast, tumor cells are both sensitive to direct and indirect plasma treatments, essentially due to the action of long-lived species. While some models have been proposed to explain the anti-cancer specificity of plasma-treated liquids[29,218], it remains important to determine the precise role of the cell membrane and its composition in the cell sensitivity or cell resistance to plasma treatment.

Second part: Preserving the anti-cancer capability of pPBS over time

5.13 Cell viability post pPBS treatment

In chapter 4, a detailed analysis of the pertinent conservation conditions of pPBS in order to preserve over time the concentrations of the long-lived reactive species (H_2O_2, NO_2^- and NO_3^-) as measured just after plasma treatment was conducted. Having established that this type of plasma-treated liquids should be stored at +4 °C or +20 °C and that temperatures that include freezing of the solution must be avoided, we wanted then to verify that the cytotoxic activity of pPBS is highly related to these RONS, by confirming that for pPBS to retain its cytotoxic activity it should be also stored at the same positive temperatures.

The cytotoxicity of the pPBS under different storage conditions was studied on adherent DC-3F cells for a treatment time (time of incubation in the pPBS) of 10 minutes and analyzed via a clonogenic assay (Figure 5.24 and Table 2). Firstly, we observed that the pPBS was highly effective in reducing the cells' viability, even after only 10 minutes of treatment. As a matter of fact, considering the total number of colonies count (normal and small colonies), the treatment of the DC-3F cells at D0 with freshly produced pPBS, maintained at room temperature for a few hours, reduced their viability by 60 %. Subsequently, the ability of pPBS to preserve its anti-cancer capability was evaluated when stored for up to 21 days at +4 °C and –20 °C. Our results show that, even after 21 days of storage at +4 °C, the pPBS retained most of its cytotoxic and cytostatic efficacy, as the percentage of apparently unaffected cells (represented by the percentage of large colonies) remained unchanged (about 16.6% at D21 versus 14.0% at D0). Actually, the cytotoxic effect (displayed by the reduction in the total number of colonies, from about 60% at D0 to about 49% at D21) slightly decreased, while the cytostatic effect (represented by the percentage of small colonies) increased concomitantly (from about 26% at D0 to about 34% at D21). Contrariwise, when the pPBS was stored at –20 °C, it was much less effective in inducing the cell's death (even after only 1 day of storage). The cytotoxic effect (reduction in the number of colonies) dropped down to about 14% of the cells at D21. Since the cytostatic effect (percentage of small colonies) remained similar to that of the pPBS stored at +4° C, the results show that 51% of the cells exposed to the pPBS stored for 21 days at –20 °C were unaffected by the pPBS.

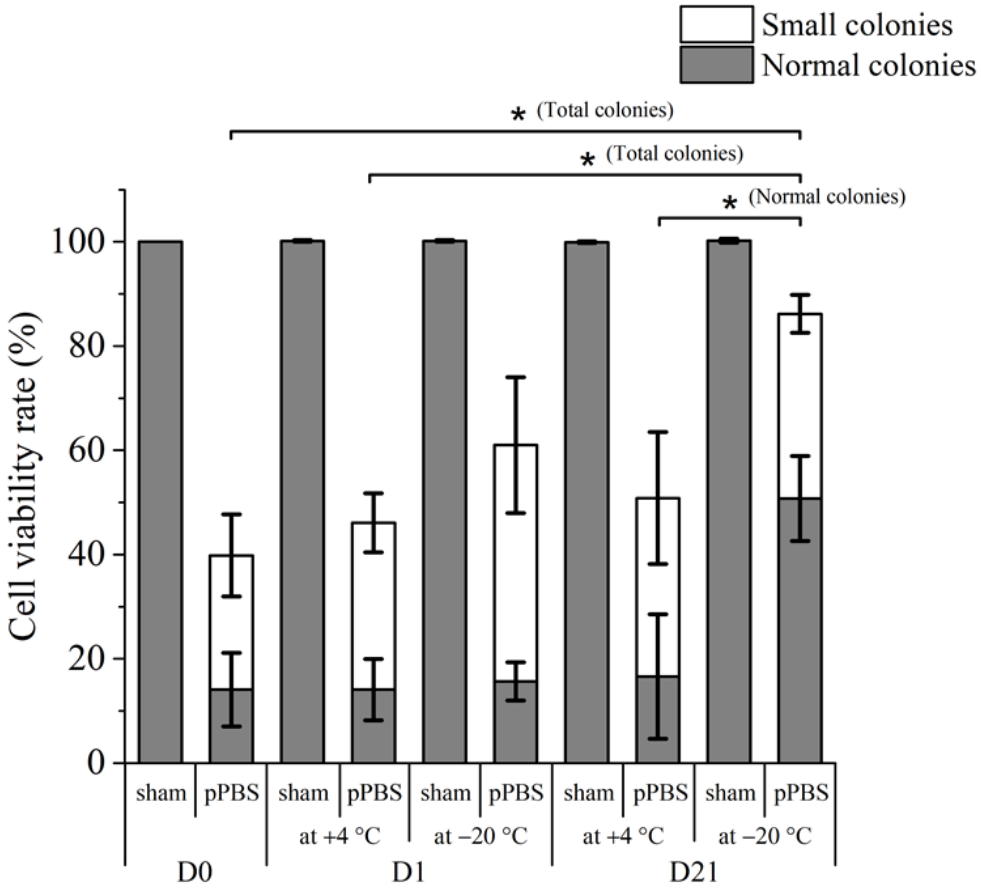

Figure 5.24 Cytotoxicity of pPBS previously stored under different storage conditions to adherent DC-3F cells. After being incubated in pPBS for 10 min, DC-3F cells were plated immediately. The cell viability rate is presented as the number of colonies formed from viable cells five days after the treatment. Results from three independent experiments (each in quadruplicate) are shown as mean values ± SD for each parameter set. Statistical significance levels are presented as p-values of < 0.05 (*), < 0.01 (**), < 0.001 (***) and < 0.0001 (****). If no statistical significance is indicated, then p-values > 0.05 (NS).

Storage conditions		Normal colonies (%)	Small colonies (%)	Total colonies (%)
Day 0	RT	14.0 ± 7.0	25.8 ± 7.9	39.8 ± 14.9
Day 1	+4°C	14.0 ± 5.9	32.0 ± 5.7	46.0 ± 11.6
	–20°C	15.7 ± 3.7	45.3 ± 13.1	61.0 ± 16.8
Day 21	+4°C	16.6 ± 11.9	34.2 ± 12.7	50.8 ± 24.6
	–20°C	50.8 ± 8.1	35.4 ± 3.7	86.2 ± 11.8

Table 2. Cytotoxicity of pPBS stored at different storage conditions as a function of colonies formed after being treated with pPBS for 10 minutes and immediately cultured for 5 days at 37 °C in a 5% CO_2 humidified cell incubator. Visible colonies were stained, counted and normalized to the number of clones in the corresponding sham, expressed as 100%. Colonies containing more than 50 cells were counted as “normal size colonies”, and those containing from *c.a.* 20 to fewer than 50 cells were counted as “small colonies”. The data are the mean ± SD of 3 independent

experiments (each in quadruplicate).

5.14 Cell membrane permeabilization post pPBS treatment

The effect on the cell membrane permeabilization of pPBS stored under different conditions was also studied on two different cell lines (DC-3F and LPB cells) of different origins. The results are presented in Figure 5.25 First of all, we observed that the plasma membrane of both cell lines was significantly permeabilized after 1 hour of contact with pPBS, regardless the storage conditions of pPBS. This effect is in agreement with what we have previously reported[12]. Contrary to the effect of the storage conditions observed on the cell's viability, the pPBS stored at +4 °C and –20 °C displayed the same capabilities (or not) of permeabilizing the cells, for both cell lines and for the different storage times studied. Interestingly, when the pPBS was stored for 21 days (both at +4 °C and –20 °C), it was still able to permeabilize the DC-3F cells but not the LPB cells. Indeed, even in conditions where the concentration of the RONS was preserved (+4 °C), the pPBS was no longer able to effectively permeabilize the LPB cells after 21 days of storage. Collectively, these results unveil that the NO_2^-, which is massively degraded upon storage at –20 °C but not at +4 °C, does not play an important role in the permeabilization of the LPB cancer cell line. This could mean that H_2O_2 is the main driver of the cellular membrane permeabilization due to pPBS. As H_2O_2 in the pPBS is also degraded from 1 to 21 days of storage (our results showed a decrease of 10% of its concentration – see section 4.3 in Chapter 4), its concentration at D21 might be under the threshold required for permeabilizing the LPB cells. However, the presence of another reactive species in pPBS (that was not studied here), responsible for the permeabilization of LPB cells and degraded over the 21 days of storage, cannot be excluded.

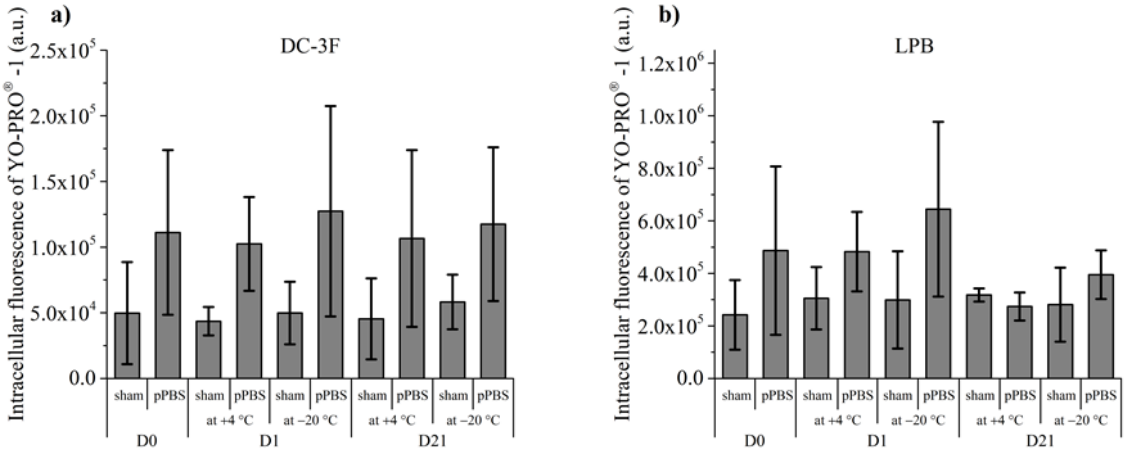

Figure 5.25 Effect of pPBS, previously stored at different storage conditions, on cell membrane permeabilization of adherent DC-3F and LPB cells. The ability of pPBS to permeabilize the cell membrane after 1 hour of treatment (incubation in pPBS) was analyzed by flow cytometry and

expressed as an increase of the intracellular fluorescence of YO-PRO®-1 iodide in permeabilized cells. The data from 3 independent experiments (each in at least 4 independent replicates) are shown as mean values ± SD for each parameter set. If no statistical significance is indicated, then p-values > 0.05 (NS).

Given that the cells permeabilization did not differ when the plasma-treated solution was stored at different temperatures, we wanted to extend our investigation on the effect of pPBS on the cells permeabilization. To do so, we used a different biological model as a target of the plasma and/or the plasma-treated solution. More specifically, we treated Giant Unilamellar Vesicles (GUVs), which consist of a lipid bilayer. Their size is comparable to that of eukaryotic cells, thus mimicking the same lipid reservoir and membrane curvature[220].

The purpose of this work was to study the plasma-induced oxidation of three different types of GUVs. The principal advantage of membrane systems such as GUVs over cellular systems is the precise control of the lipid membrane composition. Thus, because of the simplicity of the membrane composition, any unknown factors that could play a role to its permeabilization are reduced.

Different experimental conditions that result on the production of different concentrations of reactive oxygen and nitrogen species were studied. The lipids, in suspension in solutions of PBS, were treated both directly and indirectly with all three reactors that were used in this work, i.e. the single- and multi-plasma jets (R1 and R2, respectively) and the MCSD (R3).

Firstly, the DLPC (Chapter 2, section 2.2.5.1) lipids were treated by the MSCD in conditions where we observed the highest production of ozone (when 3% O_2 is used in the gas composition) or of singlet delta oxygen (when 0.5% O_2 is used in the gas composition)[132]. These conditions correspond to a high gas flow rate of 8 slm. With these experimental conditions, we achieved a high oxidation rate of the lipids that was in the range of 92.6-100%.

We continued our study by treating with the MCSD all three different types of lipids, but we adjusted the working conditions to oxidize a smaller percentage of the lipids. This was necessary to facilitate a comparative study on the oxidation rate, due to plasma treatment, between the three lipids. For the DOPC, we observed no oxidation when treated with a gas flow rate of 3 slm no matter what the gas composition was (100% He or 99.5% He / 0.5% O_2 or 97% He / 3% O_2). Similar results were obtained also when the DOPC lipids were treated by the single-plasma jet. Here, we have to underline that, for the single-plasma jet, the

experimental conditions were kept the same as for the cells' treatment, i.e. 1 slm of 99.8% He / 0.2% O_2, 8 mm of treatment distance, and 6 kV of high voltage amplitude. Subsequently, we had an oxidation rate of around 10% for DHAPC and an oxidation rate of around 30% for DLPC when treated by the MCSD. The same oxidation rates were also obtained when the single-plasma jet was used. Nevertheless, these results are not statistically significant if we take under consideration the error bars and need to be repeated in order to be conclusive. Thus, what we should keep for the direct treatment of the lipids is the very high oxidation rate at conditions that we know to be producing high fluxes of ozone and singlet delta oxygen and a slightly higher oxidation rate of the DLPC lipids (compared to DOPC and DHAPC), even if the latter is not conclusive. For those three unsaturated phospholipids used in this study (DOPC, DLPC and DHAPC), with two, four and twelve carbon-carbon double bonds on their fatty acyl acids, respectively, their oxidation rate and their variation were not a in good agreement with the unsaturation degree as we would expect the DHAPC lipids to exhibit a higher oxidation rate.

We continued our study with the indirect treatment of the lipids. The lipids were treated indirectly only by the single- and the multi-plasma jets. We observed an oxidation rate of 16% for the multi-plasma jet and an oxidation rate of 4% for the single-plasma jet (when the DLPC lipids were treated). If we take under consideration that the treatment time with R2 is 20 minutes and with R1 is 12 minutes and above all that with R2 we produce 2.5 times more H_2O_2, these results are logical even if they cannot be conclusive because they are not statistically significant (as for the direct treatment).

Third part: Plasma-electrochemotherapy

This third part of chapter 5 contains our results on the effect of the plasma alone but also in combination with μs PEFs and anti-cancer drugs (chemotherapy) against cancers both *in vitro* and *in vivo*. It is thus divided in two sections. Firstly, the results obtained with the *in vitro* experiments are presented, and, secondly, the *in vivo* application of the plasma-electrochemotherapy combined treatment is investigated.

5.15 In vitro studies of non-thermal plasma and its combination with electrochemotherapy

Electrochemotherapy (ECT) is a non-thermal, safe, and efficient tumor treatment[221–223] that is currently used in more than 150 clinics in the European Union and abroad, together with its application in veterinary oncology for treatment of metastases as well as primary tumors[224,225]. ECT is based on the combination of otherwise non- or low-permeant drugs possessing a high intrinsic cytotoxicity (e.g. hydrophilic molecules such as bleomycin or cisplatin) with the local application of a train of eight short and intense monopolar electric pulses (EPs), yet nontoxic[226,227]. The applied EPs create a transient transmembrane potential difference that causes changes in the cell membrane structure and transiently permeabilize its phospholipid bilayer[226]. This biophysical process, which is named reversible electroporation or reversible electro-permeabilization, allows for the penetration of the chemotherapeutic agent inside the cell to generate irreversible DNA damages. ECT selectively kills the tumor cells at the low doses of the chemotherapeutic agents used, since bleomycin (BLM, of 1415 Da) at low doses is only toxic for the cells dividing in the volume treated by the EPs. Overall, no serious negative effects that are related to the application of ECT on patients have ever been reported. Nevertheless, one of the main drawbacks of ECT application are muscles contraction with discomfort sensations associated with repeated electrical stimulation, mainly linked to the characteristics of the high-amplitude electric pulses used. Indeed, these EPs depolarize the neurons in the treated area and can, therefore, generate action potentials, either in the musculo-excitatory nerves or in the sensory nerves, imposing the use of at least a local anesthesia during the treatment[228]. Recent clinical studies have reported that the painful sensation that is associated to ECT can last longer for locally advanced and metastatic soft tissue sarcomas[223] and large cutaneous recurrences of breast cancer[229]. The main objective of the present study was, therefore, to determine new conditions for ECT, devoid of these side effects. We were interested in reducing the electric field strength of the classical 100 microseconds pulses used in ECT, without reducing the permeabilization of the cell membrane. We suggest a combined treatment of μsPEFs with non-thermal plasma (NTP) to outperform ECT since cell electro-permeabilization is characterized by lipids oxidation at the time of the electric pulses delivery[230]. The study was especially focused on malignant melanoma cells, a very aggressive skin cancer, which is one of the main targets of ECT[227,231,232] and plasma medicine[233,234]. The responses to the combined treatment of the plasma-treated PBS+/+ (or pPBS) with pulsed electric fields of different strengths were investigated while using adherent DC-3F Chinese hamster lung fibroblasts and adherent malignant B16-F10 murine melanoma cells. Cell membrane permeabilization was monitored by flow cytometry. In this Thesis manuscript only part of the results are presented and the reader can find more information about the work in our published article[12].

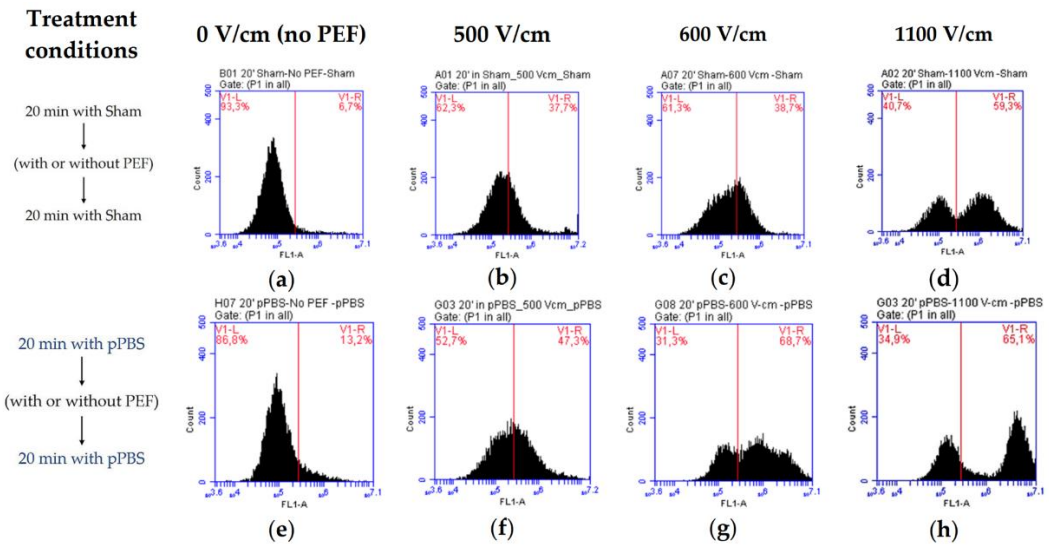

Figure 5.26 Flow cytometry analysis of the combined treatment in adherent B16-F10 murine melanoma cells to compare the effects of the pPBS (e-h) versus the control (a-d) with μsPEFs of 0 (a,e), 500 (b,f), 600 (c,g) and 1100 (d,h) V/cm. The peak of count as a function of the green fluorescence (FL1-A) shifts towards higher values of the fluorescence per cell, indicating the enhancement of the permeabilization of the cell membrane.

As we can see in Figure 5.26, for all the different voltage amplitudes used in this study we have a stronger permeabilization with the cells if they are treated with pPBS (before and after their treatment with the electric field) instead of sham, which is untreated PBS. On the top of that, we can see that we have a stronger permeabilization of the cells if pulses of 600 V/cm are applied and pPBS is also used than if just pulses of 1100 V/cm are applied. That totally supports our initial hypothesis, that if the cancer cells are being exposed to pPBS in parallel with the μsPEFs, smaller voltage amplitudes could be used in order to reach the same level of permeabilization. This allows to reduce the side effects of classical electrochemotherapy.

5.16 *In vivo* studies of non-thermal plasma and its combination with electrochemotherapy

As with the *in vitro* experiments presented in the third part of this chapter, again in the study presented here the purpose was to achieve the same tumor reduction with electrical pulses of a smaller amplitude, if pPBS is used as a parallel treatment. In this part of the fifth chapter, the experiments were conducted *in*

vivo on immunocompetent C57Bl/6J mice bearing s.c. LPB tumors that were treated with the combination of pPBS and ECT.

Subcutaneous LPB sarcoma tumors were treated either with i.v. Bleomycin (BLM) (group 1 Control) or with ECT (group 2, which received i.v. administration of BLM in the retro-orbital sinus followed by 8 square-wave EPs of 100 µs, at 1000 V/cm and 1 Hz) or with 1-hour-pPBS or 20-minutes-pPBS combined with ECT (group 4 and group 5, respectively) or with 1-hour-pPBS or 20-minutes-pPBS followed by i.v. BLM (no electric pulse, group 3 and group 6, respectively). The tested parameters in the six different groups of treatment are described in Table 2. Note that in the first *in vivo* experiment, there were 5 experimental groups (group 1 to group 5), while, in the second and third *in vivo* experiments, there were 6 experimental groups.

Groups	Treatment parameters
1	Control (i.v. administration of BLM)
2	ECT (i.v. BLM followed by 8 square-wave EPs of 100 µs, at 1000 V/cm and 1 Hz)
3	i.t. 1-hour-pPBS followed by i.v. BLM
4	i.t. 1-hour-pPBS followed by ECT
5	i.t. 20-minutes -pPBS followed by ECT
6	i.t. 20-minutes-pPBS followed by i.v. BLM

Table 2. *In vivo* studied parameters of the combined treatment with pPBS and ECT in female C57Bl/6J mice bearing s.c. murine LPB fibrosarcoma.

In the following, three different *in vivo* studies that took place under the same experimental conditions are presented. Differences observed in anti-tumor effectiveness were evaluated by tumor growth delay.

5.16.1 1st *in vivo* anti-cancer treatment combining pPBS and ECT

The tumor growth delay of the first *in vivo* experiment is shown in Figure 5.27. The efficacy of the single- and combined treatments were compared with ECT as gold standard. We did not observe a delay of tumor growth in groups receiving treatment either with pPBS alone (group 3) or with pPBS (20-min-pPBS) followed by ECT (group 5), as compared with the ECT (group 2). On the contrary, with the pPBS alone, there could be a tendency to accelerate the tumor growth, as compared with the Control (group 1). If compared to the Control group, the combined treatment employing pPBS (1-hour-pPBS) followed by ECT (group 4) delayed the tumor growth for 6 days, and ECT alone decelerated the tumor growth by 4 days.

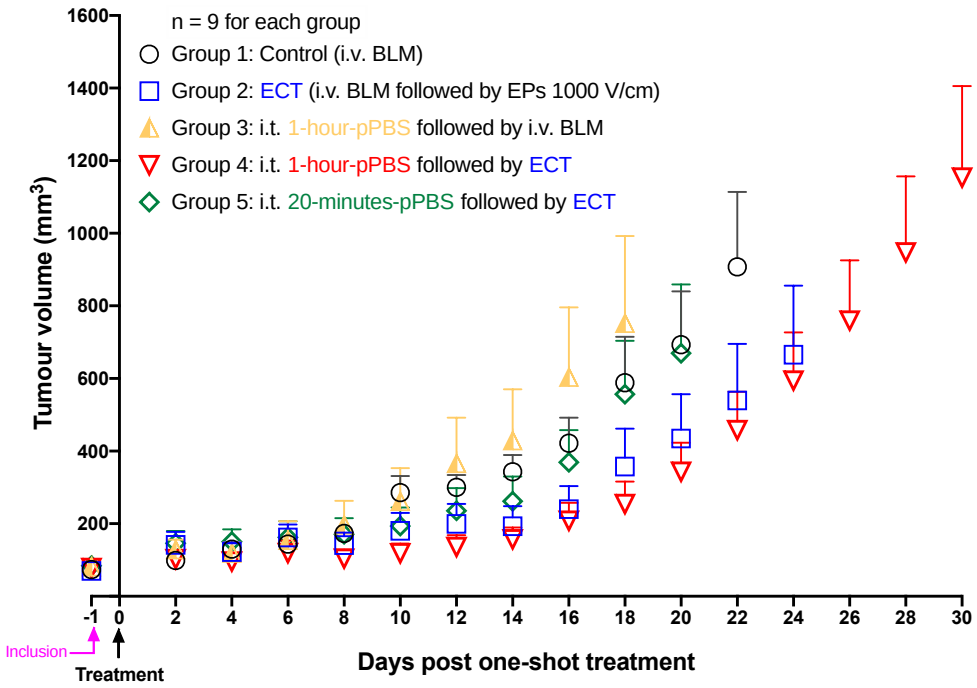

Figure 5.27 The tumor growth delay in female C57Bl/6J mice treated with pPBS combined with ECT in the first experiment. The number of mice was n = 9 mice in each experimental group. Data represented as mean ± SEM values. The tumor evolution is shown until the first animal of each group reached an endpoint.

5.16.2 2nd *in vivo* anti-cancer treatment combining pPBS and ECT

The tumor growth delay of the second *in vivo* experiment is shown in Figure 5.28. There are clearly two types of response to the treatments: a group of curves presenting all the treatments without µsPEF (groups 1, 3 and 6) and a group of curves presenting the treatments with µsPEFs (groups 2, 4 and 5). We observed that monotherapy with pPBS (i.e. without ECT), either the 20-minutes-pPBS (group 6) or the 1-hour-pPBS (group 3), decelerated the tumor growth for only 2 days, as compared with the Control (group 1), showing no obvious anti-cancer effect. Interestingly, with the combined treatment employing pPBS followed by ECT, better anti-tumor effects were observed, tumor growth delay being 4 days in group 4 (1-hour-pPBS followed by ECT) and 7 days in group 5 (20-minutes-pPBS followed by ECT). This displacement of tumor growth curves also reveals the differences in eventual synergy of ECT and the two pPBS: anti-tumor synergy effectiveness was much more pronounced with the 20-minutes-pPBS combined with ECT than with the 1-hour-pPBScombined with ECT.

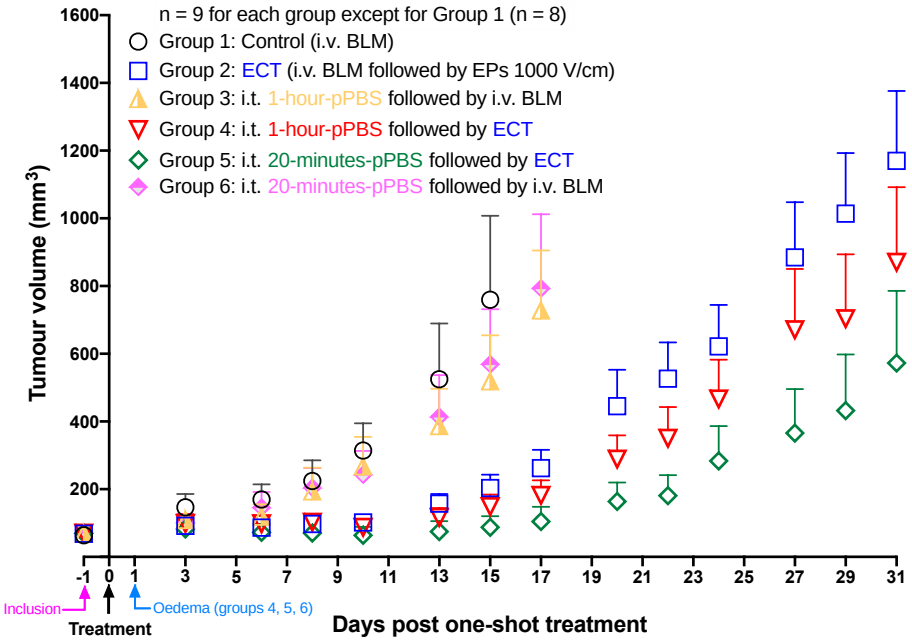

Figure 5.28 The tumor growth delay in female C57Bl/6J mice treated with pPBS combined with ECT in the second experiment. The number of mice was n = 9 mice in each experimental group. Data represented as mean ± SEM values. The tumor evolution is shown until the first animal of each group reached an endpoint.

5.16.3 3rd *in vivo* anti-cancer treatment combining pPBS and ECT

The tumor growth delay of the third *in vivo* experiment is shown in Figure 5.29. We observe that in this case all the treatment modalities that were applied succeeded to reduce the tumor volume when compared to the Control. More specifically, we can distinguish two different groups of treatment response. Firstly, we have a similar response to the tumor growth when the mice are treated by 1-hour-pPBS alone and when they are treated by 1-hour- or 20-minutes-pPBS followed by a BLM treatment. Secondly, we have a more efficient treatment if ECT is used and especially if the mice are treated with 20-minutes-pPBS followed by ECT. With this last treatment strategy, the maximum reduction of the tumor growth rate is achieved.

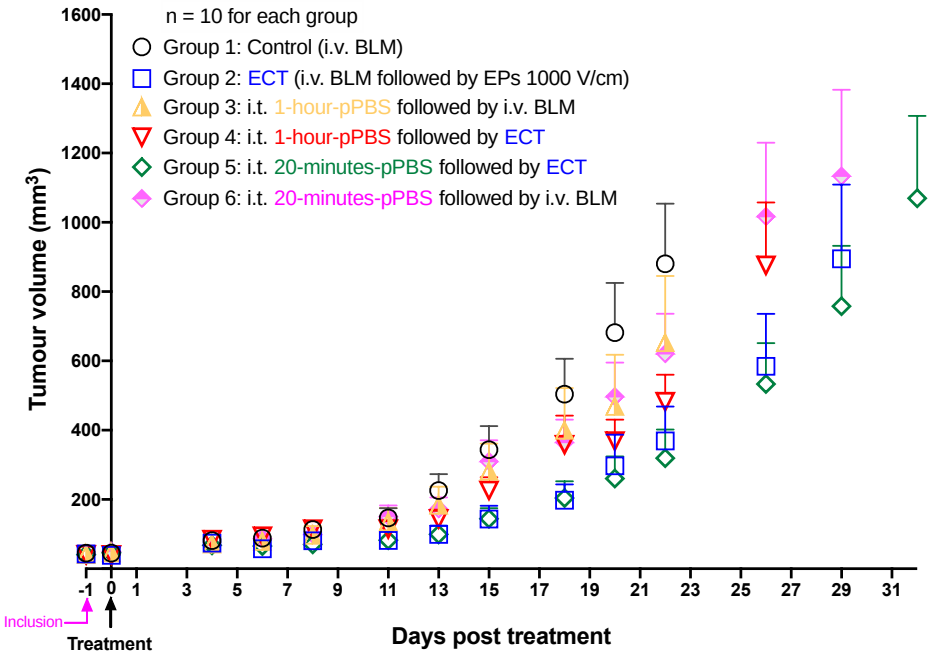

Figure 5.29 The tumor growth delay in female C57Bl/6J mice treated with pPBS combined with ECT in the third experiment. The number of mice was n = 10 mice in each experimental group. Data represented as mean ± SEM values. The tumor evolution is shown until the first animal of each group reached an endpoint.

5.16.4 Discussion

For most of the cases, we can see that a 20-minutes-pPBS treatment combined with ECT has the best results at delaying the tumor growth when compared to the other studied therapies. The main difference of the three different *in vivo* experiments is that for the first one the most efficient strategy does not include a pPBS treatment of the mice while in the second and third experiments the most efficient treatment is the treatment with a 20-minutes-pPBS followed by ECT. Collectively, more *in vivo* studies are required to obtain some conclusive information regarding the parallel use of plasma-treated liquids and ECT as an anti-cancer therapy *in vivo*.

Given that, as presented in Chapter 4, the concentration of the reactive oxygen and nitrogen species in the pPBS increases almost linearly with the increase of the plasma treatment time, someone could wonder why the 1-hour-pPBS treatment (in combination or not with ECT) is for most of the cases a less efficient strategy to delay the tumor growth than the 20-minutes-pPBS treatment

(in combination or not with ECT). To answer that, we have to recall our results from Chapter 4, where we found that, in highly acidic environments, hydrogen peroxide can oxidize nitrites leading thus to an important reduction of both species concentrations. It should be pointed out here that the 20 minutes treatment of PBS with the plasma results in a final pH of around 6, while the 1-hour plasma treatment of the PBS results in a final pH of around 2.5-3. Thus, after 1 hour of plasma treatment, the solution becomes highly acidic and the nitrite oxidation by hydrogen peroxide is highly favored. Given that, the decreased efficiency of the 1-hour treated PBS towards killing the cancer cells can be expected, as lower concentrations of H_2O_2 and NO_2^- (that were previously shown to be key players in the anti-cancer capacity of plasma-treated solutions) are present in the liquid.

Conclusions

In the fifth chapter, we thoroughly studied direct and indirect plasma treatments to bring new insights into the potential use of plasmas for cancer treatment. We showed that direct plasma treatment is slightly more efficient than indirect plasma treatment and reconstituted buffer at inducing lipid peroxidation, intracellular increase of ROS and cancer cell death in tumor cells, our data also revealed that reconstituted buffer is equivalent to indirect plasma treatment. In contrast, normal cells are quite insensitive to these two last treatment modalities. However, they are extremely sensitive to direct plasma treatment. Our data also highlight the presence in plasma-treated PBS of yet unidentified short- and/or intermediate-lived reactive species that contribute to cell death. In this study, we provide strong evidence that, *in vitro*, the concentration of RONS (H_2O_2, NO_2^- and NO_3^-) in combination with the acidic pH are the main drivers of plasma-induced PBS toxicity in tumor cells but not in normal cells, which makes ad hoc reconstituted solutions powerful anti-tumor treatments. In marked contrast, direct plasma treatment is deleterious for normal cells *in vitro* and should be avoided. On top of that, we investigated the impact of the appropriate conservation of pPBS on its anti-cancer efficacy on human cancer cells *in vitro*, by quantifying the viability and the membrane permeabilization of the cells following treatment with those solutions. The cytotoxic efficiency of the pPBS was conserved when stored at conditions that did not degrade the three aforementioned long-lived reactive species, i.e., at 4 ^oC. Contrariwise, when the pPBS was stored at -20^oC, it was less efficient at killing the cancer cells even after the first day of storage. Also, the study of the efficiency of all three reactors, i.e., cold atmospheric pressure single- and multi-jet (reactors 1 and 2) and MCSD (reactor 3), at oxidizing different types of lipids is also presented. For the experimental conditions where we have established an increased production of

reactive oxygen species, especially ozone and singlet delta oxygen, we observed a high oxidation rate of the lipids, while for the working conditions for which the production of these reactive species is lower the oxidation of the lipids is comparable to the error bars and, thus, our results are not conclusive. We also investigated the potential capabilities of the combined application of indirect non-thermal plasma treatment and microsecond Pulsed Electric Fields (μsPEFs) to outperform *in vitro* cell electro-permeabilization, the basis of electrochemotherapy (ECT). The B16-F10 cells were more sensitive to the combined treatment than DC-3F cells. Importantly, the percentage of permeabilized cells reached values like those of cells exposed to classical electroporation field amplitude (1100 V/cm) when the cells were treated with pPBS before and after being exposed only to very low PEF amplitude (600 V/cm). Although the level of permeabilization of the cells that are treated by the pPBS and the PEFs at 600 V/cm is lower than the level reached after the exposure to μsPEFs alone at 1100 V/cm, the combined treatment opens the possibility to reduce the amplitude of the EPs used in ECT, potentially allowing for a novel ECT with reduced side-effects. Finally, we conducted *in vivo* studies on inbred female immunocompetent C57Bl/6J mice. For most of the cases, we saw that a 20-minutes-pPBS treatment combined with ECT has the best results at delaying the tumor growth when compared to the other studied therapies.

General Conclusions and Perspectives

Due to the efficiency of plasma treatment against different types of tumors, a great attention of the plasma scientific community has been paid, especially during the last decade, to the understanding of the plasma interaction with cancer cells both *in vitro* and *in vivo*. The purpose of this work was to contribute towards this direction by investigating both the plasma physicochemical properties and its impact on different biological targets, with the main being various types of cancer cells. Our work was separated in three different parts. The **first** part contains the study of the gaseous phase of the plasmas and its main purpose was to provide information on the physical and chemical properties of the produced plasmas. The **second** part was an analytical investigation of the chemical composition of plasma-treated PBS (pPBS). Thus, the production in the pPBS of H_2O_2, NO_2^-, NO_3^-, •OH, $O_2(a^1\Delta_g)$, O_3, HCl^- and ONOO– was investigated. Knowing that these short- and long-lived reactive oxygen and nitrogen species are the main drivers of the anti-cancer capacity of plasma treatment in oncology, the **third** part of this work was the plasma application on biological targets and the assessment of these reactive species contribution to its cytotoxicity. This has been done in close collaboration with biologists from the Institut Curie and the Institut Gustave Roussy.

In the **third** Chapter of this Thesis, we examined several key characteristics of the produced cold atmospheric-pressure plasmas that are related with several applications in biomedicine. These characteristics are the gas temperature, the electric field and electron density in the front of the ionization wave as they might play a role on the efficiency of plasmas in different biomedical applications. We found that the localized electric field in the front of the ionization wave is constant or even decreasing at positions inside the capillary tube and when moving from the point of ignition of the plasma towards the tube orifice. On the other hand, is the electric field increases after exiting the dielectric tube while moving towards the plasma-treated target. On top of that, the same tendency is also observed for the electron density and the gas temperature. This is most probably due to the contraction of the ionization waves as they move away from the capillary, which strengthens the electric field by focusing the charge density into a smaller volume. The maximum values of the electric field, i.e. 17-18 kV/cm, are measured just before the contact of the ionization wave with the liquid. Given that to permeabilize the cellular membrane an electric field of 1-2 kV/cm is sufficient, the electric field in the front of the ionization wave could play a role on the anti-cancer

efficiency of the plasma treatment, by permeabilizing the cell membranes and, thus, facilitating the transport of plasma-produced or -induced reactive species into the cells. The above-mentioned values of the electric field were measured for a treatment distance of 8 mm. If a treatment distance of 20 mm is used, the same tendency of the electric field evolution is observed, but its actual values are significantly lower at positions outside the capillary tube. In the future, it is essential to study the impact of the liquid solution on the physical properties of the plasma. More specifically, we should understand if the increase of the localized electric field of the ionization wave is linked to the contact of the plasma with the liquid or not. On top of that, different liquids as well as other types of materials should be used as a target of the plasma to determine if the targets characteristics (structure, conductivity etc.) could play role on the composition of the produced plasma. Finally, other experimental conditions such as different gas compositions and higher or lower high voltage amplitudes and frequencies should be also studied to determine first of all if they affect the gas temperature and secondly if they change the electric field and the electron density in the front of the ionization wave. Except from the investigation of the physical properties of the plasma, its chemical composition should be also studied in the future in order to optimize the production of RONS. Thus, the concentrations of H_2O_2, NO_2^-, NO_3^-, O_3 and $O_2(a^1\Delta_g)$ should be measured by means of Laser Induced Fluorescence (LIF) and/or Fourier-transform infrared spectroscopy (FTIR).

In the **fourth** chapter, we characterized the pPBS, in terms of short-, intermediate- and long-lived reactive species concentrations for different experimental conditions and then we assessed the storage conditions (storage temperature) and the maximum period that it can retain its chemical composition. In parallel, the pH, the conductivity, and the temperature of the pPBS were also monitored. The absolute concentration of H_2O_2, NO_2^- and NO_3^- in the pPBS was measured, while in parallel we also detected the •OH, $O_2(a^1\Delta_g)$, O_3, HCl^- and ONOO– and measured their relative concentration. We found that to maximize the production of the long-lived reactive species (H_2O_2, NO_2^- and NO_3^-) a specific range of treatment distances should be used in respect always to the gas flow rate. The gas composition did not significantly affect the production of long-lived reactive species, but it played an important role on the production of short- and intermediate lived reactive species (•OH, $O_2(a^1\Delta_g)$, O_3 and HCl^-) as even a small percentage (0.2%) of molecular oxygen in the gas admixture increased significantly their concentration. The concentration of all the reactive oxygen and nitrogen species studied here increased proportionally with the increase of the plasma treatment time. This was also the case for the conductivity of the pPBS, while its pH was reduced almost linearly with the increase of the plasma treatment time. Finally, we found that when pPBS was stored at +4 °C, the concentration of the main reactive species responsible for its anti-cancer capacity,

i.e. H_2O_2 and NO_2^-, remained sufficiently stable for up to 21 days of storage. On the other hand, we showed that when pPBS was stored at temperatures below 0 °C (–20 °C and –80 °C here) the concentration of the aforementioned RONS was rapidly reduced. In fact, the freezing of pPBS results in its acidification, enabling the pH-dependent NO_2^- oxidation by H_2O_2, which in turn degrades both reactive species. However, we have shown that the freezing rate is irrelevant. We concluded that pPBS can preserve their cytotoxic activity, at least for 21 days, if stored at +20 °C or +4 °C, providing a basis for practical application of plasma-activated PBS in cancer therapy. From our experimental work, we can underline the need for new methods to quantify the short- and intermediate-lived reactive species in the plasma-treated solutions. Most of the currently available techniques do not selectively detect certain reactive species. For example, H2DCFDA is widely used to detect ROS generation during the cell cycle. Thus, we would expect it to react also with other ROS like O atoms. Selectivity tests were not implemented in this Thesis due to lack of time, but, in the future, they would be necessary to confirm if these techniques could be used for short-lived species measurement. The accurate measurements of these reactive species could enable the systematic understanding of the plasma treated liquids chemistry and therefore their utilization in various biomedical applications. On top of that, and regarding the conservation of pPBS, other factors that might affect the stability of the long-lived reactive species concentration should be studied such as packaging and the impact of light to be able to use them as medication.

In the fifth chapter, we thoroughly studied direct and indirect plasma treatments to bring new insights into the potential use of plasmas for cancer treatment. We used two models of head and neck cancer cells, CAL27 and FaDu, and three models of normal cells (1Br3, NHK, and RPE-hTERT). Cells were exposed to direct plasma treatment, indirect plasma treatment or reconstituted buffer. We showed that direct plasma treatment is slightly more efficient than indirect plasma treatment and reconstituted buffer at inducing lipid peroxidation, intracellular increase of ROS and cancer cell death in tumor cells. Our data also revealed that reconstituted buffer is equivalent to indirect plasma treatment. In contrast, normal cells are quite insensitive to these two last treatment modalities. However, they are extremely sensitive to direct plasma treatment. Our data also highlight the presence in plasma-treated PBS of yet unidentified short- and/or intermediate-lived reactive species that contribute to cell death. In this study, we provide strong evidence that, *in vitro*, the concentration of RONS (H_2O_2, NO_2^- and NO_3^-) in combination with the acidic pH are the main drivers of plasma-induced PBS toxicity in tumor cells but not in normal cells, which makes ad hoc reconstituted solutions powerful anti-tumor treatments. In marked contrast, direct plasma treatment is deleterious for normal cells *in vitro* and should be avoided. On top of that, we investigated the impact of the appropriate

conservation of pPBS on its anti-cancer efficacy on cancer cells *in vitro*, by quantifying the viability and the membrane permeabilization of the cells following treatment with those solutions. The cytotoxic efficiency of the pPBS was conserved when stored at conditions that did not degrade the three aforementioned long-lived reactive species, i.e. at 4 ^{o}C. Contrariwise, when the pPBS was stored at -20^{o}C, it was less efficient at killing the cancer cells even after the first day of storage. On top of that, the study of the efficiency of all three reactors, i.e. cold atmospheric pressure single- and multi-jet (reactors 1 and 2) and MCSD (reactor 3), at oxidizing different types of lipids is also presented. For this study, we treated the lipids both directly and indirectly. In this work, three different types of lipids were treated: a) 1,2-Dioleoyl-sn-glycero-3-phosphocholine (DOPC), b) 1,2-dilauroyl-sn-glycero-3-phosphocholine (DLPC) and c) 1,2-Didocosahexaenoyl-sn-glycero-3-phosphocholine. Besides the direct and indirect plasma treatments, we also treated the lipids with ad-hoc concentrations of hydrogen peroxide. For the experimental conditions where we have established an increased production of reactive oxygen species, especially ozone and singlet delta oxygen, we observed a high oxidation rate of the lipids, while for the working conditions for which the production of these reactive species is lower, the oxidation of the lipids is comparable to the error bars and, thus, our results are not conclusive. We also investigated the potential capabilities of the combined application of indirect plasma treatment and microsecond Pulsed Electric Fields (μsPEFs) to outperform *in vitro* cell electro-permeabilization, the basis of electrochemotherapy (ECT). Thus, PBS was plasma-treated (pPBS) and used afterwards to explore the effects of its combination with μsPEFs. Analysis of two different cell lines (DC-3F Chinese hamster lung fibroblasts and malignant B16-F10 murine melanoma cells) by flow cytometry revealed that this combination resulted in significant increases of the level of cell membrane electro-permeabilization, even at very low electric field amplitude. The B16-F10 cells were more sensitive to the combined treatment than DC-3F cells. Importantly, the percentage of permeabilized cells reached values like those of cells exposed to classical electroporation field amplitude (1100 V/cm) when the cells were treated with pPBS before and after being exposed only to very low PEF amplitude (600 V/cm). Although the level of permeabilization of the cells that are treated by the pPBS and the PEFs at 600 V/cm is lower than the level reached after the exposure to μsPEFs alone at 1100 V/cm, the combined treatment opens the possibility to reduce the amplitude of the EPs used in ECT, potentially allowing for a novel ECT with reduced side-effects. Finally, we conducted *in vivo* studies on inbred female immunocompetent C57Bl/6J mice. Here, we treated the mice with plasma-treated liquid by using treatment times of 20 minutes and 1 hour. The treatment of the mice with the liquid was followed by an ECT treatment or by a treatment with bleomycin, an anti-cancer drug. The purpose of this study was the achievement of the same level of permeabilization of tumor cells (and therefore the same

efficacy of ECT) with less intense and therefore more “comfortable” electrical pulses. For this purpose, immunocompetent C57Bl/6J mice bearing s.c. LPB tumors were treated with the combination of pPBS and ECT under conditions which did not cause any toxicity, and which were already used in clinics. These are the pPBS and the murine LPB fibrosarcoma cells utilized previously for *in vitro* studies, as described in the second and third parts of this chapter. As a future work, the capability of plasma to permeabilize the cellular membrane should be studied in detail. More specifically, the short- and intermediate-lived reactive species that are responsible for the permeabilization of the cellular membrane should be identified. On top of that, it is important that for plasma to be considered as an efficient anti-cancer strategy alone, or in combination with ECT, more *in vivo* and clinical studies are required. Finally, and to facilitate the translation of *in vitro* to *in vivo* studies, more relevant *in vitro* models should be used to better mimic the *in vivo* situation.

List of publications

Peer reviewed journals

1. Chung, T.-H.; Stancampiano, A.; **Sklias, K.**; Gazeli, K.; André, F.M.; Dozias, S.; Douat, C.; Pouvesle, J.-M.;Santos Sousa, J.; Robert, É.; Mir, L.M. Cell Electropermeabilisation Enhancement by Non-Thermal-Plasma-Treated PBS Cancers 12, 219 (2020)

2. **Sklias, K.**; Santos Sousa, J. & Girard, P.-M. Role of short- and long-lived reactive species on the selectivityand anti-cancer action of plasma treatment in vitro Cancers 13, 615 (2021)

3. **Sklias, K.**; Chung, T.-H.; Stancampiano, A.; Gazeli, K.; Darny, T.; Bauville, G.; André, F.M.; Dozias, S.; Douat, C.; Pouvesle, J.-M.; Robert, E.; Mir, L.M.; Santos Sousa, J. Preserving the anti-cancer efficacy of plasma-treated solutions over time: a prerequisite for their clinical application. (In preparation – to be submitted at Scientific Reports)

4. Chung T.-H., **Sklias K.**, M. André F., Polrot M., Stancampiano A., Gazeli K., Darny T., Bauville G., Dozias S., Douat C., Pouvesle J.-M., Robert É., Santos Sousa J. and Mir L. M. In vivo studies of non-thermal plasma and its combination with electrochemotherapy (In preparation)

COMMUNICATIONS

International:

1. TRIC - Therapeutic ROS and Immunity in Cancer, 15-17 July 2021, Greifswald, Germany (co-presenter at Oral presentation)

2. 6th International Workshop on Plasma for Cancer Treatment (IWPCT-2019), 1-3 April 2019,Antwerp, Belgium (co-author at Oral presentation)

3. 7th International Workshop on Plasma for Cancer Treatment (IWPCT-2021), 29-30 June 2021,Barcelona, Spain (Oral and Poster presentations)

4. 8th International Conference on Plasma Medicine (ICPM – 2021), 3-6 August 2021, Korea (Oral and Poster presentations)

5. 3rd World Congress on Electroporation and Pulsed Electric Fields in Biology, Medicine, Food & Environmental Technologies, Toulouse, France, September 2-6, 2019

6. 9th International Conference on Plasma Medicine (ICPM – 2022), 27 June - 1 July 2022, Utrecht, Netherlands (Invited Oral presentation)

National:

GDR-Happy bio-2018, La Rochele, France

GDR-Happy bio-2019, 4-6 November 2019, Nouan le Fuzelier, France (Oral presentation)

GDR-Happy bio-2020, 12-13 November 2020 (2 Oral presentations)

GDR-Emili, 25-28 October 2021, Paris, France

References

1. Urruticoechea, A. *et al.* Recent Advances in Cancer Therapy : An Overview. *Curr. Pharm. Des.* **16**, 3–10 (2010).
2. Kim, S. New and emerging factors in tumorigenesis : an overview. *Cancer Manag. Res.* **28**, 225–239 (2015).
3. Caiado, F., Silva-santos, B. & Norell, H. Intra-tumour heterogeneity – going beyond genetics. *FEBS J.* **283**, 2245–2258 (2016).
4. Kieft, I. E., Broers, J. L. V, Slaaf, D. W., Ramaekers, F. C. S. & Stoffels, E. Electric Discharge Plasmas Influence Attachment of Cultured CHO K1 Cells. *Bioelectromagnetics* **368**, 362–368 (2004).
5. Dubuc, A. *et al.* Use of cold-atmospheric plasma in oncology : a concise systematic review. *Ther. Adv. Med. Oncol.* **20**, 1758835918786475 (2018).
6. Schlegel, J., Köritzer, J. & Box-, V. Plasma in Cancer Treatment. *Clin. Plasma Med.* **1**, 2–7 (2013).
7. Yan, D., Sherman, J. H. & Keidar, M. Cold atmospheric plasma , a novel promising anti-cancer treatment modality. *Oncotarget* **8**, 15977–15995 (2017).
8. Gümbel, D. *et al.* Cold Atmospheric Plasma in the Treatment of Osteosarcoma. *Int J Mol Sci.* **18**, 1–13 (2017).
9. Vandamme, M. *et al.* Effects of a Non Thermal Plasma Treatment Alone or in Combination with Gemcitabine in a MIA PaCa2-luc Orthotopic Pancreatic Carcinoma Model. *PLoS One* **7**, 1–10 (2012).
10. Boxhammer, V. *et al.* Restoration of Sensitivity in Chemo — Resistant Glioma Cells by Cold Atmospheric Plasma. *PLoS One* **8**, (2013).
11. Conway, G. E. *et al.* Non-thermal atmospheric plasma induces ROS-independent cell death in U373MG glioma cells and augments the cytotoxicity of temozolomide. *Br J Cancer* **114**, 435–443 (2016).
12. Chung, T. H. *et al.* Cell electropermeabilisation enhancement by non-thermal-plasma-treated PBS. *Cancers (Basel).* **16**, 219 (2020).
13. Kim, G. C. *et al.* Air plasma coupled with antibody-conjugated nanoparticles: a new weapon against cancer. *J. Phys. D Appl. Phys.* **42**, 032005 (2009).
14. Zhu, W. *et al.* Synergistic Effect of Cold Atmospheric Plasma and Drug Loaded Core-shell Nanoparticles on Inhibiting Breast Cancer Cell Growth. *Sci. Rep.* **6**, 21974 (2016).
15. Jalili, A., Irani, S. & Mirfakhraie, R. Combination of cold atmospheric plasma and iron nanoparticles in breast cancer : gene expression and apoptosis study. *Onco Targets Ther.* **9**, 5911–5917 (2016).
16. Aryal, S. & Bisht, G. New Paradigm for a Targeted Cancer Therapeutic

Approach : A Short Review on Potential Synergy of Gold Nanoparticles and Cold Atmospheric Plasma. *Biomedicines* **5**, 38 (2017).
17. Moniruzzaman, R., Rehman, M. U., Zhao, Q., Jawaid, P. & Takeda, K. Cold atmospheric helium plasma causes synergistic enhancement in cell death with hyperthermia and an additive enhancement with radiation. *Sci. Rep.* **7**, 11659 (2017).
18. Lin, A. G., Xiang, B., Merlino, D. J., Snook, A. E. & Miller, V. Non-thermal plasma induces immunogenic cell death in vivo in murine CT26 colorectal tumors. *Oncoimmunology* **7**, 1–13 (2018).
19. Wang, M., Geilich, B. M., Keidar, M. & Webster, T. J. Killing malignant melanoma cells with mediated photodynamic therapy and cold atmospheric plasma. *Int J Nanomedicine* **12**, 4117–4127 (2017).
20. Cheng, X. *et al.* Enhancing Cold Atmospheric Plasma Treatment of Cancer Cells by Static Magnetic Field. *Bioelectromagnetics* **38**, 53–62 (2016).
21. Semmler, M. L. *et al.* Molecular Mechanisms of the E ffi cacy of Cold Cancer Treatment. *Cancers (Basel).* **12**, 1–19 (2020).
22. Gorbanev, Y., Connell, D. O. & Chechik, V. Non-Thermal Plasma in Contact with Water : The Origin of Species. *Chem. Eur.J.* **22**, 3496–3505 (2016).
23. Gorbanev, Y., Privat-maldonado, A. & Bogaerts, A. Analysis of short-lived reactive species in plasma- air-water systems : The do ' s and the don ' ts. *Anal. Chem.* **90**, 13151–13158 (2018).
24. Graves, D. B. The emerging role of reactive oxygen and nitrogen species in redox biology and some implications for plasma applications to medicine and biology. *J. Phys. D. Appl. Phys.* **45**, 1–42 (2012).
25. Hirst, A. M., Frame, F. M., Arya, M., Maitland, N. J. & Connell, D. O. Low temperature plasmas as emerging cancer therapeutics : the state of play and thoughts for the future. *Tumor Biol.* **37**, 7021–7031 (2016).
26. Bauer, G. & Graves, D. B. Mechanisms of Selective Antitumor Action of Cold Atmospheric Plasma-Derived Reactive Oxygen and Nitrogen Species. *Plasma Process Polym* **13**, 1157–1178 (2016).
27. Jablonowski, H. & Woedtke, T. Von. Research on plasma medicine-relevant plasma-liquid interaction: What happened in the past five years? *Clin. Plasma Med.* **3**, 42–52 (2015).
28. Brisset, J. L. & Pawlat, J. Chemical Effects of Air Plasma Species on Aqueous Solutes in Direct and Delayed Exposure Modes: Discharge, Post-discharge and Plasma Activated Water. *Plasma Chem. Plasma Process.* **36**, 355–381 (2016).
29. Bauer, G., Sersenová, D., Graves, D. B. & Machala, Z. Cold Atmospheric Plasma and Plasma-Activated Medium Trigger RONS-Based Tumor Cell Apoptosis. *Sci. Rep.* **9**, 1–28 (2019).
30. Jablonowski, H., San, J., Weltmann, K., Wende, K. & Reuter, S. Quantification of the ozone and singlet delta oxygen produced in gas and liquid phases

by a non- thermal atmospheric plasma with relevance for medical treatment. *Sci. Rep.* **8**, 1–12 (2018).
31. Bruggeman, P. J. *et al.* Plasma-liquid interactions: A review and roadmap. *Plasma Sources Sci. Technol.* **25**, 053002 (2016).
32. Winter, J., Tresp, H., Hammer, M. U., Iseni, S. & Kupsch, S. Tracking plasma generated H 2 O 2 from gas into liquid phase and revealing its dominant impact on human skin cells. *J. Phys. D Appl. Phys.* **47**, 285401 (2014).
33. Bekeschus, S. *et al.* Hydrogen peroxide: A central player in physical plasma-induced oxidative stress in human blood cells. *Free Radic. Res.* **48**, 542–549 (2014).
34. Jo, A., Joh, H. M., Chung, T. H. & Chung, J. W. Anticancer Effects of Plasma-Activated Medium Produced by a Microwave-Excited Atmospheric Pressure Argon Plasma Jet. *Oxidative Med. Cell. Longev* 1–17 (2020).
35. Balzer, J., Heuer, K., Demir, E., Hoffmanns, M. A. & Baldus, S. Non-Thermal Dielectric Barrier Discharge (DBD) Effects on Proliferation and Differentiation of Human Fibroblasts Are Primary Mediated by Hydrogen Peroxide. *PLoS One* **10**, 1–18 (2015).
36. Mohades, S., Laroussi, M., Sears, J., Barekzi, N. & Razavi, H. Evaluation of the effects of a plasma activated medium on cancer cells. *Phys. Plasmas* **22**, 122001 (2015).
37. Lee, S. J., Kaushik, N. K. & Choi, E. H. Responses of Solid Tumor Cells in DMEM to Reactive Oxygen Species Generated by Non-Thermal Plasma and Chemically Induced ROS Systems. *Sci. Rep.* **5**, 1–11 (2015).
38. Yang, H. *et al.* Effects of atmospheric pressure cold plasma on human hepatocarcinoma cell and its 5-fluorouracil resistant cell line. *Phys. Plasmas* **22**, 122006 (2015).
39. Sklias, K., Sousa, J. S. & Girard, P. Role of short- and long-lived reactive species on the selectivity and anti-cancer action of plasma treatment in vitro. *Cancers (Basel).* **13**, 1–29 (2020).
40. Girard, P. M. *et al.* Synergistic Effect of H2O2and NO2in Cell Death Induced by Cold Atmospheric He Plasma. *Sci. Rep.* **6**, 1–17 (2016).
41. Dezest, M. *et al.* Mechanistic insights into the impact of Cold Atmospheric Pressure Plasma on human epithelial cell lines. *Sci. Rep.* **7**, 1–17 (2017).
42. Boxem, W. Van, Paal, J. Van Der, Gorbanev, Y., Vanuytsel, S. & Smits, E. Anti-cancer capacity of plasma- treated PBS : effect of chemical composition on cancer cell cytotoxicity. *Sci. Rep.* **7**, 1–15 (2017).
43. Kurake, N. *et al.* Cell survival of glioblastoma grown in medium containing hydrogen peroxide and/or nitrite, or in plasma-activated medium. *Arch. Biochem. Biophys.* **605**, 1–11 (2016).
44. Griseti, E. et al. Anti-Cancer Potential of Two Plasma-Activated Liquids : Implication of Long-Lived Reactive Oxygen. *Cancers (Basel).* **12**, 1–15 (2020).

45. Tanaka, H. *et al.* New Hopes for Plasma-Based Cancer Treatment. *Plasma* **1**, 150–155 (2018).
46. Utsumi, F. *et al.* Effect of indirect nonequilibrium atmospheric pressure plasma on anti-proliferative activity against chronic chemo-resistant ovarian cancer cells in vitro and in vivo. *PLoS One* **8**, 1–10 (2013).
47. Haertel, B. & Ha, M. Surface molecules on HaCaT keratinocytes after interaction with non-thermal atmospheric pressure plasma. *Cell Biol. Int.* **36**, 1217–1222 (2012).
48. Strassenburg, S. *et al.* Comparison of Biological Effects on Human Keratinocytes Using Different Plasma Treatment Regimes. *Plasma Med.* **3**, 57–69 (2013).
49. Zhang, H. *et al.* Effects and Mechanism of Atmospheric-Pressure Dielectric Barrier Discharge Cold Plasma on Lactate Dehydrogenase (LDH) Enzyme. *Sci. Rep.* **5**, 1–12 (2015).
50. Li, Y. F. *et al.* In vivo skin treatment using two portable plasma devices: comparison of a 3 direct and an indirect cold atmospheric plasma treatment. *Clin. Plasma Med.* **1**, 35–39 (2013).
51. Chen, Z. *et al.* A Novel Micro Cold Atmospheric Plasma Device for Glioblastoma Both In Vitro and In Vivo. *Cancers (Basel).* **9**, 1–16 (2017).
52. Saadati, F., Mahdikia, H., Abbaszadeh, H. & Abdollahifar, M. Comparison of Direct and Indirect cold atmospheric-pressure plasma methods in the B 16 F 10 melanoma cancer cells treatment. *Sci. Rep.* **8**, 1–15 (2018).
53. Privat-Maldonado, Angela, Yury Gorbanev, Evelien Smits, A. B. Reduction of Human Glioblastoma Spheroids Using Cold Atmospheric Plasma : The Combined Effect of Short- and Long-Lived Reactive Species. *Cancers (Basel).* **10**, 394 (2018).
54. Kalghatg, S., Cerchar, E., Azizkhan-Clifford, J., Fridman, A. & Friedman, G. Selectivity of non-thermal atmospheric pressure microsecond pulsed dielectric barrier discharge plasma induced apoptosis in malignant cells over normal cells. *Plasma Med.* **1**, 1–1 (2010).
55. Iseki, S. *et al.* Selective killing of ovarian cancer cells through induction of apoptosis by nonequilibrium atmospheric pressure plasma Selective killing of ovarian cancer cells through induction of apoptosis by nonequilibrium atmospheric pressure plasma. *Appl. Phys. Lett.* **100**, 113702 (2013).
56. Guerrero-Preston, R. *et al.* Cold atmospheric plasma treatment selectively targets head and neck squamous cell carcinoma cells. *Int. J. Mol. Med.* **34**, 941–946 (2014).
57. Utsumi, F. *et al.* Selective cytotoxicity of indirect nonequilibrium atmospheric pressure plasma against ovarian clear-cell carcinoma. *Springerplus* **3**, 1–9 (2014).
58. Keidar, M. *et al.* Cold plasma selectivity and the possibility of a paradigm shift in cancer therapy. *Br. J. Cancer* **105**, 1295–1301 (2011).

59. Kim, S. J. & Chung, T. H. Cold atmospheric plasma jet-generated RONS and their selective effects on normal and carcinoma cells. *Sci. Rep.* **6**, 1–14 (2016).
60. Hirst, A. M. *et al.* Low-temperature plasma treatment induces DNA damage leading to necrotic cell death in primary prostate epithelial cells. *Br. J. Cancer* **112**, 1536–1545 (2015).
61. Biscop, E. *et al.* Influence of cell type and culture medium on determining cancer selectivity of cold atmospheric plasma treatment. *Cancers (Basel).* **11**, 1–14 (2019).
62. Yan, D. *et al.* Principles of using Cold Atmospheric Plasma Stimulated Media for Cancer Treatment. *Sci. Rep.* **5**, 1–17 (2015).
63. Yan, D. *et al.* The Strong Cell-based Hydrogen Peroxide Generation Triggered by Cold Atmospheric Plasma. *Sci. Rep.* **7**, 1–9 (2017).
64. Shen, J. *et al.* Bactericidal Effects against S . aureus and Physicochemical Properties of Plasma Activated Water stored at different temperatures. *Sci. Rep.* **6**, 1–10 (2016).
65. Judée, F., Fongia, C., Ducommun, B. & Yousfi, M. Short and long time effects of low temperature Plasma Activated Media on 3D multicellular tumor spheroids. *Sci. Rep.* **6**, 1–12 (2016).
66. Yan, D. *et al.* Stabilizing the cold plasma- stimulated medium by regulating medium ' s composition. *Sci. Rep.* **6**, 1–11 (2016).
67. Kaushik, N. K. *et al.* Biological and medical applications of plasma-activated media, water and solutions. *Biol. Chem.* **400**, 39–62 (2018).
68. Ghimire, B. *et al.* The effect of the gap distance between an atmospheric-pressure plasma jet nozzle and liquid surface on OH and N2 species concentrations. *Phys. Plasmas* **24**, 073502 (2017).
69. Anbar, M. & Taube, H. Interaction of Nitrous Acid with Hydrogen Peroxide and with Water. *J. Am. Chem. Soc.* **76**, 6243–6247 (1954).
70. Fridman, A. *Plasma Chemistry*. (2008).
71. Woedtke, T. Von, Reuter, S., Masur, K. & Weltmann, K. Plasmas for medicine. *Phys. Rep.* **530**, 291–320 (2013).
72. Lieberman,Lichtenberg,_Principles_of_Plasma_Discharges.pdf.
73. von Woedtke, T., Reuter, S., Masur, K. & Weltmann, K. D. Plasmas for medicine. *Phys. Rep.* **530**, 291–320 (2013).
74. Laroussi, M. & Lu, X. Room-temperature atmospheric pressure plasma plume for biomedical applications. *Appl. Phys. Lett.* **87**, 113902 (2005).
75. Laroussi, M. & Akan, T. Arc-free atmospheric pressure cold plasma jets: A review. *Plasma Process. Polym.* **4**, 777–788 (2007).
76. Kolb, J. F. *et al.* Cold atmospheric pressure air plasma jet for medical applications. *Appl. Phys. Lett.* **92**, 24–27 (2008).
77. Xiong, Q. *et al.* Temporal and spatial resolved optical emission behaviors of a cold atmospheric pressure plasma jet. *J. Appl. Phys.* **106**, 083302 (2009).

78. Kim, K., Kim, G., Hong, Y. C. & Yang, S. S. A cold micro plasma jet device suitable for bio-medical applications. *Microelectron. Eng.* **87**, 1177–1180 (2010).
79. Bárdos, L. & Baránková, H. Cold atmospheric plasma: Sources, processes, and applications. *Thin Solid Films* **518**, 6705–6713 (2010).
80. Förster, S., Mohr, C. & Viöl, W. Investigations of an atmospheric pressure plasma jet by optical emission spectroscopy. *Surf. Coatings Technol.* **200**, 827–830 (2005).
81. Ni, T. L., Ding, F., Zhu, X. D., Wen, X. H. & Zhou, H. Y. Cold microplasma plume produced by a compact and flexible generator at atmospheric pressure. *Appl. Phys. Lett.* **92**, 2006–2009 (2008).
82. Larousi M. Low Temperature Plasma for Biology, Hygiene, and Medicine: Perspective and Roadmap Perspective and Roadmap. *IEEE Trans. Radiat. Plasma Med. Sci.* 1–64 (2021).
83. Laroussi, M. Cold Plasma in Medicine and Healthcare: The New Frontier in Low Temperature Plasma Applications. *Front. Phys.* **8**, 1–7 (2020).
84. BARTNIKAS, R. Note on discharges in helium under a.c. conditions. **659**, 22–25 (1968).
85. S Kanazawa, M Kogoma, T. M. and S. O. Stable glow plasma at atmospheric pressure. *J. Phys. D Appl. Phys.* **21**, 836-840. (1988).
86. Svarnas, P. *et al.* Liposomal membrane disruption by means of miniaturized dielectric-barrier discharge in air : liposome characterization. *J. Phys. D. Appl. Phys.* **50**, 345403 (2017).
87. T Yokoyama, M Kogoma, T. M. and S. O. The mechanism of the stabilisation of glow plasma at atmospheric pressure. *J. Phys. D Appl. Phys.* **23**, 1125–1128 (1990).
88. Lovascio, S., Jorand, F., Jeanney, P. & Pasquiers, S. Ethanol / Acetone Mixtures Conversion in Air Dielectric Barrier Discharges. *Int. J. Plasma Environ. Sci. Technol.* **6**, 111–118 (2012).
89. Keidar, M. *Plasma Cancer Therapy*. (2020).
90. Zhang, Q. *et al.* Measurement of the electron density in a microwave plasma torch at atmospheric pressure. *Appl. Phys. Lett.* **97**, 113306 (2009).
91. Gazeli, K., Svarnas, P., Held, B., Marlin, L. & Clément, F. Possibility of controlling the chemical pattern of He and Ar 'guided streamers' by means of N2 or O2 additives. *J. Appl. Phys.* **117**, 093302 (2015).
92. Gazeli, K. *et al.* Effect of the gas flow rate on the spatiotemporal distribution of Ar(1s5) absolute densities in a ns pulsed plasma jet impinging on a glass surface. *Plasma Sources Sci. Technol.* **27**, 065003 (2018).
93. Lei, X. & Fang, Z. DBD plasma jet in atmospheric pressure neon. *IEEE Trans. Plasma Sci.* **39**, 2288–2289 (2011).
94. Li, L. *et al.* OH radicals distribution in an Ar-H2O atmospheric plasma jet

OH radicals distribution in an Ar-H 2 O atmospheric plasma jet. *Phys. Plasmas* **20**, 093502 (2013).
95. Li, Q., Zhu, W. C., Zhu, X. M. & Pu, Y. K. Effects of Penning ionization on the discharge patterns of atmospheric pressure plasma jets. *J. Phys. D. Appl. Phys.* **43**, 382001 (2010).
96. Ngo Thi, M. H., Shao, P. L., Liao, J. Der, Lin, C. C. K. & Yip, H. K. Enhancement of angiogenesis and epithelialization processes in mice with burn wounds through ROS/RNS signals generated by non-thermal N2/Ar micro-plasma. *Plasma Process. Polym.* **11**, 1076–1088 (2014).
97. Lu, X., Laroussi, M. & Puech, V. On atmospheric-pressure non-equilibrium plasma jets and plasma bullets. *Plasma Sources Sci. Technol.* **21**, 034005 (2012).
98. Winter, J., Brandenburg, R. & Weltmann, K. Atmospheric pressure plasma jets : an overview of devices and new directions. *Plasma Sources Sci. Technol.* **24**, 64001 (2015).
99. Pei, X., Kredl, J., Lu, X. & Kolb, J. F. Discharge modes of atmospheric pressure DC plasma jets operated with air or nitrogen. *J. Phys. D. Appl. Phys.* **51**, 384001 (2018).
100. Xiong, Q., Yang, Z. & Bruggeman, P. J. Absolute OH density measurements in an atmospheric pressure dc glow discharge in air with water electrode by broadband UV absorption spectroscopy. *J. Phys. D. Appl. Phys.* **48**, 424008 (2015).
101. Bruggeman, P., Cunge, G. & Sadeghi, N. Absolute OH density measurements by broadband UV absorption in diffuse atmospheric-pressure HeH 2O RF glow discharges. *Plasma Sources Sci. Technol.* **21**, 035019 (2012).
102. Al-Shamma'a, A. I., Wylie, S. R., Lucas, J. & Pau, C. F. Design and construction of a 2.45 GHz waveguide-based microwave plasma jet at atmospheric pressure for material processing. *J. Phys. D. Appl. Phys.* **34**, 2734–2741 (2001).
103. Schmidt, H. C. and M. Plasma generation and plasma sources. *Plasma Sources Sci. Technol.* **9**, 441–454 (2000).
104. Schoenbach, K. H., El-Habachi, A., Shi, W. & Ciocca, M. High-pressure hollow cathode discharges. *Plasma Sources Sci. Technol.* **6**, 468–477 (1997).
105. SOUSA, J. S. MICROPLASMA GENERATION OF HIGH FLUXES OF SINGLET DELTA OXYGEN AT ATMOSPHERIC PRESSURE FOR BIOMEDICAL APPLICATIONS. (2010).
106. Stark, R. H. & Schoenbach, K. H. Direct current glow discharges in atmospheric air. *Appl. Phys. Lett.* **74**, 3770–3772 (1999).
107. Santos Sousa, J., Bauville, G., Lacour, B., Puech, V. & Touzeau, M. ATMOSPHERIC PRESSURE GENERATION OF O2(a1Δg) BY MICROPLASMAS. in **2**, 1–7 (2008).

108. Gardoni, D., Vailati, A. & Canziani, R. Decay of Ozone in Water : A Review. **34**, 233–242 (2012).
109. Papadopoulos, P. K. *et al.* Interpretation of the gas flow field modification induced by guided streamer ('plasma bullet') propagation. *J. Phys. D. Appl. Phys.* **47**, 425203 (2014).
110. Lu, X., Naidis, G. V., Laroussi, M. & Ostrikov, K. Guided ionization waves: Theory and experiments. *Phys. Rep.* **540**, 123–166 (2014).
111. Boeuf, J. P., Yang, L. L. & Pitchford, L. C. Dynamics of a guided streamer ('plasma bullet') in a helium jet in air at atmospheric pressure. *J. Phys. D. Appl. Phys.* **46**, 015201 (2013).
112. Hofmans, M. & Sobota, A. Influence of a target on the electric field profile in a kHz atmospheric pressure plasma jet with the full calculation of the Stark shifts. *J. Appl. Phys.* **125**, 043303 (2019).
113. Muraoka, K. & Maeda, M. *Laser-aided diagnostics of plasmas and gases*. (2001).
114. Magne, L. & Pasquiers, S. LIF spectroscopy applied to the study of non-thermal plasmas for atmospheric pollutant abatement. *Comptes Rendus Phys.* **6**, 908–917 (2005).
115. Griem, H. R. *Cambridge Books Online*. *Choice Reviews Online* **48**, (2010).
116. Torres, J. *et al.* An easy way to determine simultaneously the electron density and temperature in high-pressure plasmas by using Stark broadening. *J. Phys. D. Appl. Phys.* **36**, L55–L59 (2003).
117. Obradović, B. M., Ivković, S. S. & Kuraica, M. M. Spectroscopic measurement of electric field in dielectric barrier discharge in helium. *Appl. Phys. Lett.* **92**, 2–5 (2008).
118. Cardoso, R. P., Belmonte, T., Keravec, P., Kosior, F. & Henrion, G. Influence of impurities on the temperature of an atmospheric helium plasma in microwave resonant cavity. *J. Phys. D. Appl. Phys.* **40**, 1394–1400 (2007).
119. Svarnas, P. *et al.* Parametric study of thermal effects in a capillary dielectric-barrier discharge related to plasma jet production: Experiments and numerical modelling. *J. Appl. Phys.* **124**, 064902 (2018).
120. Huber, G. H. and K. P. *MOLECULAR SPECTRA and MOLECULAR STRUCTURE*. (1979).
121. Cavendish, H. *The Law of Force of Electricity*.
122. Girard, P. M. *et al.* Synergistic Effect of H2O2 and NO2 in Cell Death Induced by Cold Atmospheric He Plasma. *Sci. Rep.* **6**, 1–17 (2016).
123. Khlyustova, A., Labay, C., Machala, Z., Ginebra, M. P. & Canal, C. Important parameters in plasma jets for the production of RONS in liquids for plasma medicine: A brief review. *Front. Chem. Sci. Eng.* **13**, 238–252 (2019).
124. Wende, K. *et al.* Identification of the biologically active liquid chemistry induced by a nonthermal atmospheric pressure plasma jet. *Biointerphases* **10**, 029518 (2015).

125. Renwu Zhou, Rusen Zhou, Peiyu Wang, Yubin Xian, A. M.-P. & Xinpei Lu, P. J. Cullen, K. (Ken) O. and K. B. Plasma activated water (PAW): generation, origin of reactive species and biological applications. *J. Phys. D. Appl. Phys.* **53**, 303001 (2020).
126. Machala, Z., Tarabov, B., Sersenov, D. & Janda, M. Chemical and antibacterial effects of plasma activated water : correlation with gaseous and aqueous reactive oxygen and nitrogen species , plasma sources and air flow conditions. *J. Phys. D. Appl. Phys.* **52**, 034002 (2019).
127. Shams El Din, A. M. & Mohammed, R. A. Kinetics of the reaction between hydrogen peroxide and hypochlorite. *Desalination* **115**, 145–153 (1998).
128. Stancampiano, A. *et al.* Mimicking of human body electrical characteristic for easier translation of plasma biomedical studies to clinical applications. *IEEE Trans. Radiat. Plasma Med. Sci.* **4**, 335–342 (2019).
129. Sousa, J. S., Bauville, G., Lacour, B., Puech, V. & Touzeau, M. Atmospheric pressure generation of O2(a1 Δg) by microplasmas. *EPJ Appl. Phys.* **47**, 1–7 (2009).
130. Bauville, G. *et al.* Singlet oxygen production in a microcathode sustained discharge. *Appl. Phys. Lett.* **90**, 3–6 (2007).
131. Sousa, J. S. *et al.* O2 (a Δ1 g) production at atmospheric pressure by microdischarge. *Appl. Phys. Lett.* **93**, 1–4 (2008).
132. Sousa, J. S. *et al.* DNA oxidation by singlet delta oxygen produced by atmospheric pressure microdischarges. *Appl. Phys. Lett.* **97**, 28–31 (2010).
133. Kuraica, M. M. & Konjević, N. Electric field measurement in the cathode fall region of a glow discharge in helium. *Appl. Phys. Lett.* **70**, 1521–1523 (1997).
134. J., F. S. Application of Quantum Mechanics to the Stark Effect in Helium. *Proc. R. Soc. Lond.* **117**, 137–163 (1927).
135. Martin, W. C. Energy Levels of Neutral Helium (4He I). *J. Phys. Chem. data* **2**, 257 (2012).
136. Griem, H. R. & Kolb, A. C. STARK PROFILE CALCULATIONS FOR THE Hß LINE OF HYDROGEN*. *Am. Astron. Soc.* 272–276 (1961).
137. Griem, P. K. and H. R. Improved Stark Profile Calculations for the Hydrogen Lines Hn, HP, Hy, and Hδ*. *Phys. Rev.* **395**, 317–325 (1967).
138. Griem, H. R. & Peach, G. Spectral Line Broadening by Plasmas. **28**, 61 (1975).
139. Zheng, Y., Wang, L., Ning, W. & Jia, S. Schlieren imaging investigation of the hydrodynamics of atmospheric helium plasma jets. *J. Appl. Phys.* **119**, 123301 (2016).
140. Gigosos, M. A. & Cardeñoso, V. New plasma diagnosis tables of hydrogen Stark broadening including ion dynamics. *J. Phys. B At. Mol. Opt. Phys.* **29**, 4795–4838 (1996).
141. Tarabová, B. *et al.* Fluorescence measurements of

peroxynitrite/peroxynitrous acid in cold air plasma treated aqueous solutions. *Phys. Chem. Chem. Phys.* **21**, 8883–8896 (2019).
142. Bader, H. & Hoigné, J. Determination of ozone in water by the indigo method. *Water Res.* **15**, 449–456 (1981).
143. Lin, H. *et al.* Feasibility Study on Quantitative Measurements of Singlet Oxygen Generation Using Singlet Oxygen Sensor Green. *J Fluoresc* **23**, 41–47 (2013).
144. Kanazawa, S., Furuki, T., Nakaji, T., Akamine, S. & Ichiki, R. Measurement of OH radicals in aqueous solution produced by atmospheric-pressure LF plasma jet. *Int. J. Plasma Environ. Sci. Technol.* **6**, 166–171 (2012).
145. Ghorbel, A., Mir, L. M. & García-Sánchez, T. Conductive nanoparticles improve cell electropermeabilization. *Nanotechnology* **30**, 495101 (2019).
146. Reis, A., Domingues, M. R. M., Amado, F. M. L., Ferrer-Correia, A. J. V. & Domingues, P. Separation of peroxidation products of diacyl-phosphatidylcholines by reversed-phase liquid chromatography-mass spectrometry. *Biomed. Chromatogr.* **19**, 129–137 (2005).
147. Xian, Y. *et al.* From short pulses to short breaks: exotic plasma bullets via residual electron control. *Sci. Rep.* **3**, 1–6 (2013).
148. Jarrige, J., Laroussi, M. & Karakas, E. Formation and dynamics of plasma bullets in a non-thermal plasma jet: Influence of the high-voltage parameters on the plume characteristics. *Plasma Sources Sci. Technol.* **19**, 065005 (2010).
149. Rols, M. Electropermeabilization , a physical method for the delivery of therapeutic molecules into cells. **1758**, 423–428 (2006).
150. Krsti, I. B. Spatio-temporally resolved electric field measurements in helium plasma jet This. *J. Phys. D. Appl. Phys.* **47**, 102001 (2014).
151. Begum, A., Laroussi, M. & Pervez, M. R. Atmospheric pressure He-air plasma jet : Breakdown process and propagation phenomenon. *AIP Adv.* **3**, 0–16 (2013).
152. Morabit, Y. *et al.* A review of the gas and liquid phase interactions in low-temperature plasma jets used for biomedical applications. *Eur. Phys. J. D* **75**, 1–26 (2021).
153. Vesna V. Kovačević, Goran B. Sretenović, Elmar Slikboer, Olivier Guaitella, A. S. and M. M. K. The effect of liquid target on a nonthermal plasma jet – imaging, electric fields, visualization of gas flow and optical emission spectroscopy. **51**, 065202 (2017).
154. Bourdon, A. & Darny, T. Numerical and experimental study of the dynamics of a μ s helium plasma gun discharge with various amounts of N 2 admixture. *Plasma Sources Sci. Technol.* **25**, 035002 (2016).
155. Liu, F., Zhang, D. & Wang, D. The in fl uence of air on streamer propagation in atmospheric pressure cold plasma jets. *Thin Solid Films* **521**, 261–264 (2012).

156. Bruggeman, P. J. *et al.* Plasma-liquid interactions: A review and roadmap. *Plasma Sources Sci. Technol.* **25**, 053002 (2016).
157. Girard, F. *et al.* Correlations between gaseous and liquid phase chemistries induced by cold atmospheric plasmas in a physiological buffer. *Phys. Chem. Chem. Phys.* **20**, 9198–9210 (2018).
158. Lu, X. *et al.* Reactive species in non-equilibrium atmospheric-pressure plasmas: Generation, transport, and biological effects. *Phys. Rep.* **630**, 1–84 (2016).
159. Cheng, X. *et al.* The Effect of Tuning Cold Plasma Composition on Glioblastoma Cell Viability. *PLoS One* **9**, 1–9 (2014).
160. Invernizzi, L. *Étude de microjets de plasma comme sources d ' espèces réactives pour des applications biomédicales Laurent Invernizzi Table des matières Remerciements*. (2016).
161. Tampieri, F., Ginebra, M. & Canal, C. Quantification of Plasma-Produced Hydroxyl Radicals in Solution and their Dependence on the pH. *Anal. Chem.* **93**, 3666–3670 (2021).
162. Girard, F. *et al.* Formation of reactive nitrogen species including peroxynitrite in physiological buffer exposed to cold atmospheric plasma. *RSC Adv.* **6**, 78457–78467 (2016).
163. Ikawa, S., Kitano, K. & Hamaguchi, S. Effects of pH on bacterial inactivation in aqueous solutions due to low-temperature atmospheric pressure plasma application. *Plasma Process. Polym.* **7**, 33–42 (2010).
164. Bundscherer, L. *et al.* Non-thermal plasma treatment induces MAPK signaling in human monocytes. *Open Chem.* **13**, 606–613 (2015).
165. Shainsky, N. *et al. Non-Equilibrium Plasma Treatment of Liquids , Formation of Plasma Acid*.
166. Girard, F. *et al.* Formation of Reactive Nitrogen Species including Peroxynitrite in Physiological Buffer exposed to Cold Atmospheric Plasma Received. *RSC Adv.* **82**, 1–11 (2016).
167. Thagard, S. M., Takashima, K. & Mizuno, A. Chemistry of the positive and negative electrical discharges formed in liquid water and above a gas-liquid surface. *Plasma Chem. Plasma Process.* **29**, 455–473 (2009).
168. Miyahara, T., Oizumi, M., Nakatani, T. & Sato, T. Effect of voltage polarity on oxidation-reduction potential by plasma in water. *AIP Adv.* **4**, 0–10 (2014).
169. Yonemori, S. & Ono, R. Effect of discharge polarity on the propagation of atmospheric-pressure helium plasma jets and the densities of OH, NO, and O radicals. *Biointerphases* **10**, 029514 (2015).
170. ANDERSEN, J. E. T. *Modern aspects of electrochemistry*. **148**, (2002).
171. Clavo, B. *et al.* Ozone Therapy as Adjuvant for Cancer Treatment : Is Further Research Warranted ? *Evidence-Based Complement. Altern. Med.* **2018**, (2018).
172. Aboubakr, H. A., Gangal, U., Youssef, M. M., Goyal, S. M. & Bruggeman, P. J.

Inactivation of virus in solution by cold atmospheric pressure plasma: Identification of chemical inactivation pathways. *J. Phys. D. Appl. Phys.* **49**, 204001 (2016).
173. Ragàs, X., Jiménez-Banzo, A., Sánchez-García, D., Batllori, X. & Nonell, S. Singlet oxygen photosensitisation by the fluorescent probe Singlet Oxygen Sensor Green®. *Chem. Commun.* **20**, 2920–2922 (2009).
174. Gollmer, A. *et al.* Singlet Oxygen Sensor Green Ò : Photochemical Behavior in Solution and in a Mammalian Cell. *Photochem. Photobiol.* **87**, 671–679 (2011).
175. Freund, E. *et al.* Physical plasma-treated saline promotes an immunogenic phenotype in CT26 colon cancer cells in vitro and in vivo. *Sci. Rep.* **9**, 1–18 (2019).
176. Sato, Y., Yamada, S., Takeda, S. & Hattori, N. Effect of Plasma-Activated Lactated Ringer ' s Solution on Pancreatic Cancer Cells In Vitro and In Vivo. *Ann. Surg. Oncol.* **25**, 299–307 (2017).
177. Bisag, A. *et al.* Plasma-activated ringer's lactate solution displays a selective cytotoxic effect on ovarian cancer cells. *Cancers (Basel).* **12**, 1–16 (2020).
178. Judée, F., Fongia, C., Ducommun, B. & Yousfi, M. Short and long time effects of low temperature Plasma Activated Media on 3D multicellular tumor spheroids. *Sci. Rep.* **6**, 1–12 (2016).
179. Damschen, D. E. & Martin, L. R. Aqueous aerosol oxidation of nitrous acid by O2, O3 AND H2O2. *Atmos. Environ.* **17**, 2005–2011 (1983).
180. Lukes, P., Dolezalova, E., Sisrova, I. & Clupek, M. Aqueous-phase chemistry and bactericidal effects from an air discharge plasma in contact with water: Evidence for the formation of peroxynitrite through a pseudo-second-order post-discharge reaction of H2O 2 and HNO2. *Plasma Sources Sci. Technol.* **23**, 015019 (2014).
181. Takenaka, N. *et al.* Fast oxidation reaction of nitrite by dissolved oxygen in the freezing process in the tropospheric aqueous phase. *J. Atmos. Chem.* **29**, 135–150 (1998).
182. Tsoukou, E., Bourke, P. & Boehm, D. Temperature Stability and Effectiveness of Plasma-Activated Liquids over an 18 Months Period. *Water* **12**, 3021 (2020).
183. Gómez, G., Pikal, M. J. & Rodríguez-Hornedo, N. Effect of initial buffer composition on pH changes during far-from-equilibrium freezing of sodium phosphate buffer solutions. *Pharm. Res.* **18**, 90–97 (2001).
184. Thorat, A. A. & Suryanarayanan, R. Characterization of Phosphate Buffered Saline (PBS) in Frozen State and after Freeze-Drying. *Pharm. Res.* **36**, 1–11 (2019).
185. Van Den Berg, L. pH changes in buffers and foods during freezing and subsequent storage. *Cryobiology* **3**, 236–242 (1966).
186. Elwell, C. Acceleration of the Gifted. *Gift. Child Q.* **2**, 21–23 (1958).

187. Han, B., Devireddy, R. V. & Bischof, J. C. Phase change behavior of biomedically relevant solutions. in *ASME International Mechanical Engineering Congress and Exposition, Proceedings* 67–75 (2002). doi:10.1115/IMECE2002-32549
188. Lee, Y.-N. & Lind, J. A. Kinetics of aqueous-phase oxidation of nitrogen(III) by hydrogen peroxide. *J. Geophys. Res.* **91**, 2793 (1986).
189. Yan, D. *et al.* The Cell Activation Phenomena in the Cold Atmospheric Plasma Cancer Treatment. *Sci. Rep.* **8**, 1–10 (2018).
190. Robert, E. *et al.* Characterization of pulsed atmospheric-pressure plasma streams (PAPS) generated by a plasma gun. *Plasma Sources Sci. Technol.* **21**, 034017 (2012).
191. Iannelli, F. *et al.* Valproic Acid Synergizes With Cisplatin and Cetuximab in vitro and in vivo in Head and Neck Cancer by Targeting the Mechanisms of Resistance. *Front. Cell Dev. Biol.* **8**, 1–19 (2020).
192. Veroli, G. Y. Di *et al.* Systems biology Combenefit : an interactive platform for the analysis and visualization of drug combinations. **32**, 2866–2868 (2016).
193. SUSAN ELMORE. Apoptosis : A Review of Programmed Cell Death. *Toxicol. Pathol.* **35**, 495–516 (2007).
194. Bauer, G. Interaction Between Cap- Derived Singlet Oxygen And Tumor Cell Protective Catalase: Update And Chances. *Clin. Plasma Med.* **9**, 17–18 (2018).
195. Bauer, G., Sersenová, D., Graves, D. B. & Machala, Z. Dynamics of Singlet Oxygen- Triggered , RONS-Based Apoptosis Induction after Treatment of Tumor Cells with Cold Atmospheric Plasma or Plasma-Activated Medium. *Sci. Rep.* **9**, 1–34 (2019).
196. Bauer, G. The synergistic effect between hydrogen peroxide and nitrite, two long-lived molecular species from cold atmospheric plasma, triggers tumor cells to induce their own cell death. *Redox Biol.* **26**, 101291 (2019).
197. Ault, T. & Hartman, E. SCAVENGING OF SINGLET MOLECULAR OXYGEN BY IMIDAZOLE COMPOUNDS : HIGH AND SUSTAINED ACTIVITIES OF CARBOXY TERMINAL HISTIDINE DIPEPTIDES AND EXCEPTIONAL ACTIVITY OF IMIDAZOLE-4-ACETIC ACID. *Photochem. Photobiol.* **51**, 59–66 (1990).
198. Tykrell, R. E. X. M. SINGLET OXYGEN INVOLVEMENT IN THE INACTIVATION OF CULTURED HUMAN FIBROBLASTS RADIATIONS. *Photochem. Photobiol.* **49**, 407–412 (1989).
199. Girard, P., Graindorge, D., Smirnova, V. & Rigolet, P. Oxidative Stress in Mammalian Cells Impinges on the Cysteines Redox State of Human XRCC3 Protein and on Its Cellular Localization. *PLoS One* **8**, 1–15 (2013).
200. Oh, J., Yajima, H., Hashida, K. & Ono, T. In-situ UV Absorption Spectroscopy for Observing Dissolved Ozone in Water. *J. Photopolym. Sci. Technol.* **29**, 427–432 (2016).

201. John, G. A. S. T. Ozonation of Water: Role of Hydroxyl Radicals as Oxidizing Intermediates. **190**, (1975).
202. Popham, P. L. & Novacky, A. Use of Dimethyl Sulfoxide to Detect Hydroxyl Radical during Bacteria-induced Hypersensitive Reaction1. *Plant Physiol.* **96**, 1157–1160 (1991).
203. Dmso, O. F., The, B. Y. & Radical, H. OXIDATION OF DMSO AND METHANESULFINIC ACID BY THE HYDROXYL RADICAL. *Free Radic. Biol. Med.* **18**, 271–277 (1995).
204. Matthew, B. Preparation and Characterization of Chloramines. *CHLORAMINE Charact.* **132**, 569–585 (1986).
205. Wu, D., Chen, L., Xu, Q., Chen, X. & Yoon, J. Design Principles, Sensing Mechanisms, and Applications of Highly Specific Fluorescent Probes for HOCl/OCl−. *Acc. Chem. Res.* **52**, 2158–2168 (2019).
206. Weiss, S. J., Slivka, A. & Wei, M. Chlorination of Taurine by Human Neutrophils. *Am. Soc. Clin. Investig.* **70**, 598–607 (1982).
207. Ghoneum, A., Abdulfattah, A. Y., Warren, B. O., Shu, J. & Said, N. Redox Homeostasis and Metabolism in Cancer : A Complex Mechanism and Potential Targeted Therapeutics. *Int. J. Mol. Med.* **21**, 3100 (2020).
208. Trachootham, D., Alexandre, J. & Huang, P. Targeting cancer cells by ROS-mediated mechanisms : a radical therapeutic approach ? *Nat. Publ. Gr.* **8**, 579–591 (2009).
209. Mitra, S., Nguyen, L. N., Akter, M. & Park, G. Impact of ROS Generated by Chemical, Physical, and Plasma Techniques on Cancer Attenuation. *Cancers (Basel).* **11**, 1–31 (2019).
210. Gorrini, C., Harris, I. S. & Mak, T. W. Modulation of oxidative stress as an anticancer strategy. *Nat. Publ. Gr.* **12**, 931–947 (2013).
211. Yanannie, D., Nourmohammadijonathan, T., Cheng, H. S. & Keidar, M. Toward understanding the selective anticancer capacity of cold atmospheric plasma — A model based on aquaporins (Review). *Am. Vac. Soc.* **10**, 040801 (2015).
212. Yusupov, M., Paal, J. Van Der, Neyts, E. C. & Bogaerts, A. Synergistic effect of electric field and lipid oxidation on the permeability of cell membrane. *BBA - Gen. Subj.* **1861**, 839–847 (2017).
213. Bengtson, C. & Bogaerts, A. On the Anti-Cancer Effect of Cold Atmospheric Plasma and the Possible Role of Catalase-Dependent Apoptotic Pathways. *Canc* **9**, 33–42 (2020).
214. Attri, P. *et al.* Generation mechanism of hydroxyl radical species and its lifetime prediction during the plasma-initiated ultraviolet (UV) photolysis. *Sci. Rep.* **5**, 1–8 (2015).
215. Perrotti, F. *et al.* Advances in Lipidomics for Cancer Biomarkers Discovery. *Int. J. Mol. Med.* **17**, 1–26 (2016).
216. Casares, D. & Escrib, P. V. Membrane Lipid Composition: Effect on

Membrane and Organelle Structure, Function and Compartmentalization and Therapeutic Avenues. *Int. J. Mol. Med.* **20**, 1–30 (2019).
217. Szlasa, W. Lipid composition of the cancer cell membrane. *J. Bioenerg. Biomembr.* **52**, 321–342 (2020).
218. Meer, G. Van, Voelker, D. R. & Feigenson, G. W. Membrane lipids : where they are and how they behave. *Nat. Publ. Gr.* **9**, 112–124 (2008).
219. Rems, L., Viano, M. & Kasimova, M. A. The contribution of lipid peroxidation to membrane permeability in electropermeabilization: A molecular dynamics study. *Bioelectrochemistry* **125**, 46–57 (2018).
220. Stein, H., Spindler, S., Bonakdar, N., Wang, C. & Sandoghdar, V. Production of isolated giant unilamellar vesicles under high salt concentrations. *Front. Physiol.* **8**, 1–16 (2017).
221. Geertsen, P. F., Rudolf, Z., Sullivan, G. C. O. & Marty, M. Standard operating procedures of the electrochemotherapy : Instructions for the use of bleomycin or cisplatin administered either systemically or locally and electric pulses delivered by the Cliniporator TM by means of invasive or non-invasive electrodes. *EJC Suppl.* **4**, 14–25 (2006).
222. Campana, L. G., Testori, A., Curatolo, P. & Quaglino, P. Treatment efficacy with electrochemotherapy : A multi- institutional prospective observational study on 376 patients with superficial tumors. *Eur. J. Surg. Oncol.* **42**, 1914–1923 (2016).
223. Campana, L. G., Bianchi, G., Mocellin, S., Valpione, S. & Rossi, C. R. Electrochemotherapy Treatment of Locally Advanced and Metastatic Soft Tissue Sarcomas : Results of a Non-Comparative Phase II Study. *World J Surg* **38**, 813–822 (2014).
224. Mir, L. M. *et al.* First clinical trial of cat soft * tissue sarcomas treatment by electrochemotherapy. *Br. J. Cancer* **76**, 1617–1622 (1997).
225. Cemazar, M. *et al.* Electrochemotherapy in Veterinary Oncology. *J Vet Intern Med* **22**, 826–831 (2008).
226. Orlowski, S. & Paoletti, C. TRANSIENT ELECTROPERMEABILIZATION OF CELLS IN CULTURE. *Biochem. Pharmacol.* **37**, 4727–4733 (1988).
227. Marty, M. *et al.* Electrochemotherapy – An easy, highly effective and safe treatment of cutaneous and subcutaneous metastases: Results of ESOPE (European Standard Operating Procedures of Electrochemotherapy) study. *EJC Suppl.* **4**, 3–13 (2006).
228. Gehl, J. *et al.* Updated standard operating procedures for electrochemotherapy of cutaneous tumours and skin metastases. *Acta Oncol. (Madr).* **57**, 874–882 (2018).
229. Matthiessen, L. W. *et al.* Electrochemotherapy for large cutaneous recurrence of breast cancer : A phase II clinical trial Electrochemotherapy for large cutaneous recurrence of breast cancer : A phase II clinical trial. *Acta Oncol. (Madr).* **51**, 713–721 (2012).

230. Breton, M. & Mir, L. M. Bioelectrochemistry Investigation of the chemical mechanisms involved in the electropulsation of membranes at the molecular level. *Bioelectrochemistry* **119**, 76–83 (2018).
231. Roux, S. *et al.* Tumor destruction using electrochemotherapy followed by CpG oligodeoxynucleotide injection induces distant tumor responses. *Cancer Immunol Immunother* **57**, 1291–1300 (2008).
232. Heller, R., Jaroszeski, M., Perrott, R., Messina, J. & Gilbert, G. Effective treatment of B16 melanoma by direct delivery of bleomycin using electrochemotherapy. *Melanoma Res.* **7**, 10–18 (1997).
233. Zucker, S. N. *et al.* Preferential induction of apoptotic cell death in melanoma cells as compared with normal keratinocytes using a non-thermal plasma torch. *Cancer Biol. Ther.* **13**, 1299–1306 (2012).
234. Pasqual-melo, G., Gandhirajan, R. K., Stoffels, I. & Bekeschus, S. Targeting malignant melanoma with physical plasmas. *Clin. Plasma Med.* **10**, 1–8 (2018).